Quantum transport and relaxation in one-dimensional interacting systems

Zur Erlangung des akademischen Grades eines

Doktors der Naturwissenschaften

der Fakultät für Physik
des Karlsruher Instituts für Technologie

genehmigte

DISSERTATION

von

Matthias Bard, M. Sc.
aus St. Wendel

Tag der mündlichen Prüfung: 09.11.2018
Referent: Prof. Dr. Alexander Mirlin
Korreferent: Prof. Dr. Alexander Shnirman

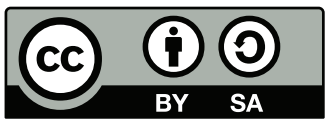

Introduction

The physics of interacting one-dimensional (1D) systems has been fascinating for decades [1–33]. Interaction effects are of crucial importance leading to peculiar phenomena such as spin-charge separation [26, 27] and charge fractionalization [24, 25]. While in the early years the physics in one dimension was studied from the theoretical point of view, nowadays many experimental realizations of 1D systems exist. Early discovered realizations were bulk materials with an internal 1D structure like organic conductors and superconductors [13] as well as ladder compounds [20, 21]. The discovery of the quantum Hall effect [34, 35] and the class of two-dimensional (2D) topological insulators [36] opened new opportunities to investigate 1D edge states [22, 23]. Advances in the nanotechnology allow now to fabricate 1D devices such as nanotubes [33], nanowires [32, 37] and Josephson junction (JJ) chains [38]. Moreover, cold atomic systems [28–31] can be used to artificially engineer 1D systems with highly tunable parameters.

Among all these realizations, JJ chains play a distinctive role since a superconductor-insulator transition (SIT) can be observed [39–43]. This quantum phase transition connects the superconducting and insulating phases, which are characterized by infinite and zero conductivity, respectively. In low dimensions, an intermediate metallic phase is usually absent due to strong localization effects. Josephson-junction chains are composed of superconducting islands smaller than the bulk coherence length. These islands are interconnected by tunneling barriers allowing for Cooper-pair hopping. If the devices are constructed in a superconducting quantum interference device (SQUID) geometry [39–43], the SIT can be investigated in a single device. Applying a perpendicular magnetic field allows the tuning of the Josephson coupling in situ without affecting other parameters of the chain. Such a device was used in Ref. [39] where the SIT was investigated experimentally. At weak magnetic fields, the chain behaves superconducting with a decreasing resistance as the temperature is lowered. At higher magnetic fields, the resistance curves become strongly non-monotonic with a sharp increase at low temperatures. However, the transition is located at unexpected low values of the Josephson coupling [44, 45].

Charging effects and the Cooper-pair tunneling compete in JJ chains. In the regime where the Cooper-pair tunneling dominates, the charge transport is characterized by a superconducting current-voltage curve [39, 46]. Reducing the Josephson coupling induces a SIT which is driven by the proliferation of quantum phase slips (QPS)[14, 47–50] — topological excitations changing the phase difference across one of the junctions by 2π. If the charging effects are dominating, i. e., in the insulating regime, the Coulomb blockade is observed [38]. Moreover, at low bias, thermally activated hopping of Cooper pairs leads to a finite conductance [51]. The onset of conduction at higher voltages is shown to be well-described by depinning physics [52, 53]. In the presence of strong random stray charges, the island charges are pinned to the disorder potential inhibiting transport. Another remarkable effect in connection with the charge disorder was discovered in a theoretical work by Matveev et al. [47]. Studying a closed ring of JJs pierced by a magnetic flux deep in the insulating regime, the authors of Ref. [47] obtained a weaker decay of the amplitude of the persistent current as a function of the system size in the presence of strong charge disorder. This surprising effect, the weakening of the insulating state by disorder, could be explained by the partially destructive interference of QPS.

An early theoretical study analyzing the SIT in JJ chains was performed by Bradley and Doniach [14]. Considering a capacitive coupling to the ground, the model of the JJ chain is mapped onto the 2D XY model displaying a Berezinskii-Kosterlitz-Thouless (BKT) transition [54–56]. Extensions of this work incorporated the effect of dissipation [57–59] and generalized it to the case of capacitive couplings to the ground and between the islands [44, 49, 57]. The connection to the physics of a Luttinger liquid was emphasized in Refs. [60–62]. Recently, the effect of disorder on the statistics of QPS is studied theoretically in Ref. [63]. The authors considered both random stray charges as well as random fluctuations of the junction area leading to a spatially fluctuating Josephson coupling. It was found that in the thermodynamic limit, the distribution of the phase-slip amplitude is Gaussian, while for a finite chain, a long tail at large amplitudes is present.

In one dimension, the SIT was observed not only in JJ chains but also in MoGe nanowires [64–66]. The transition can be induced by reducing the wire cross section or by applying a magnetic field normal to the wire and the substrate. Theoretically, the description of the destruction of superconductivity in nanowires by QPS was developed in Refs. [67, 68]. Up to the present day, there is no quantitative agreement on the parameter controlling the SIT in 1D structures as well as on the scaling close to the transition. With this theoretical work, we want to contribute to a better understanding of the SIT in 1D systems.

In recent years, the investigation of the properties of JJ chains under microwave irradiation received much attention. The current-voltage characteristics show quantized current steps in the presence of microwave radiation which are promising in the field of metrology [69]. Moreover, in the context of circuit quantum electrodynamics, JJ chains allow to reach novel regimes where many-body effects become important [70, 71]. As was shown recently in Ref. [72], JJ chains permit the realization of a tunable ohmic environment allowing for example the exploration of dissipative quantum phase transitions. Such an environment is implemented by two capacitively coupled chains that are inductively coupled to transmission lines.

A similar device was employed in Ref. [73] where the reflection coefficient of a double chain of JJs under microwave irradiation was measured. The two parallel chains are short-circuited at one end and connected to a dipole antenna at the other one enabling a coupling to the microwave radiation. In this way, antisymmetric plasma waves, i. e., modes with opposite amplitudes in both chains, can be excited. Plasma waves in this context are the collective excitations of the superconducting phases of the islands. The individual modes at quantized values of the momenta are clearly visible as resonances in the reflection coefficient. Due to the finite damping, the excited plasmons relax leading to a finite width of the resonances. Measuring the modulus as well as the phase of the reflection coefficient enables the authors of Ref. [73] to separate the internal damping from external losses related, e. g., to the leakiness of the resonator. The damping is quantified by the quality factor defined as the product of mode frequency and inverse linewidth. Chains with a large value of the Josephson coupling are characterized by an increasing quality factor upon decreasing the frequency. The quality factor of weaker devices with a lower value of the Josephson coupling show an almost flat behavior as a function of frequency with a tendency to drop at lowest measured frequencies. This type of behavior was interpreted by the authors of Ref. [73] as a hallmark of the SIT. At variance with theoretical predictions, the behavior is governed by the short-wavelength and not by the long-wavelength part of the Coulomb interaction in the chain. Moreover, apparent superconducting behavior, i. e., a growing quality factor when lowering the frequency, is observed in devices that are expected [44, 45] to be deep in the insulating regime.

The relaxation of excitations is a general phenomenon that can be observed in fermionic systems as well. In the regime of low energies, the relaxation time is usually long compared to other timescales governing the dynamics of many-body systems. This fact is essential for Landau's Fermi-liquid theory

[74–76]. The relaxation rate (inverse lifetime) of a Landau quasiparticle with energy ϵ measured from the Fermi energy ϵ_F scales as $1/\tau \sim \epsilon^2/\epsilon_\mathrm{F} \ll \epsilon$. The long lifetimes of low-energy quasiparticles are responsible for a number of interesting quantum phenomena including the quantum corrections to the conductivity [77–79] and quantum Hall interferometry [22, 23].

Relaxation processes have been studied in many solid-state setups and for several types of excitations ranging from electrons in normal metals [80–82] over Bogolyubov quasiparticles in Bose gases [83–88] and superconductors [89] to electrons in 1D wires [90, 91] and quantum Hall edge states [92–97]. The focus of most of these works was on the decay properties at low energies, where long lifetimes are expected.

In a recent work [98], it was noted that the lifetime of fermionic excitations can also become long at high energies larger than the Fermi energy. By means of scanning tunneling microscopy, the interaction-induced decay of hot electrons in an InAs nanowire is investigated. Specifically, two approaches that extract the decay properties of injected electrons are employed. Firstly, the scattering from the end of the nanowire is investigated. From the quasiparticle interference pattern, which is embedded in the differential conductance as a function of the distance to the end of the nanowire, the phase coherence length can determined. Secondly, in a Fabry-Pérot-like structure formed by adjacent stacking faults, the energy width of the resonances in the differential conductance yields the relaxation rate of the injected quasiparticle. According to the authors of Ref. [98], only electrons from the lowest subband of transverse quantization could be analyzed within their methods. In both approaches, it is found that in the low-energy regime, the relaxation rate grows as a function of energy as expected from the Fermi-liquid theory. However, as the energy exceeds the Fermi energy, the rate reaches a maximum and starts to decrease again. As a consequence, hot electrons experience a revival of their coherence. This effect opens new opportunities for quantum coherent operations in various applications and technologies.

This thesis is concerned with the transport properties of JJ chains as well as with the relaxation of plasmonic waves in JJ chains and the relaxation of fermionic excitations in quantum wires. Our study of the charge transport in JJ chains is based on a lattice model that includes capacitive couplings to the ground (C_0) as well as between the islands (C_1). Our theory is able to describe the physics in the limit of short-range ($C_0 \gg C_1$) Coulomb interaction as well as in the experimentally most relevant regime of non-local Coulomb interaction ($C_0 \ll C_1$). Moreover, we include two types of disorder: random stray charges and spatial fluctuations of the device parameters. As can be anticipated from the above discussion on the persistent current in insulating JJ chains with a ring geometry, the effect of random stray charges may as well lead to counterintuitive effects close to the SIT. In order to verify this hypothesis, we establish the phase diagram and compute the conductivity around the SIT.

Concerning the relaxation of plasmonic waves in JJ chains, we study a single chain as well as a double-chain device consisting of two capacitively coupled chains that was also used in the experiment of Ref. [73]. We derive at first the effective field theory for the antisymmetric mode in the double chain, which is excited in the experiment by means of the coupling to microwaves through the dipole antenna. Two different mechanisms contributing to the relaxation of plasmonic waves are considered: the scattering off QPS and the interaction of plasmons due to other anharmonicities like the fourth order nonlinearity originating from the expansion of the Josephson potential. With the help of this model we understand the apparent superconducting behavior of the quality factor observed in the experiment of Ref. [73] in a parameter regime where actually insulating behavior is expected. Moreover, we show how the interplay of the above mentioned mechanisms leads to an imitation of the SIT at intermediate frequencies.

Another main aspect of this thesis is the relaxation of fermionic excitations in nanowires. Motivated by the recent experiment in Ref. [98], we focus mainly on the regime of high energies above the Fermi

energy. Based on the findings of Ref. [98], we ask the following questions. Is the non-monotonic behavior of the relaxation rate and the regain of coherence a universal phenomenon? Do we find a different behavior in a quasi-1D wire if the injected electron is not in the lowest subband of transverse quantization? What is the role of the dimensionality of the system? We answer these questions by considering fermions with a parabolic energy spectrum under otherwise quite general conditions. The cases of short-range as well (screened) Coulomb interaction are analyzed in quasi-1D wires with multiple subbands and single-channel 1D wires. To better understand the relaxation in quasi-1D wires, we analyze three-dimensional (3D) and 2D bulk systems as well.

The remainder of this thesis is structured as follows. In **chapter 1**, we present a brief introduction to the Josephson effect and discuss the lattice model for JJ chains and its relation to the 2D XY model. Moreover, important theoretical methods that are used to study the transport properties of JJ chains are introduced. At the end, we discuss experiments in the context of the charge transport around the SIT and spectroscopic measurements providing information about the relaxation of plasmonic waves in JJ chains. **Chapter 2** is devoted to the introduction to the theoretical methods needed to study the interaction-induced relaxation of excitations with a focus on fermionic systems. In **chapter 3**, we turn to the discussion of the SIT in JJ chains. We start by presenting the low-energy field theory. Subsequently, we analyze the renormalization group and the transport properties around the SIT. In **chapter 4**, we consider the relaxation of plasmonic waves in JJ chains. After the introduction of the model for a double-chain device, we consider two mechanisms leading to the decay of plasmonic waves: the relaxation due to QPS and gradient anharmonicities. **Chapter 5** is devoted to the discussion of the relaxation of fermionic excitations in quantum wires at high energies. After a discussion of relaxation in higher-dimensional systems, we study the lifetime of fermions in multichannel and strictly 1D wires. Finally, we summarize our main results and outline possible directions for future projects. Technical details are presented in the appendices. For the convenience of the reader, we provide a compilation of the notations and conventions as well as a list of acronyms used throughout this thesis on pages 109 and 113, respectively.

Contents

Chapter 1

1 Fundamentals on Josephson-junction chains

This chapter is devoted to the introduction to one-dimensional (1D) Josephson junction (JJ) chains. These artificial systems are ideally suited to study transport properties in one dimension. Experimentally these chains can be fabricated with a high accuracy, and depending on the architecture a high tunability can be achieved. Of particular interest is the superconductor-insulator transition (SIT) observed in these devices [39]. Besides the interesting quantum transport properties observed in JJ chains, relaxation phenomena in 1D, which are of particular importance for this thesis as well, can be studied.

We start in Sec. 1.1 with a basic introduction to superconductivity and the Josephson effect. Further, we present a short discussion of a superconducting quantum interference device (SQUID), which is of key importance for many experiments that investigate the transport properties of JJ chains. In Sec. 1.2, we turn to the presentation of a lattice model for JJ chains. Basic properties of this model are discussed and compared to the classical two-dimensional (2D) XY model. Section 1.3 presents an introduction to the main theoretical concepts used to analyze the SIT in JJ chains. The last two sections review a few experiments related to the transport properties (Sec. 1.4) and decoherence phenomena (Sec. 1.5) in JJ chains. The theoretical investigation of the transport characteristics and the decay properties of collective modes in JJ chains are discussed in Chaps. 3 and 4, respectively.

1.1 Superconductivity and the Josephson effect

Superconductivity is a phenomenon that is characterized by a vanishing resistance and perfect diamagnetism. In 1911 H. K. Onnes made the glorious discovery of the zero-resistance state in mercury [99]. When cooling mercury to the boiling point of liquid helium, the resistance showed an abrupt drop below his measurement resolution. W. Meissner and R. Ochsenfeld observed in 1933 that the superconducting state is not only a perfect conductor but also expels weak magnetic fields [100]. After the discovery of Onnes, it took almost half a century until a microscopic theory explaining these effects was developed. In 1957 J. Bardeen, L. N. Cooper, and J. R. Schrieffer (BCS) presented a microscopic theory of superconductivity [101, 102]. This theory is based on the formation of electron bound states, so called Cooper pairs [103]. The effective attractive interaction between electrons, which leads to these bound states if it exceeds the Coulomb repulsion, can be mediated via phonons. The BCS theory

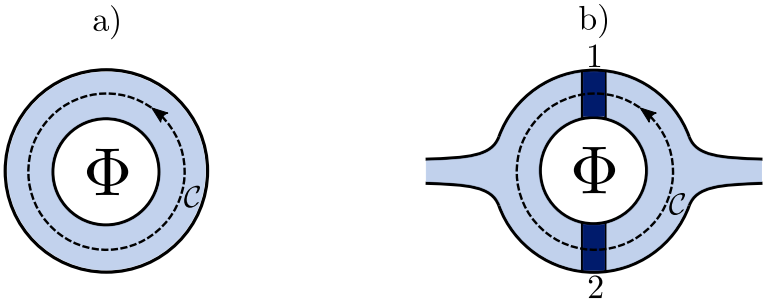

Figure 1.1: a) Superconducting ring pierced by a magnetic flux Φ. The contour $\mathcal{C}$ is assumed to be sufficiently far away from the boundaries such that the current density is negligable in this region. b) Two superconductors coupled by two tunnel barriers (dark blue areas) form a SQUID.

successfully explained many effects in conventional superconductors such as the Meissner-Ochsenfeld effect, the isotope effect, and the jump of the specific heat at the transition temperature.

Superconductivity is a macroscopic quantum phenomenon; the superconducting state can be described by a macroscopic wave function,

$$\psi(\mathbf{r}) = \sqrt{n_s(\mathbf{r})}\, \mathrm{e}^{i\theta(\mathbf{r})}, \tag{1.1}$$

where $n_s(\mathbf{r})$ is the Cooper-pair density. An interesting phenomenon that can be derived from this fact, is the flux quantization in multiply connected superconductors. As an example, we consider a superconducting ring that is pierced by a magnetic flux Φ, see Fig. 1.1 a). We assume that the ring is thick enough, such that a closed path $\mathcal{C}$ in the interior of the superconductor exists, along which the current is zero. Supercurrents, which screen the external magnetic field, flow in a narrow region close to the boundary of the superconductor. From elementary quantum mechanics the current in the presence of a vector potential $\mathbf{A}(\mathbf{r})$ is given by

$$\mathbf{j}(\mathbf{r}) = \frac{q}{2m}\left[\psi^*(\mathbf{r})\left(\frac{\hbar}{i}\nabla - \frac{q}{c}\mathbf{A}\right)\psi(\mathbf{r}) + \psi(\mathbf{r})\left(-\frac{\hbar}{i}\nabla - \frac{q}{c}\mathbf{A}\right)\psi^*(\mathbf{r})\right], \tag{1.2}$$

where the charge and mass are twice the values for an electron, $q = 2e$ and $m = 2m_e$, respectively. The reason for this is that the charge carriers are Cooper pairs. Inserting the wave function (1.1), we find

$$\mathbf{j}(\mathbf{r}) = \frac{e\hbar}{m_e} n_s(\mathbf{r})\left[\nabla\theta(\mathbf{r}) - \frac{2\pi}{\Phi_0}\mathbf{A}(\mathbf{r})\right] \tag{1.3}$$

with the (superconducting) flux quantum $\Phi_0 = \pi\hbar c/e$. Integrating the current density $\mathbf{j}(\mathbf{r})$ along a closed path $\mathcal{C}$ in the interior of the superconductor where the current vanishes, and assuming that the Cooper-pair density is homogeneous $n_s(\mathbf{r})$ =const. along the path, we find

$$0 = \oint_{\mathcal{C}} \nabla\theta(\mathbf{r})\mathrm{d}\mathbf{r} - \frac{2\pi}{\Phi_0}\oint_{\mathcal{C}} \mathbf{A}(\mathbf{r})\mathrm{d}\mathbf{r} = \oint_{\mathcal{C}} \nabla\theta(\mathbf{r})\mathrm{d}\mathbf{r} - \frac{2\pi\Phi}{\Phi_0}. \tag{1.4}$$

Since the wave function (1.1) should be single-valued, the phase θ can wind only by a multiple of 2π when going along the path $\mathcal{C}$. This leads to the quantization condition for the magnetic flux inside the hole,

$$\Phi = n\,\Phi_0, \quad n \in \mathbb{Z}. \tag{1.5}$$

Josephson effect Another fascinating phenomenon is the Josephson effect. In a seminal work [104] B. D. Josephson investigated the properties of two superconductors separated by a narrow insulating barrier. We follow Ref. [105] and derive the Josephson equations in a phenomenological way. We denote by ψ_1 and ψ_2 the many-body wave functions and by H_1 and H_2 the Hamilton operators of the two superconductors. The Schrödinger equation can be written in the following form:

$$\begin{aligned} i\hbar\frac{\partial}{\partial t}\psi_1 &= H_1\psi_1 + \mathcal{T}\psi_2, \\ i\hbar\frac{\partial}{\partial t}\psi_2 &= H_2\psi_2 + \mathcal{T}\psi_1, \end{aligned} \tag{1.6}$$

where the off-diagonal terms describe the effects due the coupling via the tunnel barrier. Assuming the tunneling to be weak, we can employ perturbation theory and use the wave functions for the isolated superconductors,

$$\psi_j = \sqrt{n_j}\,\mathrm{e}^{i\theta_j}, \quad j = 1, 2. \tag{1.7}$$

Inserting this wave function into the Schrödinger equation (1.6) and assuming homogeneous superconductors, we get

$$i\hbar\left[\frac{1}{2}\dot{n}_1 + in_1\dot{\theta}_1\right]\mathrm{e}^{i\theta_1} = E_1 n_1 \mathrm{e}^{i\theta_1} + \mathcal{T}\sqrt{n_1 n_2}\mathrm{e}^{i\theta_2}, \tag{1.8}$$

$$i\hbar\left[\frac{1}{2}\dot{n}_2 + in_2\dot{\theta}_2\right]\mathrm{e}^{i\theta_2} = E_2 n_2 \mathrm{e}^{i\theta_2} + \mathcal{T}\sqrt{n_1 n_2}\mathrm{e}^{i\theta_1}, \tag{1.9}$$

where $E_{1,2}$ is the energy of the state $\psi_{1,2}$. Splitting the real and imaginary parts in Eq. (1.8), we get

$$-\frac{\hbar}{2}\dot{n}_1\sin\theta_1 - \hbar n_1\cos\theta_1\dot{\theta}_1 = E_1 n_1\cos\theta_1 + \mathcal{T}\sqrt{n_1 n_2}\cos\theta_2, \tag{1.10}$$

$$\frac{\hbar}{2}\dot{n}_1\cos\theta_1 - \hbar n_1\sin\theta_1\dot{\theta}_1 = E_1 n_1\sin\theta_1 + \mathcal{T}\sqrt{n_1 n_2}\sin\theta_2. \tag{1.11}$$

Combining both equations, we extract

$$\dot{n}_1 = \frac{2\mathcal{T}}{\hbar}\sqrt{n_1 n_2}\sin(\theta_2 - \theta_1), \tag{1.12}$$

$$\dot{\theta}_1 = -\frac{\mathcal{T}}{\hbar}\sqrt{\frac{n_2}{n_1}}\cos(\theta_2 - \theta_1) - \frac{E_1}{\hbar}. \tag{1.13}$$

The analogous equations for the variables of the second superconductor can be obtained by interchanging $1 \leftrightarrow 2$:

$$\dot{n}_2 = -\dot{n}_1, \qquad \dot{\theta}_2 = -\frac{\mathcal{T}}{\hbar}\sqrt{\frac{n_1}{n_2}}\cos(\theta_2 - \theta_1) - \frac{E_2}{\hbar}. \tag{1.14}$$

The tunneling rate $\dot{n}_1$ is proportional to the tunneling current I. We can now state the first Josephson equation,

$$I = I_c\sin(\theta_2 - \theta_1), \tag{1.15}$$

that predicts a zero-voltage current through the junction if both superconductors have different phases (DC Josephson effect). The maximum current which the junction can sustain is denoted by I_c. If

further a finite voltage drop across the junction exists, the eigenenergies are shifted, $E_1 - E_2 = 2eV$. For identical superconductors, i. e., $n_1 = n_2$, the phase difference evolves in time according to

$$\dot{\theta}_2 - \dot{\theta}_1 = \frac{E_1 - E_2}{\hbar} = \frac{2e}{\hbar} V. \tag{1.16}$$

This means that a constant voltage drop V across the junction leads to an alternating current of frequency $2eV/\hbar$ (AC Josephson effect). The energy stored in the junction can be obtained by integrating the electrical work [106],

$$E = \int \mathrm{d}t I\, V. \tag{1.17}$$

With the help of (1.15) and (1.16), we find

$$E = E_\mathrm{J} \int_0^{\theta_2 - \theta_1} \mathrm{d}\varphi \sin\varphi = E_\mathrm{J}[1 - \cos(\theta_2 - \theta_1)] \tag{1.18}$$

with the Josephson energy $E_\mathrm{J} = \hbar I_c / 2e$.

SQUID A very powerful tool consisting of two parallel junctions is the superconducting quantum interference device (SQUID) depicted in Fig 1.1 b). We follow Ref. [106] to derive the amplitude of the supercurrent through the device. The magnetic flux piercing the device can be written as

$$\Phi = \oint_{\mathcal{C}} \mathbf{A}\mathrm{d}\mathbf{r} = \int_\text{electrodes} \mathbf{A}\mathrm{d}\mathbf{r} + \int_\text{links} \mathbf{A}\mathrm{d}\mathbf{r} = \frac{\Phi_0}{2\pi} \int_\text{electrodes} \nabla\theta \mathrm{d}\mathbf{r} + \int_\text{links} \mathbf{A}\mathrm{d}\mathbf{r}, \tag{1.19}$$

where in the last step we made use of Eq. (1.3), and assumed the contour $\mathcal{C}$ to be in the interior of the superconductor where the current can be neglected. Here, the integrals along the (superconducting) electrodes and links are directed according to the orientation of $\mathcal{C}$. The change of the phase along the whole contour is a multiple of 2π,

$$\int_\text{electrodes} \nabla\theta \mathrm{d}\mathbf{r} + \delta\theta_2 - \delta\theta_1 = 0 \qquad \mod 2\pi, \tag{1.20}$$

where the jumps of the phase across the links $\delta\theta_1$ and $\delta\theta_2$ are defined with an orientation from left to right. Introducing the gauge-invariant phase jumps

$$\gamma_i = \delta\theta_i - \frac{2\pi}{\Phi_0} \int_{\text{link}\, i} \mathbf{A}\mathrm{d}\mathbf{r}, \qquad i = 1, 2, \tag{1.21}$$

where here the integral across the i-th link is oriented from left to right, we find the constraint

$$\gamma_1 - \gamma_2 = 2\pi \frac{\Phi}{\Phi_0} \qquad \mod 2\pi. \tag{1.22}$$

If both junctions can support the same critical current, the total current through the device is given by

$$I = I_c(\sin\gamma_1 + \sin\gamma_2). \tag{1.23}$$

The maximum supercurrent with the constraint (1.22) is given by

$$I_\text{max} = 2I_c |\cos(\pi\Phi/\Phi_0)|. \tag{1.24}$$

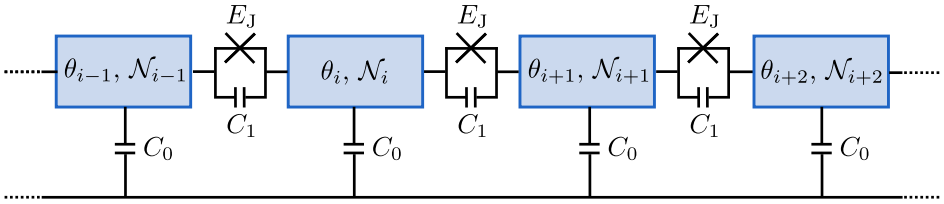

Figure 1.2: Sketch of a one-dimensional Josephson junction chain. Superconducting islands (blue rectangles) are connected via tunnel barriers which provide a capacitance C_1 and allow for the tunneling of Cooper pairs. The capacitive coupling to the ground is taken into account by the capacitance C_0. The superconducting phase of the i-th grain is denoted by θ_i, the number of Cooper pairs by $\mathcal{N}_i$.

Thus, the maximal supercurrent is modulated by the magnetic flux Φ. Such a device can be used to measure tiny magnetic fields. It further allows to tune the effective Josephson energy E_J of the junction, which is proportional to the maximal current (see above). This mechanism can be exploited to induce a superconductor-insulator transition in a Josephson junction chain with a SQUID geometry by changing the magnetic flux through the SQUIDs. More details on experiments with Josephson junction chains are discussed in Sec. 1.4.

1.2 Model for Josephson junction chains

After the short introduction to superconductivity and the Josephson effect, we discuss a linear chain of Josephson junctions. In the first part of this section, we present a lattice model for this system, and in the second part we discuss its relation to the 2D XY model. The discussion of the lattice model is based on Sec. II of Ref. [107].

Figure 1.2 shows a sketch of a 1D JJ chain. The size of the superconducting islands is assumed to be smaller than the bulk coherence length so that we can characterize them by a single phase θ. Thin tunneling barriers between the grains allow for hopping of Cooper pairs along the chain. The tunneling is characterized by the Josephson energy E_J. In our model, we consider two capacitive couplings, the junction capacitance C_1 and the ground capacitance C_0. The associated charging energy scales are $E_0 = (2e)^2/C_0$ and $E_1 = (2e)^2/C_1$. For the behavior of the theory at large scales, the charging energy E_0 is of key importance. A superconductor-insulator transition in a JJ chain takes place at $K_0 \equiv \sqrt{E_J/E_0} \sim 1$ [14, 44]. The charging energy E_1 has a strong influence on the local properties of the chain for $C_0 \ll C_1$. Namely, the local superconducting correlations at length scales shorter than the screening length $\Lambda = \sqrt{C_1/C_0} \gg 1$ are governed by the parameter $K_1 \equiv \sqrt{E_J/E_1}$. In the opposite limit $C_0 \gg C_1$, the charging energy E_1 is irrelevant. Typical values for the screening length in experiments are $\Lambda \simeq 10$ [39, 40, 50].

The lattice model of a clean JJ chain can be written in the form

$$\mathcal{H} = \frac{E_1}{2} \sum_{i,j} \left(S^{-1}\right)_{ij} \mathcal{N}_i \mathcal{N}_j + E_J \sum_i \left[1 - \cos\left(\theta_i - \theta_{i+1}\right)\right], \tag{1.25}$$

where the number of Cooper pairs and the superconducting phase of the i-th island are denoted by $\mathcal{N}_i$ and θ_i, respectively. Both variables obey the canonical commutation relations,

$$[\mathcal{N}_i, \theta_j] = i\delta_{i,j}. \tag{1.26}$$

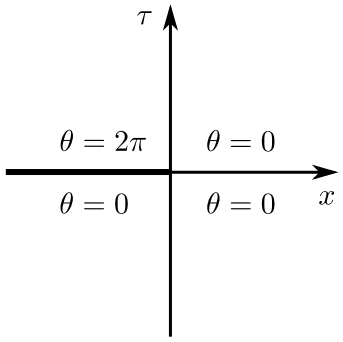

Figure 1.3: Schematic depiction of a phase-slip process in the x-τ plane. For imaginary times $\tau < 0$, the system is assumed to be in the (classical) superconducting ground state, $\theta(x) \equiv 0$. At $\tau = 0$ a phase slip occurs in the junction at $x = 0$. All the phases at $x < 0$ suddenly jump by 2π.

In the charging part of the Hamiltonian (1.25), we introduced the dimensionless capacitance matrix

$$S_{ij} = \left(2 + \frac{1}{\Lambda^2}\right)\delta_{i,j} - \delta_{i,j+1} - \delta_{i,j-1}, \tag{1.27}$$

that takes into account the capacitive couplings between the islands as well as to the ground.

The derivation of the corresponding low-energy field theory is presented in Sec. 3.1. Here, we briefly discuss qualitative features of the theory. In the limit $E_\mathrm{J} \to \infty$, the chain is in the classical superconducting ground state, where all phases are the same, $\theta_i \equiv \text{const}$. In the quasi-classical regime where the Josephson energy dominates but the charging energy is finite, small fluctuations of the phases occur. These fluctuations are the plasmonic waves. The crucial role in the destruction of the superconducting correlations are played by topological excitations, so called quantum phase slips (QPS). These are fluctuations, where the phase difference across one of the junctions jumps by 2π. Figure 1.3 illustrates a QPS process in the x-τ plane. We assume the system to be in the (classical) superconducting ground state for imaginary times $\tau < 0$. Smooth deformations of this state are not important for the purpose of the illustration. At $\tau = 0$ all phases at $x < 0$ jump by 2π resulting in a phase difference of 2π across the junction at $x = 0$. In this formulation, a QPS is a vortex of θ in space-time. In the following we present the 2D XY model and draw a few analogies to our model of Josephson junction chains.

2D XY model The classical 2D XY model describes the interaction of classical two-component spins in two spatial dimensions. A detailed discussion of this model can be found in Refs. [108–110]. The Hamiltonian

$$\mathcal{H}_\mathrm{XY} = -J \sum_{<ij>} \cos(\theta_i - \theta_j) \tag{1.28}$$

describes the exchange interaction between nearest neighboring spins of length $S = 1$. The angle θ_i denotes the orientation of the i-th spin relative to a reference direction. We assume the coupling to be ferromagnetic, $J > 0$. The classical ground state at $J \to \infty$ is the ferromagnetic state, where all spins point in the same direction [see Fig. 1.4 a)]. Small fluctuations around the ferromagnetic state can be taken into account by a gradient expansion of the Hamiltonian (1.28). The continuum Hamiltonian

$$\mathcal{H}_\mathrm{XY}^\mathrm{cont} = \frac{J}{2}\int \mathrm{d}x\mathrm{d}y \left[(\partial_x\theta)^2 + (\partial_y\theta)^2\right] \tag{1.29}$$

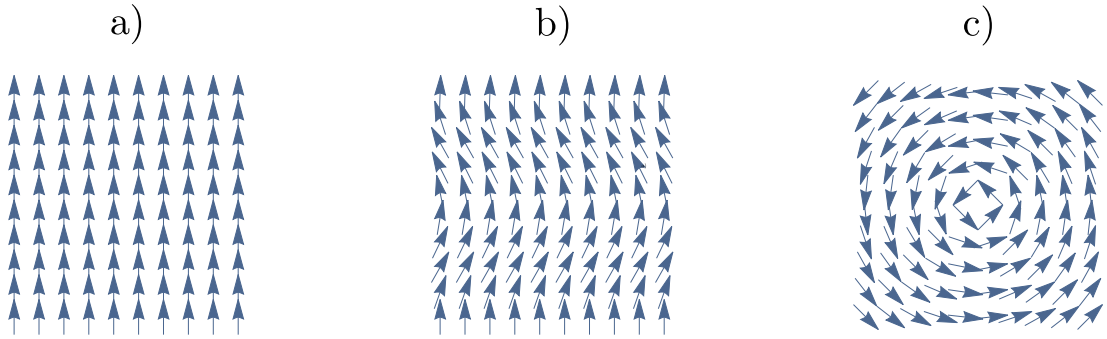

Figure 1.4: Spin configurations in the (ferromagnetic) 2D XY model. a) Ferromagnetic ground state: All spins point in the same direction. b) Smooth deformation of the ground state (spin wave); c) vortex configuration: The angle winds by 2π if one moves along a closed path around the center of the vortex.

describes the spin waves, which are the long-wavelength fluctuations of the angles in the 2D XY model [see Fig. 1.4 b)]. In JJ chains, the corresponding fluctuations are the plasmonic waves. The role of the second space dimension is played by the imaginary time. Here we considered an isotropic version of XY model. In Sec. 3.2, we study the JJ chain in the limit $C_1 = 0$. There, the plasmonic waves have a linear spectrum and are described by the continuum theory (3.16) that is completely analogous to Eq. (1.29). In a more general anisotropic XY model, the spin-wave action would be analogous to the action (3.3) corresponding to plasmonic waves with a curved spectrum.

The above continuum description is applicable to configurations that can be continuously deformed to the ground state, such as the one shown in Fig. 1.4 b). There are, however, other configurations that are topologically distinct from the ground state. An example of such a topological defect, a vortex with unit charge, is depicted in Fig. 1.4 c). A vortex in the 2D XY model corresponds to a phase slip in the case of JJ chains. The configuration of the superconducting phases in Fig. 1.3 can be continuously deformed to the configuration of the vortex in the 2D XY model depicted in Fig. 1.4 c). Berezinskii, Kosterlitz and Thouless [54, 56] demonstrated that the XY model exhibits a topological phase transition which is driven by the unbinding of vortices. This transitions is called Berezinskii-Kosterlitz-Thouless (BKT) transition. Such a transition is not accompanied by the spontaneous breaking of the $U(1)$ symmetry present in the model. Because of the Mermin-Wagner theorem [111], a continuous symmetry can not be broken in two dimension at finite temperature. However, the behavior of the correlation function $\langle \exp\{i[\theta(\mathbf{r}) - \theta(0)]\}\rangle$ changes from an exponential decay at high temperatures to a power-law decay at low temperatures (quasi long-range order).

With the help of the renormalization group, the BKT transition can be analyzed in a rigorous way. On the other hand, there is a way to qualitatively understand the existence of the phase transition, and to estimate the transition temperature. In the following we present qualitative arguments that can be found in the paper by Kosterlitz and Thouless [56]. We consider a single vortex, and divide the space into two regions: the vortex core and the outer region, where the orientation of spins changes sufficiently smoothly such that the continuum theory (1.29) is valid. The (arbitrary) length-scale a is introduced to distinguish between both parts. For a vortex of topological charge n, the angle winds by $2\pi n$ when one goes once around its center,

$$\oint \nabla\theta \mathrm{d}\mathbf{r} = 2\pi n, \quad n \in \mathbb{Z}. \tag{1.30}$$

The energy to create a vortex can be written as

$$E_n = E_n^{\text{core}} + \frac{J}{2}\int_{r>a} \mathrm{d}^2 r\,(\nabla\theta)^2. \tag{1.31}$$

A configuration that fulfills the circulation condition (1.30) can be parametrized as

$$\nabla\theta = \frac{n}{r}\hat{\mathbf{e}}_\varphi, \tag{1.32}$$

where $\hat{\mathbf{e}}_\varphi$ is the polar unit vector. The energy for a vortex in a system of size L assumes then the form

$$E_n = E_n^{\text{core}} + \pi J n^2 \ln\left(L/a\right). \tag{1.33}$$

The number of possible places of the center of the core is given by $(L/a)^2$, which leads to the entropy

$$S_n = \ln[(L/a)^2]. \tag{1.34}$$

At the temperature above which it becomes favorable to create vortices, the free energy $F_n = E_n - TS_n$ changes sign. In a large system, the core energy can neglected, and the critical temperature to create a vortex of charge n is given by

$$T_c = \frac{\pi J n^2}{2}. \tag{1.35}$$

It becomes evident that vortices of unit charge ($n = \pm 1$) are predominantly responsible for the phase transition. The result (1.35) is exact in the limit of zero fugacity $\exp\{-E_1^{\text{core}}/T\}$. In the case of a finite fugacity, vortex-antivortex pairs renormalize the transition temperature. The distortion field of a dipole of size d is a superposition of the individual vortices in the outer part of the dipole: $\nabla\theta_{\text{dip}} = \nabla\theta(x + d/2, y) - \nabla\theta(x - d/2, y)$. Since the infrared divergent contributions cancel ($L \to \infty$), the energy associated with dipoles is finite. This means that dipoles exist at any finite temperature. Below the transition they are tightly bound. At the transition the vortex-antivortex pairs dissociate destroying the (quasi-long-range) order.

There are other models that are in the same universality class (see Refs. [108, 109, 112] for details). The 2D Coulomb gas in which the interactions between charges is logarithmic shows the same critical properties as the XY model. More important for this thesis is the fact that the 2D sine-Gordon model belongs to this universality class as well. In Sec. 1.3.2, we carry out explicitly the renormalization group treatment of the sine-Gordon model. As will be shown in Chap. 3, the field theory describing the superconductor-insulator transition in JJ chains can be written in the form of a sine-Gordon theory.

1.3 Theoretical methods

This section gives an overview over the important theoretical concepts used in the discussion of the SIT in JJ chains in Chap. 3. We start in Sec. 1.3.1 with an introduction to the Luttinger liquid, which replaces the Fermi liquid in one dimension. In this thesis, the Luttinger-liquid model constitutes the Gaussian theory of Josephson junction chains. To understand the role of perturbations on top of a Gaussian theory, the renormalization group can be employed. This technique is discussed in Sec. 1.3.2. We use the renormalization group to extract the low-energy properties of Josephson junction chains. In this way, we can obtain the phase diagram and improve the bare transport calculations. The transport formalism is presented in Sec. 1.3.3. The conductivity is expressed with the help of the memory

function, which plays the role of a self-energy for the conductivity. In contrast to the conductivity, the memory function (usually) admits a perturbative expansion in the coupling constant of the scattering term. Using this formalism, the transport characteristics of Josephson junction chains are analyzed in Chap. 3.

1.3.1 Luttinger liquid model

The Luttinger liquid (LL) is a very important concept of the physics in one dimension. We present here a short qualitative introduction to this topic. More details can be found in the literature, see e. g. Refs. [12, 16, 17, 113]. In this thesis, we encounter the LL as the low-energy theory of JJ chains, see Sec. 3.1 and also Refs. [60, 61]. The concept is, however, much more generic in 1D, and appears in fermionic systems as well. Here, we follow Ref. [17] and outline the main qualitative features of the low-energy properties of 1D systems.

In higher dimensions, there is the very powerful Fermi-liquid theory introduced by Landau [74–76]. The main statement of this theory is that the low-energy excitations of an interacting Fermi system are adiabatically connected to free fermions. The ground state of free fermions at zero temperature is the filled Fermi sea. This means that the occupation number jumps by 1 at the Fermi surface. An additional fermion above the Fermi sea has an infinite lifetime since it is an eigenstate of the Hamiltonian. In a Fermi liquid, the elementary particles, so called quasiparticles, are not the free fermions but fermions dressed by particle-hole pairs (density fluctuations). These quasiparticles still have a fermionic character with renormalized parameters such as an effective mass that differs from the bare mass. At the Fermi surface the discontinuity of the occupation number survives. The amplitude of the jump is, however, smaller than 1. Due residual interactions, quasiparticles have a finite lifetime. However, as a result of the vanishing phase space for the scattering of quasiparticles at the Fermi surface, the lifetime diverges when the energy of the quasiparticle approaches the Fermi energy (see Sec. 2.2 for more details).

The situation in 1D is completely different. Because of strong interaction effects in 1D, the Fermi liquid theory breaks down. Intuitively, it is clear that particles confined to move on a line can not move individually. A collective motion is, however, easily possible. These collective excitations correspond to density fluctuations which have bosonic character. The formal description of interacting (1D) fermionic systems in terms of a bosonic theory is called bosonization [12, 16, 17]. The low-energy theory in a gapless situation of a generic 1D system assumes the form of a LL,

$$\mathcal{H} = \frac{1}{2\pi} \int \mathrm{d}x \left[uK(\partial_x \theta(x))^2 + \frac{u}{K}(\partial_x \phi(x))^2 \right], \tag{1.36}$$

where u is the velocity of the long-wavelength density fluctuations (plasmons) and K is the Luttinger parameter. For simplicity we assumed a system without a spin degree of freedom. In principle both parameters can be calculated for a specific microscopic model. In a fermionic system, $K = 1$ corresponds to a non-interacting system and $K < 1$ ($K > 1$) to fermions with repulsion (attraction). The operators in the Hamiltonian (1.36) fulfill the commutation relations

$$\left[\phi(x), \partial_{x'} \theta(x') \right] = i\pi \delta(x - x'), \tag{1.37}$$

and can be related to physical observables: The (particle number) density is given by $-\partial_x \phi/\pi$ and the (particle number) current density by $uK\partial_x \theta/\pi$. In this thesis, we come across the LL as the low-energy theory of JJ chains. The action (3.16) is equivalent to the LL Hamiltonian (1.36) (up to a rescaling of ϕ). The role of perturbations on top of the quadratic LL theory is discussed in the next section.

1.3.2 Renormalization group

The renormalization group (RG) is a powerful tool to extract the low-energy properties of a field theory. We present here a short introduction to this method and discuss in detail an example which is important for this thesis: The renormalization of the sine-Gordon theory. More details on the general procedure and further examples can be found in the literature, see e. g. Refs. [108, 114, 115].

A field theory is usually equipped with a high-energy cutoff Λ that restricts the validity of the continuum field theory. The idea of the RG is to obtain a theory with a lower cutoff Λ' but the same low-energy properties. This goal can be achieved by eliminating unimportant high-energy degrees of freedom and adapting the coupling constants of the theory. The explicit procedure in a Wilsonian type of the RG [114] can be qualitatively summarized in the following way. We start with a field theory with coupling constants $\mathbf{g}$ and ultraviolet (UV) cutoff Λ. Now, an artificial scale $\Lambda' = \Lambda/b$, $b > 1$ is introduced. Modes with energy in the range $\Lambda' < \epsilon < \Lambda$ are dubbed "fast" modes, and are integrated out. After this elimination process generically two different situations can occur. The structure of the theory is completely changed, or, besides the possible generation of a few additional couplings, the theory assumes the same form as before. In the latter scenario, the theory is renormalizable, and the effective theory can be related to the original one by adjusting the coupling constants. To read off the change of the parameters one usually rescales momenta and frequencies $(q, \omega) \to (b\,q, b\,\omega)$ to restore the initial value of the cutoff Λ. This procedure can be iterated until the (highest) typical scale of the physics under consideration is reached. This scale at which the RG is stopped could be the temperature or the external frequency at which the system is probed. By integrating in each step an infinitesimally small portion of the modes, $b = 1 + \mathrm{d}l$, differential equations (RG equations) governing the flow of the coupling constants $\mathbf{g}$ can be derived,

$$\frac{\mathrm{d}\mathbf{g}}{\mathrm{d}l} = \beta(\mathbf{g}). \tag{1.38}$$

The beta function $\beta(\mathbf{g})$ encodes the complete behavior of the renormalization of the coupling constants. Of particular interest are the points in parameter space where the beta function vanishes. Such points, where the theory is scale invariant, are called fixed points. The scale invariance typically occurs at a second order phase transition where the correlation length diverges and no finite length scale remains. The fixed points of the RG thus correspond to the (candidates for) critical points at which phase transitions occur.

Away from the critical points, terms in the theory are called relevant (irrelevant) if the corresponding coupling constant increases (decreases) in the course of the RG. Usually, the elimination process of the fast modes is performed in a perturbative way. The validity of this procedure is consequently limited to the region where the coupling constant is still small.

Let us now consider a specific example that is of particular importance for this thesis. The sine-Gordon model,

$$S = S_0 + S_1, \tag{1.39}$$

$$S_0 = \frac{1}{2\pi u K} \int \mathrm{d}x\mathrm{d}\tau \left[u^2 (\partial_x \phi)^2 + (\partial_\tau \phi)^2 \right], \tag{1.40}$$

$$S_1 = g \int \mathrm{d}x\mathrm{d}\tau \cos[2\phi(x,\tau)]. \tag{1.41}$$

The imaginary-time action (1.39) consists of the LL action S_0 and the perturbation S_1 that is of cosine form. We will see in Sec. 3.2 that this action describes the low-energy properties of a clean JJ

chain in the limit of local Coulomb interaction, cf. Eqs. (3.16) and (3.6). In the following the explicit derivation of the RG equations of this model is presented. Instead of the Wilsonian-type derivation sketched above, we use a different method to extract the RG equations that is based on correlations functions [110]. The presentation follows closely the derivation in Giamarchi's book [17, p. 56 ff]. The procedure is based on the behavior of the (time-ordered) correlation function

$$R(x_1 - x_2, \tau_1 - \tau_2) = \left\langle \mathrm{e}^{i\sqrt{2}\phi(x_1,\tau_1)} \mathrm{e}^{-i\sqrt{2}\phi(x_2,\tau_2)} \right\rangle . \tag{1.42}$$

This function can not be evaluated exactly due to the non-linearity S_1. Instead, we perform a perturbative expansion of this correlation function up to second order in g. For the average of exponentials of ϕ with respect to the Gaussian action (1.40), the formula

$$\left\langle \prod_j \mathrm{e}^{i\sigma_j \phi(\mathbf{r}_j)} \right\rangle_0 = \begin{cases} \mathrm{e}^{\frac{1}{2}K \sum_{i<j} \sigma_i \sigma_j F_1(\mathbf{r}_i - \mathbf{r}_j)}, & \sum_j \sigma_j = 0, \\ 0, & \text{else} \end{cases} \tag{1.43}$$

is helpful. Here, we introduced the short-hand notation $\mathbf{r} = (x, u\tau)$ and

$$F_1(\mathbf{r}) = \frac{1}{2} \ln \left(\frac{x^2 + (u|\tau| + a)^2}{a^2} \right) \tag{1.44}$$

with the UV cutoff a. For $g = 0$ the correlation function reads

$$R^{(0)}(\mathbf{r}_1 - \mathbf{r}_2) = \left\langle \mathrm{e}^{i\sqrt{2}\phi(x_1,\tau_1)} \mathrm{e}^{-i\sqrt{2}\phi(x_2,\tau_2)} \right\rangle_0 = \mathrm{e}^{-KF_1(\mathbf{r}_1 - \mathbf{r}_2)} \simeq \left(\frac{a}{|\mathbf{r}_1 - \mathbf{r}_2|} \right)^K . \tag{1.45}$$

The first order correction vanishes because of the neutrality condition in Eq. (1.43), while the second order correction is given by

$$\begin{aligned} \delta R = \frac{g^2}{8u^2} \mathrm{e}^{-KF_1(\mathbf{r}_1 - \mathbf{r}_2)} \sum_{\sigma = \pm} \int \mathrm{d}^2 r_3 \mathrm{d}^2 r_4 \, \mathrm{e}^{-2KF_1(\mathbf{r}_3 - \mathbf{r}_4)} \\ \times \left[\mathrm{e}^{\sqrt{2}\sigma K \left[F_1(\mathbf{r}_1 - \mathbf{r}_3) + F_1(\mathbf{r}_2 - \mathbf{r}_4) - F_1(\mathbf{r}_1 - \mathbf{r}_4) - F_1(\mathbf{r}_2 - \mathbf{r}_3) \right]} - 1 \right] . \end{aligned} \tag{1.46}$$

Let us now switch to relative and center-of-mass coordinates,

$$\mathbf{r} = (x, y) = \mathbf{r}_3 - \mathbf{r}_4, \qquad \mathbf{R} = (X, Y) = \frac{1}{2}(\mathbf{r}_3 + \mathbf{r}_4). \tag{1.47}$$

Due to the exponential in front of the square bracket in Eq. (1.46), which is a power-law of $r = |\mathbf{r}|$, large r are suppressed. We can thus expand

$$\mathrm{e}^{\sqrt{2}\sigma K \left[F_1\left(\mathbf{r}_1 - \mathbf{R} - \frac{\mathbf{r}}{2}\right) + F_1\left(\mathbf{r}_2 - \mathbf{R} + \frac{\mathbf{r}}{2}\right) - F_1\left(\mathbf{r}_1 - \mathbf{R} + \frac{\mathbf{r}}{2}\right) - F_1\left(\mathbf{r}_2 - \mathbf{R} - \frac{\mathbf{r}}{2}\right) \right]} - 1 \simeq \mathrm{e}^{-\sqrt{2}\sigma K (\mathbf{r} \cdot \nabla)[F_1(\mathbf{R} - \mathbf{r}_1) - F_1(\mathbf{R} - \mathbf{r}_2)]} - 1. \tag{1.48}$$

Expanding also the exponential, the linear term vanishes when summing over σ. The "mixing term" in the second order (contains $x\,y$) vanishes after integrating over the relative coordinates. Integrating

by parts in the center-of-mass coordinates and performing the integration over the polar angle of the relative coordinates results in the correction to the correlation function

$$\delta R = -\frac{\pi g^2 K^2 a^3}{4u^2} \mathrm{e}^{-KF_1(\mathbf{r}_1-\mathbf{r}_2)} \int_a^\infty \mathrm{d}r \left(\frac{r}{a}\right)^{3-2K} \int \mathrm{d}^2 R \, [F_1(\mathbf{R}-\mathbf{r}_1) - F_1(\mathbf{R}-\mathbf{r}_2)] \times (\partial_X^2 + \partial_Y^2)[F_1(\mathbf{R}-\mathbf{r}_1) - F_1(\mathbf{R}-\mathbf{r}_2)]. \tag{1.49}$$

With the help of

$$(\partial_X^2 + \partial_Y^2) F_1(\mathbf{R}) = 2\pi\delta(\mathbf{R}), \tag{1.50}$$

we arrive at the expression for the correlation function up to second order in g,

$$R(\mathbf{r}_1-\mathbf{r}_2) = \mathrm{e}^{-KF_1(\mathbf{r}_1-\mathbf{r}_2)} \left[1 + \frac{\pi^2 g^2 a^3 K^2}{u^2} F_1(\mathbf{r}_1-\mathbf{r}_2) \int_a^\infty \mathrm{d}r \left(\frac{r}{a}\right)^{3-2K}\right]. \tag{1.51}$$

We now recognize that this expression is the beginning of the expansion of $\exp\{-K_{\mathrm{eff}} F_1(\mathbf{r}_1-\mathbf{r}_2)\}$ in powers of g, where

$$K_{\mathrm{eff}} = K - y^2 K^2 \int_a^\infty \frac{\mathrm{d}r}{a} \left(\frac{r}{a}\right)^{3-2K} \tag{1.52}$$

and $y = \pi g a^2/u$ is the dimensionless coupling constant of the perturbation S_1. This effective exponent controls the behavior of the correlation function at low energies. It should not be sensitive to the precise value of the cutoff. Consequently, varying the cutoff, $a \to a + \mathrm{d}a$, should be compensated by adjusting the parameters,

$$K(a+\mathrm{d}a) = K(a) - y^2(a) K^2(a) \frac{\mathrm{d}a}{a}, \tag{1.53}$$

$$y^2(a+\mathrm{d}a) = \left[1 + (4-2K)\frac{\mathrm{d}a}{a}\right] y^2(a). \tag{1.54}$$

Parametrizing the cutoff in the usual way, $a(l) = a_0 \, \mathrm{e}^l$, yields the RG equations

$$\frac{\mathrm{d}K}{\mathrm{d}l} = -y^2(l) K^2(l), \tag{1.55}$$

$$\frac{\mathrm{d}y}{\mathrm{d}l} = [2 - K(l)] y(l). \tag{1.56}$$

Similar equations govern the RG of the 2D XY model [116]. More generally, they appear for all models that belong to the BKT universality class [55, 56, 116]. The corresponding RG flow is visualized in Fig. 1.5. Depending on the bare values of the action (1.39), there are two different scenarios. If $K > 2$ and y is sufficiently small (below the separatrix), the parameter y renormalizes to zero. The perturbation S_1 is *irrelevant*. The low-energy theory is of LL type. On the contrary, if $K < 2$ or for parameters above the separatrix, y flows to strong coupling. The perturbation S_1 is *relevant*. It is expected that a gap is generated. We can estimate the gap in the following way. The (perturbative) RG can be used until the point where y is of order one. At strong coupling, the cosine locks the

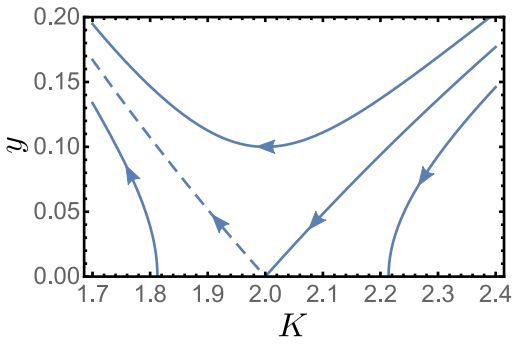

Figure 1.5: RG flow of the sine-Gordon model. For parameters below the separatrix (solid, almost straight line), y flows to zero (Luttinger-liquid phase). For $K < 2$ or above the separatrix, y flows to strong coupling.

field ϕ to its minimum at $\phi(x,\tau) = \pi$. A better approximation is to expand around this minimum, $\phi(x,\tau) = \pi + \delta\phi(x,\tau)$, leading to the action

$$S = S_0 + \frac{2uy}{\pi a^2}\int \mathrm{d}x\mathrm{d}\tau\delta\phi^2(x,\tau) = \frac{1}{2\pi uK}\int \frac{\mathrm{d}q}{2\pi}\frac{\mathrm{d}\omega}{2\pi}\left[\omega^2 + u^2q^2 + \frac{4Ku^2y}{a^2}\right]|\delta\phi(q,\omega)|^2. \tag{1.57}$$

The spectrum acquires a gap of the order of

$$\Delta = \sqrt{\frac{4Ku^2y}{a^2}} \sim \frac{u}{a}. \tag{1.58}$$

The gap can be related to the bare energy cutoff (bandwidth) Δ_0. Denoting by l^* the scale at which y is of order one, we find

$$\Delta(l^*) \simeq \Delta_0\,\mathrm{e}^{-l^*}. \tag{1.59}$$

After the discussion of the Luttinger liquid and the renormalization group, we turn in the next section to the transport formalism in 1D.

1.3.3 Transport theory: Memory-function formalism

In this section, the formalism to study charge transport in 1D systems is introduced. We employ this formalism in Secs. 3.2.2 and 3.3.2 to compute the DC conductivity of a JJ chain. In our presentation of the transport theory we follow the main steps outlined in Ref. [17]. The conductivity σ quantifies the linear response of the current j_e as a consequence of an applied electrical field E,

$$j_e(q,\omega) = \sigma(q,\omega)E(q,\omega). \tag{1.60}$$

Using the continuity equation,

$$\partial_t\rho_e + \partial_x j_e = 0 \tag{1.61}$$

with the charge density $\rho_e(x,t) = -2e\partial_x\phi/\pi$, we obtain

$$j_e(x,t) = \frac{2e}{\pi}\partial_t\phi. \tag{1.62}$$

Making use of the Heisenberg equation of motion

$$\partial_t \phi(x,t) = i[\mathcal{H}, \phi(x,t)], \tag{1.63}$$

the current operator in a LL theory with arbitrary perturbations that do not depend on $\theta(x)$ can be derived. With the LL Hamiltonian (1.36), we obtain the current operator,

$$j_e = \frac{2}{\pi} euK \partial_x \theta. \tag{1.64}$$

In the Kubo formalism [117, 118], the conductivity

$$\sigma(\omega) = \frac{i}{\omega}\left[\frac{4}{\pi}e^2 uK + \chi(\omega)\right], \tag{1.65}$$

is related to the retarded current-current correlation function

$$\chi(\omega) = -\int \mathrm{d}x \int_{-\infty}^{t} \mathrm{d}t' \mathrm{e}^{i\omega(t-t')} \left\langle \left[j_e(x,t), j_e(x',t') \right] \right\rangle. \tag{1.66}$$

For a pure LL an infinite DC conductivity is found,

$$\sigma(\omega) = 4e^2 uK \left[\delta(\omega) + \frac{i}{\pi}\mathcal{P}\frac{1}{\omega}\right], \tag{1.67}$$

where $\mathcal{P}$ denotes the principal value.

A finite conductivity requires the possibility to relax momentum. Disorder or umklapp processes which transfer momentum to the lattice are possible sources for a finite conductivity. A perturbative expansion of the $\phi\phi$ correlation function in powers of the coupling constant of the momentum relaxing perturbation is not possible in the zero-frequency limit. As shown above, the DC conductivity of a LL is infinite, while a finite perturbation is expected to produce a finite result. Such a behavior appears in the Drude formula as well. The Drude conductivity, $\sigma = ne^2\tau/m$, is proportional to the scattering time τ, which is in turn inversely proportional to the coupling constant of the momentum relaxing perturbation.

A way to circumvent this issue is to calculate the self-energy of the $\phi\phi$ correlation function in powers of the coupling constant. This procedure is used in Refs. [119, 120]. Here, we present a different method, the memory-function formalism [121–124]. At the lowest order, the two procedures yield the same result [17]. The idea is to bring the expression (1.65) to a Drude-like from,

$$\sigma(\omega) = \frac{ine^2/m}{\omega + i/\tau}. \tag{1.68}$$

Assuming a finite conductivity in the zero-frequency limit, leads according to Eq. (1.65) to $\chi(0) = -4e^2uK/\pi$. Now, we introduce the memory function

$$M(\omega) = \frac{\omega\chi(\omega)}{\chi(0) - \chi(\omega)}. \tag{1.69}$$

The conductivity can be rewritten in terms of the memory function in a Drude-like form

$$\sigma(\omega) = \frac{4i}{\pi}e^2 uK \frac{1}{\omega + M(\omega)}. \tag{1.70}$$

In this form, we can interpret the memory function as the self-energy of the conductivity, from which the characteristic time of the current relaxation can be read off. Assuming the memory function $M(\omega)$ to have a non-singular dependence on the coupling constants of the momentum relaxing perturbations, we make a hydrodynamic approximation. Without any perturbations, the current-current correlation function $\chi(\omega)$ vanishes for $\omega \neq 0$ (current commutes with the Hamiltonian). Hence, we can approximate

$$\chi(0) - \chi(\omega) \simeq \chi(0). \tag{1.71}$$

We rewrite the numerator in Eq. (1.69) as

$$\omega\chi(\omega) = -i \int \mathrm{d}x \int_0^\infty \mathrm{d}t \left(\partial_t \mathrm{e}^{i\omega t}\right) \left\langle \left[j_e(x,t), j_e(0,0)\right] \right\rangle \tag{1.72}$$

$$= i \int \mathrm{d}x \int_0^\infty \mathrm{d}t\, \mathrm{e}^{i\omega t} \left\langle \left[\partial_t j_e(x,t), j_e(0,0)\right] \right\rangle \tag{1.73}$$

$$= - \int \mathrm{d}x \int_0^\infty \mathrm{d}t\, \mathrm{e}^{i\omega t} \left\langle \left[\left[\mathcal{H}, j_e(x,t)\right], j_e(0,0)\right] \right\rangle, \tag{1.74}$$

where we integrated by parts and used the Heisenberg equation of motion. The total Hamiltonian of the system is denoted by $\mathcal{H}$. At this stage, we see already that the memory function vanishes if the Hamiltonian commutes with the current operator. Introducing the function $F(x,t) = [\mathcal{H}, j_e(x,t)]$ and making use of the Jacobi identity for commutators, we get

$$[F(x,t), j_e(0,0)] = \left[\mathcal{H}, [j_e(x,t), j_e(0,0)]\right] - [j_e(x,t), F(0,0)]. \tag{1.75}$$

The first term on the RHS of Eq. (1.75) vanishes after averaging. Substituting this result into Eq. (1.74), yields

$$\omega\chi(\omega) = \int \mathrm{d}x \left[\frac{i}{\omega} \left\langle [j_e(x,0), F(0,0)] \right\rangle - \frac{1}{\omega} \int_0^\infty \mathrm{d}t\, \mathrm{e}^{i\omega t} \left\langle [F(x,t), F(0,0)] \right\rangle \right], \tag{1.76}$$

where we integrated by parts once again. We define yet another function for convenience,

$$C(\omega) = \int \mathrm{d}x \int_0^\infty \mathrm{d}t\, \mathrm{e}^{i\omega t} \left\langle \left[F(x,t), F(0,0)\right] \right\rangle . \tag{1.77}$$

Demanding $\chi(\omega = 0)$ to be finite (already assumed above), we find

$$C(\omega = 0) = i \int \mathrm{d}x \left\langle [j_e(x,0), F(0,0)] \right\rangle, \tag{1.78}$$

and finally arrive at the expression

$$M(\omega) \simeq \frac{1}{-\chi(0)} \frac{C(\omega) - C(0)}{\omega} = \frac{\pi}{4e^2 uK} \frac{C(\omega) - C(0)}{\omega}. \tag{1.79}$$

for the memory function. The average in Eq. (1.77) can be done with respect to the Gaussian theory in the lowest order of perturbation theory since the function $F(x,t)$ is proportional to the coupling constant of the perturbation. In Secs. 3.2.2 and 3.3.2, we employ this formalism to extract the temperature dependence of the DC conductivity. To this end we combine the RG and the perturbative evaluation of the memory function.

After the discussion of the theoretical concepts employed in the description of JJ chains, we discuss in the next two sections experiments on the transport characteristics (Sec. 1.4) and the damping of plasmonic waves (Sec. 1.5) in these systems.

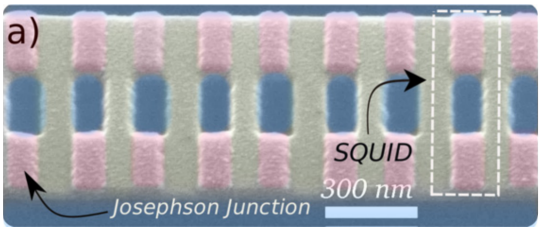

Figure 1.6: Scanning electron microscope image of a JJ chain in a SQUID geometry which was used in Ref. [50]. The superconducting islands (gray) are connected by two tunnel barriers (pink) in parallel. A magnetic flux through the holes of the SQUIDs enables the tuning of the effective Josepohson coupling.

1.4 Transport measurements

This section is devoted to the discussion of experiments on Josephson junction chains with a focus on the transport characteristics and the SIT. The first experiment investigating the SIT in 1D JJ chains is reported in Ref. [39] (see also Refs. [40, 45]). In the following we review the main aspects of this experiment that are relevant for this thesis. The superconducting islands are made of aluminum (bulk transition temperature $T_c \approx 1.2$K) and the tunnel barriers of Al_2O_3. In this experiment, a SQUID geometry is used where the superconducting islands are connected via two junctions in parallel. Figure 1.6 shows a scanning electron microscope image of a chain used in a later experiment [50] which is very similar to the device of Ref. [39]. As described in Sec. 1.1, applying a magnetic flux Φ, affects the Josephson energy

$$E_\mathrm{J} = E_\mathrm{J0} |\cos(\pi\Phi/\Phi_0)| \tag{1.80}$$

of the SQUID. Here, E_J0 is the Josephson energy in the absence of magnetic field. Increasing the flux from zero to half a flux quantum, suppresses the effective Josephson energy down to zero. This setup has the great advantage that the SIT can be observed in a single device. Only one parameter is varied in a controlled way. The Josephson energy in the absence of magnetic field is calculated using the Ambegaokar-Baratoff formula [125, 126],

$$E_\mathrm{J0} = \frac{\Phi_0}{2\pi c} I_{c0}, \quad I_{c0} = \frac{\pi\Delta_0}{2eR_T}, \tag{1.81}$$

where Δ_0 is the superconducting gap and R_T the normal tunnel resistance. The normal resistance of the whole array can be measured by applying a large voltage, $V > N(2\Delta_0/e)$, where N is the number of junctions. Alternatively, a low voltage can be used in combination with a strong magnetic field that completely suppresses superconductivity. Both methods yield almost the same result. The tunnel resistance R_T is now found by dividing the normal resistance of the whole chain by the number of SQUIDs. The capacitance of the junction (C_1 in our notations) can be estimated by measuring the junction area A (from electron microscope image), and making use of the specific capacitance $c_s = 45\ \mathrm{fF}/\mu\mathrm{m}^2$, $C_1 = c_s A$. A gold ground plane which is 1.5 μm below the chain and a rather small spacing between the islands (0.2 μm) results in a small capacitance to the ground (C_0). The electrostatic screening length $\Lambda = \sqrt{C_1/C_0}$ of these devices is approximately 10. The sample is placed

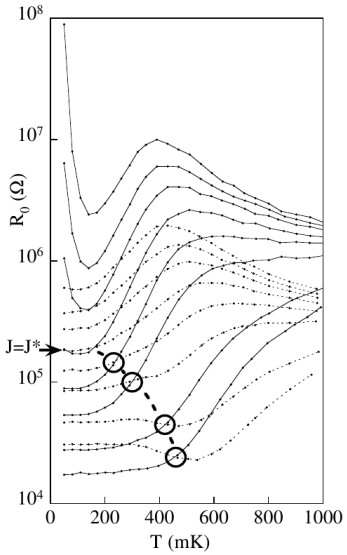

[Reprinted figure with permission from E. Chow, P. Delsing, and D. B. Haviland, Phys. Rev. Lett. **81**, 204 (1998), DOI: 10.1103/PhysRevLett.81.204, cf. Ref. [39]. Copyright 1998 by the American Physical Society.]

Figure 1.7: Experimental result of Ref. [39] for the zero-bias resistance as a function of temperature for two JJ chains with $N = 255$ (solid lines) and $N = 63$ (dashed lines). Curves from bottom to top correpsond to magnetic fields from zero to 64 G. The circles mark the crossing point of the two chains with the same magnetic field. The crossing point moves to zero temperature as the critical magnetic field is approached (marked by J*).

in a dilution refrigerator which made it possible to cool the chain down to 50 mK. The I-V curves in zero magnetic field show Josephson-like behavior with a finite slope at low bias. In the insulating regime, a zero-current state below a threshold voltage is observed. Furthermore, the temperature dependence of the resistance for two chains of length $N = 255$ and $N = 63$ are measured for various values of the magnetic flux. Fig. 1.7 shows the result of the zero-bias resistance measurement as a function of temperature. Solid and dashed curves correspond to the chains with $N = 255$ and $N = 63$, respectively. The magnetic field is increased form zero to 64 G from bottom to top. For weak magnetic fields (superconducting regime) the resistance decreases when the array is cooled and saturates at lowest temperatures probably because of finite-size effects. At high magnetic fields (insulating regime) the resistance is a non-monotonic function. In the high-temperature regime, the resistance increases as we lower T at first up to a temperature of about 400 mK for the longer chain, then decreases until it reaches a minimum at 100 mK and shoots up at lower temperatures. The upturn at lowest temperatures is clearly seen only in the longer chain. The circles in Fig. 1.7 show the crossing point of the resistance curves with the same effective E_J (magnetic field) but different length. As the Josephson coupling is reduced towards the critical value, the crossing point moves towards zero temperature. At this point, the quantum critical point, the resistance seems to be independent of length. This critical point is, however, located at an unexpectedly low value of the Josephson coupling [44, 45].

After this first experiment that investigated the SIT in JJ chains, several further experimental works on the transport characteristics of JJ chains appeared. In Ref. [41], a scaling analysis in chains up the to length of $N = 100$ is performed. The dynamical exponent as well as the exponent for the scaling of the correlation length are found. The effect of dissipation is studied experimentally in Ref. [42]. Shunting

each junction by a resistor leads to the damping of phase fluctuations, which favors superconducting correlations. Takahide et al. studied the dimensional crossover from 2D to 1D [43]. It is observed that reducing the width of the array, changes the behavior from superconducting to insulating. This can be explained by the stronger quantum fluctuations in 1D compared to 2D.

Notably longer chains are studied in Ref. [50] with a length up to $N = 2888$. In this paper, it is confirmed that QPS are responsible for the resistance at low temperatures. Indeed, as expected from the theory, the resistance is proportional to $\exp\{-\alpha\sqrt{E_J/E_1}\}$, where α is a numerical coefficient. In contrast to the observations in the earlier experiment of the same group for shorter chains [39], no strong length dependence of the resistance is found.

Besides these experiments that mainly focused on the zero-bias properties, experiments on insulating chains were performed that aimed to understand the threshold voltage above which the chain becomes conducting [52, 53]. In the experiment of Ref. [53], chains with a maximal length of $N = 5000$ were studied. The properties of the threshold voltage could be well explained by depinning physics. In the theoretical models of Refs. [52, 53], charge disorder is the source of the pinning. This observation leads to the conclusion that random stray charges play an important role in JJ chains. Furthermore, the authors of Ref. [53] make another important statement. Their measurements are performed with single-junction chains (no SQUID geometry). However, they report that additional measurements with chains of a SQUID geometry showed strongly reduced threshold voltages. This statement raises some doubts about the reliability of the data from SQUID chains also used in Ref. [39] where the SIT was located at an anomalously low value of the Josephson coupling. The authors of Ref. [53] conjecture that low-frequency flux noise or an interplay of charge and flux may affect the measurements in chains with a SQUID geometry. This shows that the investigation of the transport properties of JJ chains is still an active field of research, and further work is required to reach a consensus on the position of the SIT and related issues.

The SIT in 1D is not only observed in JJ chains but also in MoGe nanowires [64–66]. In the experiments of Refs. [64, 65], the wires were relatively short (up to $0.5\,\mu$m) while in a more recent experiment [66], wires with a maximal length of $25\,\mu$m were studied. The SIT in these semiconducting nanowires can be induced by reducing the cross section of the wire or by increasing a perpendicular magnetic field. The critical curve of the resistance as a function of temperature in Ref. [66] is essentially constant. In this experiment, the temperature range covers roughly one order of magnitude (from 2-4 K down to 0.4 K). The results of Ref. [66] are largely inconsistent with the theory of the phase-slip induced SIT in nanowires developed in Refs. [67, 68]. Moreover, there is also no consensus on the parameter controlling the transition in experimental works. This shows that many aspects of the SIT in nanowires are still under debate.

1.5 Spectroscopic measurements

Spectroscopic measurements constitute a complementary approach to experimentally probe the SIT. A recent experiment in which such measurements were performed is reported in Ref. [73]. This experiment measures the quality factor of a JJ chain device. In the following, we review important aspects of the experiment reported in Ref. [73]. The authors of Ref. [73] study two parallel chains of Al/AlOx/Al tunnel junctions on an insulating silicon substrate (see Fig. 1 a) of Ref. [73]). The 1 cm large devices consist of up to $33,000$ junctions. Both chains are separated by a distance of about $10\,\mu$m. The whole device is placed in a copper waveguide box with a distance of at least 5 mm between the chain and the metallic walls. One end of the device is connected to a dipole antenna, while the other one is

Table 1.1: Comparision between the notations of Ref. [73] and this thesis. Note that the value of the plasma frequency is same in both definitions since the factor of $\sqrt{8}$ is compensated by the different definition of the junction charging energy.

quantity	Ref. [73]	this thesis
interchain capacitance	C_0	C_0
junction capacitance	C_J	C_1
interchain charging energy	$E_0 = e^2/2C_0$	$E_0 = (2e)^2/C_0$
junction charging energy	$E_C = e^2/2C_J$	$E_1 = (2e)^2/C_1$
Josephson energy	E_J	E_J
plasma frequency	$\omega_p = \sqrt{8E_JE_C}$	$\omega_\mathrm{p} = \sqrt{E_\mathrm{J}E_1}$

short-circuited. Electromagnetic waves can be coupled to the device through a coaxial-to-waveguide transition launcher, which allows a good transmission in the frequency range of 7–12 GHz. In order to measure the standing wave modes in a wider frequency range, the standard two-tone dispersive reflectometry is used. This method makes use of the weak Kerr non-linearity leading to shifts of the resonance frequencies in dependence of the occupation of other modes. In this way, the authors can reconstruct the energy dispersion of the plasmonic waves, which is linear at low momenta with a velocity of about $1.9 \cdot 10^6$ m/s and flattens towards higher momenta approaching the plasma frequency $\omega_\mathrm{p}/2\pi \simeq 25$ GHz. The device is held at a temperature of 10 mK.

In order to measure the internal damping of the collective modes, the real and imaginary part of the reflection coefficient is measured at single-photon power. This is done via one-tone spectroscopy in a frequency range of 4–12 GHz. A dimensionless measure for the damping of the modes is the quality factor that is defined as the ratio of the mode frequency to its linewidth. By fitting their data to a model of a dissipative LC oscillator, the authors were able to separate the external from the internal damping. The external quality factor is related to losses due to the leakiness of the device. The experimental result for the internal quality factor for a few devices is shown in Fig. 3 of Ref. [73]. In the left panel, the individual modes are clearly visible as resonances in the magnitude of the reflection coefficient. The extracted internal quality factor is depicted in the right panel as a function of frequency normalized by the plasma frequency. The authors of Ref. [73] use the impedance Z and the ratio E_J/E_C to characterize their devices. The impedance Z is related to the Luttinger liquid parameter K_0 that we use in our theoretical model (see Sec. 4.1). The connection is given by

$$\pi K_0 = \frac{R_Q}{2Z}, \tag{1.82}$$

where $R_Q = 2\pi\hbar/(2e)^2 \simeq 6.5\,\mathrm{k}\Omega$ is the superconducting resistance quantum. In Ref. [73], a slightly different notation compared to this thesis is used. A comparison of the notations of both works is presented in Tab. 1.1. The quality factors of devices "a" and "b" shown in Fig. 3 b) of Ref. [73] increase when the frequency is lowered. These devices are characterized by a large ratio E_J/E_C. Reducing this ratio leads first to an almost flat frequency dependence of the quality factor (device "c"), and for even weaker junctions ("d", "e" and "f") a tendency to drop at low frequencies is observed. At this point, we note that on the basis of the values of the impedance Z, even the devices "a" and "b" are expected to be deeply in the insulating regime. Consequently, a vanishing of the quality factor at zero frequency is expected. However, in the range of measured frequencies in Fig. 3 b) of Ref. [73], such a tendency is not observed for these devices. Moreover, the authors of Ref. [73] observe a much stronger

dependence of the quality factor on the ratio E_J/E_C than on the impedance Z in weak junctions. We offer an explanation for this behavior in Chap. 4.

In order to further confirm their findings, the authors of Ref. [73] demonstrated the apparent transition from an increasing to a decreasing behavior of the quality factor in a single device. To this end, a device with the ratio $E_J/E_C \simeq 11$ was used which showed a growing quality factor when lowering the frequency. After aging the device under ambient conditions for about 1000 hours, the quality factor showed now a decreasing behavior. During the aging, the Josephson energy was reduced by about 25% due to oxidation. Annealing the device on a hot plate, almost restored the original parameters of the device, resulting again in an increasing behavior of the quality factor (see Fig. 4 of Ref. [73]). The same procedure with devices with parameters $E_J/E_C \gtrsim 70$ showed no effect.

A final remark on this experiment concerns the behavior of the low-impedance chains with a large ratio E_J/E_C, depicted in Fig. S 4 of the Supplementary Material of Ref. [73]. Among these samples, the variation of the charging energy E_0 is quite appreciable (up to a factor of $\simeq 75$) while the variation of all other parameters is much smaller. Nevertheless, when the quality factor is plotted as a function of the normalized frequency ω/ω_p, all curves seem to collapse.

The theoretical investigation of the damping of the collective modes in JJ chains is presented in Chap. 4. In Sec. 4.3, we compare our theory to the observations of the experiment described in this section.

Chapter 2

2 Fundamentals on relaxation in fermionic systems

After the introduction to Josephson junction chains, which are one-dimensional (1D) bosonic systems, we discuss in this chapter interacting fermionic systems with a focus on relaxation phenomena. Interaction-induced relaxation is a basic phenomenon that determines the dynamics of many-body systems at long time scales and is responsible for thermalization and ergodization.

The fact that the relaxation times can be long was found in Fermi liquids for low-energy excitations. The lifetime τ of a fermionic quasiparticle in a Fermi liquid with an excess energy ϵ above the Fermi sea behaves as $\tau \sim \epsilon_F/\epsilon^2$ [127]. Excitations close to the Fermi surface become well defined long-lived quasiparticles — a key ingredient for Landau's Fermi-liquid theory. In two spatial dimensions, this result acquires logarithmic corrections [128, 129] but otherwise the result stays intact. As we will see in this chapter and in Chap. 5, 1D systems are special. The universality found in higher dimensions is absent in 1D. The low-energy behavior of the lifetime depends, e. g., on the energy dispersion, the presence of spin and the form of the interaction potential [18, 130–132].

In this chapter, we introduce the fundamental concepts that are used in this thesis to compute the relaxation rate of excitations. Section 2.1 presents the basic formalism to perturbatively compute transition rates. The (generalized) golden rule introduced in this section forms the basis for the calculation of relaxation rates. In Sec. 2.2, we use the lowest order golden rule to compute the two-particle collision integral. This enables us to derive the Fermi-liquid result for the lifetime of low-energy excitations in three dimensional systems. Moreover, at the end of this section, we briefly discuss the bosonic case which will be used in Chap. 4 for the computation of the lifetime of plasmons in Josephson junction (JJ) chains. Since in 1D systems with quadratic spectrum the collision integral for two-particle scattering vanishes, we study in Sec. 2.3 the collision integral for three-particle collisions. Finally, Sec. 2.4 presents a few experimental studies on relaxation in fermionic systems with a focus on the experiment reported in Ref. [98], which studied the relaxation in nanowires.

2.1 Fermi's golden rule

Fermi's golden rule is a powerful expression to calculate transition rates between states in perturbation theory. We present here a brief introduction to the important result for the transition rate, which is

well described in the standard literature on quantum mechanics. Let us consider a physical system described by the Hamiltonian

$$\hat{\mathcal{H}} = \hat{\mathcal{H}}_0 + \hat{V} \tag{2.1}$$

consisting of a part $\hat{\mathcal{H}}_0$ that is assumed to be solvable in the sense that the eigenenergies and eigenstates are known, and a perturbation (interaction) $\hat{V}$. A specific example that is of particular importance for this thesis is the case of interacting fermions. Here, the quadratic Hamiltonian

$$\hat{\mathcal{H}}_0 = \sum_{\mathbf{p},\sigma} \epsilon(\mathbf{p})\, a^\dagger_{\mathbf{p},\sigma} a_{\mathbf{p},\sigma} \tag{2.2}$$

describes non-interacting fermions with energy spectrum $\epsilon(\mathbf{p})$. The fermionic creation and annihilation operators of the state with momentum $\mathbf{p}$ and spin projection σ are denoted by $a^\dagger_{\mathbf{p},\sigma}$ and $a_{\mathbf{p},\sigma}$, respectively. They obey the standard anti-commutation relations,

$$a^\dagger_{\mathbf{p},\sigma} a^\dagger_{\mathbf{p}',\sigma'} + a^\dagger_{\mathbf{p}',\sigma'} a^\dagger_{\mathbf{p},\sigma} = a_{\mathbf{p},\sigma} a_{\mathbf{p}',\sigma'} + a_{\mathbf{p}',\sigma'} a_{\mathbf{p},\sigma} = 0, \qquad a^\dagger_{\mathbf{p},\sigma} a_{\mathbf{p}',\sigma'} + a_{\mathbf{p}',\sigma'} a^\dagger_{\mathbf{p},\sigma} = \delta_{\mathbf{p},\mathbf{p}'}\delta_{\sigma,\sigma'}. \tag{2.3}$$

The two-body interaction of fermions via the potential $V(\mathbf{q})$ is of the form

$$\hat{V} = \frac{1}{2\mathcal{V}} \sum_{\mathbf{k},\mathbf{p},\mathbf{q},\sigma_1,\sigma_2} V(\mathbf{q})\, a^\dagger_{\mathbf{k}+\mathbf{q},\sigma_1} a^\dagger_{\mathbf{p}-\mathbf{q},\sigma_2} a_{\mathbf{p},\sigma_2} a_{\mathbf{k},\sigma_1}, \tag{2.4}$$

where $\mathcal{V}$ is the volume of the system.

The aim is to calculate the transition rate between eigenstates of the free Hamiltonian $\hat{\mathcal{H}}_0$. Denoting the initial and finial states by $|i\rangle$ and $|f\rangle$, respectively, the transition rate to the lowest order in the interaction in the long-time limit is given by (see e. g. Ref. [133])

$$\Gamma_{fi} = 2\pi |\langle f|\hat{V}|i\rangle|^2 \delta(E_i - E_f), \tag{2.5}$$

where E_i, E_f are the energies of the initial and final states, respectively. This expression is known as Fermi's golden rule. The delta function expresses the energy conservation in the process valid in the "long-time" limit.

Higher order terms can be conveniently taken into account by the T-matrix formalism (see e. g. Ref. [134]). The T-matrix is governed by the self-consistency equation

$$\hat{T} = \hat{V} + \hat{V} \frac{1}{E_i - \hat{\mathcal{H}}_0 + i0} \hat{T}. \tag{2.6}$$

By iteration, we obtain the expansion of the T-matrix in powers of the interaction $\hat{V}$:

$$\hat{T} = \hat{V} + \hat{V} \frac{1}{E_i - \hat{\mathcal{H}}_0 + i0} \hat{V} + \hat{V} \frac{1}{E_i - \hat{\mathcal{H}}_0 + i0} \hat{V} \frac{1}{E_i - \hat{\mathcal{H}}_0 + i0} \hat{V} + ... \tag{2.7}$$

The "generalized" golden rule including higher-order processes is given by [134]

$$\Gamma_{fi} = 2\pi |\langle f|\hat{T}|i\rangle|^2 \delta(E_i - E_f). \tag{2.8}$$

In the first order approximation of $\hat{T}$, we recover the "standard" golden rule expression, Eq. (2.5). Including higher-order processes, the energy in the overall process is still conserved. From the form of the T-matrix in Eq. (2.7), we see that the intermediate (virtual) transitions in higher-order terms do not conserve energy. In strictly 1D systems with quadratic spectrum, the first order processes do not contribute to relaxation. We thus need to go to the second order and discuss three-particle collisions. A deeper discussion of these processes is presented in Sec. 2.3. In the next section, we analyze the simpler case of two-particle collisions in fermionic systems in three dimensions.

2.2 Two-particle collisions

We start with the discussion of two-particle collisions in fermionic systems and analyze the relaxation rate of a fermion in the low-energy regime. In our discussion, we follow the argumentation presented in Ref. [135]. The goal of this section is to compute the relaxation rate of an additional particle with quantum numbers λ_1 above a filled Fermi sea. The collision integral [136, 137]

$$I[n_\lambda] = \frac{1}{2!}\sum_{\lambda_2,\lambda_1',\lambda_2'} W_{\lambda_1,\lambda_2}^{\lambda_1',\lambda_2'}[(1-n_{\lambda_1})(1-n_{\lambda_2})n_{\lambda_1'}n_{\lambda_2'} - n_{\lambda_1}n_{\lambda_2}(1-n_{\lambda_1'})(1-n_{\lambda_2'})] \tag{2.9}$$

describes the change of the occupation of the state with quantum numbers λ_1 as a consequence of collisions with other particles. Here, ϵ_i denotes the energy of the state with quantum numbers λ_i (determined by the free Hamiltonian $\hat{\mathcal{H}}_0$), n_λ the fermionic distribution function, the factor $1/2!$ reflects the indistinguishability of the final fermions, and the transition probability

$$W_{\lambda_1,\lambda_2}^{\lambda_1',\lambda_2'} = 2\pi|\langle 1',2'|\hat{V}|1,2\rangle|^2\delta(\epsilon_1+\epsilon_2-\epsilon_1'-\epsilon_2') \tag{2.10}$$

is determined by Fermi's golden rule, Eq. (2.5). The first term in the square brackets is associated with the scattering into, and the second one out of the state with quantum numbers λ_1. The matrix element is given by

$$\langle 1',2'|\hat{V}|1,2\rangle = \langle 0|a_{\lambda_1'}a_{\lambda_2'}\hat{V}a_{\lambda_1}^\dagger a_{\lambda_2}^\dagger|0\rangle \tag{2.11}$$

with $|0\rangle$ being the empty state. In thermal equilibrium, the distribution function is given by the Fermi-Dirac distribution,

$$n_\lambda = n_{\mathrm{F}}(\epsilon_\lambda) \equiv \frac{1}{\exp\left(\frac{\epsilon_\lambda-\mu}{T}\right)+1}, \tag{2.12}$$

where μ is the chemical potential (Fermi energy at zero temperature). The collision integral Eq. (2.9) vanishes in equilibrium. We consider the situation, in which on top of a fermionic system at equilibrium, an additional fermion is present. In order to compute the relaxation rate $1/\tau$, we linearize the collision integral by expanding in the small deviation from equilibrium, $\delta n_\lambda = n_\lambda - n_{\mathrm{F}}(\epsilon_\lambda)$, and reading off the "diagonal" coefficient,

$$I[n_\lambda] = -\frac{1}{\tau}\delta n_{\lambda_1} + ... \tag{2.13}$$

The omitted terms in the above equation are of higher order in the deviation δn_λ or "off-diagonal" ($\propto \delta n_{\lambda_{i\neq 1}}$). This leads to the expression

$$\frac{1}{\tau} = \pi\sum_{\lambda_2,\lambda_1',\lambda_2'}|\langle 1',2'|\hat{V}|1,2\rangle|^2\delta(\epsilon_1+\epsilon_2-\epsilon_1'-\epsilon_2')\Big[[1-n_{\mathrm{F}}(\epsilon_2)]n_{\mathrm{F}}(\epsilon_1')n_{\mathrm{F}}(\epsilon_2')+n_{\mathrm{F}}(\epsilon_2)[1-n_{\mathrm{F}}(\epsilon_1')][1-n_{\mathrm{F}}(\epsilon_2')]\Big]. \tag{2.14}$$

In the following, the Fermi-liquid result for the relaxation rate of a particle at low energies above the Fermi sea, $0 < \epsilon_1 \ll \epsilon_{\mathrm{F}}$, is derived. From now on, we measure all energies ϵ_i relative to the Fermi energy ϵ_{F}. We focus on the case of zero temperature, in which the Fermi function is a step function, $n_{\mathrm{F}}(\epsilon) = \Theta(-\epsilon)$. The first term in the square bracket of Eq. (2.14), associated with the in-scattering rate, vanishes at zero temperature. For our purposes the spin is unimportant; we omit it in the following. The precise form of the matrix element is of minor importance as well. We only need the

scaling with the volume $\mathcal{V}$ and the fact that the interaction (2.4) conserves the total momentum in the collision,

$$\langle 1', 2'|\hat{V}|1, 2\rangle \equiv \frac{1}{\mathcal{V}}\,\delta_{\mathbf{p}_1+\mathbf{p}_2,\mathbf{p}_1'+\mathbf{p}_2'}\,M^{\mathbf{p}_1',\mathbf{p}_2'}_{\mathbf{p}_1,\mathbf{p}_2}. \tag{2.15}$$

In the considered regime, $0 < \epsilon_1 \ll \epsilon_\mathrm{F}$, all other energies are also small, $|\epsilon_2|,|\epsilon_1'|,|\epsilon_2'| \ll \epsilon_\mathrm{F}$. We write the summation over the momentum as an integration over the directions of the momentum and the energy,

$$\frac{1}{\mathcal{V}}\sum_{\mathbf{p}} \to \nu_\mathrm{F}\int\frac{\mathrm{d}\Omega_p}{4\pi}\int\mathrm{d}\epsilon, \tag{2.16}$$

where ν_F is the density of states at the Fermi energy. In this way, the integrations over the energies and directions of the momenta decouple approximately,

$$\frac{1}{\tau} = 2\pi\langle|V|^2\rangle_\Omega\int\mathrm{d}\epsilon_2\int\mathrm{d}\epsilon_1'\int\mathrm{d}\epsilon_2'\,\delta(\epsilon_1+\epsilon_2-\epsilon_1'-\epsilon_2')n_\mathrm{F}(\epsilon_2)[1-n_\mathrm{F}(\epsilon_1')][1-n_\mathrm{F}(\epsilon_2')] \tag{2.17}$$

with the modulus squared matrix element averaged over the directions

$$\langle|V|^2\rangle_\Omega \simeq \frac{1}{2}(2\pi)^3\nu_\mathrm{F}^3\int\frac{\mathrm{d}\Omega_2}{4\pi}\int\frac{\mathrm{d}\Omega_1'}{4\pi}\int\frac{\mathrm{d}\Omega_2'}{4\pi}\left|M^{\mathbf{p}_1',\mathbf{p}_2'}_{\mathbf{p}_1,\mathbf{p}_2}\right|^2\delta(p_\mathrm{F}(\mathbf{n}_1+\mathbf{n}_2-\mathbf{n}_1'-\mathbf{n}_2')), \tag{2.18}$$

where p_F is the Fermi momentum, and $\mathbf{n}_i$ is a unit vector pointing in the direction of $\mathbf{p}_i$. Evaluating the integrations over the energies, we find

$$\frac{1}{\tau(\epsilon_1)} = \pi\langle|V|^2\rangle_\Omega\,\epsilon_1^2 \tag{2.19}$$

reflecting the available phase space for the collision processes. The angular average of the squared matrix element, Eq. (2.18), depends on the low-momentum behavior of the interaction potential and the presence of spin. It is, however, independent of the energy ϵ_1. Under the assumption $V(-\mathbf{q}) = V(\mathbf{q})$ on the interaction potential in momentum space, the matrix element is given by

$$\langle 1', 2'|\hat{V}|1, 2\rangle = \frac{1}{\mathcal{V}}\left[\delta_{\sigma_1,\sigma_1'}\delta_{\sigma_2,\sigma_2'}V(\mathbf{p}_1-\mathbf{p}_1') - \delta_{\sigma_1,\sigma_2'}\delta_{\sigma_2,\sigma_1'}V(\mathbf{p}_1-\mathbf{p}_2')\right]\delta_{\mathbf{p}_1+\mathbf{p}_2,\mathbf{p}_1'+\mathbf{p}_2'} \tag{2.20}$$

in the spinful and by

$$\langle 1', 2'|\hat{V}|1, 2\rangle = \frac{1}{\mathcal{V}}\left[V(\mathbf{p}_1-\mathbf{p}_1') - V(\mathbf{p}_1-\mathbf{p}_2')\right]\delta_{\mathbf{p}_1+\mathbf{p}_2,\mathbf{p}_1'+\mathbf{p}_2'} \tag{2.21}$$

in the spin-polarized case. The first term in each case is called direct term while the second one is called exchange term.

We compute the angular average of the squared matrix element for a specific form of the interaction explicitly in Sec. 5.1. In the low-energy regime, we obtain the results (5.18) and (5.19) for spinful and spin-polarized fermions, respectively. Moreover, the above described procedure is used in Secs. 5.1 and 5.2 to compute the relaxation rate at high energies, $\epsilon \gg \epsilon_\mathrm{F}$, in $D \geq 2$ dimensional systems as well in quasi-1D wires.

We remark that an alternative approach to calculate the relaxation rate is via the imaginary part of the self-energy (see e. g. Ref. [138]). We make use of this procedure in Sec. 4.2.1 when we discuss the lifetime of plasmons in Josephson junction chains induced by quantum phase slips. In Sec. 4.2.2, where we analyze the damping of plasmons due to gradient nonlinearities, we employ the same approach

with the collision integral as above. However, since we deal with bosonic particles, the structure of the collision integral (2.9) is different. It reads in the bosonic case (see e. g. Ref. [137])

$$I[n_\lambda] = \frac{2\pi}{2!}\sum_{\lambda_2,\lambda_1',\lambda_2'} |\langle 1',2'|\hat{V}|1,2\rangle|^2 \delta(\epsilon_1+\epsilon_2-\epsilon_1'-\epsilon_2')[(n_{\lambda_1}+1)(n_{\lambda_2}+1)n_{\lambda_1'}n_{\lambda_2'} - n_{\lambda_1}n_{\lambda_2}(n_{\lambda_1'}+1)(n_{\lambda_2'}+1)], \tag{2.22}$$

where in this case n_λ is the distribution function of bosons. The first term in the square brackets corresponds again to the in-scattering and the second one to the out-scattering rate. In order to study the relaxation of an additional boson on top of the equilibrium distribution

$$n_{\mathrm{B}}(\epsilon) = \frac{1}{\exp\left(\frac{\epsilon-\mu}{T}\right)-1}, \tag{2.23}$$

we linearize again the collision integral, $n_\lambda = n_{\mathrm{B}}(\epsilon_\lambda) + \delta n_\lambda$. As in the fermionic case discussed above, the relaxation rate is read off from the "diagonal" term of the collision integral. We then finally arrive at the expression for the relaxation rate

$$\frac{1}{\tau} = \pi \sum_{\lambda_2,\lambda_1',\lambda_2'} |\langle 1',2'|\hat{V}|1,2\rangle|^2 \delta(\epsilon_1+\epsilon_2-\epsilon_1'-\epsilon_2')\Big\{n_{\mathrm{B}}(\epsilon_2)[1+n_{\mathrm{B}}(\epsilon_1')+n_{\mathrm{B}}(\epsilon_2')] - n_{\mathrm{B}}(\epsilon_1')n_{\mathrm{B}}(\epsilon_2')\Big\}. \tag{2.24}$$

of a bosonic excitation with energy ϵ_1. In the next section, we discuss three-particle collisions that govern the relaxation in 1D systems with parabolic dispersion.

2.3 1D geometry: three-particle collisions

Pair collisions do not lead to relaxation in one dimension for particles with a dispersion with positive curvature because energy and momentum conservation allow only for permutations of the particles [130]. Therefore, three-particle collisions need to be taken into account. We follow Ref. [130] for an introduction to this topic. Making use of the "generalized" golden rule, Eq. (2.8), we can write down the collision integral for three-particle collisions of fermions

$$\begin{aligned} I[n_\lambda] = \frac{2\pi}{2!3!}\sum_{\lambda_2,\lambda_3,\lambda_1',\lambda_2',\lambda_3'} & |\langle 1',2',3'|\hat{V}\hat{G}_0\hat{V}|1,2,3\rangle|^2 \delta(E_i-E_f) \\ & \times [(1-n_{\lambda_1})(1-n_{\lambda_2})(1-n_{\lambda_3})n_{\lambda_1'}n_{\lambda_2'}n_{\lambda_3'} - n_{\lambda_1}n_{\lambda_2}n_{\lambda_3}(1-n_{\lambda_1'})(1-n_{\lambda_2'})(1-n_{\lambda_3'})], \end{aligned} \tag{2.25}$$

where $\lambda_i = (p_i, \sigma_i)$, and $E_i = \epsilon_1+\epsilon_2+\epsilon_3$ and $E_f = \epsilon_1'+\epsilon_2'+\epsilon_3'$ are the total energies before and after the collision, respectively. The Green's function operator reads explicitly

$$\hat{G}_0 = \frac{1}{E_i - \hat{\mathcal{H}}_0 + i0}. \tag{2.26}$$

The prefactor 1/2!3! takes care of the indistinguishability of incoming and outgoing particles. The first term in the square bracket of Eq. (2.25) corresponds to the rate for the scattering into and the second

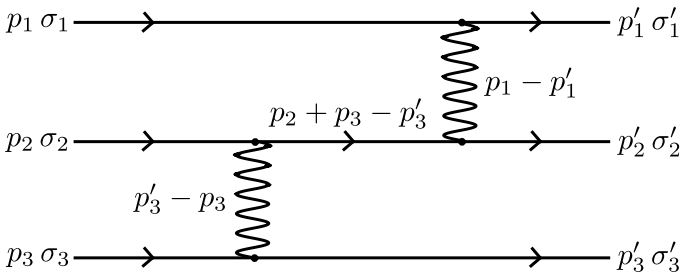

Figure 2.1: Visualization of the basic process for three-particle scattering. The total matrix element consists of all processes where the legs of incoming as well as the legs ouf outgoing particles are interchanged.

one out of the state with quantum number λ_1. Analogous to the two-particle case, we linearize the collision integral and read off the relaxation rate $1/\tau$ from the "diagonal" part,

$$\frac{1}{\tau} = \frac{2\pi}{2!3!} \sum_{\lambda_2,\lambda_3,\lambda_1',\lambda_2',\lambda_3'} |\langle 1',2',3'|\hat{V}\hat{G}_0\hat{V}|1,2,3\rangle|^2 \delta(E_i - E_f) \\ \times \Big\{ [1-n_{\mathrm{F}}(\epsilon_2)][1-n_{\mathrm{F}}(\epsilon_3)] n_{\mathrm{F}}(\epsilon_1') n_{\mathrm{F}}(\epsilon_2') n_{\mathrm{F}}(\epsilon_3') + n_{\mathrm{F}}(\epsilon_2) n_{\mathrm{F}}(\epsilon_3) [1-n_{\mathrm{F}}(\epsilon_1')][1-n_{\mathrm{F}}(\epsilon_2')][1-n_{\mathrm{F}}(\epsilon_3')] \Big\}. \tag{2.27}$$

At zero temperature, the first term in the curly brackets which is related to the in-scattering rate, vanishes. Let us now analyze the matrix element

$$\langle 1',2',3'|\hat{V}\hat{G}_0\hat{V}|1,2,3\rangle = \langle 0| a_{p_1',\sigma_1'} a_{p_2',\sigma_2'} a_{p_3',\sigma_3'} \hat{V}\hat{G}_0\hat{V} a^\dagger_{p_1,\sigma_1} a^\dagger_{p_2,\sigma_2} a^\dagger_{p_3,\sigma_3} |0\rangle \tag{2.28}$$

for three-particle collisions. For the two-body interaction (2.4), the matrix element can be written as [130]

$$\langle 1',2',3'|\hat{V}\hat{G}_0\hat{V}|1,2,3\rangle = \frac{1}{4L^2} \sum_{(abc)\in\mathcal{P}(123)} \mathrm{sign}(abc) \sum_{(a'b'c')\in\mathcal{P}(1'2'3')} \mathrm{sign}(a'b'c') \\ \times \frac{V(p_a'-p_a)V(p_c'-p_c)\delta_{p_a+p_b+p_c,p_a'+p_b'+p_c'}}{\epsilon_b+\epsilon_c-\epsilon_{c'}-\epsilon_{b+c-c'}+i0} \delta_{\sigma_a,\sigma_{a'}}\delta_{\sigma_b,\sigma_{b'}}\delta_{\sigma_c,\sigma_{c'}}, \tag{2.29}$$

where L is the system size, $\mathcal{P}(123) = \{(123)^+,(231)^+,(312)^+,(132)^-,(213)^-,(321)^-\}$ is the set of permutations of $(1,2,3)$, and the superscript of each element indicates its sign, $\mathrm{sign}(abc)$. The scattering amplitude for the three-particle matrix element is visualized in Fig. 2.1. Overall there are 36 terms in the matrix element. For a quadratic energy spectrum, $\epsilon_p = p^2/2m$, the denominator can be rewritten as

$$\begin{aligned} \epsilon_b+\epsilon_c-\epsilon_{c'}-\epsilon_{b+c-c'} &= -\frac{1}{m}(p_b-p_c')(p_c-p_c') \\ &= \frac{(p_a-p_c')(p_b-p_c')(p_c-p_c')}{m(p_c'-p_a)}. \end{aligned} \tag{2.30}$$

The energy and momentum conservation can be conveniently taken into account by parametrizing the momenta according to

$$p_k = \frac{P}{3} + q\cos\left[\varphi + \frac{2\pi(k-1)}{3}\right], \quad k = 1,2,3, \tag{2.31}$$

$$p'_k = \frac{P}{3} + q\cos\left[\varphi' + \frac{2\pi(k-1)}{3}\right], \quad k = 1,2,3. \tag{2.32}$$

Here, P has the meaning of the total momentum and $q \geq 0$ is defined by

$$E_i = E_f = \frac{P^2}{6m} + \frac{3q^2}{4m}. \tag{2.33}$$

With this parametrization, the numerator in Eq. (2.30) can be written on the mass-shell as

$$(p_a - p'_c)(p_b - p'_c)(p_c - p'_c) = \frac{q^3}{4}(\cos 3\varphi - \cos 3\varphi'), \tag{2.34}$$

which is invariant under the exchange of incoming and the exchange of outgoing particles. This leads to a great simplification since all terms in the matrix element have a common denominator,

$$\langle 1',2',3'|\hat{V}\hat{G}_0\hat{V}|1,2,3\rangle = \frac{m}{L^3q^3(\cos 3\varphi - \cos 3\varphi')} \sum_{\substack{(abc)\in\mathcal{P}(123)\\(a'b'c')\in\mathcal{P}(1'2'3')}} \operatorname{sign}(abc)\operatorname{sign}(a'b'c')\, q_{c',a}V(q_{a',a})V(q_{c',c}) \times \delta_{p_a+p_b+p_c,p'_a+p'_b+p'_c}\delta_{\sigma_a,\sigma_{a'}}\delta_{\sigma_b,\sigma_{b'}}\delta_{\sigma_c,\sigma_{c'}} \tag{2.35}$$

with the short-hand notation $q_{a',b} = p'_a - p_b$. In the spin-polarized case, the spin indices need to be omitted. As we show in Sec. 5.3, the matrix element (2.35) does not contain a pole in the spin-polarized situation because of cancellations between different processes (see Eq. (5.45) and the discussion below this equation). In the spinful case, there is, however, a pole that emerges from two consecutive two-particle scattering processes separated by an infinite time. In order to subtract those doubly counted processes, a regularization procedure is discussed in Ref. [139]. As we show in Sec. 5.3, at zero temperature such a regularization is not necessary since the Fermi functions restrict the phase space to a region that does not contain the poles.

In the next section, we discuss experiments studying the relaxation of electrons.

2.4 Measurement of the relaxation rate in nanowires

The relaxation rate of electrons in normal metals was measured by means of the time-resolved two-photon photoemission [80, 81]. This technique, consists of two steps. A first laser pulse excites an electron of the surface of the metal. A second pulse, delayed in time, emits the electron whose kinetic energy is measured. Monitoring the number of electrons for a given energy as a function of the delay time enables the measurement of the relaxation time. In these experiments qualitative agreement with the Fermi-liquid result (2.19) is found.

More relevant for this thesis is a recent experiment [98] that studied the relaxation of electrons in InAs nanowires. We summarize in the following the main aspects of this experiment that are important for

this thesis. The nanowires were grown by molecular-beam epitaxy using the gold-assisted vapor-liquid-solid technique and have a diameter of about 70 nm. They are placed on top of a gold substrate, which has a surface roughness of the order of 60 nm partially suspending the nanowires. Measurements are performed in ultra-high vacuum at a temperature of 4.2 K. The electron density is about 100 electrons per micron leading to the occupation of 3-4 1D subbands.

By means of scanning tunneling microscopy (STM), the local density of states is extracted from the measurement of the differential conductance using the lock-in technique. The differential conductance reveals interference patterns emerging from the scattering off crystallographic irregularities. The periodicity of the patterns is determined by the momentum transfer q between the incident and scattered states. In order to study relaxation effects, the authors of Ref. [98] used two different approaches: (i) the investigation of the scattering from the nanowire's end, and (ii) the investigation of the interference pattern in Fabry-Pérot resonators.

Using the first approach, the coherence length L_φ is determined. Electrons are injected via the STM tip in the vicinity of the end of the nanowire and the local differential conductance as a function of energy and the distance to the end is measured. The differential conductance shows pronounced dispersing interference patterns. A spatial Fourier transform of the data reveals the 1D subbands with a dominant mode associated with the lowest subband. The dominant visibility of the lowest subband is attributed to the enhanced phase coherence of the lowest subband in comparison to higher subbands. Figure 2.2 a) shows the differential conductance as a function of the distance to the end of the nanowire for a few energies. These curves are extracted from the raw data after filtering out all non-dispersing effects. The curves are fitted by $A|\sin(qx+\varphi)|\exp(-2x/L_\varphi)$ where q is determined from the measured energy dispersion of the lowest subband. At the highest measured energies, the decay of the standing wave is too slow to be resolved within the measured distance of 40 nm. The maximal distance is limited by surface impurities disturbing the interference patterns. The extracted energy dependence of the phase coherence length L_φ is shown in Fig. 2.2 b). Close to the Fermi-energy, the coherence length is of the order of 70 nm and shortens rapidly when increasing the energy. This behavior is in accordance with the growth of the available phase space. However, at around 80 meV, the coherence length reaches a minimum and starts to grow again at higher energies. This behavior is at variance with the expectation from the Fermi-liquid result, Eq. 2.19, valid at low energies.

The second approach utilizes a Fabry-Pérot resonator that is formed by adjacent stacking faults. Measuring the differential conductance inside a resonator away from the end of the nanowire reveals resonances with a finite width [see Fig. 2.3 a)]. The width of the resonances Γ as a function of the peak energy is depicted in Fig. 2.3 b). On top of the relaxation due to electron-electron interaction, there are several additional sources contributing to the broadening. At the Fermi energy, the relaxation rate due to electron-electron interaction should vanish. The additional broadening of the resonance at the Fermi energy is caused by the leakiness of the resonator as well as instrumental contributions from finite temperature (1 meV) and finite AC probing amplitude (3 meV). Subtracting the width at the Fermi energy yields the relaxation rate due to internal damping, $\tilde{\Gamma}(E) = \Gamma(E) - \Gamma(E_\mathrm{F})$. Again, a non-monotonic dependence of the rate as a function of energy is found. At low energies, the rate increases first until a maximum around 80 meV is reached, and decreases at higher energies. Both approaches, the investigation of the scattering from the end of the nanowire and the measurement of the width of the resonances in a Fabry-Pérot resonator agree on the non-monotonic dependence as well as on the energy position of the maximum. The first approach directly yields the phase coherence length L_φ, while in the second approach the phase coherence time τ_φ is extracted via $\tau_\varphi \sim \hbar/2\tilde{\Gamma}$. Both data can be related through the velocity v determined from the energy dispersion of the lowest subband, $L_\varphi = v\tau_\varphi$. The difference in the overall magnitude of the relaxation rate extracted from both methods

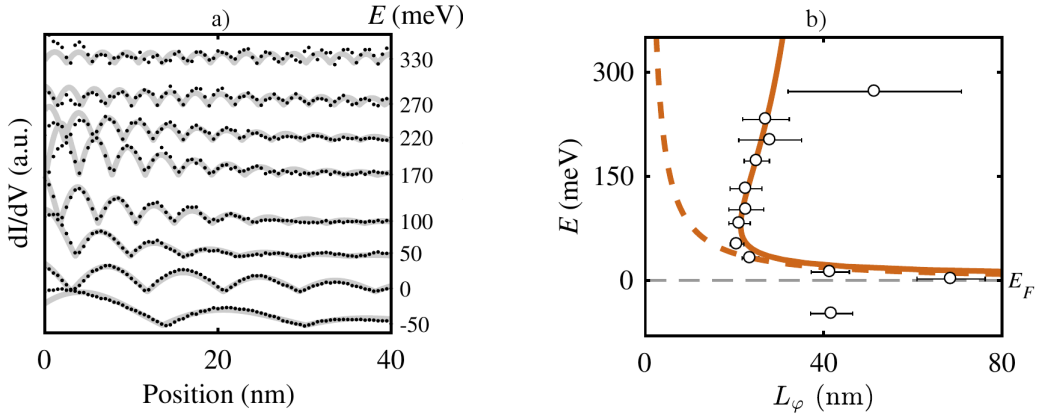

Figure 2.2: Measurement of the coherence length in a multi-channel wire (taken from Ref. [98]). a) Decay profiles of the differential conductance as a function of the distance to the nanowire's end for several energies. The data is represented by the dots, the fit to $A|\sin(qx+\varphi)\exp(-2x/L_\varphi)$ is visualized by the gray lines. At high energies, the decay is too slow to be resolved within the measured distance. b) Energy dependence of the coherence length L_φ (open circles) as extracted from a). In the low-energy regime, the coherence length shortens when incereasing the energy. The thick dashed line shows the E^{-2} behavior expected at low energies. Beyond the minimum of L_φ around 80 meV, the coherence length increases again.

is explained by the variation in the suspension of the wire leading to different dielectric constants at the end of the wire and at the position of the resonator. In conclusion, both methods demonstrate that the relaxation rate of electrons in multi-channel quantum wires shows a non-monotonic behavior as a function of energy. Electrons regain their coherence at high energies.

In Chap. 5, we study theoretically the relaxation of fermions in quasi-1D multi-channel and 1D single-channel wires. We show that under quite generic circumstances, the relaxation rate shows non-monotonic behavior with a power-law decay at high energies.

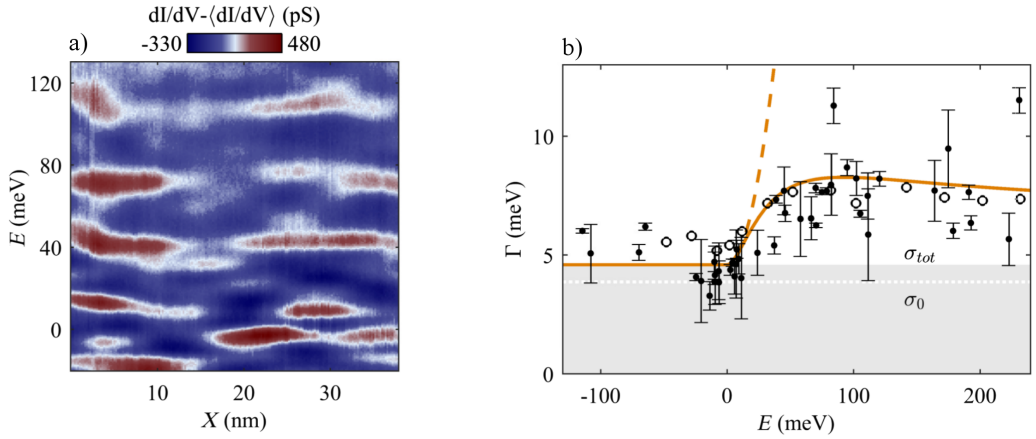

[Reprinted figure with permission from J. Reiner, A. K. Nayak, N. Avraham, A. Norris, B. Yan, I. C. Fulga, J.-H. Kang, T. Karzig, H. Shtrikman, and H. Beidenkopf, Phys. Rev. X **7**, 021016 (2017), DOI: 10.1103/PhysRevX.7.021016, cf. Ref. [98]. Copyright 2017 by the American Physical Society, link to license: https://creativecommons.org/licenses/by/4.0/.]

Figure 2.3: Measurement of the relaxation rate from Fabry-Pérot resonances (taken from Ref. [98]). a) Differential conductance inside a Fabry-Pérot resonator that is formed by two adjacent stacking faults. Quantized resonances (red areas) with a finite width are visible. b) Width Γ of the resonances as a function of the peak energy E (black dots). The finite width at the Fermi energy originates from the finite temperature and AC probing amplitude, $\sigma_0 = 3.9\,\mathrm{meV}$ (up to the dotted line inside the gray area). Additionally, the leakiness of the resonator introduces a width of about 1.1 meV. The excess energy dependent broadening (above the gray region, σ_{tot}) is related to the finite coherence time τ_φ. The data from Fig. 2.2 b) (open circles) agrees with this data (black dots) on the non-monotonic dependence and the position of the maximum.

3 Chapter 3
Superconductor-insulator transition in disordered Josephson-junction chains

One of the main goals of this thesis is the analysis of the transport properties of 1D Josephson junction (JJ) chains. There are primarily two energy scales that control the properties of these systems, the charging energy and the Josephson energy. Depending on the ratio of these energies, different properties can be observed. If the charging energy is much larger than the Josephson energy, the Cooper-pair tunneling is suppressed, and the current-voltage characteristics show the Coulomb blockade [38]. At finite temperature and in the low-bias response, an activated behavior for the Cooper-pair tunneling is found [51]. In addition, if strong charge disorder is present, the critical voltage at which the chain becomes conducting, is controlled by depinning effects [52, 53]. If the Josephson energy is the largest energy scale, superconducting current-voltage characteristics are found [46, 50]. The superconductor-insulator transition (SIT) between both regimes occurs when the charging and Josephson energy are of the same order [14, 39–44, 49, 53]. This transition is driven by the proliferation of quantum phase slips (QPS) [14, 47–50]. These fluctuations correspond to 2π windings of the phase difference across one of the junctions.

Experimentally, the SIT in JJ chains can be conveniently investigated by using devices in a superconducting quantum interference device (SQUID) geometry [39–43]. In these devices, the Josephson energy can be varied *in situ* by means of a perpendicular magnetic field. There are also a large number of theoretical works on 1D JJ chains. Bradley and Doniach [14] showed that for a model with a capacitive coupling to the ground a mapping onto the 2D XY model exists. The phase transition of such a model belongs to the Berezinskii-Kosterlitz-Thouless (BKT) universality class. In later works, effects of dissipation [57–59] and a finite capacitive coupling between the islands [44, 47, 49] were studied. The relation to the physics of Luttinger liquids (LLs) was established in Refs. [60–62]. The role of disorder was examined in connection with the persistent current in closed rings [47, 140]. There, random stray charges lead to a weaker decay of the amplitude of the persistent current with the system size. In a recent work [63], the impact of disorder on the QPS amplitude was studied.

Besides the experiments on JJ chains mentioned above, the SIT was investigated in MoGe nanowires [64–66]. The theoretical description of QPS in 1D wires was introduced in Refs. [67, 68], see also [141] for a review. Qualitatively, the experimental results in 1D structures are in accordance with the theoretical predictions. However, questions on the parameter controlling the transition as well as on the scaling properties near the SIT are still not answered satisfactorily.

In this chapter, we review our results on the SIT in JJ chains published in Ref. [107]. We study the impact of disorder on the SIT and establish the phase diagram. Furthermore, the behavior of the conductivity as a function of temperature and system size is computed in the vicinity of the SIT. Although we consider a model for JJ chains, we expect that our findings should be largely applicable to 1D superconducting nanowires as well.

Starting from the lattice model for JJ chains introduced in Sec. 1.2, we derive the effective low-energy field theory that is of sine-Gordon type. Additionally, two types of disorder are considered: random stray charges and random fluctuations of the QPS fugacity. Making use of the renormalization group (RG), the phase diagram is obtained. We find that the random stray charges reduce the impact of QPS, thus widening the regime of superconducting correlations. On the contrary, the second type of disorder, phase slips with a random amplitude, enlarge the insulating regime. Employing the memory-function formalism, the resistivity is calculated as a function of temperature for an infinite chain. Moreover, the resistance as function of system size at zero temperature is discussed. Near the SIT, both quantities are characterized by a strongly non-monotonic behavior.

This chapter is structured as follows. In Sec. 3.1, the field theory corresponding to the lattice model introduced in Sec. 1.2 is derived. Sections 3.2 and 3.3 account for this field theory in the local ($C_0 \gg C_1$) and non-local ($C_0 \ll C_1$) limit of the Coulomb interaction, respectively. In both sections, we start first with the discussion of the RG and analyze then the transport properties in the second part. Our theory is compared to experiments on the SIT in 1D in Sec. 3.4 before we summarize the main results of this chapter in Sec. 3.5.

This chapter is based on our work in Ref. [107] and in part also on our results of Ref. [142].

3.1 Field theory

The lattice model for JJ chains is introduced in Sec. 1.2. In the following, we discuss the effective low-energy theory of this model, Eq. (1.25), as well as generalizations thereof including disorder. We study the low-energy modes with momenta $q \lesssim 1$ and frequencies $\omega \lesssim \Omega_0$, where

$$\Omega_0 = \sqrt{\frac{E_\mathrm{J} E_1 E_0}{E_1 + E_0}} \tag{3.1}$$

is the plasmonic bandwidth. If not stated explicitly, all distances are measured in units of the lattice spacing. Changing the screening length Λ from zero to infinity, the frequency cutoff Ω_0 ranges from the frequency $u_0 = \sqrt{E_\mathrm{J} E_0}$ for phase oscillations of a single island to the plasma frequency $\omega_\mathrm{p} = \sqrt{E_\mathrm{J} E_0}$ related to a single junction.

A convenient description of the field theory of our model is given by the formulation in terms of the operator $\phi(x)$, which is related to the Cooper-pair density by $\pi \mathcal{N}(x) = -\partial_x \phi(x)$. The commutation relation between the operator $\phi(x)$ and the superconducting phase $\theta(x)$,

$$\Big[-\partial_x \phi(x), \theta(x')\Big] = i\pi\delta(x - x'), \tag{3.2}$$

is inherited from the canonical commutation relation (1.26) in the lattice model. The quadratic (imaginary-time) action in the continuum limit has the form

$$S_0 = \frac{\Omega_0}{2\pi^2 K} \int \frac{\mathrm{d}q}{2\pi} \frac{\mathrm{d}\omega}{2\pi} \left[\frac{\omega^2}{\Omega_0^2} + \frac{\left(1 + 1/\Lambda^2\right) q^2}{q^2 + 1/\Lambda^2} \right] \left|\phi(q,\omega)\right|^2, \tag{3.3}$$

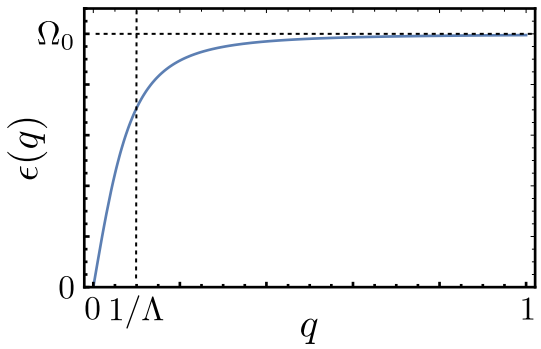

Figure 3.1: Energy dispersion of plasmonic waves in JJ chains. For momenta below $1/\Lambda$, the spectrum is approximately linear, while above this crossover scale it saturates to Ω_0.

and corresponds to plasmonic waves with the energy spectrum

$$\epsilon(q) = \frac{\omega_\mathrm{p}|q|}{\sqrt{q^2 + 1/\Lambda^2}}, \tag{3.4}$$

which is depicted in Fig. 3.1. At momenta below the inverse screening length, the dispersion is nearly linear and crosses over to a flat spectrum for higher momenta. In Eq. (3.3), the dimensionless constant

$$K = \sqrt{\frac{E_\mathrm{J}}{E_0} + \frac{E_\mathrm{J}}{E_1}} = K_0\sqrt{1+\Lambda^2} = K_1\sqrt{1+\frac{1}{\Lambda^2}} \tag{3.5}$$

is introduced, which smoothly connects K_0 in the local limit ($\Lambda \to 0$) and K_1 for $\Lambda \to \infty$.

The Gaussian action (3.3) corresponds to small long-wavelength fluctuations of the superconducting phases θ_i around the classical ground state in the superconducting regime, $\theta_i \equiv \theta(x) = \text{const}$. This action yields an accurate description of the JJ chain at low temperatures and in the regime where the Josephson energy E_J is the largest energy scale. The destruction of the superconducting phase by effects related to the charging energy is connected to the 2π windings of the phase difference across one of the junctions. These tunneling events are called quantum phase slips (QPS), which correspond to vortices in the superconducting phase $\theta(x,\tau)$ in the imaginary-time path-integral representation. For an analogy of QPS to the vortices in the 2D XY model see Sec. 1.2. These topological excitations can be taken into account by adding the term

$$S_\mathrm{ps} = \frac{y\Omega_0}{\sqrt{2\pi^3}} \int \mathrm{d}x\, \mathrm{d}\tau\, \cos\left[2\phi(x,\tau)\right], \tag{3.6}$$

to the Gaussian action (3.3). Here, y is the dimensionless fugacity (amplitude) of the phase slip. In App. A.1 a detailed derivation of Eq. (3.6) starting from the lattice model is presented. On the phenomenological level, the QPS-action can be motivated in the following way [17, 109]. From the analogy to elementary quantum mechanics, we observe that the operator $\mathrm{e}^{2i\phi(x_0,\tau_0)}$ behaves as a translation operator that shifts all superconducting phases $\theta(x,\tau)$ after the time τ_0 and to the left of x_0 by 2π. Thus, this operator creates a phase slip in the chain (see also Fig. 1.3).

In the regime $E_\mathrm{J} \gg \min(E_1, E_0)$, superconducting correlations are at least locally well established. QPS can then be thought of as tunneling processes with an exponentially small amplitude

$$y \propto e^{-\zeta K}, \tag{3.7}$$

where ζ is a numerical coefficient that depends on Λ and in principle also on the details of the ultraviolet (UV) cutoff procedure. Estimates for ζ in several parameter regimes can be found in Refs. [14, 44, 47, 49] and in App. A.2. In the following, we regard the fugacity y as a phenomenological parameter that is small for $K \gtrsim 1$, and we concentrate on the consequences of QPS on the low-energy properties of the JJ chain.

An important aspect of this work is the understanding of the influence of disorder on the transport properties of JJ chains. There are many sources for disorder in these systems. Among them, random stray charges are of particular importance. They lead to the "frustration" of the charging part of the Hamiltonian:

$$\frac{E_1}{2}\sum_{i,j} S_{ij}^{-1}\mathcal{N}_i\mathcal{N}_j \;\rightarrow\; \frac{E_1}{2}\sum_{i,j} S_{ij}^{-1}(\mathcal{N}_i - Q_i)(\mathcal{N}_j - Q_j), \tag{3.8}$$

where Q_i denote the random charges. The QPS are influenced by the random charges through the Aharonov-Casher effect [143]. When the phase difference between the grains i and $i+1$ winds by 2π, the wave function of the system acquires the phase factor

$$\mathrm{e}^{i\mathcal{Q}_i} \quad \text{with} \quad \mathcal{Q}_i = 2\pi\sum_{k\le i} Q_k. \tag{3.9}$$

Hence, in the presence of random stray charges, the QPS action (3.6) needs to be replaced by

$$S_{\mathrm{ps,Q}} = \frac{y\Omega_0}{\sqrt{2\pi^3}}\int \mathrm{d}x\,\mathrm{d}\tau\,\cos\left[2\phi(x,\tau) - \mathcal{Q}(x)\right]\,. \tag{3.10}$$

Another formal way to derive the phase slip action with a random phase in the continuum field theory is to perform the gauge transformation

$$\phi(x,\tau) \rightarrow \phi(x,\tau) - \mathcal{Q}(x)/2, \quad \mathcal{Q}(x) = 2\pi\int_{-\infty}^{x}\mathrm{d}x' Q(x')\,, \tag{3.11}$$

which eliminates the random charges from the quadratic part of the action, and leads to the form (3.10) for the phase-slip action. In principle, the statistical characteristics of the random stray charges Q might be material-dependent. For simplicity, we assume a Gaussian distribution function and short-range correlations,

$$\langle Q(x)\rangle = 0, \quad \text{and} \quad \langle Q(x)Q(x')\rangle = \frac{D_Q}{2\pi^2}\delta(x-x'). \tag{3.12}$$

Fluctuations in the charging and Josephson energies from junction to junction represent a further source of quenched disorder. Imperfections in the manufacturing process leading to fluctuations of the width of the tunnel barriers or the area of the loops of the SQUIDs in the case of chain in a SQUID geometry might be possible sources. These variations result in spatial fluctuations of the parameters of the Gaussian part of the action (3.3). However, since the charge transport is not directly affected by those fluctuations, we skip them in the following. More importantly, the local value of the QPS fugacity y is influenced which is of central importance for transport characteristics. In combination with random stray charges that provide a random phase, we consider the term

$$S_\xi = \int \mathrm{d}x\,\mathrm{d}\tau\left[\xi(x)\mathrm{e}^{2i\phi(x,\tau)} + \mathrm{h.c.}\right] \tag{3.13}$$

with a random complex amplitude ξ taking into account the fluctuations of the parameters of the junctions. As in the case of random stray charges, we assume that ξ has a Gaussian distribution function with short-range correlations [1],

$$\langle \xi(x) \rangle = 0, \quad \langle \xi(x) \xi^*(x') \rangle = \frac{u_0^2 D_\xi}{(2\pi)^2} \delta(x - x'). \tag{3.14}$$

We end this section by stating the action of our complete model,

$$S = S_0 + S_{\mathrm{ps,Q}} + S_\xi, \tag{3.15}$$

where S_0, $S_{\mathrm{ps,Q}}$, and S_ξ are defined in Eqs. (3.3), (3.10), and (3.13), respectively. In the following we analyze the action (3.15) with regard to the transport properties in Secs. 3.2 and 3.3 for the cases of local and non-local Coulomb interaction, respectively.

3.2 Local Coulomb interaction

In the regime $C_1 \ll C_0$, the interaction between charges is local in space. The energy spectrum for the plasmonic waves is completely linear, and the Gaussian part of the action is of Luttinger liquid (LL) type,

$$S_0 = \frac{1}{2\pi^2 u_0 K_0} \int \mathrm{d}x \, \mathrm{d}\tau \left[u_0^2 \left(\partial_x \phi \right)^2 + \left(\partial_\tau \phi \right)^2 \right], \tag{3.16}$$

with the LL parameter $K_0 = \sqrt{E_\mathrm{J}/E_0}$ and the plasmon velocity $u_0 = \sqrt{E_\mathrm{J} E_0}$. (The dimensions of energy and velocity coincide in this formulation since we measure all distances in units of the lattice spacing.)

Comparing our low-energy theory given by Eqs. (3.15), (3.16), (3.10), and (3.13) for a JJ chain with local charge interaction to the work performed for a disordered interacting wire by Giamarchi and Schulz [144], we observe many similarities. In particular, the term with random fugacity, Eq. (3.13), corresponds to the disorder-induced backscattering term in the case of a fermionic 1D system. Moreover, the phase-slip term with a uniform fugacity y translates into an umklapp term that arises as a consequence of a commensurate periodic potential. The random stray charges can be identified with the random forward scattering in the case of a 1D wire. We take advantage of these similarities to derive the RG equations in the following. In this way, we obtain the phase diagram as well as the transport properties at low temperatures of a disordered JJ chain with local Coulomb interaction.

3.2.1 RG equations

The RG equations for the action (3.15), where the quadratic action S_0 is given by Eq. (3.16), are obtained by following to a large extent the procedure outlined in Ref. [144]. The disorder average over the random phase-slip amplitude ξ is performed with the help of the replica trick [17, 145]. However,

[1] To facilitate the analysis, we consider only Gaussian fluctuations of ξ, which are completely determined by the second moment in (3.14). Under this assumption, the correlations between ξ and Q are absent. Deviations coming from the fluctuations beyond the Gaussian approximation are expected to be of minor importance.

the average over the stray charges is not yet performed. The replicated action that is already averaged over the realizations of ξ is given by

$$S = \sum_{i=1}^{n} \Big(S_0[\phi^i] + S_{\mathrm{ps},Q}[\phi^i] \Big) + \sum_{i,j=1}^{n} S_\xi[\phi^i, \phi^j], \tag{3.17}$$

$$S_0[\phi^i] = \frac{1}{2\pi^2 u_0 K_0} \int \mathrm{d}x \mathrm{d}\tau \left[u_0^2 (\partial_x \phi^i)^2 + (\partial_\tau \phi^i)^2 \right], \tag{3.18}$$

$$S_{\mathrm{ps},Q}[\phi^i] = \frac{y u_0}{\sqrt{2\pi^3}} \int \mathrm{d}x \mathrm{d}\tau \cos \left[2\phi^i - 2\pi \int_{-\infty}^{x} \mathrm{d}x' \, Q(x') \right], \tag{3.19}$$

$$S_\xi[\phi^i, \phi^j] = -\frac{u_0^2 D_\xi}{(2\pi)^2} \int \mathrm{d}x \mathrm{d}\tau \mathrm{d}\tau' \cos \left[2 \left(\phi^i(x,\tau) - \phi^j(x,\tau') \right) \right]. \tag{3.20}$$

We denote by $i = 1, 2, \ldots, n$ the replica index, and at the end of the calculation the limit $n \to 0$ should be performed.

The RG equations are obtained by studying the correlation function

$$R(x_1 - x_2, \tau_1 - \tau_2) = \left\langle \mathrm{e}^{i2\phi^j(x_1,\tau_1)} \mathrm{e}^{-i2\phi^j(x_2,\tau_2)} \right\rangle. \tag{3.21}$$

Here, the angular brackets indicate the average over the random variable $Q(x)$ besides the average with respect to the action (3.17). This correlator is computed perturbatively up to second order in the QPS fugacity y, and up to first order in the disorder strength D_ξ. The RG equations can be extracted from the perturbative corrections. The details of this derivation can be found in App. A.3. We obtain:

$$\frac{\mathrm{d}K_0}{\mathrm{d}l} = -\frac{1}{2} y^2 K_0^2 \Big[\mathrm{I}_0(D_Q) - \mathrm{L}_0(D_Q) \Big] - \frac{1}{2} K_0^2 D_\xi, \tag{3.22}$$

$$\frac{\mathrm{d}y}{\mathrm{d}l} = (2 - \pi K_0) y, \tag{3.23}$$

$$\frac{\mathrm{d}D_\xi}{\mathrm{d}l} = (3 - 2\pi K_0) D_\xi, \tag{3.24}$$

$$\frac{\mathrm{d}D_Q}{\mathrm{d}l} = D_Q, \tag{3.25}$$

$$\frac{\mathrm{d}u_0}{\mathrm{d}l} = -\frac{1}{2} u_0 K_0 y^2 \left[\mathrm{L}_2(D_Q) - \mathrm{I}_2(D_Q) + \frac{2}{3\pi} D_Q \right] - \frac{1}{2} u_0 K_0 D_\xi. \tag{3.26}$$

The logarithm of the running scale is denoted by l, the n-th modified Bessel function of the first kind by I_n, and the n-th modified Struve function by L_n. It should be emphasized that these equations are perturbative in y (2^{nd} order) and D_ξ (1^{st} order), while they are exact in K_0 and D_Q.

In the clean limit, $D_Q = D_\xi = 0$, the equations for y and K_0 coincide with the standard BKT equations,

$$\frac{\mathrm{d}K_0}{\mathrm{d}l} = -\frac{1}{2} y^2 K_0^2, \tag{3.27}$$

$$\frac{\mathrm{d}y}{\mathrm{d}l} = (2 - \pi K_0) y, \tag{3.28}$$

which describe a quantum superconductor-insulator transition with the critical value $\pi K_0^c = 2$ for an infinitesimally small phase-slip amplitude y. Due to the isotropy of the space-time in the clean limit, the flow for the velocity u_0 is absent.

We turn now to the discussion of the RG flow of the disordered system. In the regime $\pi K_0 > 2$, the superconducting state is not destroyed by a small phase-slip amplitude y or a small disorder strength D_ξ. On the other hand, for $\pi K_0 < 2$, QPS might proliferate. The perturbation with random fugacity ξ is irrelevant in the regime $\pi K_0 > 3/2$. We therefore ignore this term for a moment, and come back to it in the next paragraph. For any $\pi K_0 < 2$, the phase-slip fugacity y grows under the RG. However, its influence on the properties of the system is controlled by the random stray charges. If the disorder strength D_Q at the UV scale is sufficiently small, it might still be small (despite its growth under the RG) at the scale where the fugacity y becomes of order unity. In this case, localization effects are expected to develop, leading to insulating behavior. On the contrary, inspecting Eq. (3.22) in the limit $D_Q \gg 1$ reveals that the correction to K_0 originating from QPS is proportional to y^2/D_Q. Correspondingly, we find a competition between the homogeneous fugacity y and the disorder strength D_Q of stray charges. It is expected that for $D_Q \gg 1$, localization effects become important only if the combination y^2/D_Q becomes of order unity. This statement is further supported in Sec. 3.2.2, where it is demonstrated that the same parameter appears in the perturbative corrections to the conductivity.

From the scales where $D_Q \gg 1$, the RG equations can be replaced by the simplified version,

$$\frac{\mathrm{d}K_0}{\mathrm{d}l} = -\frac{1}{2}K_0^2 D_{\xi,y}, \tag{3.29}$$

$$\frac{\mathrm{d}D_{\xi,y}}{\mathrm{d}l} = (3 - 2\pi K_0) D_{\xi,y}, \tag{3.30}$$

$$\frac{\mathrm{d}u_0}{\mathrm{d}l} = -\frac{1}{2}u_0 K_0 D_{\xi,y}, \tag{3.31}$$

where the effective disorder strength is given by $D_{\xi,y} = D_\xi + 2y^2/\pi D_Q$. The equations (3.29)–(3.31) translate into the equations for a 1D system of spinless fermions with disorder-induced backscattering derived by Giamarchi and Schulz [144], by identifying our parameter πK_0 with K of Ref. [144]. We observe that strong random charges render the QPS with a homogeneous fugacity, Eq. (3.10), indistinguishable from the one with a random amplitude, Eq. (3.13). Moreover, this consideration shows that the RG equations (3.22), (3.23), (3.25), and (3.26), which are formally derived under the assumption $y \ll 1$, have in fact at $D_Q \gg 1$ the much wider range of applicability $y^2/D_Q \ll 1$. Stray charges shift the critical value of K_0 (for infinitesimal y), at which the transition to the insulating state occurs, from $2/\pi$ to $3/2\pi$. The physical reason for the suppression of the effect of QPS on the characteristics of the JJ chain in the presence of strong random stray charges is related to the interference of QPS. In the clean case, phase slips add up coherently, while random stray charges provide a random phase resulting in destructive interference of QPS.

By solving the RG equations (3.22)–(3.25) numerically, we deduce the phase diagram of the disordered JJ chain. The phase diagram in the πK_0-y plane is depicted in Fig. 3.2. We treat here πK_0 and y as independent variables [see the discussion below Eq. (3.7)]. The insulating regime is located to the left of each transition line, whereas the area to the right is characterized by strong superconducting correlations. The transition line in the clean system corresponds to the black solid line ending at $\pi K_0 = 2$. The effect of QPS with random fugacity is illustrated by the other solid lines (red: $D_\xi = 0.1$ and blue: $D_\xi = 0.2$). It can be clearly seen that this type of disorder reduces the parameter regime in which superconducting correlations dominate. On the other hand, random stray charges lead to the opposite behavior. As can be seen from the dashed lines, the transition line is shifted in favor of the superconducting regime if a small amount of stray-charge disorder is present.

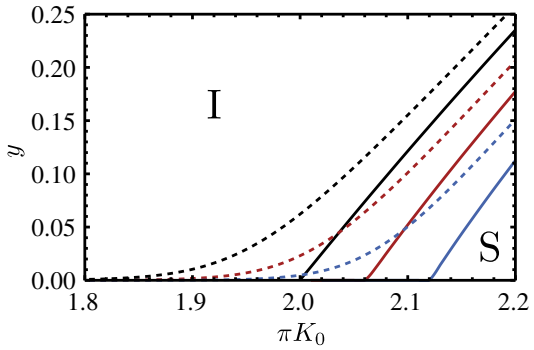

[Reprinted figure with permission from M. Bard, I. V. Protopopov, I. V. Gornyi, A. Shnirman, and A. D. Mirlin, Phys. Rev. B **96**, 064514 (2017), DOI: 10.1103/PhysRevB.96.064514, cf. Ref. [107]. Copyright 2017 by the American Physical Society.]

Figure 3.2: Phase diagram in the case of local Coulomb interaction in the πK_0-y plane. To the left of each phase boundary, the JJ chain is in the insulating (I) phase, while to the right it is characterized by strong superconducting correlations (S). The transition line in the clean case corresponds to the black solid line. The red and blue solid lines show the effect of QPS with random fugacity. They correspond to a chain without stray charges but with $D_\xi = 0.1$ (red) and $D_\xi = 0.2$ (blue). The dashed curves illustrate the effect of random stray charges ($D_Q = 10^{-12}$); the value of D_ξ is the same as the one for the solid curve with the same color.

3.2.2 Transport

Let us now study the low-temperature transport properties of a JJ chain in the regime of local Coulomb interaction, $\Lambda \ll 1$. The conductivity is obtained within the memory-function formalism that is introduced in Sec. 1.3.3. The perturbative calculation of the memory function to the lowest order in y and D_ξ can be performed following the procedure outlined in Refs. [122, 124]. We present the details of the computation of the memory function in App. A.4. A combination of the RG, which enables us to renormalize the model up to the infrared (IR) cutoff given by the temperature or the system length, and the perturbative evaluation of the memory function leads to the result for the conductivity of the system.

Clean limit

In the clean limit, $D_\xi = D_Q = 0$, our model, given by Eqs. (3.16) and (3.6), is known to be equivalent to the theory of one-dimensional fermions in a periodic potential. In this context, the action (3.6) describes umklapp scattering. In Ref. [123], it is shown that for *incommensurate* filling, the umklapp processes are very inefficient resulting in an exponentially large conductivity. Since the potential in this work is *commensurate*, the arguments of Ref. [123] do not apply. We obtain for the conductivity in the DC limit

$$\sigma(T) = \frac{8e^2 a}{y^2 h} \frac{\Gamma^2(\pi K_0)}{\Gamma^4(\pi K_0/2)} \left(\frac{2\pi a T}{u_0}\right)^{3-2\pi K_0}, \tag{3.32}$$

where the lattice spacing a is reintroduced explicitly. Including renormalization effects modifies the simple power-law behavior of the temperature dependence of the conductivity, Eq. (3.32). We incorporate the effects from the RG by renormalizing the theory from the initial UV cutoff a down to the

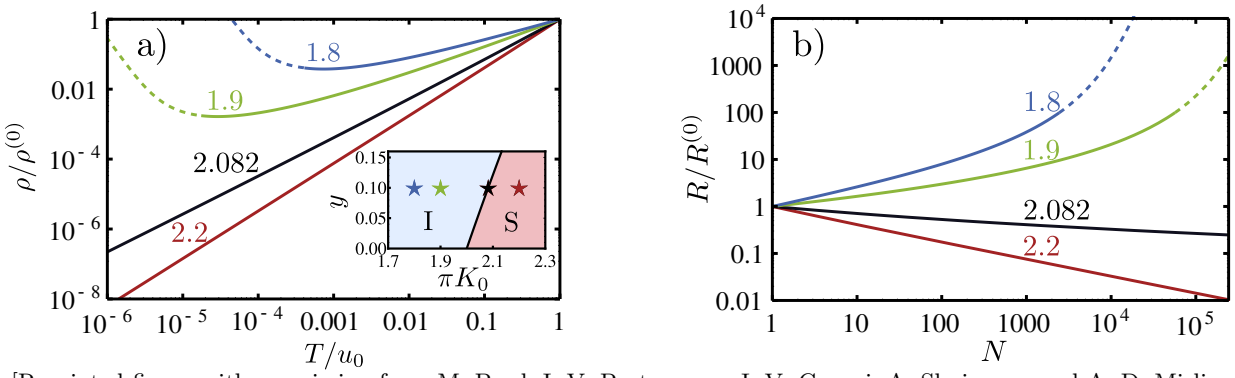

[Reprinted figure with permission from M. Bard, I. V. Protopopov, I. V. Gornyi, A. Shnirman, and A. D. Mirlin, Phys. Rev. B **96**, 064514 (2017), DOI: 10.1103/PhysRevB.96.064514, cf. Ref. [107]. Copyright 2017 by the American Physical Society.]

Figure 3.3: a) Temperature-dependent resistivity without impurities for local charge interaction. The value of πK_0 is indicated by the number close to the curve. The phase-slip amplitude is chosen to be $y = 0.1$ for every curve. Inset: Phase diagram in the πK_0-y plane. The position of the system in the phase diagram is marked by a star with the same color as the corresponding resistivity curve. In the blueish region, the chain is in the insulating phase (I), while in the reddish part, it is in the superconducting regime (S). Dashed curves represent qualitative extrapolations sketching the tendency of the flow towards the insulating fixed point. b) Behavior of the resistance as a function of the chain length N at $T = 0$ for the same parameters as in a).

thermal length $N_{\mathrm{th}}(T) = u_0/T$. At this scale, the RG described by Eqs. (3.27) and (3.28) is stopped. In the general disordered case, the velocity u_0 is renormalized as well leading to the equation for the RG scale $l^*(T)$

$$\mathrm{e}^{l^*} = \frac{u_0(l^*)}{T} \tag{3.33}$$

at which the RG is terminated. Renormalizing the cutoff a in Eq. (3.32) to the thermal length leads to the scaling

$$\sigma(T) \sim \frac{e^2}{h} \frac{u_0[l^*(T)]}{T y^2[l^*(T)]} \tag{3.34}$$

of the conductivity with temperature. In Eq. (3.34) and in analogous equations, the symbol "$\sim$" has the meaning "up to a numerical factor of order unity". Since the velocity u_0 is not renormalized in the clean limit, the RG scale at which the RG is stopped is given by $l^*(T) = \ln\left(u_0/T\right)$. A dimensionless quantity can be obtained by normalizing the conductivity by its value $\sigma^{(0)} = \sigma(T = u_0)$ at the UV scale. In Fig. 3.3 a), the temperature dependence of the normalized resistivity $\rho/\rho^{(0)}$, with $\rho = 1/\sigma$ and $\rho^{(0)} = 1/\sigma^{(0)}$ is depicted. In the superconducting phase (red, $\pi K_0 = 2.2$), the resistivity decreases when lowering the temperature. The curves belonging to the insulating regime (green and blue, $\pi K_0 = 1.9$ and $\pi K_0 = 1.8$) are characterized by a strongly non-monotonic behavior. Similar to the superconducting curves, the resistivity decreases at high temperatures because the fugacity y needs to grow fast enough to overcome the additional factor $1/T$ in Eq. (3.34). Hence, the upturn of $\rho(T)$ shows up only at lower T, where K_0 is renormalized below $3/2\pi$. Our method is perturbative in the fugacity y, which means that we need to stop the RG when $y \sim 1$. Due to the aforementioned relation of the sine-Gordon theory to a fermionic theory with umklapp scattering, the RG is expected to flow towards the

Mott-insulator fixed point whenever the umklapp term is relevant. In order to illustrate the qualitative tendency at low temperatures, we plot the extrapolation of the RG flow beyond the perturbatively accessible regime as dashed lines. The black curve ($\pi K_0 = 2.082$) corresponds to parameters on the phase boundary. With the help of the BKT equations, we obtain the behavior

$$\rho^{\mathrm{crit}}(T)/\rho^{(0)} = \frac{T/u_0}{\left[1 + (\pi K_0 - 2)\ln(u_0/T)\right]^2} \tag{3.35}$$

of the resistivity on the critical line, where we assumed that K_0 is close to the critical value $K_0^c = 2/\pi$.

The temperature-dependent resistivity $\rho(T)$ is the appropriate quantity in the thermodynamic limit $N \to \infty$, i. e., in the regime where the system size N is much larger than the thermal length $N(T)$. In this case, the RG is stopped by the thermal length $N_{\mathrm{th}}(T)$, i. e., by the temperature, and the resistance depends linearly on the system size N (Ohmic behavior). In the opposite limit, $N \ll N_{\mathrm{th}}(T)$, the proper quantity is the length-dependent resistance $R(N)$ at zero temperature. This quantity can be found by renormalizing our theory up to the point where the cutoff a hits the system size N. The scaling of the resistance is found to be

$$R(N) \sim \frac{h}{e^2} y^2[l = \ln N]. \tag{3.36}$$

Figure 3.3 b) shows the behavior of $R(N)$ normalized by the bare resistance $R^{(0)} = R(N = 1)$. The bare values for y and K_0 are the same as for the resistivity plot shown in Fig 3.3 a). The curves belonging to the insulating phase (green and blue, $\pi K_0 = 1.9$ and 1.8) show an increasing behavior with the system size. On the other hand, the curves in the superconducting regime (red, $\pi K_0 = 2.2$) as well as on the critical curve (black, $\pi K_0 = 2.082$) decrease as a function of N. The analytical behavior on the phase boundary is given by [cf. Eq. (3.35)]

$$R^{\mathrm{crit}}(N)/R^{(0)} = \frac{1}{\left[1 + (\pi K_0 - 2)\ln(N)\right]^2}. \tag{3.37}$$

The critical curve is almost constant with logarithmic corrections that lead to a slow decrease. As a consequence, there are insulating curves very close to the transition line with a weakly non-monotonic dependence [not shown in Fig. 3.3 b)]. At short system sizes, the resistance drops first and starts to increase only at larger N. This happens for systems with $K_0 > K_0^c = 2/\pi$ and large enough fugacity y such that it is in the insulating regime. The non-monotonicity of the $\rho(T)$ curves in Fig. 3.3 a) is, however, much more pronounced than in the corresponding $R(N)$ curves. This can be explained by the additional factor of T in the temperature dependence in Eq. (3.35) compared to the system-size dependence in Eq. (3.37).

Disordered system: Random stray charges

After the discussion of the clean system, we analyze the effect of random stray charges in this section. The perturbative calculation of the conductivity in the presence of stray charges is presented in App. A.4. The result reads

$$\sigma(T) \sim \begin{cases} \dfrac{e^2 a}{h y^2} \left(\dfrac{2\pi a T}{u_0}\right)^{3-2\pi K_0}, & D_Q u_0/aT \ll 1, \\ \dfrac{e^2}{h} a \dfrac{D_Q}{y^2} \left(\dfrac{2\pi a T}{u_0}\right)^{2-2\pi K_0}, & D_Q u_0/aT \gg 1. \end{cases} \tag{3.38}$$

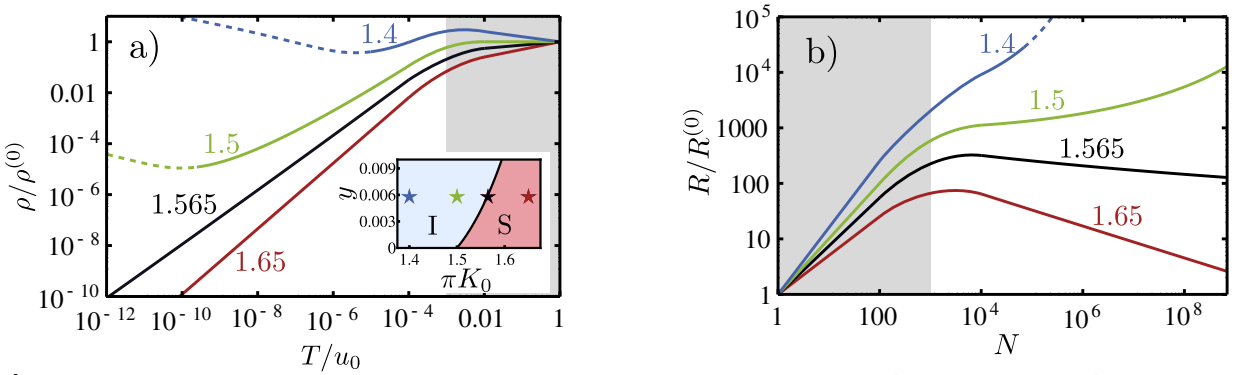

[Reprinted figure with permission from M. Bard, I. V. Protopopov, I. V. Gornyi, A. Shnirman, and A. D. Mirlin, Phys. Rev. B **96**, 064514 (2017), DOI: 10.1103/PhysRevB.96.064514, cf. Ref. [107]. Copyright 2017 by the American Physical Society.]

Figure 3.4: a) Behavior of the resistivity as a function of temperature in the presence of random offset charges for local charge interaction. The value of πK_0 is indicated by the numbers close to the curves. The values of the other parameters ($D_Q = 10^{-3}$ and $y = 6 \cdot 10^{-3}$) are the same among all curves. The regime where stray charges are weak is indicated by the gray region (the boundary is at T_Q). Although the phase-slip fugacity is relevant for the red curve ($\pi K_0 = 1.65$), it is located in the superconducting phase. Examples for systems in the insulating phase are given by the green and blue curve ($\pi K_0 = 1.5$ and $\pi K_0 = 1.4$). The dashed lines show extrapolations below the temperature T_{ps} to illustrate the tendency at very low temperatures (infinite resistivity). Inset: Stars indicate the position of the system in the phase diagram in the πK_0-y plane. To the right of the black line, the system shows superconducting correlations (S), while to the left the system is in the insulating phase (I). b) Behavior of the resistance with system size at $T = 0$ for the same parameters as for the resistivity curves. The boundary of the gray region is given by the mean free path N_Q and the beginning of the dashed line occurs at N_{ps}.

Here, we can already see that in the case of strong stray charges, the power of T is reduced by one in comparison to the weakly disordered regime. From Eq. (3.38), it can be seen that the perturbative parameter in the regime of strong stray charges, $D_Q(T) \gg 1$, is $y^2(T)/D_Q(T)$ rather than $y^2(T)$. This is the same parameter that is identified in Sec. 3.2.1 when studying the RG equations in the strongly disordered regime. Since this parameter controls the conductivity, we can support the statement made in Sec. 3.2.1 that random stray charges stabilize the superconducting phase. We thus find a competition between random stray charges and QPS. Renormalizing the UV cutoff a to the thermal length, leads to the scaling

$$\frac{\sigma(T)}{\sigma^{(0)}} \sim \begin{cases} \dfrac{y_0^2}{y^2(T)} \dfrac{u_0(T)}{T}, & D_Q(T) \ll 1, \\ \dfrac{y_0^2 D_Q(T)}{y^2(T)} \dfrac{u_0(T)}{T}, & D_Q(T) \gg 1\,, \end{cases} \tag{3.39}$$

with temperature T, where y_0 is the value of the fugacity at the UV scale. In contrast to the clean case, the velocity is renormalized. This makes it necessary to solve the equation $\mathrm{e}^{l^*} = u_0(l^*)/T$ numerically to obtain the RG scale $l^*(T)$. The temperature dependence of the resistivity $\rho = 1/\sigma$ in the presence of random stray charges is illustrated in Fig. 3.4 a). At high temperatures, where stray charges are

weak (gray region), the behavior is similar to the clean situation, Fig. 3.3 for the same value of the LL parameter K_0. Here, the values of K_0 are notably smaller compared to the clean case shown in Fig. 3.3 since the transition line is shifted quite appreciably in the presence of stray charges.

At the boundary of the gray region, the renormalized value of $D_Q(l)$ becomes of order unity. The corresponding crossover temperature is $T_Q = u_0\, D_Q^{(0)}$. If the phase-slip fugacity y is still small at this scale, the resistivity gets suppressed at lower temperatures by an additional factor of $1/D_Q(T) \propto T$ [cf. second line of Eq. (3.39)]. In order to obtain a smooth crossover between the two regimes of strong and weak random stray charges in Eq. (3.39), we interpolated between both limits in Fig. 3.4 in the crossover region.

The red curve ($\pi K_0 = 1.65$), which belongs to the superconducting regime, shows that for sufficiently strong random stray charges, the effect of QPS are suppressed. In the insulating regime, random stray charges are too weak to win over the phase slips. This is illustrated by the green and blue curves ($\pi K_0 = 1.5$ and $\pi K_0 = 1.4$). At low temperatures an upturn of the resistivity is observed. It is expected that for even lower temperatures the resistivity continues to increase since the proliferation of QPS will destroy the superconducting phase and localization effects become important. The dashed lines show this tendency obtained by an extrapolation of the RG equations beyond the perturbative regime.

From the above analysis it is evident that the temperature dependence of the resistivity in the insulating regime is strongly non-monotonic. In total, up to three different regions with alternating signs of the slope of $\rho(T)$ can be found. This behavior can be seen for the blue curve ($\pi K_0 = 1.4$). At high temperatures $T \gtrsim T_Q$ (gray region), where the stray charges are still weak, the resistivity increases for decreasing temperature. When lowering the temperature, the stray charges become strong and try to suppress the influence of QPS leading to a decrease of $\rho(T)$. At even lower temperatures, however, the phase-slip amplitude grows strongly enough to win over the stray charges. The upturn is visible only at very low temperatures where the renormalized value of K_0 is below $1/\pi$ because the additional factor of T in Eq. (3.38) needs to be overcome. This happens around the temperature $T_{\rm ps}$ where the perturbative treatment breaks down. This temperature can be estimated assuming πK_0 is not too close to 3/2,

$$T_{\rm ps} \sim u_0 \left(y^{(0)}\right)^{\frac{2}{3-2\pi K_0}} \left(\frac{u_0}{T_Q}\right)^{\frac{1}{3-2\pi K_0}}. \tag{3.40}$$

If $y^{(0)} \ll 1$, the two temperature scales T_Q and $T_{\rm ps}$ are different, $T_{\rm ps} \ll T_Q$.

The parameters of the black curve ($\pi K_0 = 1.565$) lie on the phase boundary. At sufficiently low temperatures, $T \lesssim T_Q$, where the random stray charges are strong, the analytical behavior of the resistivity on the SIT phase boundary can be found. This can be done by solving the RG Eqs. (3.29)-(3.31). Close to the critical point $K_0^c = 3/2\pi$, the renormalization of the velocity is unimportant. We obtain

$$\rho^{\rm crit}(T) \sim \frac{T/u_0}{[1 + (\pi K_0^Q - 3/2)\ln(T_Q/T)]^2}, \tag{3.41}$$

for the behavior of the resistivity at the critical line. Here, $K_0^Q = K_0[l = \ln N_Q]$ denotes the value of K_0 renormalized to the mean free path $N_Q = 1/D_Q^{(0)}$. On the critical line the resistivity vanishes as a function of temperature almost linearly with logarithmic corrections.

In order to obtain the length-dependence of the resistance R for system sizes smaller than the thermal length, we stop the RG by the system size N. We find the scaling

$$\frac{R(N)}{R^{(0)}} \sim \begin{cases} \dfrac{y^2[\ln(N)]}{y_0^2}, & N \ll 1/D_Q^{(0)}, \\ \dfrac{y^2[\ln(N)]}{y_0^2 D_Q^{(0)} N}, & N \gg 1/D_Q^{(0)}. \end{cases} \tag{3.42}$$

The behavior of $R(N)$ is presented in Fig. 3.4 b). The parameters for the resistance curves are the same as for the resistivity curves shown in Fig. 3.4 a) with the same color. Similar to the resistivity plot, in the crossover regime at $D_Q \sim 1$ both limits of Eq. (3.42) are connected by means of an interpolation. The green ($\pi K_0 = 1.5$) and blue ($\pi K_0 = 1.4$) curves belong to the insulating phase, and show a monotonic increase of the resistance. At the mean free path N_Q, the coherence of phase slips is weakened, which results in a weaker growth at an intermediate range of N. At larger system sizes beyond $N_{\rm ps} \sim u_0/T_{\rm ps}$, which has the meaning of the correlation length, the growth of the resistance starts to accelerate again. At this correlation length, the system enters the strong-coupling regime that we indicate by the dashed line. Superconducting curves close to the transition show a non-monotonic behavior. As can be seen from the red curve ($\pi K_0 = 1.65$), the resistance grows for small system sizes below the mean free path (gray region). This behavior could lead to the wrong conclusion that the system with such parameters is in the insulating regime. However, increasing the systems size beyond N_Q, the resistance starts to drop. In the thermodynamic limit and at zero temperature the resistance will vanish. This is in accordance with the position in the phase diagram shown in inset of Fig. 3.4a). The behavior for systems on the phase boundary (red curve, $\pi K_0 = 1.565$) is qualitatively similar to the black curve. At large system sizes the decay is, however, much weaker. For chains that are larger than the mean free path N_Q, we obtain

$$R^{\rm crit}(N) \sim \frac{1}{[1 + (\pi K_0^Q - 3/2)\ln(N/N_Q)]^2} \tag{3.43}$$

for the behavior of the resistance on the critical line. On the phase boundary the resistance decays as a function of the system size in a logarithmically slow fashion.

Disordered system: Random stray charges and random fugacity

After the discussion of the influences of random stray charges, the effects from the disorder which leads to phase slips with a random fugacity are studied. As opposed to random stray charges, this type of disorder leads to a reduction of the conductivity. The total memory function consist now of two parts: the contributions from QPS with a homogeneous and a random amplitude. The details of the calculation of both parts are presented in App. A.4. The conductivity of the whole system can be obtained from

$$\sigma = \frac{1}{\sigma_{\rm ps}^{-1} + \sigma_\xi^{-1}}, \tag{3.44}$$

where $\sigma_{\rm ps}$ comes from QPS with a homogeneous fugacity and can be obtained from Eq. (3.38). The quantity σ_ξ originates from QPS with a random amplitude. It is given by (see App. A.4)

$$\sigma_\xi(T) \sim \frac{e^2 a}{h D_\xi} \left(\frac{2\pi a T}{u_0}\right)^{2-2\pi K_0}. \tag{3.45}$$

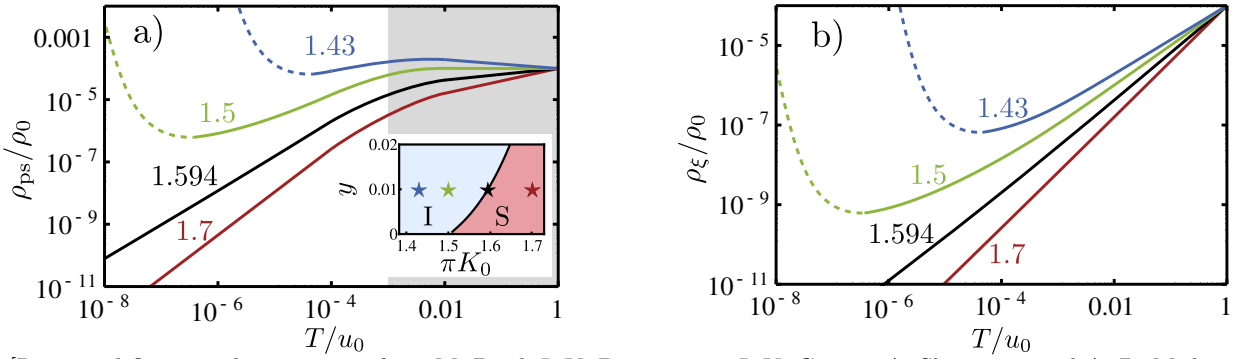

Figure 3.5: Behavior of the temperature-dependent resistivity contributions coming from phase slips with homogeneous fugacity (a) and from phase slips with random fugacity (b). The value of πK_0 is marked by the number close to the curve. All further parameters are the same among all curves: $y = 10^{-2}, D_Q = 10^{-3}$ and $D_\xi = 10^{-4}$. The tendency of the flow towards the strong-coupling fixed point (infinite resistivity) is indicated by dashed lines, which show the extrapolation of the RG flow beyond the perturbative regime. The position of the systems in the phase diagram is displayed in the inset in a). The superconducting phase (S) is located to the right of the black line, while the insulating regime (I) is to the left.

In this section, we use $\sigma_0 = e^2/h$ to normalize the conductivity. Renormalizing the theory to the thermal length N_{th}, we get

$$\frac{\sigma_\xi(T)}{\sigma_0} \sim \frac{u_0(T)}{T D_\xi(T)} \tag{3.46}$$

and

$$\frac{\sigma_{\text{ps}}(T)}{\sigma_0} \sim \begin{cases} \dfrac{1}{y^2(T)} \dfrac{u_0(T)}{T}, & D_Q(T) \ll 1, \\ \dfrac{D_Q(T)}{y^2(T)} \dfrac{u_0(T)}{T}, & D_Q(T) \gg 1. \end{cases} \tag{3.47}$$

Figure 3.5 visualizes the contributions to the resistivity originating from QPS with homogeneous and random amplitude, $\rho_{\text{ps}} = 1/\sigma_{\text{ps}}$ and $\rho_\xi = 1/\sigma_\xi$. The sum of both contributions, $\rho = \rho_{\text{ps}} + \rho_\xi$, yields the total resistivity of the system. The green and blue curves ($\pi K_0 = 1.5$ and $\pi K_0 = 1.43$) are in the insulating regime. Both contributions display a non-monotonic temperature dependence. The contribution from QPS with a random fugacity, depicted in Fig. 3.5 b), does not grow fast enough at large temperatures resulting in a decreasing behavior. These random phase slips correspond to disorder-induced backscattering processes in 1D fermionic systems. Localization effects become important only at lower temperatures. The flow to the insulating strong-coupling fixed point is illustrated by dashed lines. The temperature dependence of the contribution from homogeneous phase slips is shown in Fig. 3.5 a). Its behavior is quite similar to the case without QPS with random fugacity ($D_\xi = 0$) discussed in the previous section. This similarity can be explained by the fact that at large scales the phase-slip term with random fugacity is generated by random stray charges and QPS with a homogeneous amplitude. The behavior of ρ_{ps} in the insulating regime is more involved than that

of ρ_ξ. For example, the blue curve ($\pi K_0 = 1.43$), which is in the insulating regime, shows three regions with alternating signs of the slope of the resistivity. At high temperatures above T_Q (gray region), the resistivity grows with decreasing temperature. Below the temperature T_Q, random stray charges become strong enough to suppress the resistivity at intermediate temperatures. Finally, at low temperatures, the resistivity increases again since phase slips take over.

The contribution from homogeneous phase slips $\rho_{\rm ps}$ typically dominates the resistivity because the fluctuations of the bare fugacity are expected to be smaller than the average value of the bare fugacity. Furthermore, as can be seen from Eqs. (3.23) and (3.24), this inequality increases under renormalization.

3.3 Non-local Coulomb interaction

After the discussion of the transport characteristics of disordered JJ chains with local Coulomb interaction, we analyze the case of non-local Coulomb interaction, $\Lambda \gg 1$, in this section. This regime is relevant to many experimental realizations of 1D JJ chains. In Sec. 3.2, we have shown that the term with a random phase-slip amplitude is generated in the course of the RG when both, random stray charges and QPS with a homogeneous fugacity are present. In this respect and to simplify the presentation, we skip this term in this section, $D_\xi = 0$.

In the RG analysis, it proves advantageous to parametrize the action (3.3) in a different form (see App. A.1):

$$S_0 = \frac{1}{2\pi^2 K}\int_{-1}^{1}\frac{\mathrm{d}q}{2\pi}\int_{-\Omega_0}^{\Omega_0}\frac{\mathrm{d}\omega}{2\pi}\left[\frac{\omega^2}{\Omega_0}+\frac{\Omega_0 q^2}{q^2(1-u_{\rm g})+u_{\rm g}}\right]\left|\phi(q,\omega)\right|^2. \tag{3.48}$$

Here,

$$K = \sqrt{\frac{E_{\rm J}(E_1+E_0)}{E_1 E_0}} \tag{3.49}$$

is the effective LL parameter (the phase stiffness) at the cutoff, and $u_{\rm g} = 1/(1+\Lambda^2)$ is the group velocity of the plasmonic waves measured in units of Ω_0 at the cutoff.

3.3.1 RG treatment

In this section, we present the RG equations that are valid for any value of the screening length Λ. Details of the derivation of the RG equations can be found in App. A.5. The main steps of the derivation are sketched below.

The first step in our RG procedure is the elimination of the modes $\phi(\omega, q)$ with

$$1-\mathrm{d}l < q < 1 \qquad \text{or} \qquad (1-u_{\rm g}\mathrm{d}l)\Omega_0 < \omega < \Omega_0. \tag{3.50}$$

This region is depicted in Fig. 3.6 as a shaded region. The modes are eliminated in accordance with the spectrum. If we fix the width in momentum direction to $\mathrm{d}l$, the corresponding width in frequency direction is $u_{\rm g}\Omega_0\mathrm{d}l$. In the non-local regime, $\Lambda \gg 1$, this means that in the first steps of the renormalization procedure, the width in frequency direction is much smaller than the width in momentum direction. In the IR limit, at momentum scales much smaller than $1/\Lambda$, the modes are integrated out isotropically in both directions (as in the local case, Sec. 3.2). After each elimination process, momentum and frequency are both rescaled to restore the initial cutoffs. A peculiar feature of the Gaussian action (3.48) is that it contains irrelevant perturbations (curvature of the spectrum).

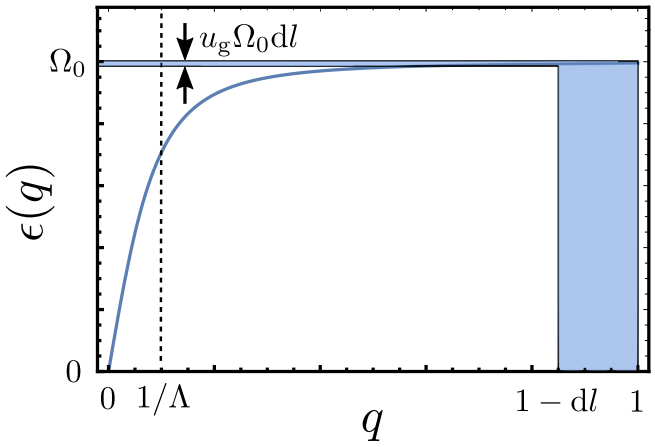

Figure 3.6: Elimination of modes in the RG procedure. If the momentum shell has width dl, the shell in frequency direction has width $u_g\Omega_0 dl$. If $\Lambda \gg 1$, in the initial steps the width in frequency direction is much smaller than the width in momentum direction.

This means that even without any QPS, $y = 0$, its parameters u_g and K are renormalized. At $y = 0$, we obtain the RG equations

$$\frac{dK}{dl} = -K\left(1 - u_g\right), \tag{3.51}$$

$$\frac{du_g}{dl} = 2u_g\left(1 - u_g\right). \tag{3.52}$$

These equations are characterized by a line of stable fixed points with $u_g = 1$ and $K = \text{const.}$ corresponding to a JJ chain with finite Λ in the infrared. Additionally, an unstable fixed point $K = u_g = 0$ exists describing a system with infinite-range Coulomb interaction.

The equation governing the evolution of the phase-slip amplitude reads (see App. A.5.1)

$$\frac{dy}{dl} = \frac{1 + u_g}{2}\left(2 - \pi K\right) y. \tag{3.53}$$

We recognize that K can indeed be viewed as the phase stiffness at the cutoff. Furthermore, due to the anisotropic elimination procedure in the momentum-frequency plane, the engineering dimension of y is $1 + u_g$. The equations (3.51), (3.52) and (3.53) describe the renormalization of the parameters K, u_g and y to the first order in the fugacity. The second order corrections are derived in App. A.5.2. Including also the effects of random stray charges, we obtain

$$\frac{dK}{dl} = -(1 - u_g)K - \frac{1}{2}y^2K^2(1 + u_g)\frac{\mathrm{I}_1(D_Q) - \mathrm{L}_1(D_Q)}{D_Q}, \tag{3.54}$$

$$\frac{du_g}{dl} = 2u_g(1 - u_g) + \frac{y^2}{2}K(1 + u_g)u_g\left[(1 + u_g)\frac{\mathrm{I}_1(D_Q) - \mathrm{L}_1(D_Q)}{D_Q} - u_g\left[\mathrm{I}_0(D_Q) - \mathrm{L}_0(D_Q)\right]\right]. \tag{3.55}$$

Equations (3.53), (3.54), and (3.55) describe the renormalization of the parameters to second order in the QPS fugacity and in the presence of random stray charges. We exploit them in Sec. 3.3.2 to investigate the transport characteristics of JJ chains in the case of non-local charge interaction. In the

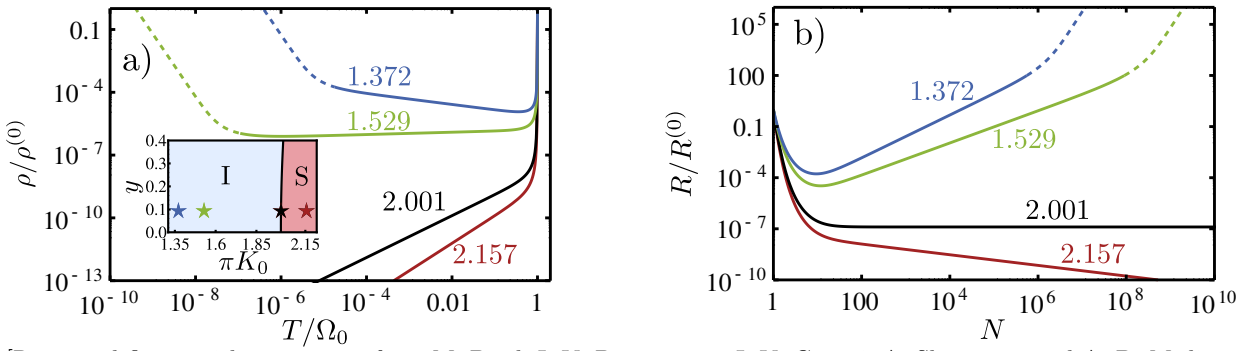

Figure 3.7: Behavior of the resistivity as a function of temperature [panel a)] and resistance a function of the system size [panel b)]. The bare fugacity is $y = 0.1$, and the screening length is $\Lambda = 10$. The value of πK_0 that governs the infrared behavior of the fugacity is indicated by the numbers close to the curves. Dashed lines represent extrapolations beyond the perturbative regime suggesting the flow towards the insulating fixed point. In the inset, stars mark the position of the systems in the phase diagram.

IR limit, we obtain from Eq. (3.55) $1 - u_\mathrm{g} \propto y^2 K$. In this limit, the RG equations can simplified to the form

$$\frac{\mathrm{d}y}{\mathrm{d}l} = \left(2 - \pi K\right) y, \tag{3.56}$$

$$\frac{\mathrm{d}K}{\mathrm{d}l} = -(1-u_\mathrm{g})K - y^2 K^2 \frac{\mathrm{I}_1(D_Q) - \mathrm{L}_1(D_Q)}{D_Q}, \tag{3.57}$$

$$\frac{\mathrm{d}u_\mathrm{g}}{\mathrm{d}l} = 2(1-u_\mathrm{g}) + y^2 K \left[2\frac{\mathrm{I}_1(D_Q) - \mathrm{L}_1(D_Q)}{D_Q} - \mathrm{I}_0(D_Q) + \mathrm{L}_0(D_Q)\right]. \tag{3.58}$$

At this point we want to stress that the Eqs. (3.56) and (3.57) are equivalent to Eqs. (3.23) and (3.22), respectively, by identifying $K_0 = K\sqrt{u_\mathrm{g}}$. Setting $u_0 = \Omega_0/\sqrt{u_\mathrm{g}}$, Eq. 3.26 can be recovered from (3.58) up to the additional term $-u_0(1 - \Omega_0^2/u_0^2)$ on the right hand side that is related to a slight difference in the renormalization schemes in the local and non-local case. This means that the Eqs. (3.53), (3.54) and (3.55) correctly reproduce the long-distance behavior analyzed in Sec. 3.2. However, at intermediate length scales, $1 \ll N \ll K$, new physics is predicted. As can be seen from Eq. (3.53), the QPS amplitude y is strongly reduced at those initial steps of the RG. This behavior was previously mentioned in Ref. [44]. After establishing the RG equations in this section, we turn to the discussion of the low-temperature transport properties of JJ chains in the regime of non-local charge interaction.

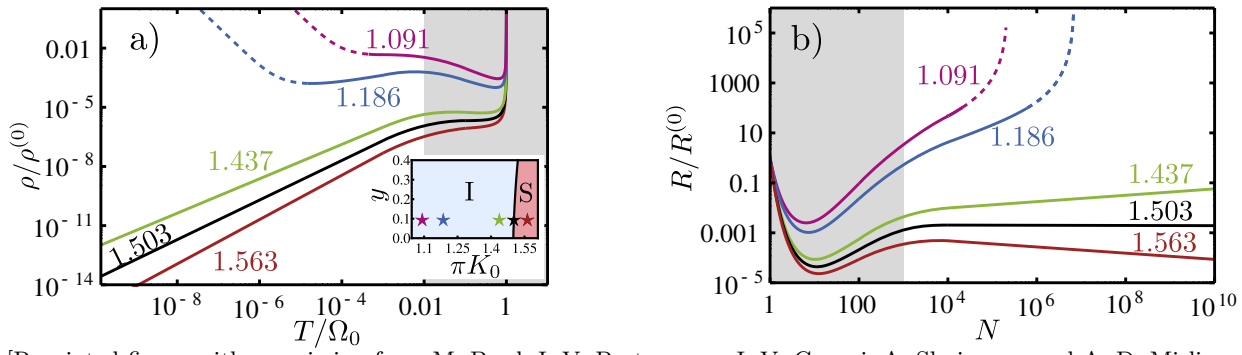

[Reprinted figure with permission from M. Bard, I. V. Protopopov, I. V. Gornyi, A. Shnirman, and A. D. Mirlin, Phys. Rev. B **96**, 064514 (2017), DOI: 10.1103/PhysRevB.96.064514, cf. Ref. [107]. Copyright 2017 by the American Physical Society.]

Figure 3.8: Panel a) shows the temperature dependence of the resistivity, panel b) the length-dependence of the resistance at zero temperature. The chain parameters are: screening length $\Lambda = 10$, strength of random stray charges $D_Q = 10^{-3}$, and bare phase-slip fugacity $y = 0.1$ in both panels. The value of πK_0 governing the behavior of the fugacity at large scales is indicated by the numbers close to the curves. Dashed lines represent extrapolations sketching the tendency of the flow towards the insulating fixed point characterized by an infinite resistivity. The position of the system in the phase diagram is marked by the star in the inset of panel a).

3.3.2 Transport in a JJ chain with non-local interaction

Analogous to the limit of local Coulomb interaction discussed in Sec. 3.2.2, we combine the results of the conductivity derived in the memory-function formalism,

$$\frac{\sigma(T)}{\sigma^{(0)}} \sim \begin{cases} \dfrac{y_0^2 N_{\mathrm{th}}(T)}{y^2(T)}, & D_Q(T) \ll 1, \\ \dfrac{y_0^2 D_Q(T) N_{\mathrm{th}}(T)}{y^2(T)}, & D_Q(T) \gg 1\,, \end{cases} \tag{3.59}$$

with the RG equations (3.53), (3.54), and (3.55). In Eq. (3.59), $N_{\mathrm{th}}(T)$ denotes the thermal length at which the renormalization is terminated by finite temperature. In the crossover regime, $D_Q(T) \sim 1$, we interpolate between both limits to obtain a smooth matching. Since in our RG treatment, the frequency cutoff Ω_0 is preserved, the temperature flows according to

$$\frac{dT(l)}{dl} = u_g T(l). \tag{3.60}$$

The thermal length, $N_{\mathrm{th}}(T)$, is then given by the scale at which the renormalized temperature $T(l)$ is equal to the cutoff Ω_0. To avoid misunderstandings, we stress that the results for the temperature dependence of the resistivity, $\rho(T)$, are given as a function of the physical temperature T. This temperature is the initial condition for the flow of $T(l)$, $T(l = 0) = T$.

The behavior of the resistivity as a function of temperature of a clean system ($D_Q = 0$) for $\Lambda = 10$ and several values of K_0 is depicted in Fig. 3.7 a). All curves in the insulating as well as in the superconducting regime show a rapid drop at temperatures close to the cutoff Ω_0. This can be explained

by the large value of K at these scales that leads to the proliferation of local superconducting correlations. At lower temperatures, the system reaches the local regime where the behavior of the phase-slip amplitude is determined by the IR stiffness K_0. For superconducting curves (red, $\pi K_0 = 2.157$) as well as for the critical curve (black, $\pi K_0 = 2.001$) the decrease continues at lower temperatures. The behavior of the critical line at low temperatures is of the form (3.35). Even in the insulating regime not too far away from the transition (green, $\pi K_0 = 1.529$), the resistivity drop continues at intermediate temperatures due to the factor $N_{\mathrm{th}}(T)$ in Eq. (3.59). At low temperatures, the resistivity starts to increase for the curves in the insulating regime (green, $\pi K_0 = 1.529$, and blue, $\pi K_0 = 1.372$). We plot as dashed lines qualitative extrapolations to illustrate the tendency of the system to flow to the localized fixed point. Fig. 3.7 b) shows the system size dependence of the resistance at $T = 0$. Since the curve on the phase boundary is almost constant [cf. Eq. (3.37)], the investigation of the length dependence of the resistance allows to locate the SIT in a more direct way.

The effects of random stray charges lead to an even more complex behavior of the resistivity and resistance, see Fig. 3.8. The stray charges can be neglected at short scales (gray region). There, the behavior of the transport characteristics is quite similar to the clean case. Reducing the temperature or increasing the system size, a strongly non-monotonic behavior of $\rho(T)$ and $R(N)$ can be observed. The origin of this behavior is the interplay of phase slips and stray charges that we have discussed already in Sec. 3.2.2 for the case of local Coulomb interaction (see also Fig. 3.4). For the resistivity curves in Fig. 3.8 a), up to four different regions with alternating signs of the slope of $\rho(T)$ can be found. At high temperatures, due to the scale dependence of the phase stiffness K, the resistivity experiences a fast drop. For the insulating curves (blue, $\pi K_0 = 1.186$, and purple, $\pi K_0 = 1.091$), phase slips become important at lower temperatures but still above T_Q (gray region) because stray charges are still weak. As can be clearly seen for the blue curve ($\pi K_0 = 1.186$), at temperatures below T_Q, the stray charges are at first strong enough to lead to a decreasing resistivity. However, at even lower temperatures, QPS take over and drive the system to the insulating fixed point. The system-size dependence of the resistance shows strongly non-monotonic behavior for insulating systems very close to the transition and for superconducting curves. After the initial drop at very short system sizes, the resistance of the superconducting curve (red, $\pi K_0 = 1.563$) increases at first for system sizes below the mean free path N_Q (gray region) since the effect of stray charges is negligible. Increasing the chain length above the mean free path, random stray charges become strong enough to overcome the growth of the phase-slip fugacity, resulting in a decreasing resistance. The intricate, strongly non-monotonic dependence of $\rho(T)$ and $R(N)$ makes it very hard to locate the SIT based on experimental data that cover only a limited range of temperatures and system sizes.

3.4 Comparison to experiment

Let us now compare our findings to relevant experimental studies. The experiment described in Ref. [39] studied the SIT in JJ chains of two different lengths, $N = 63$ and $N = 255$, in a temperature interval from 1 K down to 50 mK. More details on this experiment can be found in Sec. 1.4. The observed curves of the resistance as a function of temperature (see Fig. 1.7 or Fig. 3 of Ref. [39]) show quite similar behavior to our findings (Figs. 3.4 and 3.8). In the insulating regime, the resistance in the experiment increases at high temperatures when lowering the temperature, decreases at intermediate temperatures, and increases again at low T. One is tempted to relate the positions of the minimum and maximum of $R(T)$ at approximately 100 mK and 400 mK with our temperature scales T_{ps} and T_Q, respectively. A more quantitative comparison would necessitate the knowledge of the bare values of y

and D_Q. For shorter chains ($N = 63$), the minimum at low temperatures is absent, which probably means that they are not long enough to observe the ultimate large-N asymptotics. In Ref. [39], a wrong parameter was used to characterize the transition. As shown in the theoretical work by Choi et al. [44], the correct parameter is $K_0 = \sqrt{E_J/E_0}$. In our theory, we obtain the same parameter governing the SIT. A subsequent publication [45] from the same group that performed the experiment in Ref. [39] provides experimental evidence that this parameter is correct. Indeed, when the resistance at lowest measured temperatures is plotted versus K_0, the curves of the chains with the system sizes $N = 63$, 127 and 255 intersect in one point with a good accuracy. The extracted crossing point, the critical point, is located at $\pi K_0 \simeq 0.1$. Our theory presented in this thesis, however, predicts the transition point to be at $\pi K_0 = 3/2$ in a strongly disordered system.

A recent experiment [53] that measured the critical voltage for the onset of transport in the insulating regime is consistent with the location of the transition at $\pi K_0 = 3/2$. The experiment of Ref. [53] was performed with single-junction chains, while the one of Ref. [39] used chains in the SQUID geometry. The authors of Ref. [53] performed measurements on chains in a SQUID geometry as well, and found significantly reduced critical voltages. The mechanism underlying the discrepancy between single-junction chains and SQUID chains, which could have also played a role in the experiment of Ref. [39], is currently unknown. The authors of Ref. [53] conjecture that low-frequency flux noise or some kind of interplay between charge and flux affect the measurements in chains with a SQUID geometry.

As mentioned in the introduction to this chapter, our results are expected to apply to superconducting nanowires as well. In App. A.6, we briefly outline the mapping of the parameters of our theory to the parameters of the theory for superconducting wires [67, 68]. Experimentally, MoGe nanowires were used to investigate the SIT [64, 65]. In these experiments, the wires were rather short (up to $0.5\,\mu$m). In a more recent experiment [66], longer wires up to $25\,\mu$m were used. There, a transition was observed if the cross section of the wire is reduced or the external magnetic field perpendicular to the wire is increased. Qualitatively, the resistivity curves as a function of temperature are in agreement with theoretical predictions. On the other hand, the critical curve in Ref. [66] is basically constant. Our theory, however, predicts the resistance to vanish linearly (with logarithmic corrections) as a function of temperature. A possible explanation for this disagreement is the limited temperature range in the experiment (from 2-4 K down to 0.4 K). The lowest accessible temperature might be still too high to extract the correct IR behavior. Another possible explanation is that some coupling to the environment could have stabilized the metallic character of wires that are actually in the insulating regime.

This concise discussion of experiments on JJ chains and semiconductor nanowires demonstrates that both types of systems offer great opportunities to investigate the SIT in one dimension. Up to the current date, there is clearly more experimental work required to observe the various scaling regimes of the resistance, as obtained in our theory, and to locate the actual position of the SIT.

3.5 Summary of chapter 3

In this chapter, we have discussed the transport properties of disordered JJ chains. Starting from the lattice model that is introduced in Sec. 1.2, we derived the corresponding low-energy field theory which is of the sine-Gordon type. Our theory contains the effects from quantum phase slips and two kinds of disorder: random stray charges and a random phase-slip fugacity. We have analyzed the regime of local Coulomb interaction where the ground capacitance dominates ($C_0 \gg C_1$) as well as the regime of

non-local Coulomb interaction where the junction capacitance dominates ($C_1 \gg C_0$). The transport characteristics are obtained by combining the memory-function formalism with the RG.

The critical point is of BKT type. In the clean case, it is located at $\pi K_0 = 2$ for vanishing fugacity y. In the strongly disordered regime, it is shifted to $\pi K_0 = 3/2$ for vanishing effective strength of random phase slips $D_{\xi,y}$. In Fig. 3.2, we demonstrate that even a tiny disorder strength of random stray charges shifts the transition line quite considerably in favor of the superconducting phase. This counterintuitive behavior can be explained by the destructive interference of QPS due to the random phase induced by the stray-charge disorder. The other kind of disorder, which originates from junction-to-junction fluctuations and leads to QPS with a random fugacity, shifts the phase boundary in the opposite direction, see Fig. 3.2.

On the phase boundary the resistivity as a function of temperature goes to zero linearly with logarithmic corrections, Eq. (3.41), while the zero-temperature resistance as a function of the system size vanishes in a logarithmically slow fashion, Eq. (3.43). Away from criticality, the complete behavior is significantly more involved. In the regime of local Coulomb interaction, curves in the insulating regime show up to three different regions of behavior, see Figs. 3.4 and 3.5. At high temperatures, QPS lead to an increasing behavior of the resistivity when decreasing the temperature. At intermediate temperatures, the resistivity drops because random stray charges suppress the influence of phase slips. Upon further lowering of the temperature, the resistivity shows an upturn since QPS take over, and drive the system into the insulating fixed point. A similar behavior can be observed in the length dependence of the resistance for systems in the insulating regime very close to the critical curve. In the superconducting phase, the resistance as a function of the system size shows the first two regimes. For non-local Coulomb interaction, an additional regime at high temperatures (small system sizes) occurs, where the resistivity $\rho(T)$ (resistance $R(N)$) experiences a quick drop, see Fig. 3.8.

In essence, the behavior of $\rho(T)$ and $R(N)$ at intermediate scales is substantially different from the behavior at low temperatures or large system sizes. Consequently, identifying the location of the SIT based on experimental data in a limited range of N and T constitutes a hard problem. Comparing our findings with the experiment reported in Ref. [39] that performed transport measurements in SQUID chains, we find qualitative agreement on the behavior of the resistance as a function of temperature. Nevertheless, the experimentally found transition point of the SIT is inconsistent with our prediction. This discrepancy could be related to fact that the relatively small system sizes (up to $N = 255$) and the lowest accessible temperature of 50 mK are insufficient to probe the ultimate infrared behavior. As discussed above, the behavior of transport quantities is strongly non-monotonic leading to a behavior at intermediate scales that is completely different from the one at large scales. Another possible explanation for the unexpected location of the SIT in Ref. [39] was pointed out in Ref. [53], where it was noted that the measurements in SQUID chains could be affected by external noise or an interplay of charge and flux. The measurements reported in Ref. [53] on single-junction chains in the insulating regime are consistent with the location of the SIT predicted by theory presented in this thesis.

Before closing this chapter, we mention two possible directions for future projects. Spatial fluctuations of the LL constant K_0 are not considered here. Fluctuations of the parameters from junction to junction lead to this kind of disorder as well (besides the random QPS amplitude). Despite the fact that such fluctuations are of minor importance for the charge transport, it is expected [146] that this kind of disorder has a strong impact on the energy transport. Furthermore, the precise behavior of the insulating curves in the strong-coupling regime (dashed lines in our figures) could be analyzed. It is expected that effects of many-body localization [147, 148] become important in this regime.

Chapter 4

4 Relaxation of plasmonic waves in Josephson-junction chains

In the previous chapter we have studied the transport properties of Josephson junction (JJ) chains. Another important goal of this thesis is the analysis of the relaxation of excitations in 1D interacting systems. In this chapter, we investigate the relaxation of plasmonic waves in JJ chains. Plasmonic waves are the collective fluctuations of the superconducting phases above the superconducting ground state of the chain.

We are also motivated by a recent experiment [73] which measured the reflection coefficient in a JJ double chain under microwave irradiation. Their devices consist of two capacitively coupled chains which are short-circuited at one end, and connected to a dipole antenna at the other end. In this way, antisymmetric plasma waves (i. e., those with opposite amplitudes in both chains) can be excited via microwave radiation. The individual plasmonic modes are clearly visible as resonances in the reflection coefficient. Thereby, the energy dispersion of the plasmonic waves can be reconstructed. Due to the finite damping, the resonances of the reflection coefficient are broadened. Combining the information about the modulus and the phase of the reflection coefficient enables them to separate the internal damping from external losses related to, e. g., the damping of the connected transmission line or the leakage of the waveguide. Setups with a large Josephson energy showed a growth of the quality factor upon lowering the frequency. In samples with a lower value of the Josephson energy, the quality factor became almost independent of frequency and ultimately showed a tendency to decrease at low frequencies. The authors of Ref. [73] regard this behavior as a manifestation of the superconductor-insulator transition (SIT). At variance with theoretical predictions, it is claimed in Ref. [73] that the SIT is governed by the short-wavelength rather than the long-wavelength part of the Coulomb interaction. Specifically, the growth of the quality factor at low frequencies ("superconducting" behavior) was observed for setups that are expected to be in the insulating regime.

We analyzed theoretically the internal damping of plasmonic waves in JJ chains in Ref. [149]. Our results are reviewed in the current chapter. Two models are studied: (i) a single chain and (ii) a double chain of JJs to make closer contact to the experiment of Ref. [73]. We demonstrate that the effective theory for the antisymmetric mode of the two-chain setup is equivalent to a theory for a single chain provided that the ground capacitance can be neglected. Two sources for the relaxation of plasmonic excitations are considered: (i) the scattering of plasmonic waves from quantum phase slips (QPS) and (ii) the interaction of plasmons induced by "gradient" anharmonicities. We obtain the contribution to the decay rate of plasmonic waves for both types of decay channels. Since the gradient

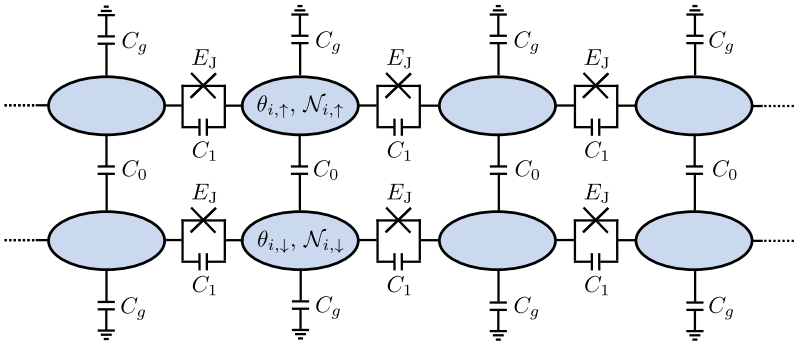

Figure 4.1: Schematic representation of two capacitively coupled JJ chains. We denote by C_1 the junction capacitance, by C_g the capacitance to the ground, and by C_0 the interchain capacitance. The number of Cooper pairs $\mathcal{N}_{i,\sigma}$ and the superconducting phase $\theta_{i,\sigma}$ on the i-th island in the chain with index $\sigma =\uparrow,\downarrow$ represent the canonically conjugate variables in the system.

nonlinearities are irrelevant from the point of view of the renormalization group (RG), its contribution to the decay rate vanishes in the low-frequency limit. We obtain the universal ω^4 scaling for this contribution to the relaxation rate. This behavior can be regarded as "superconducting". On the contrary, depending on the parameters of the system, the mechanism related to QPS can lead to both "superconducting" and "insulating" behavior. However, if the Josephson energy is much larger than the charging energy corresponding to the junction capacitance which controls the short-wavelength behavior of the Coulomb interaction, the contribution from QPS is strongly suppressed. The interplay of both channels (gradient anharmonicities and QPS) can thus result in a change of the behavior from "superconducting" to "insulating" at intermediate frequencies. Despite the fact that the system is deep in the insulating regime, the SIT can be imitated via this mechanism at intermediate frequencies.

This chapter is structured as follows. In Sec. 4.1, we briefly recall the description of a single JJ chain already outlined in Secs. 1.2 and 3.1. Moreover, we introduce the lattice model for the two-chain device and derive its field-theory description. Section 4.2 is devoted to the discussion of two decay channels for the plasmonic waves. The relaxation due to QPS is analyzed in Sec. 4.2.1, and the one related to the gradient anharmonicities in Sec. 4.2.2. The interplay of both mechanisms is studied in Sec. 4.2.3. We compare our results to the experimental findings of Ref. [73] in Sec. 4.3. Finally, we summarize our main results in Sec. 4.4. Technical details of the derivation of the field theory in the case of the double chain are presented in App. B.

This chapter is based on our work in Ref. [149].

4.1 Lattice models and low-energy theory

In this chapter, we study two similar systems: a linear JJ chain shown in Fig. 1.2 and a double chain composed of two capacitively coupled chains depicted in Fig. 4.1. The lattice model of a single chain is introduced already in Sec. 1.2. Its effective low-energy theory in terms of a sine-Gordon theory is derived in Sec. 3.1. We recall here only the results. The low-energy theory for a linear chain of Josephson junctions is of the form

$$S = S_0 + S_{\mathrm{ps}}, \tag{4.1}$$

where the imaginary-time quadratic action (at temperature T with bosonic Matsubara frequency ω_n) can be written in the form ($u_0K_0 = E_\mathrm{J} = \Omega_0 K$)

$$S_0 = \frac{1}{2\pi^2 u_0 K_0} T \sum_{\omega_n} \int \frac{\mathrm{d}q}{2\pi} \left[\omega_n^2 + \epsilon^2(q)\right] |\phi(q,\omega_n)|^2, \tag{4.2}$$

that describes plasmonic waves with the energy dispersion

$$\epsilon(q) = \frac{\omega_\mathrm{p}|q|}{\sqrt{q^2 + \alpha/\Lambda^2}}, \quad \omega_\mathrm{p} = \sqrt{E_\mathrm{J} E_1}. \tag{4.3}$$

In order to facilitate the discussion of the low-energy theory of the two-chain setup of Fig. 4.1, we have introduced the number α. In the case of a single chain, it holds $\alpha \equiv 1$. The Luttinger parameter K_0 and the plasmon velocity at low momenta u_0 are given by

$$u_0 = \sqrt{\frac{E_\mathrm{J} E_0}{\alpha}}, \qquad K_0 = \sqrt{\frac{E_\mathrm{J}}{\alpha\, E_0}}. \tag{4.4}$$

The effect of QPS is taken into account by

$$S_\mathrm{ps} = y u_0 \int \mathrm{d}x \mathrm{d}\tau \cos\left[2\phi(x,\tau)\right] \tag{4.5}$$

in the absence of random offset charges. Here, τ denotes the imaginary time and y the (ultraviolet) value of the phase-slip amplitude. In the regime $E_\mathrm{J} \gg \min(E_1, E_0)$, the superconducting correlations are (at least locally) well established leading to an exponentially small QPS amplitude,

$$y \propto \mathrm{e}^{-\zeta K}, \qquad K = \sqrt{\frac{E_\mathrm{J}}{\alpha\, E_0} + \frac{E_\mathrm{J}}{\alpha^2\, E_1}}. \tag{4.6}$$

The parameter K is the Luttinger constant for the ultraviolet plasmons (with $q \sim 1$), and ζ is a numerical coefficient which depends on the screening length Λ as well as on the ultraviolet cutoff procedure. References [14, 44, 47, 49, 63] provide estimates for ζ in various limiting cases. As in Chap. 3, we include random stray charges that provide a random phase to the QPS action, (4.5). In the presence of stray charges $Q(x)$, the phase-slip action reads

$$S_\mathrm{ps} = y u_0 \int \mathrm{d}x \mathrm{d}\tau \cos\left[2\phi(x,\tau) - \mathcal{Q}(x)\right] \quad \text{with} \quad \mathcal{Q}(x) = 2\pi \int_{-\infty}^{x} \mathrm{d}x'\, Q(x'). \tag{4.7}$$

For the sake of simplicity, we assume Gaussian white noise disorder,

$$\left\langle Q(x) \right\rangle_Q = 0, \quad \left\langle Q(x) Q(x') \right\rangle_Q = \frac{D_Q}{2\pi^2} \delta(x - x'). \tag{4.8}$$

The Hamiltonian associated with the action (4.1) reads

$$\mathcal{H} = \mathcal{H}_0 + \mathcal{H}_\mathrm{ps}, \tag{4.9}$$

where the quadratic part is given by

$$\mathcal{H}_0 = \frac{1}{2\pi^2} \int \frac{\mathrm{d}q}{2\pi} \left[\frac{\epsilon^2(q)}{u_0 K_0} |\phi(q)|^2 + u_0 K_0 q^2 |\pi\theta(q)|^2\right], \tag{4.10}$$

and the phase-slip term is of the form

$$\mathcal{H}_{\rm ps} = y u_0 \int \mathrm{d}x \cos[2\phi(x) - \mathcal{Q}(x)]. \tag{4.11}$$

As derived in Sec. 3.1, the Eqs. (4.1), (4.2) and (4.7) describe the low-energy theory of a JJ chain. We make two remarks. First, in this chapter we are interested in the effects at moderate momenta $q \lesssim 1/\Lambda$. For this reason we replace the energy spectrum (4.3) by its low-momentum expansion

$$\epsilon(q) \simeq u_0(1 - q^2 l_c^2)|q|, \qquad l_c = \Lambda/\sqrt{2\alpha}, \tag{4.12}$$

where the length l_c (which up to a numerical factor equals the screening length Λ) determines the scale for the bending of the plasmonic energy spectrum.

Second, the only nonlinear term so far is the one describing the effects due to QPS. In the limit of low momenta, $q \ll 1/\Lambda$, the effective theory given by Eqs. (4.1), (4.2) and (4.5) is of the standard sine-Gordon form describing the SIT occuring at $\pi K_0 = 2$ [44] (see also Sec. 3.2). This phase transition is governed by the proliferation of QPS. In this sense, the term (4.5) is the most important nonlinearity of the system. There are of course other nonlinear terms possible. As an example, we consider the expansion of the Josephson potential in Eq. (1.25) to the fourth order leading to the nonlinearity in the effective Hamiltonian

$$\mathcal{H}_{\rm nl} = -\frac{E_{\rm J}}{\alpha^3\, 4!} \int \mathrm{d}x \left(\partial_x \theta\right)^4, \tag{4.13}$$

which corresponds to the term

$$S_{\rm nl} = -\frac{\alpha}{4!\pi^4 E_{\rm J}^3} \int \mathrm{d}x \mathrm{d}\tau \left(\partial_\tau \phi\right)^4. \tag{4.14}$$

in the effective action. As opposed to the phase-slip term (4.5), the non-linearity (4.13) and all further nonlinear terms that can be added to the effective Hamiltonian are constructed from the local charge ($\mathcal{N} \propto \partial_x \phi$) and current densities ($\propto \partial_x \theta$). Hence, they contain a high power of gradients making them irrelevant in the renormalization group sense. This is the reason why we did not consider them in Chap. 3. In the following, we call those nonlinearities "gradient" anharmonicities to distinguish them from the nonlinearity arising from QPS. Despite the unimportance of the gradient anharmonicities, they can dominate the decay of plasmonic waves at high frequencies provided that the bare amplitude of phase slips is small. This point is discussed in more details in Sec. 4.2.3.

In summary, the effective action for a linear JJ chain is of the form

$$S = S_0 + S_{\rm ps} + S_{\rm nl}, \tag{4.15}$$

where S_0 and $S_{\rm ps}$ are given by Eqs. (4.2) and (4.7), respectively. For the gradient anharmonicities described by $S_{\rm nl}$, we take Eq. (4.13) as a particular example. In the end of Sec. 4.2.2, we argue that our main statements do not rely on this specific choice.

We turn now to the analysis of the two-chain system depicted in Fig. 4.1. Here, C_0 and C_g denote the interchain capacitance and the capacitance to the ground, respectively. The Hamiltonian of the lattice model for this system is given by

$$\mathcal{H} = \frac{E_1}{2} \sum_{i,j} \sum_{\sigma,\sigma'=\uparrow,\downarrow} [\mathcal{S}^{-1}]_{\sigma,\sigma'}(i,j) \mathcal{N}_{i,\sigma} \mathcal{N}_{j,\sigma'} + E_{\rm J} \sum_{i,\sigma=\uparrow,\downarrow} [1 - \cos(\theta_{i+1,\sigma} - \theta_{i,\sigma})], \tag{4.16}$$

with

$$\mathcal{S}(i,j) = \tilde{s}_{i,j} \begin{pmatrix} 1 & 0 \\ 0 & 1 \end{pmatrix} + \frac{C_0}{C_1} \delta_{i,j} \begin{pmatrix} 1 & -1 \\ -1 & 1 \end{pmatrix} \tag{4.17}$$

and

$$\tilde{s}_{i,j} = (2 + C_g/C_1)\delta_{i,j} - \delta_{i,j+1} - \delta_{i,j-1}. \tag{4.18}$$

The indices $\uparrow, \downarrow$ are associated with the two chains.

On the Gaussian level, the Hamiltonian (4.16) contains two modes, symmetric and antisymmetric. The analog of these modes in a spinful Luttinger liquid are the charge and spin modes. We focus here on the properties of the antisymmetric mode which can be excited through a coupling to a dipole antenna [73]. For the sake of simplicity, we assume further that $C_g \ll C_0$. We are not completely sure how well this assumption holds in the experiment of Ref. [73]. On the other hand, we think that this assumption is not very important for our main conclusions. More precisely, in the case of $C_g \sim C_0$, our analysis should stay valid, apart from some modifications of numerical factors of order unity. In the regime $C_g \lesssim C_0$, both chains are well coupled, and the splitting between symmetric and antisymmetric modes is large.[1]

Completely analogous to the spin-charge separation in quantum wires, the velocity (at small momenta) of the symmetric ("charge") mode, $u_{\mathrm{ch}} = 2\sqrt{e^2 E_{\mathrm{J}}/C_g}$ is, in the limit $C_g \ll C_0$, much larger than the velocity of the antisymmetric ("spin") mode, $u_{\mathrm{s}} = \sqrt{2e^2 E_{\mathrm{J}}/C_0}$. As a result, the symmetric mode can be integrated out leading to an effective theory for the antisymmetric mode. The details of the derivation can be found in App. B. The resulting theory is of the same form as for the single chain. The same action given by Eqs. (4.15), (4.2), (4.7) and (4.13), including the parameters defined in Eqs. (4.12) and (4.4), describes the antisymmetric mode of the double chain. But in this case, the value of the numerical coefficient α is 2.

Starting from Eqs. (4.15), (4.2), (4.7) and (4.13), we carry out the analysis of the decay of plasmonic waves in the setups depicted in Figs. 1.2 and 4.1 in the next section.

4.2 Relaxation of plasmonic waves

Due to the interaction among plasmonic waves, those collective long-wavelength excitations above the superconducting ground state are not stable. After the excitation of a plasmon mode, e. g., by a microwave, it can decay into several plasma waves of lower energy. We consider two different mechanisms for the decay of plasmons, which are associated with the two nonlinearities in the action (4.15): the scattering off QPS and gradient anharmonicities. Both channels of the plasmon decay are discussed separately in Secs. 4.2.1 and 4.2.2, respectively. Their interplay is analyzed in Sec. 4.2.3.

4.2.1 Relaxation due to phase slips

In this section, we analyze the decay processes due to the scattering off QPS. In our computation of the lifetime, we follow closely the approaches of Refs. [119, 120]. For the purpose of this section, the curvature of the plasmonic spectrum is of minor importance. We approximate it here by the linear spectrum

$$\epsilon(q) = u_0|q|. \tag{4.19}$$

[1] In the opposite limit $C_0 \ll C_g$, both chains are nearly decoupled. Here, instead of describing the system in terms of symmetric and antisymmetric modes, it is more natural to work in the basis of individual chains. If $C_0 = 0$, both chains are fully decoupled, and can be described within the single-chain theory with the replacement $C_0 \to C_g$.

Accordingly, the quadratic part of the action is given by

$$S_0 = \frac{1}{2\pi^2 u_0 K_0} \int \mathrm{d}x \mathrm{d}\tau \left[u_0^2 (\partial_x \phi)^2 + (\partial_\tau \phi)^2 \right]. \tag{4.20}$$

Expanding the phase-slip action, Eq. (4.5), in powers of ϕ reveals that the plasmonic mode is able to decay into an arbitrary large number of low-energy modes. In our approach, we obtain directly the sum of all these contributions. A convenient way to extract the relaxation rate is via the computation of the imaginary part of the self-energy (of the Fourier transform) of the correlation function

$$G(\mathbf{r}) = \left\langle \left\langle \phi(\mathbf{r})\phi(0) \right\rangle_S \right\rangle_Q, \tag{4.21}$$

where $\mathbf{r} = (x, \tau)$, and we denote by $\langle \cdot \rangle_S$ the average with respect to the full action, $S = S_0 + S_{\mathrm{ps}}$. In the absence of QPS, $y = 0$, the imaginary-time Green function is given by

$$G_0(\mathbf{q}) = \frac{\pi^2 u_0 K_0}{\omega_n^2 + u_0^2 q^2}, \qquad \mathbf{q} = (q, \omega_n) \tag{4.22}$$

with ω_n being the (bosonic) Matsubara frequency. Introducing the self-energy Σ, we can express the full Green function as

$$G(\mathbf{q}) = \frac{1}{G_0^{-1}(\mathbf{q}) - \Sigma(\mathbf{q})} = \frac{\pi^2 u_0 K_0}{\omega_n^2 + u_0^2 q^2 - \pi^2 u_0 K_0 \Sigma(\mathbf{q})}. \tag{4.23}$$

The inverse lifetime of a plasmonic wave can be extracted by means of the imaginary part of the retarded self-energy on the mass shell,

$$\frac{1}{\tau(\omega)} = \frac{\pi^2 K_0 u_0}{2\omega} \operatorname{Im} \Sigma^R(q = \omega/u_0, \omega). \tag{4.24}$$

The self-energy is computed perturbatively in the phase-slip amplitude y. In imaginary time, the Matsubara self-energy $\Sigma(\mathbf{r})$ is obtained from the perturbative expansion of the Green function, Eq. (4.21),

$$G(\mathbf{r}) = G_0(\mathbf{r}) + \int \mathrm{d}^2 r_1 \mathrm{d}^2 r_2 G_0(\mathbf{r} - \mathbf{r}_1) \Sigma(\mathbf{r}_1 - \mathbf{r}_2) G_0(\mathbf{r}_2), \tag{4.25}$$

where

$$\Sigma(\mathbf{r}) = 2y^2 u_0^2 \left[\mathrm{e}^{-2C_0(\mathbf{r}) - D_Q|x|} - \delta(\mathbf{r}) \int \mathrm{d}^2 r_0 \mathrm{e}^{-2C_0(r_0) - D_Q|x_0|} \right] + \mathcal{O}(y^4). \tag{4.26}$$

The correlation function C_0 in the exponential is given by

$$C_0(\mathbf{r}) = \frac{2}{\beta N} \sum_{\mathbf{q}} (1 - \cos \mathbf{q}\mathbf{r}) G_0(\mathbf{q}) \tag{4.27}$$

$$= \frac{\pi K_0}{2} \ln \left[\frac{u_0^2 \beta^2}{\pi^2} \sinh\left(\frac{\pi}{u_0 \beta}(x + i u_0 \tau) \right) \sinh\left(\frac{\pi}{u_0 \beta}(x - i u_0 \tau) \right) \right], \tag{4.28}$$

where N is the number of junctions per chain, and $\beta = 1/T$. It is convenient to analytically continue the imaginary-time result (4.26) first to real time t before Fourier transforming it. The dependence

of the first term in Eq. (4.26) on the imaginary time τ is governed by the Matsubara time-ordered function

$$\chi^T(x,\tau) = \mathrm{e}^{-2C_0(x,\tau)}. \tag{4.29}$$

The corresponding retarded function can be found following the standard route [17],

$$\chi^R(x,t) = \frac{2\Theta(t)\Theta\left(u_0 t - |x|\right)\sin\left(\pi^2 K_0\right)\left(\frac{\pi}{\beta u_0}\right)^{2\pi K_0}}{\left|\sinh\frac{\pi}{u_0\beta}\left(x+u_0 t\right)\sinh\frac{\pi}{u_0\beta}\left(x-u_0 t\right)\right|^{\pi K_0}}, \tag{4.30}$$

where Θ is the Heaviside step function. According to Eq. (4.24), the lifetime is related to the Fourier transform of the self-energy. Since the second term in Eq. (4.26) does not contribute to the imaginary part of the self-energy, we find

$$\mathrm{Im}\,\Sigma^R(q,\omega) = 2u_0^2 y^2\,\mathrm{Im}\int \mathrm{d}x\mathrm{d}t\,\mathrm{e}^{-i(qx-\omega t)}\chi^R(x,t)\mathrm{e}^{-D_Q|x|}. \tag{4.31}$$

In order to proceed, we switch to the light-cone variables $z_\pm = \pi(u_0 t \pm x)/(u_0\beta)$:

$$\begin{aligned}\mathrm{Im}\,\Sigma^R(q,\omega) = 2u_0 y^2\sin(\pi^2 K_0)\left(\frac{\pi}{u_0\beta}\right)^{2\pi K_0-2}\mathrm{Im}\int_0^\infty \mathrm{d}z_+\int_0^\infty \mathrm{d}z_-\frac{\exp\{i\frac{\beta}{2\pi}(\omega-u_0 q)z_+\}}{\left(\sinh z_+\right)^{\pi K_0}}\\ \times\frac{\exp\{i\frac{\beta}{2\pi}(\omega+u_0 q)z_-\}}{\left(\sinh z_-\right)^{\pi K_0}}\,\mathrm{e}^{-\frac{D_Q u_0\beta}{2\pi}|z_+-z_-|}.\end{aligned} \tag{4.32}$$

The relaxation rate due to QPS is given by Eqs. (4.24) and (4.32). In the following, we analyze them in several limiting cases.

Clean case

In the limit of weak disorder, $D_Q \ll \min(q, T/u_0)$, it is justified to set $D_Q = 0$ leading to the decoupling of the integrations. In this case, the imaginary part of the self-energy is given by

$$\begin{aligned}\mathrm{Im}\,\Sigma^R(q,\omega) = 2u_0 y^2\sin(\pi^2 K_0)\left(\frac{2\pi}{u_0\beta}\right)^{2\pi K_0-2}\mathrm{Im}\Bigg\{\mathrm{B}\left(1-\pi K_0,\frac{\pi K_0}{2}-i\frac{\beta}{4\pi}(\omega+u_0 q)\right)\\ \times\mathrm{B}\left(1-\pi K_0,\frac{\pi K_0}{2}-i\frac{\beta}{4\pi}(\omega-u_0 q)\right)\Bigg\},\end{aligned} \tag{4.33}$$

where $B(x,y)$ is the Euler Beta function. With the help of Eq. (4.24), the decay rate is found in the clean limit. It is given by

$$\frac{1}{\tau(\omega)} \sim u_0 y^2\begin{cases}\left(\frac{2\pi T}{u_0}\right)^{2\pi K_0-3}, & \omega \ll T,\\ \frac{T}{u_0}\left(\frac{2\pi\omega T}{u_0^2}\right)^{\pi K_0-2}, & \omega \gg T.\end{cases} \tag{4.34}$$

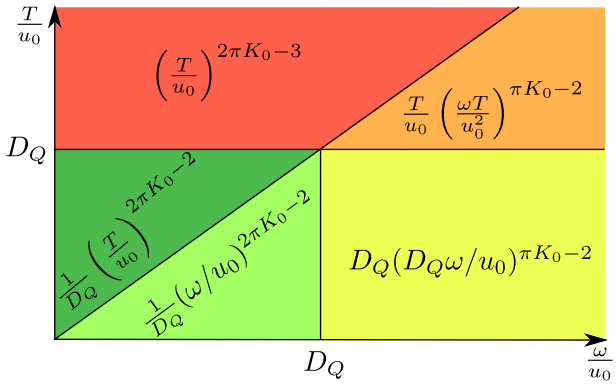

[Reprinted figure with permission from M. Bard, I. V. Protopopov, and A. D. Mirlin, Phys. Rev. B **98**, 224513 (2018), DOI: 10.1103/PhysRevB.98.224513, cf. Ref. [149]. Copyright 2018 by the American Physical Society.]

Figure 4.2: Dependence of the decay rate of plasmonic waves due the scattering off QPS in different regimes in the frequency-temperature plane. The dependence of $1/(\tau u_0 y^2)$ is indicated in each regime.

Disordered case

In the regime of strong disorder, $D_Q \gg \max(q, T/u_0)$, the most important contribution of the integrations in Eq. (4.32) originates from the region where z_+ and z_- are close to each other. The result for the imaginary part of the self-energy reads

$$\operatorname{Im}\Sigma^R(q,\omega) \simeq 8u_0\frac{y^2}{D_Q}\sin(\pi^2 K_0)\left(\frac{2\pi}{u_0\beta}\right)^{2\pi K_0-1}\operatorname{Im}\mathrm{B}\left(1-2\pi K_0, \pi K_0 - i\frac{\beta\omega}{2\pi}\right), \tag{4.35}$$

which is independent of momentum. Correspondingly, the decay rate in the limit of strong disorder, $D_Q \gg \max(q, T/u_0)$, is given by

$$\frac{1}{\tau(\omega)} \sim u_0\frac{y^2}{D_Q}\begin{cases}\left(\frac{2\pi T}{u_0}\right)^{2\pi K_0-2}, & \omega \ll T,\\ \left(\frac{\omega}{u_0}\right)^{2\pi K_0-2}, & \omega \gg T.\end{cases} \tag{4.36}$$

In the moderately disordered regime, two cases need to be considered. If $q \ll D_Q \ll T/u_0$, the result for the clean case, the first line of Eq. (4.34), is still applicable. In the regime $T/u_0 \ll D_Q \ll q$, the integration over z_- in Eq. (4.32) is effectively limited by $\pi T/u_0 q \ll 1$ at the upper limit. Moreover, the dependence on z_- in the exponential function associated with D_Q can be neglected. In this way, we obtain the relaxation rate

$$\frac{1}{\tau(\omega)} \sim u_0 y^2\ D_Q\left(\frac{D_Q\omega}{u_0}\right)^{\pi K_0-2}, \quad T \ll u_0 D_Q \ll \omega. \tag{4.37}$$

Equations (4.34), (4.36) and (4.37) constitute the main result of this section. They determine the decay rate of plasmonic waves due to QPS in different regimes. Figure 4.2 summarizes the behavior in the frequency-temperature plane. The decay rate scales with frequency, temperature and disorder strength as a power-law with non-universal exponents that are determined by the Luttinger parameter

K_0. If the system is deep in the superconducting regime, $K_0 \gg 1$, the decay rate vanishes in the zero-frequency limit. On the other hand, in the insulating regime with sufficiently small K_0, the rate grows when lowering the frequency.

4.2.2 Relaxation due to gradient nonlinearities

We discuss now the impact of the gradient nonlinearities associated with the term $\mathcal{H}_{\rm nl}$ in the effective Hamiltonian. Although being irrelevant in the renormalization group sense, at intermediate scales, these terms yield similar contributions to the relaxation of plasmonic waves as QPS. We analyze the nonlinearity (4.13) originating from the quartic term of the expansion of the Josephson potential.

The perturbative analysis of the relaxation of plasmonic waves due to gradient nonlinearities was performed in other contexts in Refs. [150–152]. We use the energy spectrum (4.12) since the perturbation theory for a linear spectrum is ill-defined.

To compute the matrix element associated with the decay process, we decompose the superconducting phase θ into usual bosonic creation ($b_q^\dagger$) and annihilation operators (b_q). The connection is given by [17]

$$\theta(x) = i\sqrt{\frac{\pi}{2N}} \sum_{q\neq 0} \frac{\mathrm{sign}(q)}{\sqrt{|q|}} \mathrm{e}^{-a|q|/2} \mathrm{e}^{iqx} (b_q^\dagger - b_{-q}), \tag{4.38}$$

where N denotes the number of junctions per chain, and a is the ultraviolet cutoff which can be sent to zero here. The calculation of the relaxation rate outlined below follows the procedure of Ref. [152]. Making use of the methods described in Sec. 2.2, we can express the relaxation rate via the collision integral [cf. Eq. (2.24)],

$$\frac{1}{\tau(q_1)} = \frac{2\pi}{2} \sum_{q_2,q_1',q_2'} \left| M_{q_1,q_2}^{q_1',q_2'} \right|^2 \delta(E_i - E_f) \Big\{ n_{\rm B}(\epsilon_{q_2})[1 + n_{\rm B}(\epsilon_{q_1'}) + n_{\rm B}(\epsilon_{q_2'})] - n_{\rm B}(\epsilon_{q_1'}) n_{\rm B}(\epsilon_{q_2'}) \Big\}, \tag{4.39}$$

where the matrix element

$$M_{q_1,q_2}^{q_1',q_2'} = \langle 0 | b_{q_2'} b_{q_1'} \mathcal{H}_{\rm nl} b_{q_1}^\dagger b_{q_2}^\dagger | 0 \rangle, \tag{4.40}$$

and $E_{i(f)}$ is the total energy of the initial (final) plasmons. We obtain

$$M_{q_1,q_2}^{q_1',q_2'} = -\frac{\pi^2 E_{\rm J}}{4\alpha^3 N} \,\mathrm{sign}(q_1 q_2 q_1' q_2') \sqrt{|q_1 q_2 q_1' q_2'|}\, \delta_{q_1+q_2,q_1'+q_2'} \tag{4.41}$$

for the matrix element. A plasmonic wave with $q_1 > 0$ (moving to the right) can decay via this nonlinearity by scattering off a thermal plasmon with momentum $q_2 < 0$ (moving to the left). This process is illustrated in Fig. 4.3. The conservation laws dictate the momentum of the left moving plasmon

$$q_2 = -\frac{3}{2} q_1 q_1' q_2' l_c^2 + \mathcal{O}(q_1^5 l_c^4) \tag{4.42}$$

to be much smaller than the momentum q_1. The sum over q_2' in Eq. 4.39 can be performed with the help of the momentum conservation. We can rewrite the delta function associated with the energy conservation as

$$\delta(E_i - E_f) = \frac{2}{3u_0(q_1+q_2)|q_{1,+}' - q_{1,-}'|l_c^2} \delta(q_1' - q_{1,+}'), \tag{4.43}$$

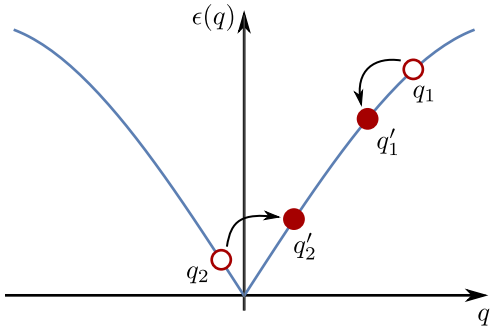

Figure 4.3: Dominant decay process induced by nonlinearities for a right moving plasmonic wave with momentum q_1.

where

$$q'_{1,\pm} \simeq \frac{q_1}{2} \pm \sqrt{\frac{q_1^2}{4} + \frac{2q_2}{3q_1 l_c^2}}. \tag{4.44}$$

The requirement that $q'_{1,\pm}$ is real limits q_2 to lie inside the interval

$$q_* < q_2 < 0, \qquad q_* = -\frac{3}{8} q_1^3 l_c^2. \tag{4.45}$$

Performing the continuum limit, $N \to \infty$, we go over from summations to integrations over momenta, $N^{-2} \sum_{q_2, q_1'} \to \int \mathrm{d}q_2 \mathrm{d}q_1'/(2\pi)^2$. After the integration over q_1', we obtain

$$\begin{aligned} \frac{1}{\tau(q_1)} = \frac{\pi^3 E_\mathrm{J}^2 q_1}{96\alpha^6} \int_{q_*}^{0} \mathrm{d}q_2 \frac{q'_{1,+} q'_{1,-} |q_2|}{u_0 (q_1 + q_2) |q'_{1,+} - q'_{1,-}| l_c^2} \\ \times \left\{ n_\mathrm{B}(\epsilon_{q_2}) [1 + n_\mathrm{B}(\epsilon_{q'_{1,+}}) + n_\mathrm{B}(\epsilon_{q'_{1,-}})] - n_\mathrm{B}(\epsilon_{q'_{1,+}}) n_\mathrm{B}(\epsilon_{q'_{1,-}}) \right\}. \end{aligned} \tag{4.46}$$

As can be seen from Eq. (4.42), we can neglect the q_2-dependence in the denominator compared to q_1. In the following we focus on the regime where the momentum q_1 is much larger than the thermal momentum T/u_0 but not too large, such that $\beta u_0 q_1^3 l_c^2 \ll 1$. In this regime, the bosonic distribution function related to the plasmon with momentum q_2 can be replaced by $1/\beta u_0 |q_2|$, and the distribution function associated with the plasmon with momentum $q'_{1,+}$ can be neglected. In the regime $-3q_1^2 l_c^2/2\beta u_0 < q_2 < 0$, we can replace the Bose function associated with the plasmon with momentum $q'_{1,-}$ by $1/\beta u_0 q'_{1,-}$, while we neglect it for $q_* < q_2 < -3q_1^2 l_c^2/2\beta u_0$. The latter regime of q_2 yields the main contribution to the integral in Eq. (4.46). After the evaluation of the integration, we obtain

$$\frac{1}{\tau(q_1)} \simeq \frac{\pi^3 E_\mathrm{J}^2 T q_1^4}{768\alpha^6 u_0^2} = \frac{\pi^3}{768\alpha^5} \frac{E_\mathrm{J}}{E_0} T q_1^4 \tag{4.47}$$

for the behavior of the relaxation rate (under the assumption $\beta u_0 q_1 \gg 1$, $q_1^2 l_c^2 \ll 1$, and $\beta u_0 q_1^3 l_c^2 \ll 1$).

The scaling of the relaxation rate due to gradient nonlinearities, Eq. (4.47), constitutes the main result of this section. As a function of frequency the decay rate scales as ω^4. It vanishes in the limit of low frequencies as expected from the irrelevance of the term (4.13) in the RG sense.

The result (4.47) is obtained for the particular anharmonic form (4.13). How universal is this result? Phenomenologically, various terms of the kind $(\partial_x\phi)^n(\partial_x\theta)^m$ can be present in an effective theory. Terms with $n+m>4$ are less relevant than the $(\partial_x\theta)^4$ term studied here. They yield a smaller contribution to the decay rate of plasmons, and can thus be neglected. On the contrary, a term that is cubic in the density, $\propto(\partial_x\phi)^3$, is more relevant in the RG sense. Since the conservation laws do not allow the decay of a single plasmon into two particles, the second order perturbation theory is necessary to yield a finite relaxation rate. The corresponding process is the same one as depicted in Fig. 4.3 leading to the identical ω^4 scaling of the decay rate [150–152].

4.2.3 Interplay of QPS and gradient nonlinearities

In Secs. 4.2.1 and 4.2.2, we have studied the relaxation of plasmonic waves due to QPS and gradient nonlinearities, respectively. The latter mechanism results in a universal ω^4 scaling, while the decay rate due to QPS is characterized by a non-universal exponent reflecting the SIT controlled by the value of K_0. In the following we analyze the interplay of both mechanisms. For definiteness, we assume that the considered frequencies are larger than temperature.

We analyze the plasmon decay by means of the dimensionless parameter $\omega\tau$ which we expect to be proportional to the quality factor examined in Ref. [73]. Deep inside the superconducting phase, $\pi K_0\gg 1$, the decay of plasmonic waves is dominated by the gradient anharmonicities leading to the ω^{-3} scaling of the quality factor [cf. Eqs. (4.34), (4.36), (4.37) and (4.47)]. The contribution from QPS becomes visible only for small enough values of the Luttinger parameter K_0. In the case of weak disorder, phase slips dominate the low-frequency behavior of the quality factor if $\pi K_0<6$ leading to the $\omega^{3-\pi K_0}$ scaling. If the random offset charges are strong, QPS dominate only for $\pi K_0<3$ resulting in the $\omega^{3-2\pi K_0}$ behavior of the quality factor. Moreover, as consequence of QPS, for sufficiently small values of K_0 ($\pi K_0<3$ for weak and $\pi K_0<3/2$ for strong charge disorder), the quality factor decreases when lowering the frequency. The overall frequency behavior for $\omega\tau$ is then non-monotonic. The maximum of the quality factor occurs around the crossover frequency at which the QPS become important. The overall behavior of the quality factor in the regime $\pi K_0\ll 1$ is illustrated in Fig. 4.4.

Another important point that should be emphasized here is the exponential smallness of the phase-slip amplitude y, Eq. (4.6). As result, the crossover frequency where QPS set in and dominate over the gradient anharmonicities is exponentially small for $E_\mathrm{J}\gg E_1$. Thus, even deep in the insulating phase, $\pi K_0\ll 1$, the quality factor is governed by the gradient anharmonicities leading to a *growing* behavior of the quality factor with lowering the frequency in a wide range of frequencies if $E_\mathrm{J}\gg E_1$. A downturn of the quality factor indicating insulating behavior of the system in the infrared limit occurs only at exponentially small frequencies.

We compare our findings to the experimental results of Ref. [73] in the next section.

4.3 Comparison to experiment

A comparison of our results for the quality factor to the experiment of Ref. [73] reveals qualitative agreement. A detailed description of the experiment is presented in Sec. 1.5. For a comparison of the notation used in this thesis and the one of Ref. [73] see Tab. 1.1. The internal quality factor for several samples is shown in Fig. 3 b) of Ref. [73]. From the measured values of the impedance Z, which is proportional to $1/K_0$ [see Eq. (1.82)], it is expected that all of the devices shown in this figure are nominally in the insulating phase. However, the quality factors of the samples with a large ratio of E_J/E_1 grow when the frequency is lowered suggesting the systems to be in the superconducting

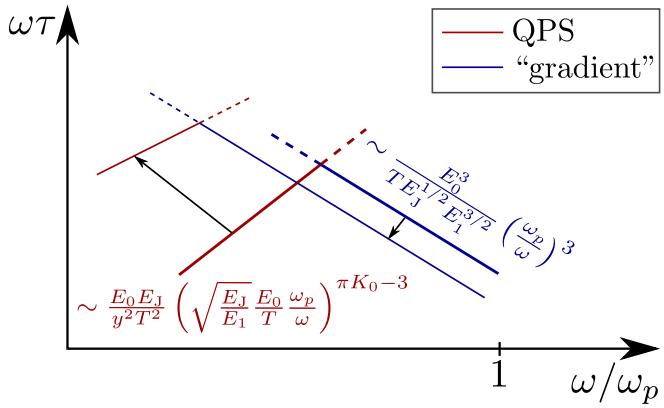

[Reprinted figure with permission from M. Bard, I. V. Protopopov, and A. D. Mirlin, Phys. Rev. B **98**, 224513 (2018), DOI: 10.1103/PhysRevB.98.224513, cf. Ref. [149]. Copyright 2018 by the American Physical Society.]

Figure 4.4: Schematic frequency dependence of the quality factor in a double-log scale in the insulating regime, $E_0 \gg E_J$. The change under an increase of E_J is indicated by the arrows (thick lines correspond to a lower value of E_J). The crossover frequency below which the QPS contribution (red lines) dominates over the contribution from gradient nonlinearities (blue lines) is exponentially small in the parameter $\sqrt{E_J/E_1}$. Increasing E_J further into the superconducting regime would lead to a monotonic dependence of $\omega\tau$ (not shown here). The formulas near the curves indicate the scaling of the QPS and gradient anharmonicity contributions in the regime $\omega \gg T$, and are based on Eqs. (4.34) and (4.47), respectively. The formula for the QPS contribution is the one for a clean system. In the presence of disorder, the behavior of the phase-slip contribution can be deduced from Eqs. (4.36) and (4.37), which does not modify the qualitative appearance of the plot.

regime. This seemingly contradictory behavior can be explained with the smallness of the crossover scale at which effects due to QPS set in. This frequency scale is exponentially small in the parameter $\sqrt{E_J/E_1}$. The downturn of the quality factor signaling the insulating character of the system can thus not be observed in their range of measured frequencies.

The quality factors of samples with reduced values of both K_0 and E_J/E_1 show a more or less flat behavior at intermediate frequencies and a tendency to decrease towards lower frequencies. Our theory is qualitatively consistent with the observed behavior in those devices: the phase-slip contribution dominates the frequency dependence of the quality factor in the insulating regime at low frequencies. It would be beneficial if the measurement method of Ref. [73] could be extended to lower frequencies.

The change of the behavior of the quality factor from increasing to decreasing as K_0 and E_J/E_1 are reduced is interpreted as a transition by the authors of Ref. [73]. Based on our theory presented in this thesis, we firmly believe that the observed change of the behavior is not related to the SIT. All samples are in the insulating regime and should show a decreasing quality factor at low frequencies. As mentioned above, the downturn of the quality factor occurs only at exponentially small frequencies in the regime $E_J \gg E_1$, which is below the lowest measured frequencies for the apparent superconducting samples.

We can further analyze the experimental results of the quality factor with regard to various input parameters. Let us first look at the more insulating chains. The experiment reports that the quality factor for their weakest junctions (low E_J/E_1 and large Z) is more sensitive to the parameter E_J/E_1 than to the parameter $Z \propto 1/K_0$. We can explain this observation in the following way. In these samples, the parameter K_0 determining the exponent of the power law of the QPS contribution is very small. As a result, even large changes of the order of 20% (as in the experiment) modify the exponent only marginally since the value of K_0 remains still small. On the contrary, the QPS amplitude depends exponentially on the square root of E_J/E_1 leading to a strong dependence of the quality factor with respect to this parameter.

Moreover, we compare our theory to the experimental results in low-impedance chains showing apparently superconducting behavior. Several curves of this kind are depicted in Fig. S 4 in the Supplementary Material of Ref. [73]. Due to the large value of E_J/E_1 for all devices, effects originating from QPS should be negligible in the range of measured frequencies. As expected, the quality factors of all samples grow upon lowering the frequency. Moreover, the frequency dependence of the quality factor is in accordance with our theoretical prediction ($\propto \omega^{-3}$) related to the gradient nonlinearities. Analyzing the dependence of the prefactor, we remark that the charging energy E_0 is varied particularly strongly in the experiment (factor of ~ 75), while other parameters are varied less strongly. Nevertheless, all experimental curves seem to collapse if plotted as a function of the normalized frequency ω/ω_p. Our theory, however, predicts a strong power-law dependence (E_0^3) on the charging energy E_0 for the quality factor. We propose that a different type of nonlinearity might be the origin for this behavior. Some kind of nonlinear capacitances could lead to another contribution to the quality factor with a prefactor that has a weaker dependence on the charging energy E_0. Identifying and analyzing further types of nonlinearities remains an interesting prospect for future research.

4.4 Summary of chapter 4

To conclude, we have analyzed the relaxation of plasmonic waves in JJ chains. Besides a single linear chain, we have studied two capacitively coupled chains to make contact to a recent experiment [73]. We have demonstrated that in the parameter regime where the capacitance to the ground (C_g) can

be neglected, the theory for the antisymmetric mode in the double chain is equivalent to a theory for a single chain. Such a mapping was possible since the symmetric mode is characterized by a large velocity as a consequence of the strong Coulomb interaction in this regime.

We have studied two decay mechanisms for plasmonic waves: the scattering from QPS and the interaction due to gradient nonlinearities. The former leads to a relaxation rate that scales with frequency as a power law with a non-universal exponent that is governed by the Luttinger parameter $K_0 = \sqrt{E_\mathrm{J}/E_0}$. The results for the relaxation rate due to the scattering off QPS in different parameter regimes are given by Eqs. (4.34), (4.36) and (4.37). These results are also summarized in Fig. 4.2. It is important to note here the exponential dependence of the phase-slip amplitude on the parameter $\sqrt{E_\mathrm{J}/E_1}$ leading to a strong sensitivity of the decay rate on this parameter.

The second source for the decay of plasmonic waves is the interaction of them induced by other nonlinear terms (gradient nonlinearities). As a particular example, we have studied the lowest-order anharmonicity originating from the Josephson potential. This nonlinear term yields a contribution to the relaxation rate which scales as the fourth power of frequency. As expected from the irrelevance of this nonlinearity in the renormalization group sense, this contribution to the decay rate vanishes in the zero-frequency limit. However, if the bare QPS amplitude is small, the phase-slip contribution may be subleading compared to the one from this nonlinearity in a wide frequency range.

In order to study the interplay of both decay channels, we have analyzed the product of mode frequency and lifetime, a dimensionless quantity that is expected to be proportional to the quality factor studied in the experiment of Ref. [73]. The schematic behavior of this quantity is illustrated in Fig. 4.4 in the insulating regime, $K_0 \ll 1$. Due to the exponentially small QPS amplitude in the parameter $\sqrt{E_\mathrm{J}/E_1}$, the phase-slip contribution becomes important only at very low frequencies in the regime $E_\mathrm{J} \gg E_1$. It is characterized by a non-universal power law leading to a decrease of the quality factor upon lowering the frequency. The high-frequency behavior is dominated by other nonlinear terms such as the one originating from the expansion of the Josephson potential leading to the universal ω^{-3} scaling of the quality factor. Combining both behaviors results in a non-monotonic frequency dependence of the quality factor. This behavior is qualitatively consistent with the observations in Ref. [73]. In particular, we can explain the apparent "superconducting" behavior of samples that are nominally in the insulating regime. According to our predictions, the downturn of the quality factor is visible only at lower frequencies outside the range of measured frequencies. Our theory strongly suggests that the change in the behavior of the quality factor observed in Ref. [73] is not related to the SIT. Concerning the dependence of the prefactor of the contribution from gradient nonlinearities there is a discrepancy between our prediction and the experimental results of Ref. [73]. When plotted as a function of the rescaled frequency ω/ω_p, the experimental low-impedance curves (with a large value of E_J/E_1) show a very weak dependence on the charging energy E_0. We predict, however, for the specific example of the lowest-order nonlinearity originating from the expansion of the Josephson potential, a strong dependence proportional to E_0^3. This disagreement might be explained by another type of nonlinearity with a weaker dependence on E_0. To elucidate this point, further nonlinear terms need to be identified and analyzed in a future research project.

Chapter 5

5 Relaxation of high-energy fermions in quantum wires

After the discussion of the relaxation of bosonic excitations in Josephson junction (JJ) chains in the previous chapter, we turn now to the analysis of the relaxation of fermionic excitations in quantum wires. It has been known for a long time that fermionic excitations at *low* energies are characterized by a large relaxation time in comparison to other microscopic time scales. This fact is at the heart of Landau's Fermi-liquid theory [74–76]. A Landau quasiparticle with energy ϵ above the Fermi sea has the relaxation rate (inverse lifetime) $1/\tau(\epsilon) \propto \epsilon^2/\epsilon_\mathrm{F} \ll \epsilon$ [127]. The slow relaxation of quasiparticles at low energies leads to a plenty of quantum phenomena observed in experiments on electronic systems at low temperatures, such as quantum corrections to the conductivity [77–79] and quantum Hall interferometry [22, 23].

Considering the significance of relaxation processes, they were studied in several solid state systems. As a brief selection, we mention here electrons in normal metals [80–82], Bogolyubov quasiparticles in superconductors [89] and Bose gases [83–88], electrons in 1D quantum wires [90, 91] and quantum Hall edge channels [92–97]. Most of these works concentrated on the excitations at low energies, where the relaxation is *expected* to be slow.

Recently, it was pointed out in Ref. [98] that the relaxation rate of electrons in a semiconductor nanowire becomes small again at energies much larger than the Fermi energy. By means of scanning tunneling microscopy, the decoherence rate of injected electrons was measured. In accordance with the Fermi-liquid theory, a growth of the relaxation rate at low energies was observed. However, above a certain threshold at energies much larger than the Fermi energy, the relaxation rate starts to decrease again. This means that the electrons experience a revival of their coherence at high energies. This effect was explained in Ref. [98] by the properties of the relaxation of electrons in the lowest subband of transverse quantization.

Based on the findings of Ref. [98], we can ask the questions: Is the non-monotonicity of the decay rate and the revival of the coherence a universal phenomenon? What happens if the high-energy electron is not in the lowest subband of transverse quantization? Can we find a similar behavior in higher-dimensional systems as well?

We answered these questions in Ref. [153]. In this chapter, we review these results. It is demonstrated that the non-monotonic behavior of the relaxation rate as well as the revival of the coherence of hot electrons is quite generic. To this end, we investigate various models of interacting fermions in quasi-1D multi-channel and strictly 1D wires. In order to study quasi-1D systems, it turns out to be useful to

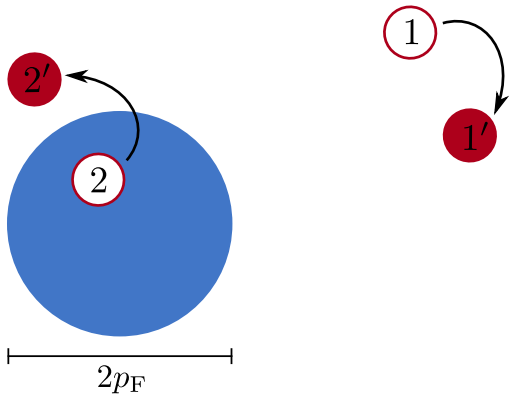

Figure 5.1: Relaxation process in higher dimensions ($D \geq 2$). A fermion with momentum $\mathbf{p}_1$ relaxes by scattering off a particle inside the isotropic Fermi sea with momentum $\mathbf{p}_2$. The momenta after the collision are denoted by $\mathbf{p}_1'$ and $\mathbf{p}_2'$.

first examine isotropic 2D and 3D systems. Under the assumption of an interaction potential decaying sufficiently fast as a function of momentum, it is shown that, regardless of the model, the relaxation rate decays in a power-law fashion as a function of the momentum p_1 of the hot electron. The rate decays as $1/p_1$ in 2D, 3D and quasi-1D systems. In strictly 1D wires, the decay is particularly strong: it scales as $1/p_1^5$. In our analysis, we concentrate on interaction potentials $V(q)$ that are characterized by a single momentum scale q_0 below which the interaction can be expanded, $V(q) = V_0(1 - q^2/q_0^2)$, and above which it is suppressed sufficiently strongly. Furthermore, we show that the non-monotonic behavior of the relaxation rate is found in the case of Coulomb interaction as well.

This chapter is structured as follows. We start in Sec. 5.1 with the discussion of interacting fermions with parabolic spectrum in 2D and 3D systems. Section 5.2 is devoted to the quasi-1D multi-channel wires with parabolic dispersion. In the first part, Sec. 5.2.1, we introduce the model of multi-channel wires, and in the subsequent Secs. 5.2.2 and 5.2.3, we analyze the cases of one and two lateral dimensions, respectively. In Sec. 5.3, we consider fermions with parabolic dispersion in a 1D wire. We compare our findings to the experiment of Ref. [98] in Sec. 5.4 before summarizing our main results in Sec. 5.5.

This chapter is based on our work in Ref. [153].

5.1 Isotropic 3D and 2D cases

Before studying the one-dimensional case, we consider the higher dimensional situation. Specifically, we investigate the decay of high-energy fermions with parabolic spectrum in $D \geq 2$ spatial dimensions. On top of a filled D-dimensional isotropic Fermi sea with Fermi momentum p_F, a fermion occupies a state with momentum $p_1 = |\mathbf{p}_1| \gg p_F$. The interaction potential is assumed to be characterized by a single momentum scale q_0. At small momenta, $q \lesssim q_0$, the interaction potential can be expanded, $V(q) \sim V_0(1 - q^2/q_0^2)$, while at high momenta, $q \gg q_0$, it is sufficiently strongly suppressed. A possible model interaction is given by an exponential decay, e. g., $V(q) = V_0 \exp\{-(q/q_0)^2\}$. Such a strong decay is, however, not necessary. We explicitly demonstrate in the end of this section that our results are valid in the case of screened Coulomb interaction in 2D and 3D as well (only power-law decay). Throughout this section we assume $q_0 \gtrsim p_F$, whereas the ratio of p_1 and q_0 can be arbitrary. An

introduction to two-particle collisions and the relaxation of fermions can be found in Sec. 2.2. The relaxation rate (inverse lifetime) of the hot fermion can be computed by means of Fermi's golden rule [cf. Sec. 2.2 and in particular Eq. (2.14)],

$$\frac{1}{\tau_{p_1}} = \frac{1}{2!}\int \mathrm{d}\mathbf{p}_2\mathrm{d}\mathbf{p}_1'\mathrm{d}\mathbf{p}_2'\,\delta\left(E_\mathrm{i}-E_\mathrm{f}\right)\delta\left(\mathbf{P}_\mathrm{i}-\mathbf{P}_\mathrm{f}\right)n_\mathrm{F}(\epsilon_2)[1-n_\mathrm{F}(\epsilon_1')][1-n_\mathrm{F}(\epsilon_2')]\left|M^{\mathbf{p}_1',\mathbf{p}_2'}_{\mathbf{p}_1,\mathbf{p}_2}\right|^2. \tag{5.1}$$

We take into account only the out-scattering rate here because we assume the additional fermion to be at high energies above the filled Fermi sea. We denote by $\mathbf{p}_1$ and $\mathbf{p}_2$ ($\mathbf{p}_1'$ and $\mathbf{p}_2'$) the momenta before (after) the collision, see Fig. 5.1. Furthermore, E_i and $\mathbf{P}_i$ (E_f and $\mathbf{P}_f$) are the total energy and total momentum before (after) the scattering. The conservation of the total energy and momentum are taken into account by the delta functions, and we use the short-hand notation $\epsilon_i \equiv \epsilon_{\mathbf{p}_i} = \mathbf{p}_i^2/2m$. The matrix element $M^{\mathbf{p}_1',\mathbf{p}_2'}_{\mathbf{p}_1,\mathbf{p}_2}$ is composed of a direct and an exchange term. For spin-polarized fermions [cf. Eq. (2.21)],

$$\left|M^{\mathbf{p}_1',\mathbf{p}_2'}_{\mathbf{p}_1,\mathbf{p}_2}\right|^2 = \Big[V(|\mathbf{p}_1-\mathbf{p}_1'|)-V(|\mathbf{p}_1-\mathbf{p}_2'|)\Big]^2, \tag{5.2}$$

while for fermions with spin, we obtain after the spin summation [cf. Eq. (2.20)]

$$\left|M^{\mathbf{p}_1',\mathbf{p}_2'}_{\mathbf{p}_1,\mathbf{p}_2}\right|^2 = \Big[V(|\mathbf{p}_1-\mathbf{p}_1'|)\Big]^2+\Big[V(|\mathbf{p}_1-\mathbf{p}_2'|)\Big]^2-V(|\mathbf{p}_1-\mathbf{p}_1'|)V(|\mathbf{p}_1-\mathbf{p}_2'|). \tag{5.3}$$

Making use of the rotational invariance, we can rewrite Eq. (5.1) as (see App. C.1)

$$\frac{1}{\tau_{p_1}} = \frac{S_{D-2}}{2p_1^{D-2}}\int_0^\infty \mathrm{d}P P^{D-1}\int_{|P/2-p_1|}^{P/2+p_1} q^{2D-3}\mathrm{d}q\int_0^\pi \mathrm{d}\varphi\,\mathrm{d}\varphi'\,\Big(\sin\varphi\sin\varphi'\Big)^{D-2}\delta\left(\epsilon_1-\frac{p_1^2}{2m}\right) \times n_\mathrm{F}(\epsilon_2)[1-n_\mathrm{F}(\epsilon_1')][1-n_\mathrm{F}(\epsilon_2')]w_q(\varphi,\varphi'). \tag{5.4}$$

We denote by S_D the volume of the D-dimensional sphere ($S_{D=0}=2$). The physical meaning of P and q in Eq. (5.4) are the total and relative momentum of the particles, $P = \left|\mathbf{p}_1+\mathbf{p}_2\right| = |\mathbf{p}_1'+\mathbf{p}_2'|$ and $2q = \left|\mathbf{p}_1-\mathbf{p}_2\right| = |\mathbf{p}_1'-\mathbf{p}_2'|$. The angle φ (φ') denotes the angle between the total and relative momentum before (after) the scattering. The energies ϵ_i and $\epsilon_{i'}$ are now expressed in terms of the integration variables,

$$2m\epsilon_{1,2} = \frac{P^2}{4}+q^2\pm Pq\cos\varphi, \tag{5.5}$$

$$2m\epsilon_{1,2}' = \frac{P^2}{4}+q^2\pm Pq\cos\varphi'. \tag{5.6}$$

The delta function in Eq. (5.4) guarantees that the momentum of the incoming high-energy fermion is p_1, leading to

$$\varphi = \varphi_0 := \arccos\frac{p_1^2-q^2-P^2/4}{Pq}. \tag{5.7}$$

The limits of the integration over q ensure that $0<\varphi_0<\pi$. The properly angle-averaged squared matrix element is given by

$$w_q(\varphi,\varphi') = S_{D-3}\int_0^\pi d\gamma\,\big(\sin\gamma\big)^{D-3}\left[V_+-V_-\right]^2 \tag{5.8}$$

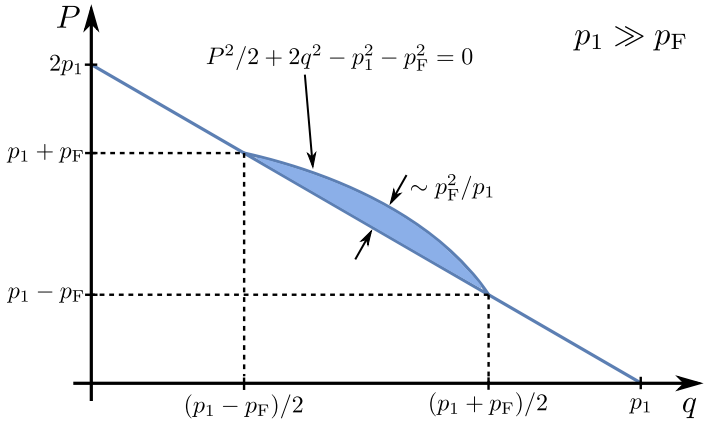

[Reprinted figure with permission from M. Bard, I. V. Protopopov, and A. D. Mirlin, Phys. Rev. B **97**, 195147 (2018), DOI: 10.1103/PhysRevB.97.195147, cf. Ref. [153]. Copyright 2018 by the American Physical Society.]

Figure 5.2: Phase space restriction in $D \geq 2$ at high energies ($p_1 \gg p_\mathrm{F}$). The distribution function $n_\mathrm{F}(p_2)$ restricts the contribution of the integrations over q and P to a small vicinity of the point $(p_1/2, p_1)$. This region is located between the line $P/2 + q = p_1$ and the ellipse $P^2/2 + 2q^2 - p_1^2 - p_\mathrm{F}^2 = 0$ (shaded area).

and

$$w_q(\varphi, \varphi') = S_{D-3} \int_0^\pi d\gamma \left(\sin\gamma\right)^{D-3} \left[V_+^2 + V_-^2 - V_+ V_-\right] \tag{5.9}$$

in the spin-polarized and spinful cases, respectively, with

$$V_\pm = V\left[q\sqrt{2\left(1 \pm \cos\varphi\cos\varphi' \pm \cos\gamma\sin\varphi\sin\varphi'\right)}\right]. \tag{5.10}$$

For $D = 2$, the integration over γ in Eqs. (5.8) and (5.9) should be regarded as a summation,

$$S_{-1} \int \frac{\mathrm{d}\gamma}{\sin\gamma} \longrightarrow \sum_{\gamma=0,\pi}. \tag{5.11}$$

Equation (5.4) can be used to compute the relaxation rate at arbitrary temperature and momentum p_1. It can be significantly simplified if $T = 0$ and $p_1 \gg p_\mathrm{F}$. In this case, the distribution function $n_\mathrm{F}(\epsilon_2)$ restricts the contribution of the integration to the region close to the point $P = p_1$, $q = p_1/2$ (cf. Fig. 5.2). In the whole integration domain, the angle φ_0 is small,

$$\varphi_0 \simeq 2\frac{\sqrt{P + 2q - 2p_1}}{\sqrt{p_1}} \lesssim \frac{p_\mathrm{F}}{p_1} \ll 1. \tag{5.12}$$

Contrary to the situation at low-energies, the distribution functions of the outgoing fermions are unimportant here since the typical momenta after the collision are large compared to the Fermi momentum. At high energies, they merely exclude almost forward scattering processes that are characterized by

$$\min(\varphi', \pi - \varphi') < \varphi_0' = \arccos\frac{p^2/4 + q^2 - p_\mathrm{F}^2}{pq} \lesssim \frac{p_\mathrm{F}}{p_1}. \tag{5.13}$$

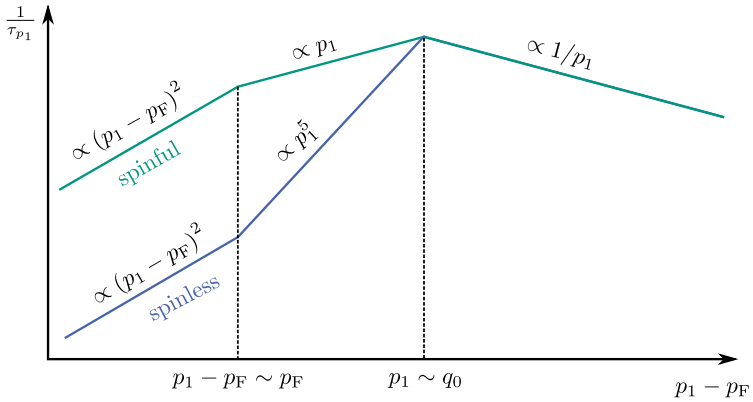

Figure 5.3: Schematic plot (on log-log scale) of the relaxation rate in 3D as a function of momentum. At large momenta, $p_1 \gg q_0$, the rate decays as $1/p_1$ [cf. Eq. (5.17)] independent of the presence of spin. In the intermediate regime, $p_F \ll p_1 \ll q_0$, the decay rate for spinful (spin-polarized) fermions behaves as p_1 (p_1^5) [cf. Eqs. (5.15) and (5.16), respectively]. In the low-energy regime (Fermi-liquid), $p_1 - p_F \ll p_F$, the rate scales as $(p_1 - p_F)^2$. Due to the Hartree-Fock cancellation, the prefactor is smaller for spinless fermions, see Eqs. (5.18) and (5.19).

Assuming $q_0 \gtrsim p_F$, the smallness of φ_0 and φ_0' justifies the decoupling of the integration over φ' in Eq. (5.4). We find

$$\frac{1}{\tau_{p_1}} \sim m p_1^{D-2} p_F^D \int_0^\pi d\varphi' \left(\sin\varphi'\right)^{D-2} w_{p_1/2}(0,\varphi'). \tag{5.14}$$

We used here the typical value of $\varphi_0 \sim p_F/p_1$ and the available area in the q-P plane, $\sim p_F^3/p_1$. The symbol "$\sim$" in Eq. (5.14) and in analogous equations below has the meaning "up to a number of order order unity". The precise value of this number is non-universal; it depends on the specific form of the interaction.

The relaxation rate depends on the relation between p_1 and q_0 as well as on the presence of spin. In the regime $p_F \ll p_1 \ll q_0$, it is possible to expand the function $w_{p_1/2}$ in powers of p_1^{-1}. In the presence of spin, the function $w_{p_1/2}$ is given by Eq. (5.9), leading to the estimate $w_{p_1/2} \sim V_0^2$, and resulting in the relaxation rate

$$\frac{1}{\tau_{p_1}} \sim m V_0^2 p_F^D p_1^{D-2}, \qquad p_F \ll p_1 \ll q_0. \tag{5.15}$$

In this case, the rate is fully determined by the available phase space. In contrast, for spin-polarized fermions in the same regime, the Hartree-Fock cancellation leads to the vanishing of the leading contribution, cf. Eq. (5.8). Hence, the relaxation rate is suppressed compared to the spinful case. We obtain

$$\frac{1}{\tau_{p_1}} \sim m V_0^2 \frac{p_F^D p_1^{D+2}}{q_0^4}, \qquad p_F \ll p_1 \ll q_0. \tag{5.16}$$

In the regime $p_F \lesssim q_0 \ll p_1$ (containing the physically most relevant case $q_0 \sim p_F$), the presence of spin is irrelevant. The squared matrix element $w_{p_1/2}(0,\varphi')$ is of the order of V_0 at $\varphi' = 0$. However, it

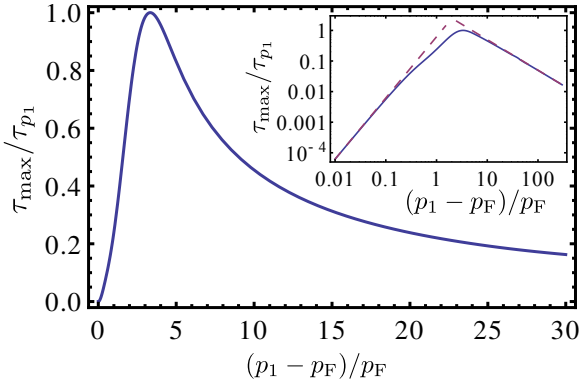

Figure 5.4: Numerical evaluation of the relaxation rate in $D = 3$, as given by Eq (5.4) with the model interaction $V(q) = V_0 \exp\{-q^2/2p_F^2\}$. The decay rate shows a non-monotonic behavior with a maximum around $p_1 \simeq 4p_F$. The rate is normalized by its maximal value $\tau_{\max}^{-1}$. Inset: The same plot in the double-log scale. The analytical results $1/\tau_{p_1} \propto (p_1 - p_F)^2$ and $1/\tau_{p_1} \propto 1/p_1$ at $p_1 - p_F \ll p_F$ and $p_1 \gg p_F$, respectively, are shown by dashed lines.

decays very quickly above $\varphi' \sim q_0/p_1$. Hence, the integration over φ' is limited by $q_0/p_1 \ll 1$, leading to

$$\frac{1}{\tau_{p_1}} \sim mV_0^2 \frac{p_F^D q_0^{D-1}}{p_1}, \qquad p_F \lesssim q_0 \ll p_1. \tag{5.17}$$

This important result demonstrates that the decay rate of hot fermions scales in a universal fashion as $1/p_1$ in any dimension $D \geq 2$.

In the low-energy limit, the decay rate scales as $1/\tau_{p_1} \propto (p_F - p_1)^2$ [127] (up to logarithmic factors in $D = 2$ [128, 129]), which is the Fermi-liquid result. For fermions with spin, we obtain

$$\frac{1}{\tau_{p_1}} \sim mV_0^2 p_F^{2D-4}(p_1 - p_F)^2, \qquad p_1 - p_F \ll p_F \lesssim q_0, \tag{5.18}$$

whereas for spin-polarized particles the Hartree-Fock cancellation leads to a smaller prefactor,

$$\frac{1}{\tau_{p_1}} \sim mV_0^2 \frac{p_F^{2D}}{q_0^4}(p_1 - p_F)^2, \qquad p_1 - p_F \ll p_F \lesssim q_0. \tag{5.19}$$

The Eqs. (5.15) - (5.19) predict a non-monotonic dependence of the relaxation rate. Figure 5.3 illustrates the behavior for $D = 3$. At low momenta, $p_1 - p_F \ll p_F$, the rate increases according to the Fermi-liquid result with different prefactors for spinless and spinful particles. Beyond the intermediate regime, $p_F \ll p_1 \ll q_0$, the decay rate decreases as $1/p_1$ irrespective of the dimensionality and the presence of spin.

The numerical evaluation of the integrations in Eq. (5.4) confirms our analytical predictions. Figure 5.4 illustrates the numerical result for the model interaction $V(q) = V_0 \exp\{-q^2/2p_F^2\}$.

Let us now ask the question whether our results remain applicable in the case of Coulomb interaction. We emphasize again that the behavior (5.17) results from the kinematics of the scattering process and

the inability of the interaction to transfer momenta larger than q_0 [see discussion before Eq. (5.17)]. Although the decay of the screened Coulomb interaction

$$V_{2\mathrm{D}}(q) = \frac{2\pi e^2}{\kappa + q}, \qquad V_{3\mathrm{D}}(q) = \frac{4\pi e^2}{\kappa^2 + q^2}, \tag{5.20}$$

is rather weak, our result (5.17) is still valid. Here, κ is the inverse screening length. Even interaction potentials $V(q)$ which behave at large momenta as $1/q^\alpha$ with $\alpha > (D-1)/2$ decay strongly enough for the result (5.17) to apply. This can be seen from looking at Eqs. (5.9) and (5.10). We observe that $w_q(0,\varphi') \sim q^{-2\alpha} \sin^{-2\alpha}(\varphi'/2)$, such that the integration in Eq. (5.14) is dominated by small $\varphi' \sim q_0/p_1$ if $\alpha > (D-1)/2$. Thus, we find the behavior (5.17) even for the rather weak power-law decay. With the help of $V_0 \sim e^2/\kappa$ in 2D, $V_0 \sim e^2/\kappa^2$ in 3D, and $q_0 \sim \kappa$, the decay rate of high-energy fermions interacting via the screened Coulomb interaction (5.20) with $\kappa \gtrsim p_\mathrm{F}$ is of the form

$$\frac{1}{\tau_{p_1}} \sim \frac{me^4}{p_1} \times \begin{cases} \dfrac{p_\mathrm{F}^2}{\kappa}, & D = 2, \\ \dfrac{p_\mathrm{F}^3}{\kappa^2}, & D = 3. \end{cases} \tag{5.21}$$

To conclude this section, we qualitatively explain the $1/p_1$ scaling of the relaxation rate of hot fermions in (5.17) and (5.21). Due to the suppression of the interaction potential at momentum transfers larger than q_0, the energy gain of the cold particle coming from the Fermi sea can be at most of the order $q_0^2/2m$. This energy transfer is associated with a momentum transfer which is almost perpendicular to $\mathbf{p}_1$. The momentum transfer in the direction of $\mathbf{p}_1$ is of the order of q_0^2/p_1. At this point, the velocity p_1/m of the hot particle entered. Consequently, the phase space is reduced by the factor $q_0/p_1 \ll 1$, giving rise to the $1/p_1$ decay of the relaxation rate. It should be noted that the specific decay as $1/p_1$ relies on the parabolic dispersion relation. However, the decay of $1/\tau$ at high energies is more general, and survives for any dispersion relation with a velocity that increases as a function of momentum.

5.2 Multi-channel quantum wires

After the detailed discussion of the relaxation processes for particles with isotropic parabolic energy dispersion in $D \geq 2$ in the previous section, we now study the relaxation in quasi-one-dimensional multi-channel quantum wires. It is shown that the non-monotonic behavior of the decay rate obtained in Sec. 5.1 is found in quasi-1D wires as well.

5.2.1 Setup

We start by introducing our model, which describes multi-channel quantum wires with 1D parabolic energy bands that are labeled by an index $\mathbf{n}$ associated with the transverse quantization,

$$\epsilon_{\mathbf{n}}(p) = \frac{p^2}{2m} + \Delta_{\mathbf{n}}. \tag{5.22}$$

We denote by p the longitudinal momentum along the wire axis (z-axis), and $\Delta_{\mathbf{n}}$ determines the bottom of the $\mathbf{n}$-th band. The Fermi sea occupies one or more low-lying bands. The Fermi momentum in the lowest band is denoted by p_F. An illustration of the band structure can be found in Fig. 5.5.

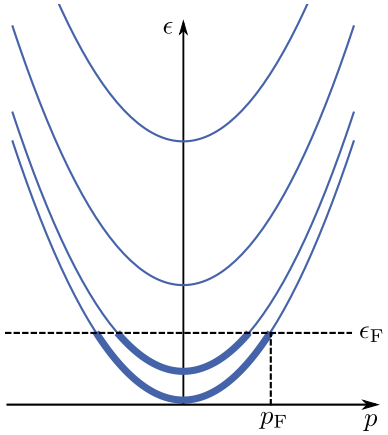

Figure 5.5: Band structure of a multi-channel wire with parabolic bands labeled by an index $\mathbf{n}$ of transverse quantization. The bold lines correspond to the occupied parts of the band structure (Fermi sea). We denote by p the longitudinal momentum and by p_F the Fermi momentum of the lowest band.

The electrons inside the wire interact via the potential $V(|\mathbf{r}|) = V(|\mathbf{r}^\perp|, z)$, which assumes the form

$$V_{\mathbf{n}_1,\mathbf{n}_2;\mathbf{n}_1',\mathbf{n}_2'}(q) \equiv \int d\mathbf{r}_1^\perp d\mathbf{r}_2^\perp V(|\mathbf{r}_1^\perp - \mathbf{r}_2^\perp|, q)\psi^*_{\mathbf{n}_1}(\mathbf{r}_1^\perp)\psi^*_{\mathbf{n}_2}(\mathbf{r}_2^\perp)\psi_{\mathbf{n}_1'}(\mathbf{r}_1^\perp)\psi_{\mathbf{n}_2'}(\mathbf{r}_2^\perp) \tag{5.23}$$

in the band representation. The wave functions of transverse quantization are denoted by $\psi_\mathbf{n}(\mathbf{r}^\perp)$, and the integration domain is the cross section of the wire.

We aim to investigate the relaxation of a hot fermion injected with some longitudinal momentum p_1 into a band with index $\mathbf{n}_1$ such that its energy is much larger than the Fermi energy, $\epsilon_{\mathbf{n}_1}(p_1) \gg \epsilon_\mathrm{F}$. To achieve this goal, we need to know the wave functions $\psi_\mathbf{n}(\mathbf{r}^\perp)$ and the positions $\Delta_\mathbf{n}$ of the energy bands. As we demonstrate below, the collision processes at high energies generate excitations of electrons into high energy bands. For this reason, the microscopic details of the wave functions of transverse quantization are of minor importance. They can be approximated by plane waves with e. g. periodic boundary conditions. In this case, the index $\mathbf{n}$ corresponds to the transverse momentum. Figure 5.6 shows two relevant setups: a 2D electron gas with finite width d (strip), where the index is an integer, $\mathbf{n} = 0, \pm 1, \ldots$, and a wire with 2D cross section (characteristic size d), where $\mathbf{n} = (n_x, n_y)$ is a 2D vector of integers.

Due to the correspondence between the band index and the transverse quantization, it follows that

$$\Delta_\mathbf{n} = \Delta_0 |\mathbf{n}|^2, \qquad \Delta_0 \sim \frac{1}{md^2}. \tag{5.24}$$

Furthermore, we demand the conservation of transverse momentum in the matrix element of the interaction ("selection rule"),

$$V_{\mathbf{n}_1,\mathbf{n}_2;\mathbf{n}_1'\mathbf{n}_2'}(q) = \frac{1}{d^{D_\perp}} V_{\mathbf{n}_1-\mathbf{n}_1'}(q)\delta_{\mathbf{n}_1+\mathbf{n}_2-\mathbf{n}_1'-\mathbf{n}_2'}, \tag{5.25}$$

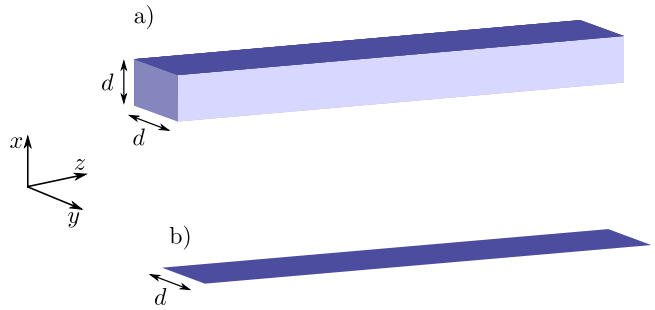

Figure 5.6: Geometry of a quasi-1D wire. a) A wire with 2D cross section of characteristic size d to investigate the crossover to 3D. b) 2D strip of finite width d to investigate the crossover to 2D.

where $D_\perp = 1, 2$ is the transverse dimensionality of the wire. Analogous to Sec. 5.1, the interaction potential is assumed to be approximately isotropic,

$$V_{\mathbf{n}}(q) \simeq V\left(Q \equiv \sqrt{q^2 + 4\pi^2|\mathbf{n}|^2/d^2}\right). \tag{5.26}$$

Furthermore, we assume that it can be expanded at small momenta,

$$V(Q) \simeq V_0\left(1 - Q^2/q_0^2\right), \qquad Q \ll q_0, \tag{5.27}$$

and is suppressed sufficiently strongly at $Q \gg q_0$. This means that the decay rate is governed by momentum transfers up to the order of q_0.

5.2.2 Quasi-1D setup with one lateral dimension

We begin with the analysis of quasi-1D wires with a strip geometry of width d, see Fig. 5.6 b). Within this model we can study the crossover to two spatial dimensions. We assume weak interactions and make use of Fermi's golden rule to compute the relaxation rate,

$$\frac{1}{\tau} = \frac{1}{2!}\int \mathrm{d}p_2\,\mathrm{d}p_1'\,\mathrm{d}p_2' \sum_{n_2,n_{1'},n_{2'}} \delta(p_1 + p_2 - p_1' - p_2')\,\delta_{n_1+n_2,n_{1'}+n_{2'}}\,\delta(\epsilon_1 + \epsilon_2 - \epsilon_{1'} - \epsilon_{2'}) \times F(\lambda_1, \lambda_2; \lambda_{1'}, \lambda_{2'}). \tag{5.28}$$

We use here the shorthand notation $\lambda_i = (n_i, p_i)$, and $\epsilon_i \equiv \epsilon_{n_i}(p_i)$ is defined in Eq. (5.22). The conservation of transverse momentum is taken into account by the Kronecker delta restricting the summation over band indices. The function F in Eq. (5.28) contains the distribution functions as well as the squared matrix element,

$$F(\lambda_1, \lambda_2; \lambda_{1'}, \lambda_{2'}) = n_{\mathrm{F}}(\epsilon_2)[1 - n_{\mathrm{F}}(\epsilon_{1'})][1 - n_{\mathrm{F}}(\epsilon_{2'})]\left|M_{\lambda_1,\lambda_2}^{\lambda_{1'},\lambda_{2'}}\right|^2. \tag{5.29}$$

In the spin-polarized case, the modulus square of the matrix element reads

$$\left|M_{\lambda_1,\lambda_2}^{\lambda_{1'},\lambda_{2'}}\right|^2 = \frac{1}{d^2}\left[V_{n_1-n_{1'}}(p_1 - p_1') - V_{n_1-n_{2'}}(p_1 - p_2')\right]^2, \tag{5.30}$$

while it is given by

$$\left|M^{\lambda_{1'},\lambda_{2'}}_{\lambda_1,\lambda_2}\right|^2 = \frac{1}{d^2}\left[\left[V_{n_1-n_{1'}}(p_1-p_1')\right]^2 + \left[V_{n_1-n_{2'}}(p_1-p_2')\right]^2 - V_{n_1-n_{1'}}(p_1-p_1')V_{n_1-n_{2'}}(p_1-p_2')\right] \quad (5.31)$$

in the spinful case. It turns out to be useful to introduce the longitudinal momentum transfer $q = p_1 - p_1'$ as an integration variable instead of p_1'. The integrations over p_2 and p_2' can be performed by exploiting the delta functions corresponding to the conservation of energy and longitudinal momentum. We find

$$\frac{1}{\tau} = \frac{m}{2}\sum_{\{n_i\}}\int\frac{\mathrm{d}q}{|q|}F_{\{n_i\}}\left(p_1, p_1-q+\frac{m\Delta_{\text{eff}}}{q}; p_1-q, p_1+\frac{m\Delta_{\text{eff}}}{q}\right), \quad (5.32)$$

where the energy Δ_{eff} is defined as

$$\Delta_{\text{eff}} = \Delta_0(n_1^2+n_2^2-n_{1'}^2-n_{2'}^2). \quad (5.33)$$

The details of the calculation of the relaxation rate can be found in App. C.2.1. We obtain the following behavior of the relaxation rate of a high-energy electron with total momentum $p_1^{\text{tot}} = \sqrt{p_1^2+p_{1\perp}^2} \gg p_{\text{F}}$ in a multi-channel wire with a 2D strip geometry:

$$\frac{1}{\tau_\epsilon} \sim \begin{cases} mV_0^2p_{\text{F}}^2, & p_{\text{F}} \ll p_1^{\text{tot}} \ll q_0, \quad \text{spinful}, \\ m^3V_0^2\dfrac{p_{\text{F}}^2}{q_0^4}\epsilon^2, & p_{\text{F}} \ll p_1^{\text{tot}} \ll q_0, \quad \text{spinless}, \\ \sqrt{m}V_0^2p_{\text{F}}^2\dfrac{q_0}{\sqrt{\epsilon}}, & p_{\text{F}} \lesssim q_0 \ll p_1^{\text{tot}};\ (p_{1\perp},p_1) \notin A, \end{cases} \quad (5.34)$$

where the transverse momentum $p_{1\perp} = n_1/d$ is introduced. This result coincides to a large extent with the findings of an isotropic 2D system analyzed in Sec. 5.1. Both results differ when the momentum is large and points almost in the transverse direction. More precisely, if the momentum $(p_1, p_{1\perp})$ is contained in the region

$$A = \left\{(p_1,p_{1\perp}) : p_{1\perp} > q_0^2d \quad \text{and} \quad \frac{p_1}{p_{1\perp}} < \frac{1}{q_0d}\right\}, \quad (5.35)$$

which is depicted in Fig. 5.7, the decay rate is suppressed more strongly compared to the isotropic 2D result. This difference is a consequence of the transverse quantization. In order to explain this effect, we consider the case in which the momentum of the initial hot electron points exactly in the transverse direction, $p_1 = 0$. This means that the electron sits at the bottom of a high-energy band. A relaxation process is thus inevitably accompanied by a transition to a lower band with a momentum transfer $\gtrsim 1/d$ in the direction of the initial momentum. In case of this momentum transfer exceeding $q_0^2/p_{1\perp}$, the corresponding process is strongly suppressed (see explanation in the end of Sec. 5.1). From this consideration, the first condition in (5.35) can be inferred. In App. C.2.1, we show that the decay rate is suppressed for a small finite momentum component in the longitudinal direction as well [second condition in (5.35)]. In region A, the relaxation rate is governed by the behavior of the interaction at large momenta, leading to a decay faster than $1/\sqrt{\epsilon}$. Since it depends on the large-momentum tail of $V(q)$, the behavior is non-universal. The continuum limit can be performed by fixing the momenta p_{F},

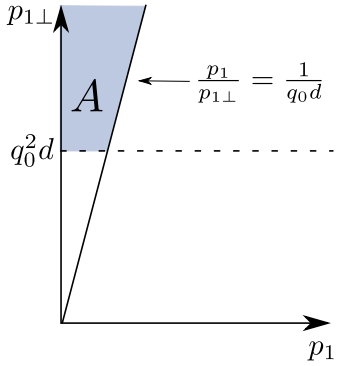

[Reprinted figure with permission from M. Bard, I. V. Protopopov, and A. D. Mirlin, Phys. Rev. B **97**, 195147 (2018), DOI: 10.1103/PhysRevB.97.195147, cf. Ref. [153]. Copyright 2018 by the American Physical Society.]

Figure 5.7: Non-universal regime (5.35) for the relaxation rate in quasi-1D wires in the plane spanned by the longitudinal (p_1) and transverse ($p_{1\perp}$) momentum. In the shaded region, the decay rate decreases as a function of energy ϵ faster than $1/\sqrt{\epsilon}$. The actual behavior is non-universal because it is determined by the large-momentum tail of $V(q)$.

q_0, p_1, $p_{1\perp}$ and sending d to infinity. In this limit, the regime (5.35) disappears and the usual behavior for a 2D isotropic Fermi sea is recovered.

Completely analogous to the case of an isotropic system in 2D, our results are valid as well for interaction potentials decaying at large q as $1/q^\alpha$ with $\alpha > 1/2$. In particular, the decay of the screened Coulomb interaction, Eq. (5.20), is fast enough to belong to this class.

5.2.3 Quasi-1D setup with two lateral dimensions

After the analysis of the geometry with one lateral dimension in the previous section, we discuss now a quasi-1D wire with two lateral dimensions depicted in Fig. 5.6 a). In contrast to the situation in Sec. 5.2.2, each electron now has two discrete indices: $n_i \to \mathbf{n}_i = (n_{i,x}, n_{i,y})$. Moreover, according to Eq. (5.25), the replacement $V_n^{(2)}(p)/d \to V_{\mathbf{n}}^{(3)}(p)/d^2$ should be performed in the matrix element.

There is one further complication here compared to the case with only one lateral dimension. Whenever the integer vectors $(\mathbf{n}_{1'} - \mathbf{n}_1)$ and $(\mathbf{n}_{1'} - \mathbf{n}_2)$ are perpendicular to each other, a "vertical" relaxation process with zero longitudinal momentum transfer is possible. As can be seen from Eq. (5.32), these processes yield a formally (logarithmically) diverging contribution to the relaxation rate. The broadening of the delta function related to the energy conservation by other processes regularizes the logarithmic singularity. As a consequence, the contribution from these processes acquires a logarithmic factor $\sim \ln(p_{1\perp}/p_\mathrm{F})$ compared to "non-singular" processes. Apart from that, due to the above mentioned orthogonality condition of the vectors $(\mathbf{n}_{1'} - \mathbf{n}_1)$ and $(\mathbf{n}_{1'} - \mathbf{n}_2)$, only few processes belong to the "singular" class. This leads to the additional factor $(p_\mathrm{F} q_0 d^2)^{-1} \ll 1$ suppressing the contribution of singular processes. This power-law suppression dominates over the logarithmic enhancement in a parametrically broad regime of momenta $p_{1\perp}$ of the hot particle, where the singular processes are subleading. The contribution from singular processes is dominating only at very large $p_{1\perp}$ (under the assumption that our model is still valid at such high energies). In this regime, the $1/p_1^\mathrm{tot}$ decay of the relaxation rate is modified, however, only by a logarithmic factor slightly enhancing the rate. Moreover, these singular processes are not allowed in more realistic models without a perfect parabolic

dispersion relation. A slight anisotropy in the energy spectrum is enough to forbid such processes. In what follows, we consider only the subclass of non-singular processes.

The details of the derivation of the relaxation rate of a high-energy electron with total momentum $p_1^{\rm tot} = \sqrt{p_1^2 + p_{1\perp}^2} \gg p_{\rm F}$ in a multi-channel wire with two lateral dimensions can be found in App. C.2.2. We state here the result:

$$\frac{1}{\tau_\epsilon} \sim \begin{cases} m^{3/2} V_0^2 p_{\rm F}^3 \sqrt{\epsilon}, & p_{\rm F} \ll p_1^{\rm tot} \ll q_0, \quad \text{spinful}, \\ m^{7/2} V_0^2 \dfrac{p_{\rm F}^3}{q_0^4} \epsilon^{5/2}, & p_{\rm F} \ll p_1^{\rm tot} \ll q_0, \quad \text{spinless}, \\ \sqrt{m} V_0^2 p_{\rm F}^3 \dfrac{q_0^2}{\sqrt{\epsilon}}, & p_{\rm F} \lesssim q_0 \ll p_1^{\rm tot}, \ (\mathbf{p}_{1\perp}, p_1) \notin A, \end{cases} \tag{5.36}$$

which is consistent with the corresponding findings for a 3D system with an isotropic Fermi sea, Sec. 5.1. As in the situation of a wire with one transverse direction (2D strip, Sec. 5.2.2), there is a region A, Eq. (5.35), where the relaxation rate is further suppressed due to the discreteness of the spectrum.

Similar to the 3D system with an isotropic Fermi sea, our results are valid as well for interaction potentials $V(q)$ with the power-law behavior $1/q^\alpha$, $\alpha > 1$, at large q. In particular, the case of the screened Coulomb interaction $V_{\rm 3D}(q)$, Eq. (5.20), is contained in this class of potentials.

5.3 One-dimensional wires and triple collisions

In Secs. 5.1 and 5.2, we have demonstrated that the non-monotonic behavior of the relaxation rate as a function of energy is a generic property in $D \geq 2$ dimensions as well as in multi-channel wires with many bands (quasi-1D). Here, we study a single-channel 1D wire with quadratic energy dispersion.

Energy and momentum conservation allow in 1D only permutations of the particles via two-particle collisions. Thus, in contrast to the situation in Secs. 5.1 and 5.2, two-particle collisions do not lead to relaxation, and one has to consider three-particle collisions. An introduction to three-particle collisions is presented in Sec. 2.3. In a number of works [18, 130, 131, 139, 150–152, 154–163], the effect of three-particle collisions was studied in the regime where the energy is much smaller than the Fermi energy. However, not much is known about the high-energy limit, $\epsilon \gg \epsilon_{\rm F}$. Recently, we investigated this case in Ref. [153]. In the following, we review these results.

Fermi's golden rule assumes the form

$$\frac{1}{\tau_{p_1}} = \frac{1}{2!3!} \int \mathrm{d}p_2 \mathrm{d}p_3 \mathrm{d}p_1' \mathrm{d}p_2' \mathrm{d}p_3' \, \delta\left(E_{\rm i} - E_{\rm f}\right) \delta\left(P_i - P_f\right) n_{\rm F}(\epsilon_2) n_{\rm F}(\epsilon_3) \times [1 - n_{\rm F}(\epsilon_1')][1 - n_{\rm F}(\epsilon_2')][1 - n_{\rm F}(\epsilon_3')] \left| M_{p_1,p_2,p_3}^{p_1',p_2',p_3'} \right|^2 \tag{5.37}$$

in the case of three-particle collisions [see also Eq. (5.1) and notations therein]. We denote by $M_{p_1,p_2,p_3}^{p_1',p_2',p_3'}$ the matrix element for triple collisions. For spinful fermions, the spin summation in the symbol $\left| M_{p_1,p_2,p_3}^{p_1',p_2',p_3'} \right|^2$ is implied implicitly. The actual form of the matrix element is discussed below.

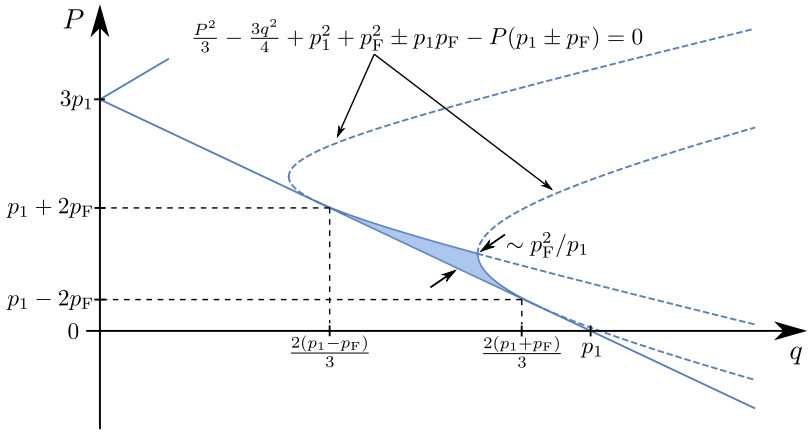

[Reprinted figure with permission from M. Bard, I. V. Protopopov, and A. D. Mirlin, Phys. Rev. B **97**, 195147 (2018), DOI: 10.1103/PhysRevB.97.195147, cf. Ref. [153]. Copyright 2018 by the American Physical Society.]

Figure 5.8: Kinematics of 1D triple collisions in the q-P plane. The Fermi functions $n_F(\epsilon_2)$ and $n_F(\epsilon_3)$ restrict the contribution of the integrations over q and P to the close vicinity of the point $(2p_1/3, p_1)$ for large momenta $p_1 \gg p_F$. This region is illustrated by the shaded area between the two hyperbolas and the line $P/3 + q = p_1$.

We can conveniently take into account the momentum and energy conservation by the parametrization

$$p_k = \frac{P}{3} + q\cos\left[\varphi + \frac{2\pi(k-1)}{3}\right], \quad k = 1,2,3, \tag{5.38}$$

$$p'_k = \frac{P}{3} + q\cos\left[\varphi' + \frac{2\pi(k-1)}{3}\right], \quad k = 1,2,3, \tag{5.39}$$

of the momenta [152, 157]. Here, $-\infty < P < \infty$ has the meaning of the total momentum of the particles, whereas $q \geq 0$ corresponds to the relative momentum in the case of two-particle processes, and is related to the total energy via

$$E_i = E_f = \frac{P^2}{6m} + \frac{3q^2}{4m}. \tag{5.40}$$

In terms of these variables, we can recast the relaxation rate in the form [see also Eq. (5.4) of Sec. 5.1]

$$\frac{1}{\tau_{p_1}} = \frac{m}{2}\int_{-\infty}^{\infty} dP \int_{|P/3-p_1|}^{\infty} q\,dq \int_{-\pi}^{\pi} d\varphi\, d\varphi'\, \delta\left[p_1 - p_1(P,q,\varphi)\right] n_F(\epsilon_2) n_F(\epsilon_3) \times [1-n_F(\epsilon'_1)][1-n_F(\epsilon'_2)][1-n_F(\epsilon'_3)] w_q(\varphi,\varphi'). \tag{5.41}$$

The function $w_q(\varphi,\varphi')$ is the modulus squared of the three-particle matrix element, $\left|M^{p'_1,p'_2,p'_3}_{p_1,p_2,p_3}\right|^2$, evaluated on the mass shell, and $p_1(P,q,\varphi)$ is defined by Eq. (5.38).

In the analysis of Eq. (5.41), we can largely follow the similar procedure described in Sec. 5.1. As illustrated in Fig. 5.8, the Fermi distributions $n_F(\epsilon_2)$ and $n_F(\epsilon_3)$ only yield a contribution in the

integrations over P and q in the vicinity of the point $(q = 2p_1/3, P = p_1)$ provided that $p_1 \gg p_\mathrm{F}$. The angle φ is fixed by the delta function to

$$\varphi_0 = \pm \arccos \frac{p_1 - P/3}{q}, \qquad |\varphi_0| \lesssim \frac{p_\mathrm{F}}{p_1}. \tag{5.42}$$

In contrast to the low-energy regime, the Fermi functions corresponding to the outgoing particles are irrelevant. This is completely analogous to the higher-dimensional cases and assumes only that the interaction potential is able to transfer momenta of the order of p_F. Therefore, Eq. (5.41) can be simplified to

$$\frac{1}{\tau_{p_1}} \sim m p_\mathrm{F}^2 \int_{-\pi}^{\pi} d\varphi' w_{2p_1/3}\left(\varphi \sim \frac{p_\mathrm{F}}{p_1}, \varphi'\right). \tag{5.43}$$

So far we took into account only the kinematics of the triple-collision processes. In order to proceed, we need to analyze the matrix element $M^{p_1',p_2',p_3'}_{p_1,p_2,p_3}$. The matrix element for three-particle processes can be derived in the second-order perturbation theory of the two-body interaction [131, 139, 157, 158]. For spin-polarized particles it can be obtained from the vacuum expectation value

$$M^{p_1',p_2',p_3'}_{p_1,p_2,p_3} = \left\langle a_{p_3} a_{p_2} a_{p_1} \middle| \hat{V} \frac{1}{E - \hat{\mathcal{H}}_0 + i0} \hat{V} \middle| a^\dagger_{p_1} a^\dagger_{p_2} a^\dagger_{p_3} \right\rangle, \tag{5.44}$$

where $\hat{\mathcal{H}}_0$ and $\hat{V}$ denote the free and interaction parts of the Hamiltonian, respectively. In Sec. 2.3, we have demonstrated that Eq. (5.44) can be recast in the form

$$M^{p_1',p_2',p_3'}_{p_1,p_2,p_3} = M_q(\varphi,\varphi') = \frac{4m}{3q^2} \frac{\sum_{j,k=0}^{2} \Gamma_q\left(\varphi + \frac{2\pi k}{3}, \varphi' + \frac{2\pi j}{3}\right)\left[\cos\left(\varphi + \frac{2\pi k}{3}\right) - \cos\left(\varphi' + \frac{2\pi j}{3}\right)\right]}{\cos 3\varphi - \cos 3\varphi'}, \tag{5.45}$$

with

$$\Gamma_q(\varphi,\varphi') = [V(q_{10}) - V(q_{20})][V(q_{01}) - V(q_{02})] - 2V(q_{12})V(q_{21}) + 2V(q_{11})V(q_{22}). \tag{5.46}$$

Here, we use the shorthand notation

$$q_{kj} = q\left[\cos\left(\varphi + \frac{2\pi k}{3}\right) - \cos\left(\varphi' + \frac{2\pi j}{3}\right)\right]. \tag{5.47}$$

for the individual momentum transfers in the collision. Due to the indistinguishability of the fermions, the matrix element $M_q(\varphi,\varphi')$ is an antiperiodic function of both angles with period $2\pi/3$. The typical scaling of the energy denominators in Eq. (5.44) leads to the factor $1/q^2$, whereas the denominator $\cos 3\varphi - \cos 3\varphi'$ reflects the fact that the energy denominators become small for special constellations with $\varphi = \varphi' \mod 2\pi/3$. However, exploiting the symmetry of the function $\Gamma_q(\varphi,\varphi')$ under the exchange of φ and φ', it can be shown that the zero of the denominator in Eq. (5.45) does not introduce a pole, and the matrix element $M_q(\varphi,\varphi')$ is an analytic function of the angles φ and φ'.

A detailed analysis of Eq. (5.45) reveals that for $q \gg q_0 \gtrsim p_\mathrm{F}$, the function $M_q(\varphi \sim p_\mathrm{F}/q, \varphi')$ is of the order of $m p_\mathrm{F} V_0^2/q_0 q^2$ for $\varphi' \lesssim q_0/q$, while it is strongly suppressed for $\varphi' > q_0/q$ (up to the periodicity mentioned above). More precisely, for fixed $\tilde{\varphi}$ and $\tilde{\varphi}'$ and $q \gg q_0$, the matrix element scales according to

$$M_q\left(q_0\tilde{\varphi}/q, q_0\tilde{\varphi}'/q\right) = \frac{4m}{9q^2}\left[V^2(q_-) + V(0)(V(q_-) - q_- V'(q_-))\right] - \langle q_- \to q_+ \rangle, \tag{5.48}$$

where $q_\pm = \sqrt{3}q_0(\tilde{\varphi} \pm \tilde{\varphi}')/2$ and V' denotes the derivative of the interaction potential with respect to momentum. In the derivation of Eq. (5.48), we do not take into account the terms with a momentum transfer of the order of q since they are strongly suppressed. As can be seen from Eq. (5.48), the $1/q^2$ behavior of the matrix element which is already there in Eq. (5.45) for generic values of the angles φ and φ' is still present in the regime φ, $\varphi' \lesssim q_0/q$, where the energy denominators are of the order of q_0^2/m only. This can be explained by the involved cancellations of different collision processes in Eq. (5.45).

In the regime $\tilde{\varphi}, \tilde{\varphi}' \lesssim 1$, the matrix element in Eq.(5.48) possesses the scaling

$$M_q\left(q_0\tilde{\varphi}/q, q_0\tilde{\varphi}'/q\right) \sim \frac{mV_0^2}{q^2}\tilde{\varphi}\tilde{\varphi}' = \frac{mV_0^2}{q_0^2}\varphi\varphi'. \tag{5.49}$$

Using $\tilde{\varphi} \sim p_\mathrm{F}/q_0 \lesssim 1$ in Eq. (5.49) and inserting this estimate into Eq. (5.43), we find

$$\frac{1}{\tau_{p_1}} \sim \frac{m^3 p_\mathrm{F}^4 V_0^4}{q_0 p_1^5}, \qquad p_1 \gg q_0 \gtrsim p_\mathrm{F} \quad \text{(spinless)}. \tag{5.50}$$

Equation (5.50) is one of the main results of the present section. We find that the relaxation rate for spinless fermions at large momenta, $p_1 \gg q_0$, scales as a power-law, $1/\tau_{p_1} \propto p_1^{-5}$. We assumed here that the characteristic momentum scale of the interaction potential is larger than the Fermi momentum, $q_0 \gtrsim p_\mathrm{F}$. This scaling can be compared to the higher-dimensional result, Eq. (5.17). As in the higher-dimensional case, the reduction of the phase space by the inability of the interaction to transfer momenta larger than q_0 leads to the factor $1/p_1$. On top of that, in the 1D single-channel case, the partial cancellations between direct and exchange terms in the three-particle matrix element result in an additional factor $1/p_1^4$.

Let us now study the intermediate regime, where the momentum of the hot fermion (p_1) is larger than the Fermi momentum but smaller than the characteristic momentum scale q_0. In this regime, the interaction potential $V(q)$ can be expanded to fourth order leading to the squared matrix element

$$w_q(\varphi, \varphi') \sim \frac{m^2 V_0^4 q^{12} \sin^2(3\varphi)\sin^2(3\varphi')}{q_0^{16}}. \tag{5.51}$$

Performing the integration over φ' in Eq. (5.43) and employing the estimates $q \sim 2p_1/3$ and $\varphi \sim p_\mathrm{F}/p_1$, we arrive at

$$\frac{1}{\tau_{p_1}} \sim \frac{m^3 p_\mathrm{F}^4 V_0^4}{q_0^{16}} p_1^{10}, \qquad p_\mathrm{F} \ll p_1 \ll q_0 \quad \text{(spinless)}. \tag{5.52}$$

The regime at energies much smaller than the Fermi energy is analyzed in App. C.3. We obtain the scaling

$$\frac{1}{\tau_{p_1}} \sim \frac{m^3 p_\mathrm{F}^6 V_0^4}{q_0^{16}} (p_1 - p_\mathrm{F})^8, \quad p_1 - p_\mathrm{F} \ll p_\mathrm{F} \ll q_0, \qquad \text{(spinless)}, \tag{5.53}$$

which reproduces the result found in Ref. [131] in the situation in which the Fermi momentum is of the same order as the characteristic momentum of the interaction q_0.

In the case of spinful fermions, the matrix element is given by the generalization of Eq. (5.44), cf. Sec. 2.3. Performing the spin summation and parametrizing the momenta according to Eqs. (5.38) and (5.39), the modulus squared matrix element is of a similar form as Eq. (5.45). Unlike the situation in the spinless case, non-integrable poles emerge in the squared matrix element at $\varphi' = \varphi \mod 2\pi/3$. At zero temperature, however, the Fermi distributions of the outgoing particles exclude the region close

to these singularities with a characteristic width of the order of p_F/p_1. At finite temperature, the naive expression for the matrix element needs to be regularized. In Ref. [139] it is demonstrated that the singularity emerges as a consequence of two consecutive two-particle collisions which are separated by an infinite time. The authors of Ref. [139] demonstrate that a proper subtraction of these double-counted two-particle processes yields a finite relaxation rate. For our purposes, such a regularization scheme is not needed since we limit ourselves to zero temperature.

In the high-energy limit, $p_1 \gg q_0$, all the terms in the transition probability w_q with momentum transfers q that are of the order of p_1 can be omitted. In the range of small angles, $\varphi < p_\mathrm{F}/p_1$ and $\varphi' < q_0/p_1$, the transition amplitude can be brought to the simplified form

$$w_q(\varphi,\varphi') \simeq 2m^2V_0^2\left(V_0''\right)^2\left[\varphi^4 + 14\varphi^2\left(\varphi'\right)^2 + \left(\varphi'\right)^4\right]. \tag{5.54}$$

Here, the singularity at $\varphi = \varphi'$ does not show up since all singular terms contain the interaction potential with a large momentum transfer of the order of p_1. The omitted terms yield only a small correction because we assume the potential to decay sufficiently fast at large momentum transfers, and the singular points are outside the integration domain (see above). Hence, it is justified to neglect them in Eq. (5.54). The squared matrix element is strongly suppressed for values of the angle φ' beyond q_0/p_1 (modulo $2\pi/3$). A comparison of Eqs. (5.54) and (5.49) shows that the presence of spin solely leads to the additional factor $(\varphi'/\varphi)^2 \sim (q_0/p_\mathrm{F})^2$. The scaling with the momentum p_1 is not modified. Correspondingly, the relaxation rate is enhanced compared to the spin-polarized case but possesses the same scaling with p_1,

$$\frac{1}{\tau_{p_1}} \sim \frac{m^3p_\mathrm{F}^2q_0V_0^4}{p_1^5}, \qquad p_1 \gg q_0 \gg p_\mathrm{F} \quad \text{(spinful)}. \tag{5.55}$$

In the intermediate regime, where the momentum p_1 is much larger than the Fermi momentum p_F but smaller than the momentum scale q_0 of the interaction potential, all momentum transfers are small compared to q_0. It is thus legitimate to expand the interaction potential $V(q)$ to second order leading to the squared matrix element

$$w_q(\varphi,\varphi') \sim \frac{m^2V_0^4}{q_0^4}f(\varphi,\varphi') \tag{5.56}$$

with a function $f(\varphi,\varphi')$ that does not depend on q and has second order poles at $\varphi = \varphi' \mod 2\pi/3$. As discussed above [see paragraph below Eq. (5.53)], those poles are not contained in the integration domain of φ' at zero temperature. The Fermi functions of the outgoing particles exclude the singular points with a typical distance of the order of p_F/p_1. With these ingredients we find

$$\frac{1}{\tau_{p_1}} \sim \frac{m^3p_\mathrm{F}V_0^4}{q_0^4}p_1, \qquad p_\mathrm{F} \ll p_1 \ll q_0 \quad \text{(spinful)}. \tag{5.57}$$

The fact that the scalings (5.55) and (5.57) do not match at $p_1 = q_0$ is related to the neglect of the terms with poles in φ' and a large momentum transfer in the interaction potential in the derivation of Eq. (5.55) [cf. discussion below Eq. (5.54)]. As a consequence, there is another intermediate regime connecting the scalings (5.55) and (5.57). The boundaries of this regime are non-universal since they depend on the large-momentum tail of $V(q)$.

The analysis of the low-energy limit for spinful fermions is presented in App. C.3. The result reads

$$\frac{1}{\tau_{p_1}} \sim \frac{m^3V_0^4}{q_0^4}(p_1 - p_\mathrm{F})^2, \quad p_1 - p_\mathrm{F} \ll p_\mathrm{F} \ll q_0 \quad \text{(spinful)}. \tag{5.58}$$

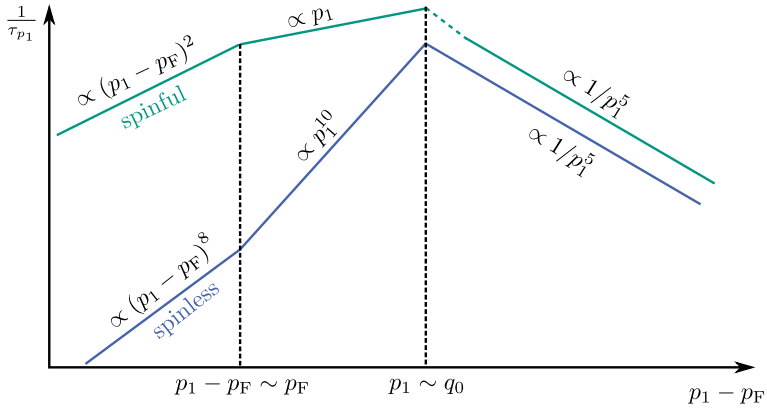

Figure 5.9: Schematic illustration of the relaxation rate in 1D on the double-log scale for spinless and spinful fermions. In the low-energy regime, the relaxation rate is given by Eqs. (5.58) and (5.53) for spinful and spinless fermions, respectively. In the latter case, the rate is strongly suppressed due to the Hartree-Fock cancellation. At intermediate momenta, $p_F \ll p_1 \ll q_0$, the rate increases as p_1 [cf. Eq. (5.57)] for spinful and as p_1^{10} [cf. Eq. (5.52)] for spin-polarized fermions. In the high-energy regime, $p_1 \gg q_0$, the relaxation rate behaves as $1/p_1^5$ in both cases. The prefactor for spin-polarized fermions is, however, reduced by the factor p_F^2/q_0^2 compared to spinful case, cf. Eqs. (5.50) and (5.55), respectively. For spinful fermions there is a narrow non-universal regime near $p_1 \sim q_0$ (dashed line).

We can compare this result to the one of Ref. [132] for the case of unscreened Coulomb interaction. The scaling law found in Ref. [132] agrees with our result (5.58) besides logarithmic factors that are related to the Coulomb interaction. We discuss the effect of Coulomb interaction below. Note that the energy scaling of the relaxation rate is the same as for a standard Fermi liquid. Of course, for a weak interaction V_0, the prefactor is strongly reduced compared to the Fermi-liquid result since in 1D two-particle processes do not contribute to relaxation.

Figure 5.9 illustrates the momentum dependence of the relaxation rate in 1D for spinful and spin-polarized fermions. It shows that the non-monotonicity of the relaxation rate as well as the regain of coherence at high energies is not only found in higher dimensions but survives also in strictly 1D systems.

Figure 5.10 presents the results of the numerical evaluation of the integrations in Eq. (5.41) for spin-polarized fermions in 1D. The model interaction $V(q) = \exp(-q^2/p_F^2)$ with a characteristic scale q_0 equal to the Fermi momentum p_F was used. Our analytical results predict in the low-energy regime, $p_1 - p_F \ll p_F$, the $(p_1 - p_F)^8$ scaling, and at $p_1 \gg p_F$ the p_1^{-5} scaling of the relaxation rate [see Eqs. (5.53) and (5.50), respectively]. Our analytical predictions agree very well with these numerical results. It is interesting to note that the relaxation rate possesses a local minimum in the crossover regime around $p_1 = 3p_F$.

Coulomb interaction Let us now turn to the discussion of the Coulomb interaction in 1D. Surprisingly, the three-particle matrix element (5.45) for spinless fermions vanishes for pure Coulomb interaction, $V(q) = e^2 \ln 1/a|q|$ [157]. This result is unexpected since the model of spinless fermions in-

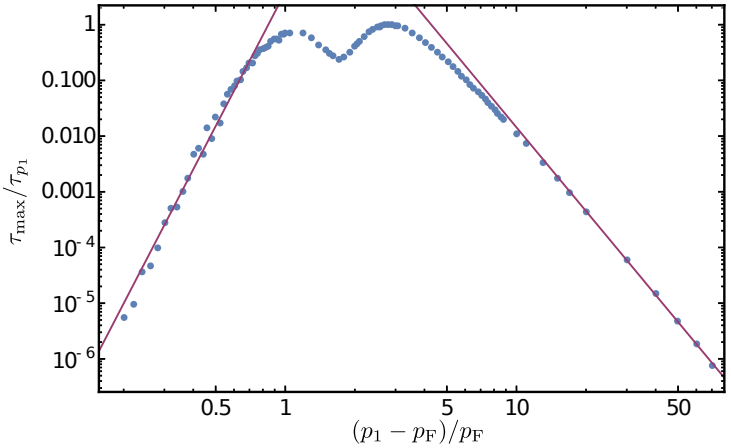

Figure 5.10: Relaxation rate $1/\tau_{p_1}$ for spinless fermions in 1D on the log-log scale. The result was obtained by a numerical evaluation of Eq. (5.41) using the model interaction $V(q) = \exp(-q^2/p_F^2)$, which corresponds to $q_0 = p_F$. Introducing a small temperature, $T/\epsilon_F = 0.01$, smeared the Fermi-distributions. The low- and high-energy asymptotes, Eqs. (5.53) and (5.50), are plotted as straight lines.

teracting via the 1D Coulomb interaction is not integrable [157]. Hence, we introduce a short-distance cutoff for the 1D Coulomb interaction, $d \equiv 1/q_0$, which corresponds to the finite width of the 1D channel, resulting in the form

$$V_{1D}(q) = e^2 \int \mathrm{d}x\, e^{iqx} \frac{1}{\sqrt{x^2 + 1/q_0^2}} = 2e^2 K_0(|q|/q_0) \tag{5.59}$$

for the Coulomb interaction in momentum space. Here, K_0 denotes the modified Bessel function of the second kind. In the limit $q \gg q_0$, the interaction potential (5.59) decays exponentially. In this respect, it belongs to the class of interactions studied in the rest of this section. However, the low-momentum behavior is different. Nevertheless, for spinless fermions, the form of the three-particle matrix element, Eq. (5.48), stays the same apart from the replacement of the divergent constant $V(0)$ by

$$V\left[\frac{q_0^2}{2q}\left(\tilde{\varphi}^2 - (\tilde{\varphi}')^2\right)\right] \simeq -2e^2 \ln \frac{q_0 \left|\tilde{\varphi}^2 - (\tilde{\varphi}')^2\right|}{q}. \tag{5.60}$$

In the regime $\tilde{\varphi}, \tilde{\varphi}' \lesssim 1$, we obtain

$$M_q\left(q_0\tilde{\varphi}/q, q_0\tilde{\varphi}'/q\right) \sim \frac{me^4}{q^2} \ln\frac{q}{q_0} \ln\left|\frac{\tilde{\varphi} - \tilde{\varphi}'}{\tilde{\varphi} + \tilde{\varphi}'}\right|, \quad q \gg q_0. \tag{5.61}$$

Using the expression (5.43), we find the scaling of the relaxation rate at high energies,

$$\frac{1}{\tau_{p_1}} \sim \frac{m^3 p_F^3 e^8 \ln^2 p_1/q_0}{p_1^5}, \qquad p_1 \gg q_0 \gtrsim p_F \quad \text{(spinless)}. \tag{5.62}$$

As a result, we observe that the singular behavior of the Coulomb interaction potential enhances the scattering rate in this regime compared to the previous result, Eq. (5.50), by the factor $(q_0/p_\mathrm{F}) \ln^2 p_1/q_0$. The power-law scaling as $1/p_1^5$ is, however, unchanged.

If the momentum of the incident particle is smaller than the momentum scale of the interaction, $p_1 \lesssim q_0$, the Coulomb potential (5.59) can be approximated by

$$V_\mathrm{1D}(q) \simeq e^2 \left(1 + \frac{q^2}{4q_0^2}\right) \ln \frac{q_0}{|q|}. \tag{5.63}$$

The dominant behavior of the matrix element for triple collisions, Eq. (5.45), is given by [157]

$$M_q(\varphi, \varphi') \sim \frac{me^4 \ln q/q_0}{q_0^2} \sum_{k=1}^{3} \frac{\ln\left|\sin\frac{\varphi-\varphi'+2\pi k/3}{2}\right|}{1 + 2\cos\left(\varphi - \varphi' + 2\pi k/3\right)} - \left\langle \varphi' \to -\varphi' \right\rangle. \tag{5.64}$$

The main contribution to the decay rate at $p_1 \ll q_0$ still originates from the regime of small angles φ' in the integration in Eq. (5.43). The expression for the matrix element (5.64) can be simplified in this regime to the form [see also Eq. (5.61)]

$$M_q\left(\varphi, \varphi'\right) \sim \frac{me^4}{q_0^2} \ln \frac{q}{q_0} \ln \left|\frac{\varphi - \varphi'}{\varphi + \varphi'}\right|, \quad q \ll q_0. \tag{5.65}$$

This leads to the behavior

$$\frac{1}{\tau_{p_1}} \sim \frac{m^3 p_\mathrm{F}^3 e^8 \ln^2 p_1/q_0}{q_0^4 p_1}, \quad p_\mathrm{F} \ll p_1 \ll q_0 \quad \text{(spinless)} \tag{5.66}$$

of the decay rate.

In the low-energy regime, we translate the result of Ref. [157] to our notations:

$$\frac{1}{\tau_{p_1}} \sim \frac{m^3 e^8 \ln^2 p_\mathrm{F}/q_0}{q_0^4 p_\mathrm{F}^2} (p_1 - p_\mathrm{F})^4, \quad p_1 - p_\mathrm{F} \ll p_\mathrm{F} \ll q_0, \quad \text{(spinless)}. \tag{5.67}$$

Compared to the corresponding result for a short-range interaction, Eq. (5.53), a power-law with a smaller power is found.

After the analysis of the relaxation of spinless fermions interacting via Coulomb interaction, we now discuss spinful fermions with Coulomb interaction. Completely analogous to the situation of a short-range potential, in the regime $p_1 \gg q_0 \gg p_\mathrm{F}$, the main contribution comes from small angles, $\varphi, \varphi' \lesssim q_0/q$. Moreover, terms in the squared matrix element $w_q(\varphi, \varphi')$ containing the interaction potential with a large momentum transfer of the order of p_1 can be omitted. We can thus approximate the squared matrix element by

$$w_q\left(q_0\tilde{\varphi}/q, q_0\tilde{\varphi}'/q\right) \sim \frac{m^2 e^8 \ln^2 q/q_0}{q^4} \Big\{ \Big[V_\mathrm{1D}(q_+) - q_+ V_\mathrm{1D}'(q_+) - V_\mathrm{1D}(q_-) + q_- V_\mathrm{1D}'(q_-)\Big]^2 + \Big[V_\mathrm{1D}(q_+) - q_+ V_\mathrm{1D}'(q_+)\Big]\Big[V_\mathrm{1D}(q_-) - q_- V_\mathrm{1D}'(q_-)\Big] \Big\}, \tag{5.68}$$

where $q_\pm = \sqrt{3}q_0(\tilde{\varphi} \pm \tilde{\varphi}')/2$ and the interaction potential V_{1D} is given by Eq. (5.59). Just as for a short-range interaction, the squared matrix element (5.68) does not possess any poles. Making use of $\tilde{\varphi} \sim p_\mathrm{F}/q_0 \ll 1$ in Eq. (5.68) and employing Eq. 5.43, we obtain

$$\frac{1}{\tau_{p_1}} \sim \frac{m^3 p_\mathrm{F}^2 q_0 e^8 \ln^2 p_1/q_0}{p_1^5}, \qquad p_1 \gg q_0 \gtrsim p_\mathrm{F} \quad \text{(spinful)}. \tag{5.69}$$

At lower momenta of the incident particle, $p_\mathrm{F} \ll p_1 \ll q_0$, the Coulomb interaction (5.59) can be approximated by

$$V_{1\mathrm{D}}(q) \simeq e^2 \ln \frac{q_0}{|q|}, \tag{5.70}$$

leading to

$$w_q(\varphi, \varphi') \sim \frac{m^2 e^8 \ln^2 q/q_0}{q^4(\cos 3\varphi - \cos 3\varphi')^2} \left[\sum_{j=0}^{2} \sin\left(\frac{\varphi+\varphi'}{2} + \frac{2\pi j}{3}\right) \ln \left| \sin\left(\frac{\varphi+\varphi'}{2} + \frac{2\pi j}{3}\right) \right| \right]^2 + \left\langle \varphi' \to -\varphi' \right\rangle. \tag{5.71}$$

We keep here only the leading behavior of the squared matrix element given by the large factor $\ln q_0/q$. In the regime of small φ and φ', the expression in Eq. (5.71) can be simplified,

$$w_q(\varphi, \varphi') \sim \frac{m^2 e^8 \ln^2 q/q_0}{q^4} \left[\frac{\ln^2 |\varphi - \varphi'|}{(\varphi+\varphi')^2} + \left\langle \varphi' \to -\varphi' \right\rangle \right]. \tag{5.72}$$

The divergence at $\varphi' = \varphi$ in the integration in Eq. (5.43) is cut off at $\varphi' - \varphi \sim p_\mathrm{F}/p_1$ [see the discussion in the paragraph below Eq. (5.53)]. Evaluating the integral, we find

$$\frac{1}{\tau_{p_1}} \sim \frac{m^3 e^8 p_\mathrm{F}}{p_1^3} \ln^2 \frac{p_1}{q_0} \ln^2 \frac{p_\mathrm{F}}{p_1}, \quad p_\mathrm{F} \ll p_1 \ll q_0, \quad \text{(spinful)}. \tag{5.73}$$

The limit of low energies for spinful fermions interacting via unscreened Coulomb interaction, Eq. (5.70), is analyzed in Ref. [132]. Adapted to our notations, the result is

$$\frac{1}{\tau_{p_1}} \sim \frac{m^3 e^8 \ln^2 \frac{q_0}{p_\mathrm{F}} \ln^2 \frac{p_1 - p_\mathrm{F}}{p_\mathrm{F}}}{p_\mathrm{F}^4} (p_1 - p_\mathrm{F})^2, \quad p_1 - p_\mathrm{F} \ll p_\mathrm{F} \ll q_0 \quad \text{(spinful)}. \tag{5.74}$$

Compared to the case of a short-range interaction potential, Eq. (5.58), we find the same leading behavior $\sim (p_1 - p_\mathrm{F})^2$. This scaling originates from the phase space contribution $\sim (p_1 - p_\mathrm{F})^4$ together with the strongly enhanced transition probability which yields a factor $(p_1 - p_\mathrm{F})^{-2}$ (see App. C.3).

Looking at Eqs. (5.62), (5.66) and (5.67) for spinless, and at Eqs. (5.69), (5.73) and (5.74) for spinful fermions, we observe that the relaxation rate shows non-monotonic behavior for the case of the Coulomb interaction (5.59) in 1D systems as well. In the case of spin-polarized fermions, the relaxation rate grows as $(p_1 - p_\mathrm{F})^4$ in the low-energy regime but then decays as $1/p_1$, and eventually as $1/p_1^5$ at high energies. For spinful fermions, $1/\tau$ grows at low momenta as $(p_1 - p_\mathrm{F})^2$, then decays as $1/p_1^3$ and ultimately as $1/p_1^5$. Certainly, in a real physical wire, the strictly 1D behavior is found only for energies of the hot fermion that are below the bottom of the second subband.

Completely analogous to the higher dimensional case (see a discussion in the end of Sec. 5.1), the actual $1/p_1^5$ behavior of the relaxation rate is related to the specific form of the energy spectrum. However, the decay of the relaxation rate at high energies is a general feature of all dispersion relations with a velocity that is increasing with momentum.

5.4 Comparison to experiment

We can compare our results to the experimental findings of Ref. [98]. By means of scanning tunneling microscopy (STM), the authors of Ref. [98] measured the phase coherence length L_φ as well as the phase coherence time as a function of energy for a multi-band wire. Details of the experiment are discussed in Sec. 2.4. In this paper, it is found (see Fig. 2.2 of this thesis or Fig. 2 of Ref. [98]) that near the Fermi energy the phase coherence length is about 70 nm, then decreases rapidly to a minimum of roughly 20 nm at around 80 meV above the Fermi energy. Upon further increasing the energy, the coherence length grows again. At the highest measured energy of 330 meV, shown in Fig. 2.2 a) (Fig. 2 (b) of Ref. [98]), the decay of the oscillations is not visible on the length scale of 40 nm, hence implying a coherence length $L_\varphi \gtrsim 100\,\text{nm}$. This data point is not shown in Fig. 2.2 b) (Fig. 2 (c) of Ref. [98]). Taking into account this data point would suggest an even stronger decay of L_φ at high energies.

Within our theory, we find a $1/p$ scaling of the decay rate $1/\tau$ in the large-momentum limit for multi-channel wires with parabolic dispersion. The associated mean free path is $l = v\tau$, where the velocity is $v = p/m$. As a result, we find that the mean free path induced by electron-electron interaction behaves linearly as a function of energy ϵ for hot electrons in a multi-channel wire. Under the assumption that the leading contribution to the decay of the coherent oscillations measured via STM is determined by the relaxation due to electron-electron interaction, we get the same behavior for the coherence length, $L_\varphi \propto \epsilon$. This result agrees well with the observations of Ref. [98]. As discussed above, the coherence length increases from $\simeq 20$ nm to $\simeq 100$ nm when the energy is increased from 80 meV to 330 meV. On the other hand, we should note that our model does not incorporate the specific dispersion of the InAs nanowire. Ab initio calculations as well as STM measurements in Ref. [98] suggest an energy dispersion of the subbands of this wire that is quadratic only at low momenta and rather linear at high momenta. Our aim was not to explain this specific experiment quantitatively, but rather to demonstrate that the non-monotonic behavior of the relaxation rate is a general phenomenon. We hope that our work will stimulate future experiments with different setups which could verify our general predictions about the regain of coherence at high energies.

5.5 Summary of chapter 5

In summary, we have investigated the interaction-induced relaxation rate of hot fermions in quantum wires as a function of energy. We have demonstrated that under quite general circumstances, the relaxation rate $1/\tau$ decays as a power-law at high energies. Together with the increase of the collision rate in the low-energy regime, a non-monotonic behavior is found. This means that electrons with energies much larger than the Fermi energy regain their coherence with increasing energy.

As a starting point, we considered systems in $D \geq 2$ dimensions, where the relaxation rate decays according to Eq. (5.17) as $1/p$ at large momenta. We derived this result under the assumption of a parabolic dispersion and a sufficiently fast decaying interaction potential at large momenta. It should be emphasized here that the Coulomb interaction is contained in this class of interactions, so that our results are valid in this case as well, see Eq. (5.21). The decay of the relaxation rates as $1/p$ can be explained by the increase of the velocity of the hot fermion compared to the velocity of the cold particles inside the Fermi sea. Due to the suppression of the interaction potential beyond momentum transfers of the order of q_0, the momentum transfer of the hot particle is almost perpendicular to the direction of its initial momentum, with a deviation of the order of q_0/p. Figure 5.3 illustrates schematically the momentum dependence of the relaxation rate for spinless and spinful particles in

a 3D system from the Fermi-liquid to the ultra-hot regime. The numerical result for $1/\tau$ shown in Fig. 5.4 verifies our analytical predictions.

We were particularly interested in the relaxation of fermions in quasi-1D wires. Such systems host multiple subbands of transverse quantization and were studied experimentally with regard to the relaxation at high energies in Ref. [98]. In essence, we obtain the same results as in bulk systems, see Eqs. (5.34) and (5.36) for multi-channel wires with one and two lateral dimensions, respectively. However, at very high energies, there is a non-universal regime in which the discreteness of the transverse energy spectrum is important. This regime exists for ultra-hot particles whose momenta point nearly perpendicular to the wire axis, see Fig. 5.7. Here, the relaxation rate decays faster than $1/p$. The actual behavior is non-universal since it depends on the specific form of the large-momentum tail of the interaction.

Another central goal was the investigation of the relaxation rate in 1D single-channel wires. We have shown that the non-monotonicity of $1/\tau$ is present in strictly 1D systems as well. In contrast to higher dimensions and multi-channel wires, the relaxation rate is determined by three-particle collisions. Here, we obtain a much stronger decay of the relaxation rate at high energies, $1/\tau \propto 1/p^5$, see Eq. (5.50). The origin for this strong decay is twofold: (i) as in higher dimensions, a factor $1/p$ originates from the velocity mismatch and the limitation on the possible momentum transfer, and (ii) a factor $1/p^4$ emerges from partial cancellations in the three-particle matrix element. The behavior of the relaxation rate over the whole range of momenta for spinless as well as spinful fermions in a 1D system is depicted schematically in Fig. 5.9. The numerical evaluation of $1/\tau$, shown in Fig. 5.10, verifies our analytical predictions. The analysis of the Coulomb interaction in single-channel wires has shown that the decay of the relaxation rate in the high-energy limit persists in this case as well. Due to the singular behavior of the Coulomb interaction at low momenta, the scaling of $1/\tau$ as a function of momentum is enhanced by logarithmic factors in the ultra-hot regime, see Eqs. (5.62) and (5.69).

In conclusion, we have shown that the revival of coherence at high energies is a quite generic feature which might be employed in quantum-technology applications. Independent of the dimensionality of the system, in single-channel and multi-channel wires as well as in 2D and 3D systems, a regain of the phase coherence is found. Besides this general observation, we want to emphasize that the decay of the relaxation rate at high energies is particularly strong in strictly 1D single-channel wires.

Before closing this chapter, we remark a possible extension of this work. In this chapter, we neglected the influence of disorder on the scattering. We can ask the question about the fate of our results in the presence of disorder. We expect that generally two cases should be distinguished. In the first scenario, the electrons in the Fermi sea behave diffusively on the times scales relevant for the collision process. Due to the diffusive motion, the inelastic scattering rate in the low-energy limit is strongly enhanced [164]. At high energies, however, the relevant time scale determined by the typical energy transfer is shorter such that a ballistic motion is possible at large enough energies. The enhancement of the scattering rate is thus presumably weaker at high energies. This means that the non-monotonic behavior of the relaxation rate should survive in this kind of disordered system. The second scenario is that of strong disorder leading to localization [147, 148]. In such a situation, the inelastic scattering rate vanishes at low energies. However, at sufficiently high energies, the relaxation rate becomes finite [165]. A deeper analysis of the relaxation rate in disordered systems poses an interesting research project for the future.

Conclusion

In this thesis, we have studied the transport properties and relaxation phenomena in 1D interacting systems. The electrical transport has been investigated in Josephson junction (JJ) chains which show the remarkable phenomenon of a superconductor-insulator transition (SIT). These systems also offer the possibility to examine relaxation phenomena: we have considered the decay of excited plasmonic waves in such devices. In addition to the relaxation of bosonic excitations in JJ chains, we have discussed the relaxation of high-energy fermions in quantum wires. In the following, we summarize the main results of this thesis and present a prospect for future research projects.

After the introductory Chaps. 1 and 2, we turned in Chap. 3 to the discussion of the transport characteristics of JJ chains. In these systems, a quantum phase transition can be observed [39–43] which connects the superconducting and insulating phases characterized by infinite and zero conductivity, respectively. Starting from a lattice model that contains capacitive couplings to the ground (C_0) as well as between the superconducting grains (C_1), a low-energy theory in terms of a sine-Gordon model was derived. The SIT is driven by the proliferation of quantum phase slips (QPS) — 2π windings of the phase difference across one of the junctions. In contrast to previous theoretical studies of the phase transition in JJ chains [14, 44, 49, 57], our model incorporates disorder effects. Two sources of disorder are considered: random offset charges as well as a random QPS amplitude arising from the interplay of fluctuations of the Josephson energy and random stray charges. The phase diagram is obtained by means of the renormalization group (RG) which predicts a quantum phase transition in the Berezinskii-Kosterlitz-Thouless (BKT) universality class. The ultimate low-energy behavior is governed by the ratio of the Josephson energy E_J to the charging energy E_0 associated with the ground capacitance C_0. In a clean system, the critical point is located at $K_0 = \sqrt{E_\mathrm{J}/E_0} = 2/\pi$ for an infinitesimal value of the QPS amplitude, while in the strongly disordered case, the critical value is reduced to $K_0 = 3/2\pi$. As can be seen from Fig. 3.2, even a small amount of random offset charges shifts the phase boundary quite appreciably in favor of the superconducting phase. This at first glance surprising effect can be explained by the destructive interference of QPS. Phase slips acquire a random phase via the Aharonov-Casher effect due to the charge disorder. The second type of disorder, arising from spatial variations of the junction parameters and leading to QPS with a fluctuating amplitude, shifts the transition line in the opposite direction, cf. Fig. 3.2.

The transport properties were obtained within the memory-function formalism. The behavior of electrical transport quantities at the phase boundary constitutes a central result of this thesis. At the transition line, the resistivity ρ vanishes linearly with a logarithmic correction as a function of temperature T, see Eq. (3.41). We further studied the length dependence of the resistance R at zero temperature. At the critical line, this quantity vanishes logarithmically as the system size N is increased, see Eq. (3.43). The overall behavior of $\rho(T)$ and $R(N)$ is strongly non-monotonic. In the case of local Coulomb interaction, $C_1 \ll C_0$, the resistivity in the insulating regime shows up to three different regimes, cf. Figs. 3.4 and 3.5. At relatively high temperatures, where by assumption the offset charges are weak, QPS lead to a growth of the resistivity. Upon lowering T, the random offset charges become stronger and suppress the influence of QPS resulting in a decreasing behavior of the

resistivity. However, at low temperatures, phase slips ultimately take over driving the system into the insulating fixed point. The same behavior is found for resistance curves in the insulating regime close to criticality upon increasing the system size. In the superconducting phase only the first two regimes emerge in the length dependence of R. Random offset charges are in this case strong enough to win over the QPS. In the regime of non-local Coulomb interaction, $C_0 \ll C_1$, an additional regime at high T (small N) shows up, where the resistivity (resistance) exhibits a fast drop upon lowering T (increasing N). Accordingly, up to four different regimes can be observed, see Fig. 3.8.

Comparing our results to the experiment reported in Ref. [39], where the temperature dependent resistance of JJ chains with a SQUID geometry was measured, yields qualitative agreement. The experimental resistance curves as a function of temperature show three different regimes in the insulating phase: upon lowering the temperature, the resistance first increases, then decreases and eventually shoots up at low T, similar to Fig. 3.4 a). However, there is disagreement between our prediction and the experimental result of Ref. [39] concerning the location of the SIT. There are several possible reasons for this discrepancy. The chains in the experiment of Ref. [39] might be too short (up to $N = 255$) or the temperature too high (50 mK) to probe the ultimate infrared behavior. Indeed, our work clearly demonstrates that the overall dependences of $\rho(T)$ and $R(N)$ are strongly non-monotonic, making it difficult to extract the position of the phase boundary based on experimental data available in a limited range of T and N. Moreover, it was pointed out in Ref. [53] that the measurements in SQUID chains might be affected by an external noise or an interplay of charge and flux. Our prediction of the location of the SIT is consistent with the observations made in Ref. [53], where the threshold voltages for the onset of transport in the insulating regime were measured in single-junction chains.

A few issues have been left out in our theory on the SIT. We mention two possible directions for the extension of the work presented in Chap. 3. Firstly, the random spatial variations of the Luttinger constant K_0 were not included into our theory. Such fluctuations are of course also present as a result of the spatial variations of the junction parameters. Assuming their strength to be small, they are expected to be of minor significance for the charge transport. However, from a related work on quantum wires [146] we can anticipate that the thermal transport should be affected since such fluctuations can localize the bosonic modes. Secondly, it would be interesting to study the fate of the insulating resistivity curves inside the strong-coupling regime. We expect a transition to a many-body localized phase [147, 148] characterized by infinite resistivity. Experimentally, localization effects were observed in 2D disordered systems close to the SIT [166]. We think that similar effects should be observable in 1D as well.

Josephson-junction chains allow not only for the investigation of interesting transport properties but also offer the opportunity to study the relaxation of excitations in 1D systems. This was demonstrated recently in an experiment [73] which analyzed the quality factor of plasmonic waves in a double chain of JJs. We studied the decay of plasmonic waves in JJ chains in Chap. 4. Motivated by the experiment, we analyzed two capacitively coupled chains as well as a single linear chain. It was shown that in the parameter regime where the ground capacitance (C_g) can be neglected, the theory for the antisymmetric mode in the double chain can be mapped onto a theory for a single chain. Two mechanisms contributing to the relaxation of plasmonic waves are considered: the scattering off QPS and the interaction of the plasma waves due to gradient anharmonicities. The contribution originating from QPS leads to a power-law scaling of the relaxation rate with a non-universal exponent that depends on K_0. Figure 4.2 shows its scaling in different parameter regimes. It should be further emphasized that the phase-slip contribution is exponentially small in the parameter $\sqrt{E_J/E_1}$, where E_1 is the charging energy related to the junction capacitance.

The second contribution to the decay of plasmons emerges from the gradient nonlinearities. As an example, we analyzed the quartic term arising in the expansion of the Josephson potential. Its contribution leads to the universal ω^4 scaling of the relaxation rate. As expected from the irrelevance of this term in the RG, it vanishes in the zero-frequency limit. Nevertheless, this contribution dominates the relaxation rate in a wide range of frequencies if the bare QPS amplitude is small.

The interplay of both channels is studied by means of the product of mode frequency and lifetime, a dimensionless quantity expected to be proportional to the quality factor which is studied experimentally in Ref. [73]. We find that in the insulating regime, $K_0 \ll 1$, the quality factor is a non-monotonic function of frequency, see Fig. 4.4. Our main result in this context is that the quality factor is dominated by the gradient-anharmonicity contribution, which scales as ω^{-3}, down to a crossover frequency that is exponentially small in the parameter $\sqrt{E_\mathrm{J}/E_1}$. Only at even lower frequencies, the quality factor decreases with frequency. This explains the apparent superconducting behavior of the quality factor observed in the experiment for devices that are expected to be in the insulating regime. The insulating behavior would show up only at lower frequencies outside the range of measured frequencies. Accordingly, we stress that the observed change in the behavior of the quality factor from increasing to decreasing in Ref. [73] is not related to the SIT. Our prediction of the ω^{-3} scaling of the quality factor at high frequencies for devices with a large value of E_J/E_1 is in accordance with the data of Ref. [73]. However, the experimental data suggests a very weak dependence of the quality factor of these devices with respect to the charging energy E_0. Our theory, however, predicts a strong dependence scaling as E_0^3. This result is obtained for the particular example of the quartic nonlinearity originating from the Josephson potential. We suppose that a different type of nonlinearity is responsible for this behavior. It would be interesting to search for other types of nonlinearities which result in a weaker dependence on E_0 and lead to a quantitative agreement with the experiment.

Relaxation plays a central role in fermionic systems as well. Therefore, besides the decay of bosonic excitations in JJ chains, we studied the relaxation of fermionic excitations in quantum wires. Motivated by a recent experiment [98], we focused in Chap. 5 on the decay at high energies larger than the Fermi energy. We investigated the decay of fermions in quasi-1D wires with several channels of transverse quantization as well as in single-channel wires. To better understand the quasi-1D case, we also considered isotropic 2D and 3D systems. Our main result is the power-law decay of the relaxation rate $1/\tau$ at high energies in all these systems and under quite general circumstances. Accordingly, fermions regain their coherence at high energies larger than the Fermi energy.

As a starting point we considered the case of higher dimensions $D \geq 2$ and obtained $1/\tau \propto p^{-1}$ in the regime where the momentum p of the hot particle is larger than the Fermi momentum, cf. Eq. (5.17). This specific form rests on the assumption of a parabolic energy dispersion and the interaction potential decaying sufficiently fast at high momenta. It should be stressed that the screened Coulomb interaction belongs to this class of interactions so that our results remain valid for this case, see Eq. (5.21). The decay of the relaxation rate at high momenta is related to the velocity mismatch between the high-energy fermion and the ones occupying the Fermi sea as well as the limited possible momentum transfer by the interaction. For a non-parabolic energy spectrum, the decay of the relaxation rate persists provided that the velocity is an increasing function of momentum. The non-monotonic behavior of the relaxation rate for spinful and spin-polarized fermions in three dimensions is depicted schematically in Fig. 5.3.

In quasi-1D setups, i. e., in wires with multiple subbands, we obtained to a large extent the same results as in higher-dimensional systems, as can be seen from Eqs. (5.34) and (5.36) for multi-channel systems with one and two lateral dimensions, respectively. The only difference is a non-universal

regime, depicted in Fig. 5.7, where the discreteness of the spectrum is important leading to a decay of $1/\tau$ at high energies which is faster than $1/p$.

In the case of strictly 1D wires with a parabolic spectrum, two-particle collisions do not lead to relaxation, and one has to consider three-particle scattering processes. Here, we obtain a particularly strong decay of the relaxation rate at high momenta proportional to $1/p^5$, see Eq. (5.50). A factor of $1/p$ emerges due to the same reasons as in the higher-dimensional cases while the additional factor $1/p^4$ is related to partial cancellations in the three-particle matrix element. The schematic behavior of the non-monotonic decay rate from low to large momenta is illustrated in Fig. 5.9. An analysis of the Coulomb interaction in 1D wires has shown that, up to logarithmic factors related to the singular behavior of the Coulomb potential at low momenta, the relaxation rate decays as the same power-law at high momenta, see Eqs. (5.62) and (5.69).

Comparing our results of the decay rate to the findings of the experiment of Ref. [98], we obtain qualitative agreement although the energy spectrum of the nanowires analyzed in the experiment is not parabolic. We hope that our quite general result, the revival of the coherence of fermions at high energies, initiates further experimental studies of the decay rate in various setups.

In our calculation of the relaxation rate we assumed clean systems. It would be interesting to analyze the influence of disorder on the relaxation rate. Preliminary considerations show that one should distinguish two cases. If the electrons in the Fermi sea behave diffusively on the time scales relevant for the scattering process, it is known that the inelastic scattering rate at low energies is enhanced [164]. At high energies, the relevant time scale, which is determined by the typical energy transfer, is smaller. Accordingly, the motion might remain ballistic leading to a weaker enhancement. As a consequence, the non-monotonic behavior of the relaxation rate persists. If the disorder is strong enough to cause localization [147, 148], the relaxation rate vanishes at low energies. On the other hand, at higher energies, the relaxation rate is finite [165]. A detailed analysis of the decay rate as a function of energy is missing up to the present date.

In conclusion, we have shown that the transport and the relaxation in 1D interacting systems are characterized by many fascinating effects. After a long time of intensive research on the physics of 1D systems that started many decades ago, this field is still very active today. We can expect that further technological improvements will offer many opportunities for applications based on the fundamental properties of 1D systems. Moreover, there are still many aspects in the field of 1D physics that are waiting to be discovered.

List of publications

In the following, the list of publications of the author of this thesis is presented:

- M. Bard: *"Phase slips and the superconductor-insulator transition in disordered wires"*, Master's thesis, Karlsruhe Institute of Technology, (2014). Reference [142] in this bibliography.
- M. Bard, I. V. Protopopov, I. V. Gornyi, A. Shnirman, and A. D. Mirlin: *"Superconductor-insulator transition in disordered Josephson-junction chains"*, Phys. Rev. B **96**, 064514 (2017). Reference [107] in this bibliography.
- M. Bard, I. V. Protopopov, and A. D. Mirlin: *"Long lifetimes of ultrahot particles in interacting Fermi systems"*, Phys. Rev. B **97**, 195147 (2018). Reference [153] in this bibliography.
- M. Bard, I. V. Protopopov, and A. D. Mirlin: *"Decay of plasmonic waves in Josephson junction chains"*, arXiv:1810.00807 (submitted to Phys. Rev. B.). Reference [149] in this bibliography.

Bibliography

[1] S.-I. Tomonaga, "Remarks on Bloch's Method of Sound Waves applied to Many-Fermion Problems," *Prog. Theor. Phys.*, vol. 5, pp. 544–569, Jul 1950.

[2] J. M. Luttinger, "An Exactly Soluble Model of a Many-Fermion System," *J. Math. Phys.*, vol. 4, no. 9, pp. 1154–1162, 1963.

[3] E. H. Lieb and W. Liniger, "Exact Analysis of an Interacting Bose Gas. I. The General Solution and the Ground State," *Phys. Rev.*, vol. 130, pp. 1605–1616, May 1963.

[4] D. C. Mattis and E. H. Lieb, "Exact Solution of a Many-Fermion System and Its Associated Boson Field," *J. Math. Phys.*, vol. 6, pp. 304–312, Feb 1965.

[5] C. N. Yang, "Some Exact Results for the Many-Body Problem in one Dimension with Repulsive Delta-Function Interaction," *Phys. Rev. Lett.*, vol. 19, pp. 1312–1315, Dec 1967.

[6] M. Gaudin, "Un systeme a une dimension de fermions en interaction," *Phys. Lett. A*, vol. 24, pp. 55–56, Jan 1967.

[7] B. Sutherland, "Further Results for the Many-Body Problem in One Dimension," *Phys. Rev. Lett.*, vol. 20, pp. 98–100, Jan 1968.

[8] V. J. Emery, A. Luther, and I. Peschel, "Solution of the one-dimensional electron gas on a lattice," *Phys. Rev. B*, vol. 13, pp. 1272–1276, Feb 1976.

[9] J. Sólyom, "The fermi gas model of one-dimensional conductors," *Adv. Phys.*, vol. 28, pp. 201–303, Apr 1979.

[10] F. D. M. Haldane, "General Relation of Correlation Exponents and Spectral Properties of One-Dimensional Fermi Systems: Application to the Anisotropic $S = \frac{1}{2}$ Heisenberg Chain," *Phys. Rev. Lett.*, vol. 45, pp. 1358–1362, Oct 1980.

[11] F. D. M. Haldane, "'Luttinger liquid theory' of one-dimensional quantum fluids: I. Properties of the Luttinger model and their extension to the general 1D interacting spinless Fermi gas," *J. Phys. C*, vol. 14, no. 19, pp. 2585–2609, 1981.

[12] F. D. M. Haldane, "Effective Harmonic-Fluid Approach to Low-Energy Properties of One-Dimensional Quantum Fluids," *Phys. Rev. Lett.*, vol. 47, pp. 1840–1843, Dec 1981.

[13] D. Jérome and H. J. Schulz, "Organic conductors and superconductors," *Adv. Phys.*, vol. 31, no. 4, pp. 299–490, 1982.

[14] R. M. Bradley and S. Doniach, "Quantum fluctuations in chains of Josephson junctions," *Phys. Rev. B*, vol. 30, pp. 1138–1147, Aug 1984.

[15] J. von Delft and H. Schoeller, "Bosonization for beginners refermionization for experts," *Ann. Phys.*, vol. 7, no. 4, pp. 225–305, 1998.

[16] A. O. Gogolin, A. A. Nersesyan, and A. M. Tsvelik, *Bosonization and Strongly Correlated Systems.* Cambridge [u.a.]: Cambridge University Press, 1. publ. ed., 1998.

[17] T. Giamarchi, *Quantum Physics in One Dimension.* International series of monographs on physics ; 121, Oxford: Clarendon Press, 2004.

[18] A. Imambekov, T. L. Schmidt, and L. I. Glazman, "One-dimensional quantum liquids: Beyond the Luttinger liquid paradigm," *Rev. Mod. Phys.*, vol. 84, pp. 1253–1306, Sep 2012.

[19] D. B. Haviland, S. H. M. Persson, P. Delsing, and C. D. Chen, "Fabrication and measurement of one-dimensional arrays of small capacitance Josephson junctions," *J. Vac. Sci. Technol.*, vol. 14, pp. 1839–1843, May 1996.

[20] E. Dagotto and T. M. Rice, "Surprises on the Way from One- to Two-Dimensional Quantum Magnets: The Ladder Materials," *Science*, vol. 271, pp. 618–623, Feb 1996.

[21] E. Dagotto, "Experiments on ladders reveal a complex interplay between a spin-gapped normal state and superconductivity," *Rep. Prog. Phys.*, vol. 62, pp. 1525–1571, Nov 1999.

[22] Y. Ji, Y. Chung, D. Sprinzak, M. Heiblum, D. Mahalu, and H. Shtrikman, "An electronic Mach-Zehnder interferometer," *Nature*, vol. 422, pp. 415–418, Mar 2003.

[23] I. Neder, M. Heiblum, Y. Levinson, D. Mahalu, and V. Umansky, "Unexpected Behavior in a Two-Path Electron Interferometer," *Phys. Rev. Lett.*, vol. 96, p. 016804, Jan 2006.

[24] K.-V. Pham, M. Gabay, and P. Lederer, "Fractional excitations in the Luttinger liquid," *Phys. Rev. B*, vol. 61, pp. 16397–16422, Jun 2000.

[25] H. Steinberg, G. Barak, A. Yacoby, L. N. Pfeiffer, K. W. West, B. I. Halperin, and K. L. Hur, "Charge fractionalization in quantum wires," *Nat. Phys.*, vol. 4, pp. 116–119, Dec 2007.

[26] O. M. Auslaender, "Spin-Charge Separation and Localization in One Dimension," *Science*, vol. 308, pp. 88–92, Apr 2005.

[27] Y. Jompol, C. J. B. Ford, J. P. Griffiths, I. Farrer, G. A. C. Jones, D. Anderson, D. A. Ritchie, T. W. Silk, and A. J. Schofield, "Probing Spin-Charge Separation in a Tomonaga-Luttinger Liquid," *Science*, vol. 325, pp. 597–601, Jul 2009.

[28] H. Moritz, T. Stöferle, M. Köhl, and T. Esslinger, "Exciting Collective Oscillations in a Trapped 1D Gas," *Phys. Rev. Lett.*, vol. 91, p. 250402, Dec 2003.

[29] T. Kinoshita, "Observation of a One-Dimensional Tonks-Girardeau Gas," *Science*, vol. 305, pp. 1125–1128, Aug 2004.

[30] H. Moritz, T. Stöferle, K. Günter, M. Köhl, and T. Esslinger, "Confinement Induced Molecules in a 1D Fermi Gas," *Phys. Rev. Lett.*, vol. 94, p. 210401, Jun 2005.

[31] G. Pagano, M. Mancini, G. Cappellini, P. Lombardi, F. Schäfer, H. Hu, X.-J. Liu, J. Catani, C. Sias, M. Inguscio, and L. Fallani, "A one-dimensional liquid of fermions with tunable spin," *Nat. Phys.*, vol. 10, pp. 198–201, Feb 2014.

[32] N. Wang, Y. Cai, and R. Zhang, "Growth of nanowires," *Mater. Sci. Eng. R Rep.*, vol. 60, pp. 1–51, Mar 2008.

[33] E. A. Laird, F. Kuemmeth, G. A. Steele, K. Grove-Rasmussen, J. Nygård, K. Flensberg, and L. P. Kouwenhoven, "Quantum transport in carbon nanotubes," *Rev. Mod. Phys.*, vol. 87, pp. 703–764, Jul 2015.

[34] K. v. Klitzing, G. Dorda, and M. Pepper, "New Method for High-Accuracy Determination of the Fine-Structure Constant Based on Quantized Hall Resistance," *Phys. Rev. Lett.*, vol. 45, pp. 494–497, Aug 1980.

[35] D. C. Tsui, H. L. Stormer, and A. C. Gossard, "Two-Dimensional Magnetotransport in the Extreme Quantum Limit," *Phys. Rev. Lett.*, vol. 48, pp. 1559–1562, May 1982.

[36] M. Konig, S. Wiedmann, C. Brune, A. Roth, H. Buhmann, L. W. Molenkamp, X.-L. Qi, and S.-C. Zhang, "Quantum Spin Hall Insulator State in HgTe Quantum Wells," *Science*, vol. 318, no. 5851, pp. 766–770, 2007.

[37] H. J. Fan, P. Werner, and M. Zacharias, "Semiconductor Nanowires: From Self-Organization to Patterned Growth," *Small*, vol. 2, pp. 700–717, Jun 2006.

[38] D. B. Haviland and P. Delsing, "Cooper-pair charge solitons: The electrodynamics of localized charge in a superconductor," *Phys. Rev. B*, vol. 54, pp. R6857–R6860, Sep 1996.

[39] E. Chow, P. Delsing, and D. B. Haviland, "Length-Scale Dependence of the Superconductor-to-Insulator Quantum Phase Transition in One Dimension," *Phys. Rev. Lett.*, vol. 81, pp. 204–207, Jul 1998.

[40] D. Haviland, K. Andersson, and P. Ågren, "Superconducting and Insulating Behavior in One-Dimensional Josephson Junction Arrays," *J. Low Temp. Phys.*, vol. 118, no. 5-6, pp. 733–749, 2000.

[41] W. Kuo and C. D. Chen, "Scaling Analysis of Magnetic-Field-Tuned Phase Transitions in One-Dimensional Josephson Junction Arrays," *Phys. Rev. Lett.*, vol. 87, p. 186804, Oct 2001.

[42] H. Miyazaki, Y. Takahide, A. Kanda, and Y. Ootuka, "Quantum Phase Transition in One-Dimensional Arrays of Resistively Shunted Small Josephson Junctions," *Phys. Rev. Lett.*, vol. 89, p. 197001, Oct 2002.

[43] Y. Takahide, H. Miyazaki, and Y. Ootuka, "Superconductor-insulator crossover in Josephson junction arrays due to reduction from two to one dimension," *Phys. Rev. B*, vol. 73, p. 224503, Jun 2006.

[44] M.-S. Choi, J. Yi, M. Y. Choi, J. Choi, and S.-I. Lee, "Quantum phase transitions in Josephson-junction chains," *Phys. Rev. B*, vol. 57, pp. R716–R719, Jan 1998.

[45] D. Haviland, K. Andersson, P. Ågren, J. Johansson, V. Schöllmann, and M. Watanabe, "Quantum phase transition in one-dimensional Josephson junction arrays," *Physica C*, vol. 352, pp. 55–60, Apr 2001.

[46] A. Ergül, D. Schaeffer, M. Lindblom, D. B. Haviland, J. Lidmar, and J. Johansson, "Phase sticking in one-dimensional Josephson junction chains," *Phys. Rev. B*, vol. 88, p. 104501, Sep 2013.

[47] K. A. Matveev, A. I. Larkin, and L. I. Glazman, "Persistent Current in Superconducting Nanorings," *Phys. Rev. Lett.*, vol. 89, p. 096802, Aug 2002.

[48] I. M. Pop, I. Protopopov, F. Lecocq, Z. Peng, B. Pannetier, O. Buisson, and W. Guichard, "Measurement of the effect of quantum phase slips in a Josephson junction chain," *Nat. Phys.*, vol. 6, pp. 589–592, Aug 2010.

[49] G. Rastelli, I. M. Pop, and F. W. J. Hekking, "Quantum phase slips in Josephson junction rings," *Phys. Rev. B*, vol. 87, p. 174513, May 2013.

[50] A. Ergül, J. Lidmar, J. Johansson, Y. Azizoğlu, D. Schaeffer, and D. B. Haviland, "Localizing quantum phase slips in one-dimensional Josephson junction chains," *New J. Phys.*, vol. 15, no. 9, p. 095014, 2013.

[51] J. Zimmer, N. Vogt, A. Fiebig, S. V. Syzranov, A. Lukashenko, R. Schäfer, H. Rotzinger, A. Shnirman, M. Marthaler, and A. V. Ustinov, "Thermally activated conductance in arrays of small Josephson junctions," *Phys. Rev. B*, vol. 88, p. 144506, Oct 2013.

[52] N. Vogt, R. Schäfer, H. Rotzinger, W. Cui, A. Fiebig, A. Shnirman, and A. V. Ustinov, "One-dimensional Josephson junction arrays: Lifting the Coulomb blockade by depinning," *Phys. Rev. B*, vol. 92, p. 045435, Jul 2015.

[53] K. Cedergren, R. Ackroyd, S. Kafanov, N. Vogt, A. Shnirman, and T. Duty, "Insulating Josephson Junction Chains as Pinned Luttinger Liquids," *Phys. Rev. Lett.*, vol. 119, p. 167701, Oct 2017.

[54] V. L. Berezinskii, "Destruction of long-range order in one-dimensional and two-dimensional systems with a continuous symmetry group. I. Classical systems," *Sov. Phys. JETP*, vol. 32, pp. 493–500, 1971.

[55] V. L. Berezinskii, "Destruction of long-range order in one-dimensional and two-dimensional systems possessing a continuous symmetry group. II. Quantum systems," *Sov. Phys. JETP*, vol. 34, pp. 610–616, Mar 1972.

[56] J. M. Kosterlitz and D. J. Thouless, "Ordering, metastability and phase transitions in two-dimensional systems," *J. Phys. C*, vol. 6, no. 7, p. 1181, 1973.

[57] S. E. Korshunov, "Effect of dissipation on the low-temperature properties of a tunnel-junction chain," *Sov. Phys. JETP*, vol. 68, pp. 609–618, Mar 1989.

[58] P. A. Bobbert, R. Fazio, G. Schön, and G. T. Zimanyi, "Phase transitions in dissipative Josephson chains," *Phys. Rev. B*, vol. 41, pp. 4009–4016, Mar 1990.

[59] P. A. Bobbert, R. Fazio, G. Schön, and A. D. Zaikin, "Phase transitions in dissipative Josephson chains: Monte Carlo results and response functions," *Phys. Rev. B*, vol. 45, pp. 2294–2304, Feb 1992.

[60] R. Fazio and H. van der Zant, "Quantum phase transitions and vortex dynamics in superconducting networks," *Phys. Rep.*, vol. 355, no. 4, pp. 235 – 334, 2001.

[61] R. Fazio, K.-H. Wagenblast, C. Winkelholz, and G. Schön, "Tunneling into one-dimensional Josephson chains and Luttinger liquids," *Physica B*, vol. 222, no. 4, pp. 364 – 369, 1996. Proceedings of the ICTP Workshop on Josephson Junction Arrays.

[62] L. I. Glazman and A. I. Larkin, "New Quantum Phase in a One-Dimensional Josephson Array," *Phys. Rev. Lett.*, vol. 79, pp. 3736–3739, Nov 1997.

[63] A. E. Svetogorov and D. M. Basko, "Effect of disorder on coherent quantum phase slips in Josephson junction chains," *Phys. Rev. B*, vol. 98, p. 054513, Aug 2018.

[64] A. Bezryadin, C. N. Lau, and M. Tinkham, "Quantum suppression of superconductivity in ultrathin nanowires," *Nature*, vol. 404, pp. 971–974, Apr 2000.

[65] A. T. Bollinger, R. C. Dinsmore, A. Rogachev, and A. Bezryadin, "Determination of the Superconductor-Insulator Phase Diagram for One-Dimensional Wires," *Phys. Rev. Lett.*, vol. 101, p. 227003, Nov 2008.

[66] H. Kim, S. Jamali, and A. Rogachev, "Superconductor-Insulator Transition in Long MoGe Nanowires," *Phys. Rev. Lett.*, vol. 109, p. 027002, Jul 2012.

[67] A. D. Zaikin, D. S. Golubev, A. van Otterlo, and G. T. Zimányi, "Quantum Phase Slips and Transport in Ultrathin Superconducting Wires," *Phys. Rev. Lett.*, vol. 78, pp. 1552–1555, Feb 1997.

[68] D. S. Golubev and A. D. Zaikin, "Quantum tunneling of the order parameter in superconducting nanowires," *Phys. Rev. B*, vol. 64, p. 014504, Jun 2001.

[69] W. Guichard and F. W. J. Hekking, "Phase-charge duality in Josephson junction circuits: Role of inertia and effect of microwave irradiation," *Phys. Rev. B*, vol. 81, p. 064508, Feb 2010.

[70] Y. Zhang, L. Yu, J. Q. Liang, G. Chen, S. Jia, and F. Nori, "Quantum phases in circuit QED with a superconducting qubit array," *Sci. Rep.*, vol. 4, p. 4083, Feb 2014.

[71] J. Puertas Martinez, S. Leger, N. Gheeraert, R. Dassonneville, L. Planat, F. Foroughi, Y. Krupko, O. Buisson, C. Naud, W. Guichard, S. Florens, I. Snyman, and N. Roch, "A tunable Josephson platform to explore many-body quantum optics in circuit-QED," *ArXiv e-prints*, Feb 2018. 1802.00633 [cond-mat.mes-hall].

[72] G. Rastelli and I. M. Pop, "Tunable ohmic environment using Josephson junction chains," *Phys. Rev. B*, vol. 97, p. 205429, May 2018.

[73] R. Kuzmin, R. Mencia, N. Grabon, N. Mehta, Y.-H. Lin, and V. E. Manucharyan, "Quantum electrodynamics of a superconductor-insulator phase transition," *ArXiv e-prints*, May 2018. arXiv:1805.07379 [cond-mat.supr-con].

[74] L. D. Landau, "The theory of Fermi-liquids," *Sov. Phys. JETP*, vol. 3, p. 920, 1957.

[75] L. D. Landau, "Oscillations in a Fermi-liquid," *Sov. Phys. JETP*, vol. 5, p. 101, 1957.

[76] L. D. Landau, "On the theory of the Fermi-liquid," *Sov. Phys. JETP*, vol. 8, p. 70, 1958.

[77] G. Bergmann, "Weak localization in thin films: a time-of-flight experiment with conduction electrons," *Phys. Rep.*, vol. 107, no. 1, pp. 1 – 58, 1984.

[78] F. V. Tikhonenko, D. W. Horsell, R. V. Gorbachev, and A. K. Savchenko, "Weak Localization in Graphene Flakes," *Phys. Rev. Lett.*, vol. 100, p. 056802, Feb 2008.

[79] J. G. Checkelsky, Y. S. Hor, M.-H. Liu, D.-X. Qu, R. J. Cava, and N. P. Ong, "Quantum Interference in Macroscopic Crystals of Nonmetallic Bi_2Se_3," *Phys. Rev. Lett.*, vol. 103, p. 246601, Dec 2009.

[80] C. A. Schmuttenmaer, M. Aeschlimann, H. E. Elsayed-Ali, R. J. D. Miller, D. A. Mantell, J. Cao, and Y. Gao, "Time-resolved two-photon photoemission from cu(100): Energy dependence of electron relaxation," *Phys. Rev. B*, vol. 50, pp. 8957–8960, Sep 1994.

[81] T. Hertel, E. Knoesel, M. Wolf, and G. Ertl, "Ultrafast Electron Dynamics at Cu(111): Response of an Electron Gas to Optical Excitation," *Phys. Rev. Lett.*, vol. 76, pp. 535–538, Jan 1996.

[82] M. Aeschlimann, M. Bauer, S. Pawlik, W. Weber, R. Burgermeister, D. Oberli, and H. C. Siegmann, "Ultrafast Spin-Dependent Electron Dynamics in fcc Co," *Phys. Rev. Lett.*, vol. 79, pp. 5158–5161, Dec 1997.

[83] T. Kinoshita, T. Wenger, and D. S. Weiss, "A quantum Newton's cradle," *Nature*, vol. 440, pp. 900–903, Apr 2006.

[84] S. Hofferberth, I. Lesanovsky, B. Fischer, T. Schumm, and J. Schmiedmayer, "Non-equilibrium coherence dynamics in one-dimensional Bose gases," *Nature*, vol. 449, pp. 324–327, Sep 2007.

[85] S. T. Beliaev, "Energy-Spectrum of a Non-ideal Bose Gas," *Sov. Phys. JETP*, vol. 7, p. 299, Aug 1958.

[86] S. Tan, M. Pustilnik, and L. I. Glazman, "Relaxation of a High-Energy Quasiparticle in a One-Dimensional Bose Gas," *Phys. Rev. Lett.*, vol. 105, p. 090404, Aug 2010.

[87] Z. Ristivojevic and K. A. Matveev, "Decay of Bogoliubov quasiparticles in a nonideal one-dimensional Bose gas," *Phys. Rev. B*, vol. 89, p. 180507, May 2014.

[88] Z. Ristivojevic and K. A. Matveev, "Decay of Bogoliubov excitations in one-dimensional Bose gases," *Phys. Rev. B*, vol. 94, p. 024506, Jul 2016.

[89] W. Nessler, S. Ogawa, H. Nagano, H. Petek, J. Shimoyama, Y. Nakayama, and K. Kishio, "Femtosecond time-resolved study of the energy and temperature dependence of hot-electron lifetimes in $bi_2sr_2cacu_2O_{8+\delta}$," *Phys. Rev. Lett.*, vol. 81, pp. 4480–4483, Nov 1998.

[90] Y.-F. Chen, T. Dirks, G. Al-Zoubi, N. O. Birge, and N. Mason, "Nonequilibrium Tunneling Spectroscopy in Carbon Nanotubes," *Phys. Rev. Lett.*, vol. 102, p. 036804, Jan 2009.

[91] G. Barak, H. Steinberg, L. N. Pfeiffer, K. W. West, L. Glazman, F. von Oppen, and A. Yacoby, "Interacting electrons in one dimension beyond the Luttinger-liquid limit," *Nat. Phys.*, vol. 6, pp. 489–493, May 2010.

[92] C. Altimiras, H. le Sueur, U. Gennser, A. Cavanna, D. Mailly, and F. Pierre, "Non-equilibrium edge-channel spectroscopy in the integer quantum Hall regime," *Nat. Phys.*, vol. 6, pp. 34–39, Oct 2009.

[93] C. Altimiras, H. le Sueur, U. Gennser, A. Cavanna, D. Mailly, and F. Pierre, "Tuning Energy Relaxation along Quantum Hall Channels," *Phys. Rev. Lett.*, vol. 105, p. 226804, Nov 2010.

[94] H. le Sueur, C. Altimiras, U. Gennser, A. Cavanna, D. Mailly, and F. Pierre, "Energy Relaxation in the Integer Quantum Hall Regime," *Phys. Rev. Lett.*, vol. 105, p. 056803, Jul 2010.

[95] N. Paradiso, S. Heun, S. Roddaro, L. Sorba, F. Beltram, and G. Biasiol, "Impact of electron heating on the equilibration between quantum Hall edge channels," *Phys. Rev. B*, vol. 84, p. 235318, Dec 2011.

[96] E. V. Deviatov, A. Lorke, G. Biasiol, and L. Sorba, "Energy Transport by Neutral Collective Excitations at the Quantum Hall Edge," *Phys. Rev. Lett.*, vol. 106, p. 256802, Jun 2011.

[97] M. G. Prokudina, S. Ludwig, V. Pellegrini, L. Sorba, G. Biasiol, and V. S. Khrapai, "Tunable Nonequilibrium Luttinger Liquid Based on Counterpropagating Edge Channels," *Phys. Rev. Lett.*, vol. 112, p. 216402, May 2014.

[98] J. Reiner, A. K. Nayak, N. Avraham, A. Norris, B. Yan, I. C. Fulga, J.-H. Kang, T. Karzig, H. Shtrikman, and H. Beidenkopf, "Hot Electrons Regain Coherence in Semiconducting Nanowires," *Phys. Rev. X*, vol. 7, p. 021016, May 2017.

[99] H. K. Onnes, "The resistance of pure mercury at helium temperatures," *Comm. Phys. Lab. Univ. Leiden*, vol. 119, 120, 122, 1911.

[100] W. Meissner and R. Ochsenfeld, "Ein neuer Effekt bei Eintritt der Supraleitfähigkeit," *Naturwiss.*, vol. 21, pp. 787–788, Nov 1933.

[101] J. Bardeen, L. N. Cooper, and J. R. Schrieffer, "Microscopic Theory of Superconductivity," *Phys. Rev.*, vol. 106, pp. 162–164, Apr 1957.

[102] J. Bardeen, L. N. Cooper, and J. R. Schrieffer, "Theory of Superconductivity," *Phys. Rev.*, vol. 108, pp. 1175–1204, Dec 1957.

[103] L. N. Cooper, "Bound electron pairs in a degenerate fermi gas," *Phys. Rev.*, vol. 104, pp. 1189–1190, Nov 1956.

[104] B. Josephson, "Possible new effects in superconductive tunnelling," *Phys. Lett.*, vol. 1, no. 7, pp. 251 – 253, 1962.

[105] H. Ibach and H. Lüth, *Festkörperphysik*. Springer Berlin Heidelberg, 2009.

[106] M. Tinkham, *Introduction to superconductivity*. Dover books on physics, Mineola, NY: Dover Publ., 2. ed., 2004.

[107] M. Bard, I. V. Protopopov, I. V. Gornyi, A. Shnirman, and A. D. Mirlin, "Superconductor-insulator transition in disordered Josephson-junction chains," *Phys. Rev. B*, vol. 96, p. 064514, Aug 2017.

[108] A. Altland and B. D. Simons, *Condensed matter field theory*. Cambridge [u.a.]: Cambridge Univ. Press, 2. ed., [repr.] ed., 2012.

[109] L. Benfatto, C. Castellani, and T. Giamarchi, "Beresinskii-Kosterlitz-Thouless transition within the sine-Gordon approach: the role of the vortex-core energy," *ArXiv e-prints*, 2012. arXiv:1201.2307 [cond-mat].

[110] J. V. José, L. P. Kadanoff, S. Kirkpatrick, and D. R. Nelson, "Renormalization, vortices, and symmetry-breaking perturbations in the two-dimensional planar model," *Phys. Rev. B*, vol. 16, pp. 1217–1241, Aug 1977.

[111] N. D. Mermin and H. Wagner, "Absence of Ferromagnetism or Antiferromagnetism in One- or Two-Dimensional Isotropic Heisenberg Models," *Phys. Rev. Lett.*, vol. 17, pp. 1133–1136, Nov 1966.

[112] P. Minnhagen, "The two-dimensional Coulomb gas, vortex unbinding, and superfluid-superconducting films," *Rev. Mod. Phys.*, vol. 59, pp. 1001–1066, Oct 1987.

[113] J. von Delft and H. Schoeller, "Bosonization for beginners - refermionization for experts," *Ann. Phys.*, vol. 7, no. 4, pp. 225–305, 1998.

[114] K. G. Wilson, "The renormalization group: Critical phenomena and the Kondo problem," *Rev. Mod. Phys.*, vol. 47, pp. 773–840, Oct 1975.

[115] M. E. Fisher, "Renormalization group theory: Its basis and formulation in statistical physics," *Rev. Mod. Phys.*, vol. 70, pp. 653–681, Apr 1998.

[116] J. M. Kosterlitz, "The critical properties of the two-dimensional xy model," *J. Phys. C*, vol. 7, no. 6, p. 1046, 1974.

[117] G. D. Mahan, *Many-particle physics*. Physics of solids and liquids, New York [u.a.]: Kluwer Academic, Plenum Publ., 3. ed., 2000.

[118] P. Coleman, *Introduction to many-body physics*. Cambridge: Cambridge Univ. Press, 2015.

[119] M. Oshikawa and I. Affleck, "Electron spin resonance in $s = \frac{1}{2}$ antiferromagnetic chains," *Phys. Rev. B*, vol. 65, p. 134410, Mar 2002.

[120] B. Rosenow, A. Glatz, and T. Nattermann, "Frequency-temperature crossover in the conductivity of disordered luttinger liquids," *Phys. Rev. B*, vol. 76, p. 155108, Oct 2007.

[121] W. Götze and P. Wölfle, "Homogeneous Dynamical Conductivity of Simple Metals," *Phys. Rev. B*, vol. 6, pp. 1226–1238, Aug 1972.

[122] T. Giamarchi, "Umklapp process and resistivity in one-dimensional fermion systems," *Phys. Rev. B*, vol. 44, pp. 2905–2913, Aug 1991.

[123] A. Rosch and N. Andrei, "Conductivity of a Clean One-Dimensional Wire," *Phys. Rev. Lett.*, vol. 85, pp. 1092–1095, Jul 2000.

[124] A. D. Mirlin, D. G. Polyakov, and V. M. Vinokur, "Transport of Charge-Density Waves in the Presence of Disorder: Classical Pinning Versus Quantum Localization," *Phys. Rev. Lett.*, vol. 99, p. 156405, Oct 2007.

[125] V. Ambegaokar and A. Baratoff, "Tunneling Between Superconductors," *Phys. Rev. Lett.*, vol. 10, pp. 486–489, Jun 1963.

[126] V. Ambegaokar and A. Baratoff, "Tunneling Between Superconductors," *Phys. Rev. Lett.*, vol. 11, pp. 104–104, Jul 1963.

[127] J. J. Quinn and R. A. Ferrell, "Electron Self-Energy Approach to Correlation in a Degenerate Electron Gas," *Phys. Rev.*, vol. 112, pp. 812–827, Nov 1958.

[128] A. V. Chaplik, "Energy spectrum and electron scattering processes in inversion layers," *Sov. Phys. JETP*, vol. 33, p. 997, Nov 1971.

[129] G. F. Giuliani and J. J. Quinn, "Lifetime of a quasiparticle in a two-dimensional electron gas," *Phys. Rev. B*, vol. 26, pp. 4421–4428, Oct 1982.

[130] A. M. Lunde, K. Flensberg, and L. I. Glazman, "Three-particle collisions in quantum wires: Corrections to thermopower and conductance," *Phys. Rev. B*, vol. 75, p. 245418, Jun 2007.

[131] M. Khodas, M. Pustilnik, A. Kamenev, and L. I. Glazman, "Fermi-Luttinger liquid: Spectral function of interacting one-dimensional fermions," *Phys. Rev. B*, vol. 76, p. 155402, Oct 2007.

[132] T. Karzig, L. I. Glazman, and F. von Oppen, "Energy Relaxation and Thermalization of Hot Electrons in Quantum Wires," *Phys. Rev. Lett.*, vol. 105, p. 226407, Nov 2010.

[133] J. J. Sakurai, *Modern quantum mechanics*. Reading, Mass.: Addison-Wesley, rev. ed., reprinted with corr. ed., 1995.

[134] H. Bruus and K. Flensberg, *Many-body quantum theory in condensed matter physics : an introduction*. Oxford graduate texts, Oxford: Oxford Univ. Press, repr. ed., 2006.

[135] P. Coleman, *Introduction to many-body physics*. Cambridge: Cambridge Univ. Press, 2015.

[136] E. M. Lifshitz and L. P. Pitaevskij, *Course of theoretical physics*, vol. 10: Physical kinetics. Oxford: Pergamon Press, 1. ed., 1981.

[137] A. Kamenev, *Field theory of non-equilibrium systems*. Cambridge: Cambridge Univ. Press, 1. publ. ed., 2011.

[138] L. D. Landau and E. M. Lifshitz, *Course of theoretical physics*, vol. 9: Statistical physics, Pt. 2 : theory of condensed state. Butterworth-Heinemann, reprint. ed., 2002.

[139] A. P. Dmitriev, I. V. Gornyi, and D. G. Polyakov, "Coulomb drag between ballistic quantum wires," *Phys. Rev. B*, vol. 86, p. 245402, Dec 2012.

[140] I. V. Protopopov and M. V. Feigel'man, "Coherent transport in Josephson-junction rhombi chain with quenched disorder," *Phys. Rev. B*, vol. 74, p. 064516, Aug 2006.

[141] K. Arutyunov, D. Golubev, and A. Zaikin, "Superconductivity in one dimension," *Phys. Rep.*, vol. 464, no. 1, pp. 1 – 70, 2008.

[142] M. Bard, "Phase slips and the superconductor-insulator transition in disordered wires," Master's thesis, Karlsruhe Institute of Technology, 2014.

[143] Y. Aharonov and A. Casher, "Topological Quantum Effects for Neutral Particles," *Phys. Rev. Lett.*, vol. 53, pp. 319–321, Jul 1984.

[144] T. Giamarchi and H. J. Schulz, "Anderson localization and interactions in one-dimensional metals," *Phys. Rev. B*, vol. 37, pp. 325–340, Jan 1988.

[145] S. F. Edwards and P. W. Anderson, "Theory of spin glasses," *J. Phys. F*, vol. 5, no. 5, p. 965, 1975.

[146] R. Fazio, F. W. J. Hekking, and D. E. Khmelnitskii, "Anomalous Thermal Transport in Quantum Wires," *Phys. Rev. Lett.*, vol. 80, pp. 5611–5614, Jun 1998.

[147] I. V. Gornyi, A. D. Mirlin, and D. G. Polyakov, "Interacting Electrons in Disordered Wires: Anderson Localization and Low-T Transport," *Phys. Rev. Lett.*, vol. 95, p. 206603, Nov 2005.

[148] D. Basko, I. Aleiner, and B. Altshuler, "Metal-insulator transition in a weakly interacting many-electron system with localized single-particle states," *Ann. Phys.*, vol. 321, pp. 1126–1205, May 2006.

[149] M. Bard, I. V. Protopopov, and A. D. Mirlin, "Decay of plasmonic waves in Josephson junction chains," *Phys. Rev. B*, vol. 98, p. 224513, Dec 2018. (arXiv:1810.00807 [cond-mat.supr-con]).

[150] S. Apostolov, D. E. Liu, Z. Maizelis, and A. Levchenko, "Thermal transport and quench relaxation in nonlinear Luttinger liquids," *Phys. Rev. B*, vol. 88, p. 045435, Jul 2013.

[151] J. Lin, K. A. Matveev, and M. Pustilnik, "Thermalization of Acoustic Excitations in a Strongly Interacting One-Dimensional Quantum Liquid," *Phys. Rev. Lett.*, vol. 110, p. 016401, Jan 2013.

[152] I. V. Protopopov, D. B. Gutman, and A. D. Mirlin, "Relaxation in Luttinger liquids: Bose-Fermi duality," *Phys. Rev. B*, vol. 90, p. 125113, Sep 2014.

[153] M. Bard, I. V. Protopopov, and A. D. Mirlin, "Long lifetimes of ultrahot particles in interacting Fermi systems," *Phys. Rev. B*, vol. 97, p. 195147, May 2018.

[154] A. Imambekov and L. I. Glazman, "Universal Theory of Nonlinear Luttinger Liquids," *Science*, vol. 323, pp. 228–231, Jan 2009.

[155] A. Imambekov and L. I. Glazman, "Phenomenology of One-Dimensional Quantum Liquids Beyond the Low-Energy Limit," *Phys. Rev. Lett.*, vol. 102, p. 126405, Mar 2009.

[156] T. Micklitz and A. Levchenko, "Thermalization of Nonequilibrium Electrons in Quantum Wires," *Phys. Rev. Lett.*, vol. 106, p. 196402, May 2011.

[157] Z. Ristivojevic and K. A. Matveev, "Relaxation of weakly interacting electrons in one dimension," *Phys. Rev. B*, vol. 87, p. 165108, Apr 2013.

[158] K. A. Matveev and A. Furusaki, "Decay of Fermionic Quasiparticles in One-Dimensional Quantum Liquids," *Phys. Rev. Lett.*, vol. 111, p. 256401, Dec 2013.

[159] I. V. Protopopov, D. B. Gutman, M. Oldenburg, and A. D. Mirlin, "Dissipationless kinetics of one-dimensional interacting fermions," *Phys. Rev. B*, vol. 89, p. 161104, Apr 2014.

[160] T. Micklitz, J. Rech, and K. A. Matveev, "Transport properties of partially equilibrated quantum wires," *Phys. Rev. B*, vol. 81, p. 115313, Mar 2010.

[161] K. A. Matveev, "Equilibration of a one-dimensional quantum liquid," *J. Exp. Theor. Phys.*, vol. 117, pp. 508–516, sep 2013.

[162] M. Arzamasovs, F. Bovo, and D. M. Gangardt, "Kinetics of Mobile Impurities and Correlation Functions in One-Dimensional Superfluids at Finite Temperature," *Phys. Rev. Lett.*, vol. 112, p. 170602, Apr 2014.

[163] I. V. Protopopov, D. B. Gutman, P. Schmitteckert, and A. D. Mirlin, "Dynamics of waves in one-dimensional electron systems: Density oscillations driven by population inversion," *Phys. Rev. B*, vol. 87, p. 045112, Jan 2013.

[164] B. L. Altshuler and A. G. Aronov, *Electron-electron interaction in disordered conductors, in Electron-electron interactions in disordered systems.* Amsterdam: North Holland, 1985.

[165] I. V. Gornyi, A. D. Mirlin, M. Müller, and D. G. Polyakov, "Absence of many-body localization in a continuum," *Ann. Phys.*, vol. 529, p. 1600365, Feb 2017.

[166] M. Ovadia, D. Kalok, I. Tamir, S. Mitra, B. Sacépé, and D. Shahar, "Evidence for a Finite-Temperature Insulator," *Sci. Rep.*, vol. 5, p. 13503, Aug 2015.

[167] M.-R. Li and E. Orignac, "Heat conduction and Wiedemann-Franz law in disordered Luttinger liquids," *EPL*, vol. 60, no. 3, p. 432, 2002.

[168] M.-S. Choi, M. Y. Choi, T. Choi, and S.-I. Lee, "Cotunneling Transport and Quantum Phase Transitions in Coupled Josephson-Junction Chains with Charge Frustration," *Phys. Rev. Lett.*, vol. 81, pp. 4240–4243, Nov 1998.

[169] M.-S. Choi, M. Y. Choi, and S.-I. Lee, "Capacitively coupled Josephson-junction chains: straight versus slanted coupling," *J. Phys.: Condens. Matter*, vol. 12, no. 6, p. 943, 2000.

List of Figures

Notations and Conventions

We present here a compilation of notations and conventions used throughout this thesis:

- Apart from a few occasions, where we explicitly reintroduce $\hbar$, we use units, in which $\hbar = c = k_B = 1$. Here, $\hbar$ denotes the reduced Planck's constant, k_B Boltzmann's constant, and c the velocity of light.
- Integral signs without specified limits should be understood to run over the whole real line:

$$\int \mathrm{d}x \ldots \equiv \int_{-\infty}^{\infty} \mathrm{d}x \ldots$$

- The Fermi-Dirac distribution function is denoted by

$$n_{\mathrm{F}}(\epsilon) = \frac{1}{\exp\left(\frac{\epsilon-\mu}{T}\right)+1},$$

  where μ is the chemical potential (Fermi energy at zero temperature).
- The Bose-Einstein distribution function is denoted by

$$n_{\mathrm{B}}(\epsilon) = \frac{1}{\exp\left(\frac{\epsilon-\mu}{T}\right)-1},$$

  where the chemical potential is zero for the bosons considered in this thesis, $\mu = 0$.
- Bold symbols denote two- or three-component vectors in two or three dimensions, respectively. Occasionally, one component of a two-dimensional vector is given by the imaginary time.

Next, we introduce the basic notations used throughout the thesis:

a	lattice spacing (ultraviolet cutoff)
C_1	junction capacitance
C_0	ground capacitance (single chain), interchain capacitance (double chain)
C_g	ground capacitance (double chain)
E_1	charging energy related to C_1: $E_1 = (2e)^2/C_1$
E_0	charging energy related to C_0: $E_0 = (2e)^2/C_0$
E_g	charging energy related to C_g: $E_g = (2e)^2/C_g$
E_{J}	Josephson energy
e	elementary charge (italic 'e')
e	Euler's number (upright 'e')

t	(real) time
τ	imaginary time
τ_p	relaxation time as a function of momentum p
$\tau(\omega)$	relaxation time as a function of frequency ω
N	number of junctions (per chain)
$\mathcal{N}$	number of (excess) Cooper pairs
θ	superconducting phase
K	Luttinger parameter (phase stiffness) at the cutoff ($q \sim 1$)
K_0	Luttinger parameter in the case of local Coulomb interaction
Λ	screening length of 1D Coulomb interaction
Ω_0	plasmonic bandwidth in Josephson junction chain
ω_p	plasma frequency of Josephson junction
u_g	group velocity at the cutoff normalized by Ω_0
u_0	velocity of plasmons in Josephson junction chains with local Coulomb interaction
D_Q	disorder strength of random stray charges
D_ξ	disorder strength of phase slips with a random amplitude (variation of device parameters)
$D_{\xi,y}$	effective disorder strength (combination of phase slips with regular and random amplitude)
y	fugacity (amplitude) of a phase slip
ϕ	bosonic field related to density of Cooper pairs
Φ	magnetic flux
Φ_0	(superconducting) magnetic flux quantum
l	logarithm of running RG scale
l_c	length scale related to the curvature of the energy spectrum
T	temperature
β	inverse temperature, $\beta = 1/T$
N_th	thermal length
M	memory function
σ	conductivity
R	resistance
d	width of lateral dimension
D	(spatial) dimension
Δ_n	spacing of subbands
m	mass
p_F	Fermi momentum
ϵ_F	Fermi energy
V	interaction
V_0	zero-momentum component of interaction potential
q_0	characteristic momentum scale of interaction

p	(fermionic) momentum
q	(bosonic) momentum
ϵ	energy
ω	(angular) frequency
$M_{p_1,p_2}^{p_1',p_2'}$	two-particle matrix element
$M_{p_1,p_2,p_3}^{p_1',p_2',p_3'}$	three-particle matrix element
w_q	transition probability (modulus squared matrix element)
$B(x,y)$	Euler Beta function, $B(x,y) = \Gamma(x)\Gamma(y)/\Gamma(x+y)$
$\Gamma(x)$	Gamma function
Im	imaginary part
$\mathcal{P}$	principal value
$\delta(x)$	delta function
$\delta_{i,j}$	Kronecker delta
$\Theta(x)$	Heaviside step function
$\mathrm{sign}(x)$	signum function
$I_n(x)$	modified Bessel function of the first kind
$K_n(x)$	modified Bessel function of the second kind
$L_n(x)$	modified Struve function

Acronyms

1D one-dimensional iii–vi, 1, 5, 9, 13, 16–18, 21, 22, 24, 25, 28, 29, 31, 32, 35, 37, 44, 45, 53, 67, 68, 73, 78–80, 82, 84, 86–92, 123, 124, 129, 131, 132, 137, 139, 141, 142

2D two-dimensional iii, iv, vi, 1, 5–8, 12, 17, 31, 33, 68, 74, 76, 77, 88, 90, 91, 135, 137

3D three-dimensional vi, 68, 77, 87, 88, 91, 138, 140

BKT Berezinskii-Kosterlitz-Thouless iv, 7, 12, 31, 36, 40, 50, 89

IR infrared 38, 45, 47, 48, 50, 115, 125

JJ Josephson junction iii–vi, 1, 5, 7–10, 13, 15–18, 20, 21, 31–35, 37, 38, 45–47, 49, 50, 53, 54, 56, 65, 67, 89–91, 107, 115, 118, 119, 125, 129, 143, 148

LL Luttinger liquid 9, 10, 12, 14, 31, 35, 41, 45, 51

QPS quantum phase slips iii–vi, 6, 18, 31–34, 36–38, 41–47, 49–51, 53–61, 63–65, 89–91, 118, 120, 125, 128, 144, 145, 150

RG renormalization group 10–12, 15, 32, 35–48, 50, 54, 62, 89, 91, 115, 118, 120, 125–128, 145, 150

SIT superconductor-insulator transition iii–vi, 1, 8, 16–18, 31, 32, 42, 48–51, 53, 54, 56, 63, 64, 66, 89–91, 128

SQUID superconducting quantum interference device iii, 1, 2, 4, 5, 16, 18, 31, 34, 50, 51, 90

STM scanning tunneling microscopy 28, 86, 87

UV ultraviolet 10, 11, 34, 37–39, 41, 129

Appendix A

A SIT in JJ chains

This appendix provides a few further details to the superconductor-insulator transition in Josephson junction chains discussed in Chap. 3. In the first part, Sec. A.1, a detailed derivation of the field theory for Josephson junction chains is given. Section A.2 discusses the field theory in the limit $\Lambda \to 0$ (local Coulomb interaction). The RG equations in the case of local charge interaction are derived in A.3, and the memory functions needed for the transport properties are computed in A.4. Section A.5 is devoted to the derivation of the RG equations in the non-local case. Finally, in Sec. A.6 we provide a mapping of the parameters of our theory on JJ chains to the parameters of the theory of Ref. [67] on superconducting wires. The whole appendix A is based on the appendix of Ref. [107].

A.1 Derivation of the field theory in the non-local case

Starting from the lattice model introduced in Sec. 1.2, we derive here the low-energy field theory in a more rigorous way compared to Sec. 3.1. Our procedure follows the standard route outlined in the literature [14, 44, 58, 109, 110, 112]. In order to avoid infrared (IR) divergences, we assume a finite system of N_x junctions and islands in a ring geometry. We assume a clean system and aim to derive the Eqs. (3.3) and (3.6). Disorder can be included straightforwardly.

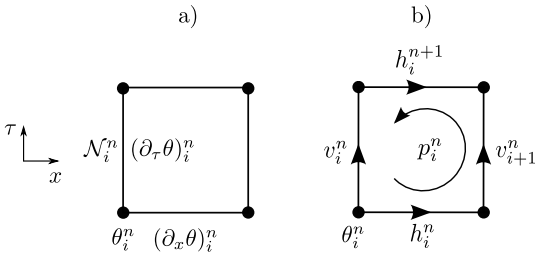

Figure A.1: Variables in the space-time lattice before (left) and after (right) the Villain approximation and Poisson resummation over charges.

Our goal is to derive a path-integral formulation of the partition function. We start by discretizing the imaginary time into N_τ steps of size $\Delta\tau$. We chose the step width to be of the order of the characteristic time for the local dynamics of the system,

$$\Delta\tau = \sqrt{\frac{E_1 + E_0}{E_\mathrm{J} E_1 E_0}} = \frac{1}{\Omega_0}, \tag{A.1}$$

which interpolates between $1/\sqrt{E_\mathrm{J}E_0}$ in the local regime ($\Lambda \to 0$) and $1/\sqrt{E_\mathrm{J}E_1}$ in the case of infinite-range Coulomb interaction ($\Lambda \to \infty$). At each lattice point in the space-time lattice a resolution of identity,

$$\mathbb{1} = \sum_{\mathcal{N}} \int_{-\pi}^{\pi} \frac{\mathrm{d}\theta}{2\pi} \left|\mathcal{N}\right\rangle \left\langle\theta\right| \mathrm{e}^{-i\theta\mathcal{N}}, \tag{A.2}$$

is introduced. Here, $\mathcal{N}$ is the charge and θ the phase of the superconducting island. The phases θ_i^n are attributed tot the lattice sites $(x,\tau) = (i,n)$ and the island charges $\mathcal{N}_i^n$ to the vertical links of the lattice. The discrete partial derivatives of θ are denoted by $\partial_x\theta$ and $\partial_\tau\theta$, and are attributed to the horizontal and vertical links, respectively. See the left panel of Fig. A.1 for a summary of our notations.

The action in these variables reads

$$S = -i \sum_{\text{vert.links}} \mathcal{N}_i^n \left(\partial_\tau\theta\right)_i^n + \frac{E_1\Delta\tau}{2} \sum_{\text{vert.links}} S_{ij}^{-1} \mathcal{N}_i^n \mathcal{N}_j^n + E_\mathrm{J}\Delta\tau \sum_{\text{hor.links}} \left(1 - \cos\left[\left(\partial_x\theta\right)_i^n\right]\right). \tag{A.3}$$

After a Poisson resummation over the charges $\{\mathcal{N}\}_i^n$ in favor of a new integer-valued variable v_i^n that is defined on vertical links, and making use of the Villain approximation

$$\exp[-E_\mathrm{J}\Delta\tau(1-\cos\gamma)] \approx \sum_h \exp\left[-\frac{E_\mathrm{J}\Delta\tau}{2}(\gamma + 2\pi h)^2\right], \tag{A.4}$$

we find

$$S = \frac{K_1^2}{2K} \sum_{\text{vert.links}} S_{ij} \Big[\left(\partial_\tau\theta\right)_i^n - 2\pi v_i^n\Big] \Big[\left(\partial_\tau\theta\right)_j^n - 2\pi v_j^n\Big] + \frac{K}{2} \sum_{\text{hor.links}} \Big[\left(\partial_x\theta\right)_i^n - 2\pi h_i^n\Big]^2. \tag{A.5}$$

Here, we defined $K = \sqrt{E_\mathrm{J}(E_1+E_0)/E_1E_0}$ and introduced the integer-valued variable h_i^n that we attribute to the horizontal links. The partition function can be computed by

$$Z = \int_0^{2\pi} D\theta \sum_{\{v\},\{h\}} e^{-S}, \tag{A.6}$$

where the integration over all phase variables is limited to the interval $(0,\, 2\pi)$. Performing the summation over the longitudinal part ("zero curl") of the vector field (h_i^n, v_i^n) extends the integration over the superconducting phases to the whole real line (ordinary Gaussian integral). After the summation over the longitudinal part of (h_i^n, v_i^n) and integration over the phases, we obtain an action for the "vorticity" of the vector field (h_i^n, v_i^n). It contains the circulation of (h_i^n, v_i^n) around each elementary plaquette of the lattice (cf. right panel of Fig. A.1),

$$p_i^n = h_i^n + v_{i+1}^n - h_i^{n+1} - v_i^n, \tag{A.7}$$

and the two circulations over the "global loops" of the lattice,

$$H_0 = \sum_i h_i^0 \qquad \text{and} \qquad V_0 = \sum_n v_0^n. \tag{A.8}$$

The action assumes now the form in Fourier space (with dimensionless frequency ω)

$$S = \frac{2\pi^2}{N_x N_\tau E_0 \Delta\tau} \bar{V}_0^2 + \frac{2\pi^2 E_\mathrm{J} \Delta\tau}{N_x N_\tau} \bar{H}_0^2 + \frac{2\pi^2 K}{N_x N_\tau} \sum_{(q,\omega)\neq 0} U^{-1}(\omega, q) |p(\omega, q)|^2, \tag{A.9}$$

where

$$U(\omega, q) = \Delta(\omega) + \frac{\Delta(q)}{(1-u_\mathrm{g})\Delta(q) + u_\mathrm{g}}, \tag{A.10}$$

$$\Delta(\xi) = 2(1-\cos\xi)\,, \qquad u_\mathrm{g} = \frac{1}{1+\Lambda^2}, \tag{A.11}$$

and

$$\bar{V}_0 = N_x V_0 + \sum_{i=1}^{N_x - 1} i \sum_n p_i^n, \quad \bar{H}_0 = N_\tau H_0 - \sum_{n=1}^{N_\tau - 1} n \sum_i p_i^n. \tag{A.12}$$

Performing Poisson resummation over V_0, it can be seen that this summation is equivalent to the summation over the sectors with different total charge. We therefore drop it. It is easy to show that the action (A.9) can be recast in the form

$$S = \frac{2\pi^2 E_\mathrm{J} \Delta\tau}{N_x} \sum_{n=0}^{N_\tau - 1} H_n^2 + \frac{2\pi^2 K}{N_x N_\tau} \sum_{q\neq 0,\omega} U^{-1}(\omega, q) |p(\omega, q)|^2, \tag{A.13}$$

where in the second sum all the terms with $q = 0$ are excluded and [cf. definition (A.8)]

$$H_n = \sum_i h_i^n. \tag{A.14}$$

We proceed by introducing the field $\tilde{\phi}$ through a Hubbard-Stratonovich transformation that decouples the vortex interaction term in Eq. (A.13):

$$\begin{aligned} &\exp\left\{ -\frac{2\pi^2 K}{N_x N_\tau} \sum_{q\neq 0,\omega} U^{-1}(\omega, q) |p(\omega, q)|^2 \right\} \propto \\ &\qquad \int \mathcal{D}\tilde{\phi} \exp\left\{ -\frac{1}{2\pi^2 K N_x N_\tau} \sum_{q\neq 0,\omega} U(\omega, q) |\tilde{\phi}(\omega, q)|^2 + \frac{2i}{N_x N_\tau} \sum_{q\neq 0,\omega} \tilde{\phi}(\omega, q) p^*(\omega, q) \right\}. \end{aligned} \tag{A.15}$$

The way the field $\tilde{\phi}(x, \tau)$ introduced, it has no $q = 0$ Fourier components. But, the fields H_n in Eq. (A.13) are related to the local circulations p_i^n by the equation $H^n - H^{n+1} = \sum_i p_i^n$. The sum over H_n is thus constrained. The constraint can be taken into account by introducing a field $\phi_0(\tau)$:

$$\delta\left(H_n - H_{n+1} - \sum_i p_i^n \right) = \int_0^\pi \frac{d\phi_0(n)}{\pi} \exp\left[-2i\phi_0(n) \left(H^n - H^{n+1} - \sum_i p_i^n \right) \right]. \tag{A.16}$$

After performing the summation over H_n, the action reads

$$S = \frac{1}{2\pi^2 K N_x N_\tau} \sum_{q,\omega} U(\omega, q) |\phi(\omega, q)|^2 + 2i \sum_{x,\tau} \phi(x,\tau) p(x,\tau), \tag{A.17}$$

where the field ϕ is compact in time direction (compactification radius π) and has the mode expansion

$$\phi(x,\tau) = \phi_0(\tau) + \frac{\pi m \tau}{N_\tau} + \frac{1}{N_x} \sum_{q \neq 0} \tilde{\phi}_q(\tau), \qquad m \in \mathbb{Z}. \tag{A.18}$$

Apart from the Villain transformation, all transformations in the lattice model so far were exact. Nevertheless, because of the discretization of time, our procedure does not capture the physics at time scales shorter than $\Delta\tau$ which is the characteristic time for a phase slip. It is expected that a finite action cost for phase slips, which are related to the vorticities $p(x,\tau)$, originates from those times scales. Hence the action (A.17) needs to be corrected by adding the term

$$\delta S = S_{\text{short}} \sum_{x,\tau} p^2(x,\tau). \tag{A.19}$$

In the case when the superconducting correlations are (locally) well established, $S_{\text{short}} \gg 1$, the summation over $p(x,\tau)$ can be performed to lowest order in the amplitude $y = \exp\{-S_{\text{short}}\}$ for QPS. The action

$$S = \frac{1}{2\pi^2 K N_x N_\tau} \sum_{q,\omega} U(\omega, q) |\phi(\omega, q)|^2 + 2y \sum_{x,\tau} \cos 2\phi(x,\tau) \tag{A.20}$$

is of sine-Gordon type. The function $U(\omega, q)$ is defined in Eqs. (A.10) and (A.11). Taking the continuum limit ($|\omega|, |q| \ll 1$), we obtain

$$S = \frac{1}{2\pi^2 K} \int_{-1}^{1} \frac{dq}{2\pi} \int_{-\Omega_0}^{\Omega_0} \frac{d\omega}{2\pi} U(\omega, q) |\phi(\omega, q)|^2 + 2y\Omega_0 \int dx d\tau \cos 2\phi(x,\tau)\,, \tag{A.21}$$

where the dimension of frequency is reintroduced and

$$U(\omega, q) = \frac{\omega^2}{\Omega_0} + \frac{q^2 \Omega_0}{(1-u_{\text{g}})q^2 + u_{\text{g}}}, \quad u_{\text{g}} = \frac{1}{1+\Lambda^2}, \tag{A.22}$$

$$K = \sqrt{\frac{E_{\text{J}}(E_1 + E_0)}{E_1 E_0}}, \quad \Omega_0 = \sqrt{\frac{E_{\text{J}} E_1 E_0}{E_1 + E_0}}. \tag{A.23}$$

At this point we have reproduced Eqs. (3.3) and (3.6) of the main text.

We can give another justification for the transition form Eq. (A.17) to Eq. (A.21). Looking at Eq. (A.21) with $y \sim 1$, we recognize that this action can be understood as an expansion in harmonics $\cos n\phi$. From the RG equations of the action (A.17) discussed in the main text, we know that the phase-slip amplitude y is strongly reduced in the first few steps of the RG in the case when the system has strong local superconducting correlations ($K \gg 1$ at short scales). It is easy to see that the amplitudes for higher harmonics renormalize to zero even faster. Conclusively, we can state that the action (A.21) yields a proper description of JJ chains if length scales larger than the lattice spacing and time scales larger than $\Delta\tau$ are considered. The next section (App. A.2) yields further insights on this point by discussing the action (A.17) in the infinite-range limit, $\Lambda \to \infty$.

A.2 Infinite-range interaction

This appendix is devoted to the discussion of the theory of JJ chains in the infinite-range limit, $\Lambda \to \infty$. We draw here another connection between the lattice model and the sine-Gordon theory. In this way we further support the results of App. A.1, obtain an estimate for the fugacity, Eq. (3.7), and compare our findings to previous works.

We start from Eq. (A.13). In the limit $\Lambda \to \infty$, where the interaction between vorticities $U^{-1}(\omega, q)$ is gapped and momentum independent, we can approximate

$$\frac{1}{V}\sum_{q\neq 0,\omega} U^{-1}(\omega,q)|p(\omega,q)|^2 \simeq \frac{1}{V}\sum_{q\neq 0,\omega}|p(\omega,q)|^2 = \sum_{n,i}\left(p_i^n\right)^2 \frac{1}{N_x}\sum_n\left[\sum_i p_i^n\right]^2 .$$

Now the summation over vorticities $\{p\}$ can be performed. Here, because of the constraint $H^n - H^{n+1} = \sum_i p_i^n$ an auxiliary field $\phi^n \in (0,\pi)$ can be introduced [cf. Eq. (A.16)]. This leads to the action

$$S = \frac{(2\pi)^2 K_1}{2N_x}\sum_n (H^n)^2 + 2i\sum_n \phi^n\left(H^{n+1} - H^n\right) - \Delta\tau\sum_n U(\phi^n), \tag{A.24}$$

where

$$\begin{aligned} \mathrm{e}^{-\frac{U(\phi)}{\sqrt{E_\mathrm{J}E_1}}} &= \sum_z \mathrm{e}^{2i\phi z}\exp\left[-f(z)\right], \\ f(z) &= -\frac{(2\pi)^2 K_1}{2N_x}z^2 - \ln\int_0^\pi \frac{d\omega}{\pi} e^{2i\omega z}(g(\omega))^{N_x}, \\ g(\omega) &= \sum_p \exp\left[-\frac{K_1(2\pi)^2 p^2}{2} - 2i\omega p\right]. \end{aligned} \tag{A.25}$$

The action (A.24) corresponds to a particle on a ring with momentum H and coordinate ϕ that moves in the periodic potential $U(\phi)$. Exploiting the periodicity of $f(z)$ (period N_x), we find

$$\mathrm{e}^{-\frac{U(\phi)}{\sqrt{E_\mathrm{J}E_1}}} = \sum_{z_0=0}^{N_x-1}\mathrm{e}^{2i\phi z_0}\exp[-f(z_0)]\sum_{z_1}\mathrm{e}^{2iN_x z_1\phi} = \frac{\pi}{N_x}\sum_{z_0=1}^{N_x-1}\mathrm{e}^{2i\phi z_0}\exp[-f(z_0)]\sum_k \delta\left(\phi - \frac{\pi k}{N_x}\right). \tag{A.26}$$

As a result $U(\phi)$ is not a smooth function, but for $N_x \gg 1$ the exponential $\exp\left[-U(\phi)/\sqrt{E_\mathrm{J}E_1}\right]$ converges in the distributional sense to the discrete Fourier transform

$$\frac{1}{\pi}\exp\left[-\frac{U(\phi)}{\sqrt{E_\mathrm{J}E_1}}\right] \to \sum_{z_0=0}^{N_x-1}\mathrm{e}^{2i\phi z_0}\exp[-f(z_0)]. \tag{A.27}$$

It turns out that in the regime $N_x \gg 1$ and $K_1 \gg 1$, we approximately find

$$U(\phi) \simeq 2y(N_x)[1-\cos 2\phi] + \mathrm{const}\,, \tag{A.28}$$

where

$$y(N_x) = \sqrt{E_\mathrm{J}E_1}N_x\exp\left[-2\pi^2 K_1\left(1-\frac{1}{N_x}\right)\right]. \tag{A.29}$$

This means that we obtain in this limit again a (zero-dimensional) sine-Gordon model. The QPS amplitude at scale N_x for an infinite-range interaction is given by Eq. (A.29). We can compare those findings with the results of Refs. [47, 49]. There, the effective QPS amplitude at scale N_x reads (in our notations)

$$y(N_x) \propto E_{\mathrm{J}}^{3/4} E_1^{1/4} N_x \mathrm{e}^{-8K_1(1-\gamma/N_x)}, \tag{A.30}$$

with $\gamma = 1/2 + \pi^2/8$. Our result (A.29) has the same form in its dependence on K_1 and N_x. However, the numerical coefficient in the exponent of (A.29) deviates from the one in (A.30). This discrepancy in the numerical coefficient is related to the inaccuracy of our theory at the scale of the ultraviolet cutoff $N_x = 1$.

A.3 Derivation of RG equations for local interaction

Here, we briefly discuss the derivation of the RG equations in the regime of local Coulomb interaction, Eqs. (3.22)–(3.26) of Sec. 3.2.1. An introduction to the RG and a detailed derivation of the RG equations of a sine-Gordon theory can be found in Sec. 1.3.2. The correlation function (3.21) is computed perturbatively to second order in y and first order in D_ξ. Up to this order, phase slips with homogeneous and random fugacity do not mix. The correction due to QPS with random fugacity ($\propto D_\xi$) can be read off directly from Ref. [144]. The zeroth order result is

$$R^{(0)}(\mathbf{r}) = \mathrm{e}^{-2\pi K_0 F_1(\mathbf{r})}, \tag{A.31}$$

where

$$F_1(x,\tau) = \frac{1}{2} \ln \left(\frac{x^2 + (u_0|\tau| + a)^2}{a^2} \right). \tag{A.32}$$

Since during the RG an anisotropy between space and time is generated, the slightly generalized function

$$\begin{aligned} R(\mathbf{r}) &= \mathrm{e}^{-2\pi K_0 \tilde{F}_1(\mathbf{r})}, \\ \tilde{F}_1(x,\tau) &= F_1(x,\tau) + \frac{d}{K_0} \cos\left(2\theta_{\mathbf{r}}\right) \end{aligned} \tag{A.33}$$

needs to be considered. Here $\theta_{\mathbf{r}}$ is the angle between the vector $(x, u_0\tau)$ and the x-axis. The anisotropy parameter d vanishes initially but gets generated in the course of the RG [144]. It proves convenient to reintroduce the lattice spacing a. The second-order correction can be extracted by using the equality for the average with respect to the Gaussian action (3.16).

$$\begin{aligned} &\lim_{n\to 0} \sum_{a=1}^{n} \left\langle \mathrm{e}^{2i[\phi^j(\mathbf{r}_1) - \phi^j(\mathbf{r}_2)]} \cos\left[2\phi^a(\mathbf{r}_1)\right] \cos\left[2\phi^a(\mathbf{r}_2)\right] \right\rangle_0 \\ &\quad = \frac{1}{4} \mathrm{e}^{-2\pi K_0 [F_1(\mathbf{r}_1 - \mathbf{r}_2) + F_1(\mathbf{r}_3 - \mathbf{r}_4)]} \sum_{\sigma=\pm} \left[\mathrm{e}^{2\pi K_0 \sigma [F_1(\mathbf{r}_1 - \mathbf{r}_3) + F_1(\mathbf{r}_2 - \mathbf{r}_4) - F_1(\mathbf{r}_1 - \mathbf{r}_4) - F_1(\mathbf{r}_2 - \mathbf{r}_3)]} - 1 \right]. \end{aligned} \tag{A.34}$$

Assuming the Gaussian distribution function

$$P[Q] = \exp\left\{ -\frac{\pi^2}{D_Q a} \int \mathrm{d}x\, Q^2(x) \right\} \tag{A.35}$$

for the random stray charges, we obtain

$$\left\langle \cos[\mathcal{Q}(x_3)]\cos[\mathcal{Q}(x_4)] + \sin[\mathcal{Q}(x_3)]\sin[\mathcal{Q}(x_4)] \right\rangle_Q = \exp\left\{ -D_Q \frac{|x_3 - x_4|}{a} \right\}. \tag{A.36}$$

Thus, the second order correction reads [here $\mathbf{r}_i = (x_i, u_0\tau_i)$]:

$$\begin{aligned} \frac{y^2}{16\pi^3 a^4} \mathrm{e}^{-2\pi K_0 F_1(\mathbf{r}_1-\mathbf{r}_2)} \int \mathrm{d}^2 r_3 \mathrm{d}^2 r_4 \mathrm{e}^{-2\pi K_0 F_1(\mathbf{r}_3-\mathbf{r}_4)} \mathrm{e}^{-D_Q \frac{|x_3-x_4|}{a}} \\ \times \sum_{\sigma=\pm} \left[\mathrm{e}^{2\pi K_0 \sigma [F_1(\mathbf{r}_1-\mathbf{r}_3)+F_1(\mathbf{r}_2-\mathbf{r}_4)-F_1(\mathbf{r}_1-\mathbf{r}_4)-F_1(\mathbf{r}_2-\mathbf{r}_3)]} - 1 \right]. \end{aligned} \tag{A.37}$$

Since the first exponential function in the integrand of the above expression is a power-law of $r = |\mathbf{r}_3 - \mathbf{r}_4|$, the square bracket can be expanded in small r and the integration over the polar angle of $\mathbf{r}$ can be performed. For the integration over the center-of-mass coordinates $\mathbf{R} = (\mathbf{r}_3 + \mathbf{r}_4)/2$, the identities

$$\int \mathrm{d}^2 R \left[F_1(\mathbf{R}-\mathbf{r}_1) - F_1(\mathbf{R}-\mathbf{r}_2) \right] \left(\partial_X^2 + \partial_Y^2 \right) \left[F_1(\mathbf{R}-\mathbf{r}_1) - F_1(\mathbf{R}-\mathbf{r}_2) \right] = -4\pi F_1(\mathbf{r}_1 - \mathbf{r}_2), \tag{A.38}$$

$$\int \mathrm{d}^2 R \left[F_1(\mathbf{R}-\mathbf{r}_1) - F_1(\mathbf{R}-\mathbf{r}_2) \right] \left(\partial_X^2 - \partial_Y^2 \right) \left[F_1(\mathbf{R}-\mathbf{r}_1) - F_1(\mathbf{R}-\mathbf{r}_2) \right] = -2\pi \cos 2\theta_{\mathbf{r}_1-\mathbf{r}_2}. \tag{A.39}$$

are useful. Finally, we arrive at the second order correction

$$\begin{aligned} 2\pi \frac{y^2}{2} K_0^2 \int_a^\infty \frac{\mathrm{d}r}{a} \left(\frac{r}{a} \right)^{3-2\pi K_0} \Bigg\{ F_1(\mathbf{r}_1 - \mathbf{r}_2) \left[\mathrm{I}_0\left(D_Q \frac{r}{a} \right) - \mathrm{L}_0\left(D_Q \frac{r}{a} \right) \right] \\ + \frac{1}{2} \cos 2\theta_{\mathbf{r}_1-\mathbf{r}_2} \left[\mathrm{I}_2\left(D_Q \frac{r}{a} \right) - \mathrm{L}_2\left(D_Q \frac{r}{a} \right) - \frac{2}{3\pi} D_Q \frac{r}{a} \right] \Bigg\}, \end{aligned} \tag{A.40}$$

where I_n and L_n are modified Bessel functions of the first kind and modified Struve functions, respectively. Combining this result with the zeroth order term, we can reexponentiate to obtain the form $\exp\left[-2\pi K_0^{\mathrm{eff}} \tilde{F}_1(\mathbf{r}_1 - \mathbf{r}_2) \right]$ with

$$K_0^{\mathrm{eff}} = K_0 - \frac{y^2}{2} K_0^2 \int_a^\infty \frac{\mathrm{d}r}{a} \left(\frac{r}{a} \right)^{3-2\pi K_0} \left[\mathrm{I}_0\left(D_Q \frac{r}{a} \right) - \mathrm{L}_0\left(D_Q \frac{r}{a} \right) \right], \tag{A.41}$$

$$d_{\mathrm{eff}} = d - \frac{y^2}{4} K_0^2 \int_a^\infty \frac{\mathrm{d}r}{a} \left(\frac{r}{a} \right)^{3-2\pi K_0} \left[\mathrm{I}_2\left(D_Q \frac{r}{a} \right) - \mathrm{L}_2\left(D_Q \frac{r}{a} \right) - \frac{2}{3\pi} D_Q \frac{r}{a} \right], \tag{A.42}$$

and

$$\tilde{F}_1(\mathbf{r}) = F_1(\mathbf{r}) + \frac{d_{\mathrm{eff}}}{K_0^{\mathrm{eff}}} \cos\left(2\theta_{\mathbf{r}} \right). \tag{A.43}$$

The effective constants K_0^{eff} and d_{eff} govern the low-energy properties of the correlation function R. A variation of the cutoff $a \to a + \mathrm{d}a$ should not affect them. Hence, we obtain

$$K_0(a+\mathrm{d}a) = K_0(a) - \frac{y^2}{2}K_0^2\left[\mathrm{I}_0\left(D_Q\right) - \mathrm{L}_0\left(D_Q\right)\right]\frac{\mathrm{d}a}{a}, \tag{A.44}$$

$$d(a+\mathrm{d}a) = d(a) - \frac{y^2}{4}K_0^2\left[\mathrm{I}_2\left(D_Q\frac{r}{a}\right) - \mathrm{L}_2\left(D_Q\frac{r}{a}\right) - \frac{2}{3\pi}D_Q\frac{r}{a}\right]\frac{\mathrm{d}a}{a}, \tag{A.45}$$

$$y^2(a+\mathrm{d}a) = y^2(a)\left(\frac{a+da}{a}\right)^{4-2\pi K_0}, \tag{A.46}$$

$$D_Q(a+da) = D_Q(a)\frac{a+da}{a}. \tag{A.47}$$

After parametrizing $a(l) = \mathrm{e}^l$, we arrive at the equations for K_0, y and D_Q [cf. Eqs. (3.22)–(3.25)]. The renormalization of u_0 can be inferred from the renormalization of d by [144]

$$\frac{\mathrm{d}u_0}{\mathrm{d}l} = -2\frac{u_0}{K_0}\frac{\mathrm{d}d}{\mathrm{d}l}. \tag{A.48}$$

The renormalization due to S_ξ up to the first order in D_ξ is the same as in Ref. [144].

A.4 Memory function

Here the details of the computation of the memory function in regime of local charge interaction are presented. The results are used in Sec. 3.2.2 to study the transport characteristics in the local limit. An introduction to the memory-function formalism can be found in Sec. 1.3.3. The Hamiltonian corresponding to the action (3.15) in the limit $\Lambda \to 0$ reads

$$\mathcal{H} = \mathcal{H}_0 + \mathcal{H}_{\text{ps}} + \mathcal{H}_\xi, \tag{A.49}$$

$$\mathcal{H}_0 = \frac{1}{2}\int \mathrm{d}x\,\left[u_0K_0\left(\partial_x\theta\right)^2 + \frac{u_0}{\pi^2K_0}\left(\partial_x\phi\right)^2\right], \tag{A.50}$$

$$\mathcal{H}_{\text{ps},Q} = \frac{yu_0}{\sqrt{2\pi^3}a^2}\int \mathrm{d}x\,\cos\left[2\phi(x) - \mathcal{Q}(x)\right], \tag{A.51}$$

$$\mathcal{H}_\xi = \int \mathrm{d}x\,\left[\frac{\xi(x)}{a^{3/2}}\mathrm{e}^{2i\phi(x)} + \text{h.c.}\right]. \tag{A.52}$$

For convenience, we reintroduced explicitly the lattice spacing a; the parameter u_0 is also rescaled by a such that it has the dimension length divided by time. The commutator of $\mathcal{H}$ and the current operator can be separated into the two parts $F = F_{\text{ps}} + F_\xi$, where

$$F_{\text{ps}} = -2\sqrt{\frac{2}{\pi}}ieu_0^2K_0\frac{y}{a^2}\Big[\sin 2\phi(x)\cos\mathcal{Q}(x) + \cos 2\phi(x)\sin\mathcal{Q}(x)\Big], \tag{A.53}$$

$$F_\xi = -4\pi e\frac{u_0}{a^{3/2}}K_0\left[\xi(x)\mathrm{e}^{2i\phi(x)} - \xi^*(x)\mathrm{e}^{-2i\phi(x)}\right]. \tag{A.54}$$

As a next step we calculate the correlation function

$$C(\omega) = \int \mathrm{d}x\int_0^\infty \mathrm{d}t\,\mathrm{e}^{i\omega t}\left\langle\left[F(x,t),F(0,0)\right]\right\rangle, \tag{A.55}$$

where the angular brackets compromise the averaging with respect to $\mathcal{H}$ as well as over disorder. The averaging can be performed with respect to $\mathcal{H}_0$ instead of $\mathcal{H}$ if one is interested only in the lowest order result in y and D_ξ. Moreover, up to this order, the correlator $C(\omega)$ can be separated into two independent parts, $C = C_{\rm ps} + C_\xi$. The next two sections present the calculation of each of them.

A.4.1 Random fugacity part

The computation of the memory function of a disordered 1D system can be found in Ref. [167]. In order to provide a complete presentation, we present the main steps here as well. We start by computing the (time-ordered) correlator

$$C_\xi(x,\tau) = \left\langle T_\tau F_\xi(x,\tau) F_\xi(0,0) \right\rangle \tag{A.56}$$

in imaginary time τ. The average over the quadratic Hamiltonian yields

$$\left\langle \mathrm{e}^{2i\phi(x,\tau)} \mathrm{e}^{-2i\phi(0,0)} \right\rangle_0 = \mathrm{e}^{-2\pi K_0 F_1(x,\tau)}, \tag{A.57}$$

where at finite temperature $1/\beta$

$$F_1(x,\tau) = \frac{1}{2} \ln \left[\frac{\beta^2 u_0^2}{\pi^2 a^2} \sinh\left(\frac{\pi}{u_0 \beta} x_+ \right) \sinh\left(\frac{\pi}{u_0 \beta} x_- \right) \right] \tag{A.58}$$

and $x_\pm = x \pm i u_0 \tau$. Performing the disorder average, we find

$$C_\xi(x,\tau) = -8e^2 \frac{u_0^4}{a^3} K_0^2 D_\xi \delta(x) \mathrm{e}^{-2\pi K_0 F_1(x,\tau)}. \tag{A.59}$$

In order to find the retarded correlation function, this result should be analytically continued (cf. Ref. [17]),

$$C_\xi(t>0) = A \left(\frac{\pi a}{u_0 \beta} \right)^{2\pi K_0} \left[\sinh\left(\frac{\pi t}{\beta} \right) \right]^{-2\pi K_0}, \tag{A.60}$$

where $A = 16e^2 (u_0^4/a^3) K_0^2 D_\xi \sin(\pi^2 K_0)$. Fourier transforming the result to real frequency results in

$$C_\xi(\omega) = \int_0^\infty \mathrm{d}t\, \mathrm{e}^{i\omega t} C_\xi(t) = \frac{A\, a}{u_0} \left(\frac{2\pi a}{\beta u_0} \right)^{2\pi K_0 - 1} \mathrm{B}\left(1 - 2\pi K_0, \pi K_0 - \frac{i\omega\beta}{2\pi} \right), \tag{A.61}$$

where $\mathrm{B}(x,y)$ is Euler's Beta function. Strictly speaking, the integral in Eq. (A.61) does not converge for $2\pi K_0 > 1$. However, the result can be analytically continued. In the DC limit, $\omega \to 0$, the memory function reads

$$M_\xi(T) = \frac{2\pi i\, \Gamma^2(\pi K_0) u_0 K_0}{\Gamma(2\pi K_0) a} D_\xi \left(\frac{2\pi a T}{u_0} \right)^{2\pi K_0 - 2}, \tag{A.62}$$

and leads to Eq. (3.45) of the main text.

A.4.2 Phase-slip part

The calculation of the phase-slip part goes completely analogous. The correlation function $C_{\rm ps}$ has the form

$$C_{\rm ps}(x,\tau)=\Big\langle T_\tau F_{\rm ps}(x,\tau)F_{\rm ps}(0,0)\Big\rangle=-\frac{4}{\pi}e^2(u_0/a)^4K_0^2y^2\mathrm{e}^{-2\pi K_0F_1(x,\tau)}\mathrm{e}^{-D_Q|x|/a} \tag{A.63}$$

in imaginary time. The analytic continuation to real time reads

$$C_{\rm ps}(\omega)=\gamma\left(\frac{\pi a}{u_0\beta}\right)^{2\pi K_0}\int_0^\infty \mathrm{d}t\int_{-u_0t}^{u_0t}\mathrm{d}x\frac{e^{i\omega t}\mathrm{e}^{-D_Q|x|/a}}{\left[\sinh\left(\frac{\pi}{u_0\beta}(u_0t-x)\right)\sinh\left(\frac{\pi}{u_0\beta}(u_0t+x)\right)\right]^{\pi K_0}} \tag{A.64}$$

with $\gamma=(8/\pi)e^2(u_0/a)^4K_0^2y^2\sin(\pi^2K_0)$. Introducing the light-cone variables $z=\pi/(u_0\beta)\,(u_0t+x)$ and $\bar z=\pi/(u_0\beta)\,(u_0t-x)$ yields

$$C_{\rm ps}(\omega)=\gamma\frac{u_0\beta^2}{2\pi^2}\left(\frac{\pi a}{u_0\beta}\right)^{2\pi K_0}\int_0^\infty\mathrm{d}z\int_0^\infty\mathrm{d}\bar z\,\frac{e^{i\frac{\beta\omega}{2\pi}(z+\bar z)}\mathrm{e}^{-\frac{D_Qu_0\beta}{2\pi a}|z-\bar z|}}{\left[\sinh(z)\sinh(\bar z)\right]^{\pi K_0}}. \tag{A.65}$$

Outside the region $0<K_0<1/\pi$, the integrals are divergent. However, analytic continuation can be employed to extend the result for all $K_0>0$. In the following we analyze the integrals in the limit of weak and strong disorder. In the case of weak disorder, $D_Qu_0\beta/a\ll1$, we obtain in the zeroth order

$$C_{\rm ps}^{(0)}(\omega)=\frac{\gamma}{4}\frac{u_0\beta^2}{2\pi^2}\left(\frac{2\pi a}{u_0\beta}\right)^{2\pi K_0}\mathrm{B}^2\left(1-\pi K_0,\frac{\pi K_0}{2}-\frac{i\beta\omega}{4\pi}\right). \tag{A.66}$$

The first order correction in the limit $\omega\to0$ is of the form

$$C_{\rm ps}^{(1)}(\omega)\overset{\omega\to0}{\to}-\frac{D_Qu_0\beta}{2\pi a}\gamma\frac{u_0\beta^2}{2\pi^2}\left(\frac{\pi a}{u_0\beta}\right)^{2\pi K_0}\left(A_1(K_0)+\frac{i\beta\omega}{2\pi}A_2(K_0)\right), \tag{A.67}$$

with the dimensionless functions A_1 and A_2 that are defined as

$$A_1(K_0)=\int_0^\infty\mathrm{d}z\int_0^\infty\mathrm{d}\bar z\,\frac{|z-\bar z|}{\left(\sinh z\sinh\bar z\right)^{\pi K_0}},\qquad A_2(K_0)=\int_0^\infty\mathrm{d}z\int_0^\infty\mathrm{d}\bar z\,\frac{(z+\bar z)|z-\bar z|}{\left(\sinh z\sinh\bar z\right)^{\pi K_0}}. \tag{A.68}$$

In the zero-frequency limit, the memory function is given by

$$M_{\rm ps}(T)=\frac{iu_0K_0}{2a}y^2\left[\frac{\Gamma^4(\pi K_0/2)}{\Gamma^2(\pi K_0)}\left(\frac{2\pi aT}{u_0}\right)^{2\pi K_0-3}-2^{3-2\pi K_0}\frac{1}{\pi}\sin\left(\pi^2K_0\right)A_2(K_0)D_Q\left(\frac{2\pi aT}{u_0}\right)^{2\pi K_0-4}\right]. \tag{A.69}$$

In the clean limit, $D_Q=0$, a similar result was found in Ref. [122] in the context of umklapp scattering in 1D systems. In the opposite limit of strong disorder, $D_Qu_0\beta/a\gg1$, the main contribution to the integrals comes from the region close to the diagonal $z=\bar z$. The result reads

$$C_{\rm ps}(\omega)\approx\gamma\frac{u_0\beta^2}{2\pi^2}\left(\frac{\pi a}{u_0\beta}\right)^{2\pi K_0}\int_0^\infty\mathrm{d}z\,\frac{e^{i\frac{\beta\omega}{\pi}z}}{\left[\sinh(z)\right]^{2\pi K_0}}\int_0^\infty\mathrm{d}\bar z\,\mathrm{e}^{-\frac{D_Qu_0\beta}{2\pi a}|z-\bar z|} \tag{A.70}$$

$$\approx\gamma\frac{2a^2}{u_0D_Q}\left(\frac{2\pi a}{u_0\beta}\right)^{2\pi K_0-1}\mathrm{B}\left(1-2\pi K_0,\pi K_0-\frac{i\beta\omega}{2\pi}\right). \tag{A.71}$$

In the DC limit, the memory function is given by

$$M_{\rm ps}(T) = \frac{2iu_0K_0}{a}\frac{\Gamma^2(\pi K_0)}{\Gamma(2\pi K_0)}\frac{y^2}{D_Q}\left(\frac{2\pi aT}{u_0}\right)^{2\pi K_0-2}. \tag{A.72}$$

The equations (A.69) and (A.72) lead to Eq. (3.38) in Sec. 3.2.2.

A.5 Non-local Coulomb interaction: RG analysis

This section in the appendix is devoted to the details of the derivation of the RG equations for JJ chains with non-local Coulomb interaction. In the main text those equations are discussed in Sec. 3.3.1. We start from Eqs. (3.48) and (3.10).

A.5.1 Lowest-order scaling

The RG equations to zeroth order in the fugacity for K and $u_{\rm g}$, Eqs. (3.51) and (3.52), can be obtained by straightforward dimensional analysis. The equation for the phase-slip amplitude is found following the standard procedure [17]. In a Wilsonian type of the RG we average the QPS action over the fast modes. Using the cutoff procedure stated in the main text (Sec. 3.3.1), we get

$$\frac{dy(l)}{dl} = \frac{1+u_{\rm g}}{2}y(l)\left[2-\pi K\varepsilon\left(u_{\rm g}\right)\right], \tag{A.73}$$

where

$$\varepsilon(u_{\rm g}) = \frac{4}{\pi(1+u_g)}\int_0^1 {\rm d}q\left(\frac{1}{q^2+1}+u_{\rm g}\frac{q^2+u_{\rm g}(1-q^2)}{2q^2+u_{\rm g}(1-q^2)}\right). \tag{A.74}$$

For $0 \le u_{\rm g} \le 1$, the function $\varepsilon(u_{\rm g})$ is smooth. At $u_{\rm g}=1$ the function assumes the universal value $\varepsilon(1)=1$, which leads to the correct scaling of y at the IR fixed point $u_{\rm g}=1$. However, at $u_{\rm g}=0$ the function is non-universal; it depends on the precise cutoff procedure. Using our cutoff procedure, we find $\varepsilon(0)=1$. Furthermore, the maximal variation of $\epsilon(u_{\rm g})$ on the interval $0 \le u_{\rm g} \le 1$ is of the order of 2%. As a result we set $\varepsilon(u_{\rm g}) \equiv 1$ which yields Eq. (3.53).

A.5.2 Correlation functions and second-order correction

In order to derive the RG equations to second order in the fugacity y, we study the behavior of the vertex function

$$R(\mathbf{r}_1) = \left\langle {\rm e}^{2i\phi(\mathbf{r}_1)}{\rm e}^{-2i\phi(0)}\right\rangle \tag{A.75}$$

under the variation of the cutoff. From the requirement

$$R_{{\rm d}l}(x_1(1+{\rm d}l),\tau_1(1+u_{\rm g}{\rm d}l),u_{\rm g}(0),K(0)) = R_{l=0}(x_1,\tau_1,u_{\rm g}({\rm d}l),K({\rm d}l)). \tag{A.76}$$

the scaling equations can be extracted. We denote by $R_{{\rm d}l}$ the correlation function in the theory with momentum cutoff $|q| \le 1-{\rm d}l$ whereas $R_{l=0}$ denotes for the correlation function with initial cutoff $|q| \le 1$. The zeroth-order correlation function reads

$$R^{(0)}(\mathbf{r}_1) = {\rm e}^{-2KF(\mathbf{r}_1)} \tag{A.77}$$

with

$$F(\mathbf{r}) = \pi^2 \int_{|q|<1} \frac{\mathrm{d}q}{2\pi} \int_{|\omega|<\Omega_0} \frac{\mathrm{d}\omega}{2\pi} \frac{2 - 2\cos qx \cos \omega\tau}{\frac{\omega^2}{\Omega_0} + \frac{\Omega_0 q^2}{(1-u_\mathrm{g})q^2+u_\mathrm{g}}}. \tag{A.78}$$

The equations (3.51) and (3.52) can be straightforwardly obtained with the help of the condition (A.76). The second order correction reads (cf. similar discussion in App. A.3)

$$\delta R = \frac{y^2}{4\pi^3} K^2 \mathrm{e}^{-2KF(\mathbf{r}_1)} \int \mathrm{d}^2 r\, \mathrm{e}^{-2KF(\mathbf{r})} \mathrm{e}^{-2\pi^2 D_Q |x|} \int \mathrm{d}^2 R \left[\mathbf{r} \cdot \nabla_{\mathbf{R}} \left(F(\mathbf{R} - \mathbf{r}_1) - F(\mathbf{R})\right)\right]^2. \tag{A.79}$$

Here, the time is made dimensionless by rescaling it with Ω_0. Cross terms of the form $x \cdot \tau$ vanish because the function $F(\mathbf{r})$ is even in x and τ. Rewriting the integrations over the center-of-mass coordinates in Fourier space yields

$$\delta R = \frac{y^2}{4\pi^3} K^2 \mathrm{e}^{-2KF(\mathbf{r}_1)} \int \frac{\mathrm{d}^2 q}{(2\pi)^2} \left[I_x q^2 + I_\tau \omega^2\right] \left(2 - 2\cos \mathbf{q}\mathbf{r}_1\right) F^2(\mathbf{q}), \tag{A.80}$$

where

$$I_\zeta = \int \mathrm{d}^2 r\, \zeta^2\, \mathrm{e}^{-2KF(\mathbf{r})} \mathrm{e}^{-D_Q|x|}, \qquad \zeta = x, \tau\,, \tag{A.81}$$

and

$$F(\mathbf{q}) = -\frac{2\pi^2}{\omega^2 + \frac{q^2}{(1-u_\mathrm{g})q^2+u_\mathrm{g}}}. \tag{A.82}$$

After the first step of RG, we find

$$\begin{aligned} \delta R_{\mathrm{d}l}(\tilde{x}_1, \tilde{\tau}_1) = \frac{y^2(0)}{4\pi^3} K^2(0) \mathrm{e}^{-2K(0)F_{\mathrm{d}l}(\tilde{x}_1, \tilde{\tau}_1, u_\mathrm{g}(0))} \int_{|q|<1-\mathrm{d}l} \frac{\mathrm{d}q}{2\pi} \int_{|\omega|<1-u_\mathrm{g}\mathrm{d}l} \frac{\mathrm{d}\omega}{2\pi} \left(2 - 2\cos \mathbf{q}\tilde{\mathbf{r}}_1\right) \\ \times F^2(\mathbf{q}, u_\mathrm{g}(0)) \left[q^2\, I_{x,\mathrm{d}l}(K(0), u_\mathrm{g}(0), D_Q(0)) + \omega^2\, I_{\tau,\mathrm{d}l}(K(0), u_\mathrm{g}(0), D_Q(0))\right]. \end{aligned} \tag{A.83}$$

From the zeroth-order result (see above) it holds

$$K(0) F_{\mathrm{d}l}(\tilde{x}_1, \tilde{\tau}_1, u_\mathrm{g}(0)) = K^{(0)}(\mathrm{d}l) F_0(x_1, \tau_1, u_\mathrm{g}^{(0)}(\mathrm{d}l)), \tag{A.84}$$

$$x_1(1 + \mathrm{d}l) = \tilde{x}_1, \qquad \tau_1(1 + u_\mathrm{g}\mathrm{d}l) = \tilde{\tau}_1. \tag{A.85}$$

The superscript (0) indicates that only corrections for $y = 0$ are taken into account. A straightforward calculation shows that

$$\begin{aligned} I_{x,\mathrm{d}l}(K(0), u_\mathrm{g}(0), D_Q(0)) &= (1 + \mathrm{d}l)^3 (1 + u_\mathrm{g}\mathrm{d}l)\, I_{x,0}(K^{(0)}(\mathrm{d}l), u_\mathrm{g}^{(0)}(\mathrm{d}l), D_Q(\mathrm{d}l)), \\ I_{\tau,\mathrm{d}l}(K(0), u_\mathrm{g}(0), D_Q(0)) &= (1 + \mathrm{d}l)(1 + u_\mathrm{g}\mathrm{d}l)^3\, I_{\tau,0}(K^{(0)}(\mathrm{d}l), u_\mathrm{g}^{(0)}(\mathrm{d}l), D_Q(\mathrm{d}l)). \end{aligned} \tag{A.86}$$

The disorder strength of stray charges is renormalized according to $D_Q(\mathrm{d}l) = (1 + \mathrm{d}l) D_Q(0)$. The integrals in Eq. (A.83) over momentum and frequency are rescaled as $\tilde{q} = (1+\mathrm{d}l)q$ and $\tilde{\omega} = (1+u_\mathrm{g}\mathrm{d}l)\omega$. Moreover, we make use of

$$K^2(0) F_{\mathrm{d}l}^2(\mathbf{q}, u_\mathrm{g}(0)) = (1 + \mathrm{d}l)^2 (1 + u_\mathrm{g}\mathrm{d}l)^2 \left(K^{(0)}(\mathrm{d}l)\right)^2 F_0^2(\tilde{\mathbf{q}}, u_\mathrm{g}^{(0)}(\mathrm{d}l)). \tag{A.87}$$

Now, we obtain

$$\begin{aligned}\delta R_{\mathrm{d}l}(\tilde{r}_1, u_{\mathrm{g}}(0), K(0), D_Q(0)) &= \frac{y^2(0)}{4\pi^3}(1+\mathrm{d}l)^2(1+u_{\mathrm{g}}\mathrm{d}l)^2\left(K^{(0)}(\mathrm{d}l)\right)^2 \mathrm{e}^{-2K^{(0)}(\mathrm{d}l)F_0(r_1,u_{\mathrm{g}}^{(0)}(\mathrm{d}l))} \\ &\times \int_{|\mathbf{q}|<1}\frac{\mathrm{d}^2\tilde{q}}{(2\pi)^2}\left[\tilde{q}^2 I_{x,0}(K^{(0)}(\mathrm{d}l), u_{\mathrm{g}}^{(0)}(\mathrm{d}l), D_Q(\mathrm{d}l)) + \tilde{\omega}^2 I_{\tau,0}(K^{(0)}(\mathrm{d}l), u_{\mathrm{g}}^{(0)}(\mathrm{d}l), D_Q(\mathrm{d}l)\right] \\ &\times \left[2-2\cos\tilde{\mathbf{q}}\mathbf{r}_1\right] F_0^2(\tilde{\mathbf{q}}, u_{\mathrm{g}}^{(0)}(\mathrm{d}l)).\end{aligned} \tag{A.88}$$

The correlation function R (up to second order) can now be written as

$$\begin{aligned}R_{\mathrm{d}l}(\mathbf{r}_1) = \mathrm{e}^{-2KF(\mathbf{r}_1)}&\left\{1+\frac{y^2(\mathrm{d}l)}{4\pi^3}K^2\int\frac{\mathrm{d}^2q}{(2\pi)^2}\left[q^2 I_{x,0}+\omega^2 I_{\tau,0}\right](2-2\cos\mathbf{q}\mathbf{r}_1)F_0^2(\mathbf{q})\right\} \\ &\times\left\{1+\frac{\pi}{2}(1+u_{\mathrm{g}})y^2(0)K^3\mathrm{d}l\int\frac{\mathrm{d}^2q}{(2\pi)^2}\left[q^2 I_{x,0}+\omega^2 I_{\tau,0}\right](2-2\cos\mathbf{q}\mathbf{r}_1)F_0^2(\mathbf{q})\right\},\end{aligned} \tag{A.89}$$

where we suppressed the superscript (0) to make the equation better readable. Furthermore, the scaling law for the fugacity

$$y(\mathrm{d}l) = \left[1+\left(1+u_{\mathrm{g}}-\frac{\pi}{2}(1+u_{\mathrm{g}})K\right)\mathrm{d}l\right]y(0). \tag{A.90}$$

is used. The correlation function (A.89) should be compared to the correlation function calculated with the original cutoff but with rescaled couplings,

$$\begin{aligned}R_{l=0} = \mathrm{e}^{-2K(0)F_0(\mathbf{r}_1,u_{\mathrm{g}}(0))}&\left\{1-2\,\delta K\,F_0(\mathbf{r}_1)-2K\frac{\partial F_0}{\partial u_{\mathrm{g}}}\delta u_{\mathrm{g}}\right\} \\ &\times\left\{1+\frac{y^2(\mathrm{d}l)}{4\pi^3}K^2\int\frac{\mathrm{d}^2q}{(2\pi)^2}\left[q^2 I_{x,0}+\omega^2 I_{\tau,0}\right](2-2\cos\mathbf{q}\mathbf{r}_1)F_0^2(\mathbf{q})\right\},\end{aligned} \tag{A.91}$$

where the corrections $\delta K = K(\mathrm{d}l)-K(0)$ and $\delta u_{\mathrm{g}} = u_{\mathrm{g}}(\mathrm{d}l)-u_{\mathrm{g}}(0)$ are introduced. The renormalization of the quadratic action at all momenta $\mathbf{q}$ can be done only in the framework of a functional RG. Instead of a functional RG we limit ourselves to the renormalization of the long-wavelength limit of $F_0(\mathbf{q})$:

$$F_0(\mathbf{q}) \simeq \frac{-2\pi^2}{\omega^2+q^2/u_{\mathrm{g}}}. \tag{A.92}$$

In this way we find

$$\begin{aligned}\delta K &= -\frac{1}{2}(1+u_{\mathrm{g}})y^2K^3 I_{\tau,0}\,\mathrm{d}l, \\ \delta u_{\mathrm{g}} &= \frac{1}{2}(1+u_{\mathrm{g}})y^2K^2u_{\mathrm{g}}(I_{\tau,0}-u_{\mathrm{g}}I_{x,0})\,\mathrm{d}l.\end{aligned} \tag{A.93}$$

This approximation is justified since at the initial stage of the RG the dominant effect on the renormalization of K and u_{g} originates from the zeroth order in the fugacity y. Furthermore, at large scales where the local limit is reached, our approximation yields the asymptotically correct form for

the renormalization to second order in y. To the level of our accuracy, we can compute the functions $I_{x,0}$ and $I_{\tau,0}$ in the local limit:

$$I_x \simeq C\frac{1}{K}\left[\mathrm{I}_0(D_Q) - \mathrm{L}_0(D_Q) - \frac{\mathrm{I}_1(D_Q) - \mathrm{L}_1(D_Q)}{D_Q}\right], \tag{A.94}$$

$$I_\tau \simeq C\frac{1}{K}\frac{\mathrm{I}_1(D_Q) - \mathrm{L}_1(D_Q)}{D_Q}, \tag{A.95}$$

where C is a number that is set to unity, and I_n and L_n denote modified Bessel functions of the first kind and modified Struve functions, respectively. Finally, we can state the RG equations up to second order in the QPS amplitude:

$$\frac{\mathrm{d}K}{\mathrm{d}l} = -(1-u_\mathrm{g})K - \frac{1}{2}y^2K^2(1+u_\mathrm{g})\frac{\mathrm{I}_1(D_Q) - \mathrm{L}_1(D_Q)}{D_Q}, \tag{A.96}$$

$$\frac{\mathrm{d}y}{\mathrm{d}l} = \frac{1+u_\mathrm{g}}{2}\left[2-\pi K\right]y, \tag{A.97}$$

$$\frac{\mathrm{d}u_\mathrm{g}}{\mathrm{d}l} = 2u_\mathrm{g}(1-u_\mathrm{g}) + \frac{y^2}{2}K(1+u_\mathrm{g})u_\mathrm{g}\left[(1+u_\mathrm{g})\frac{\mathrm{I}_1(D_Q) - \mathrm{L}_1(D_Q)}{D_Q} - u_\mathrm{g}\left(\mathrm{I}_0(D_Q) - \mathrm{L}_0(D_Q)\right)\right], \tag{A.98}$$

$$\frac{\mathrm{d}D_Q}{\mathrm{d}l} = D_Q. \tag{A.99}$$

Those equations lead to Eqs. (3.56)–(3.58) of Sec. 3.3.1 in the main text. The Bessel and Struve functions have the following asymptotic behavior:

$$\mathrm{I}_0(x) - \mathrm{L}_0(x) \sim \begin{cases} 1 - \frac{2}{\pi}x, & x \to 0, \\ \frac{2}{\pi x}, & x \to \infty, \end{cases} \tag{A.100}$$

$$\frac{1}{x}\left[\mathrm{I}_1(x) - \mathrm{L}_1(x)\right] \sim \begin{cases} \frac{1}{2} - \frac{3}{2\pi}x, & x \to 0, \\ \frac{2}{\pi x}, & x \to \infty. \end{cases} \tag{A.101}$$

The scaling equation for the temperature can be inferred from the rescaling of frequencies as $\tilde{\omega} = (1 + u_\mathrm{g}\mathrm{d}l)\omega$. The result is stated in Eq. (3.60).

A.6 Gaussian phase fluctuations: Comparison of JJ chains with superconducting nanowires

We expect that a model similar to the one introduced in Sec. 3.1 should also describe the properties of multi-channel disordered superconducting wires close to the SIT and deeply in the superconducting and insulating phases [47, 67, 68]. By comparing our action to the one derived in Ref. [67, 68] in the context of a dirty multi-channel wire, the following correspondence of parameters is found:

$$\frac{1}{aE_0} \leftrightarrow \frac{\tilde{C}}{e^2}, \qquad \frac{a}{E_1} \leftrightarrow \frac{s\,\sigma}{e^2\Delta}, \qquad aE_\mathrm{J} \leftrightarrow s\,\sigma\Delta/e^2. \tag{A.102}$$

Here $\tilde{C}$ is the capacitance per unit length, σ the conductance in the normal state, s the cross section of the wire, and Δ is the modulus of the superconducting order parameter. Further, a is the lattice

spacing of JJ chain that we reintroduced into our action. The behavior of the capacitance per unit length of the wire in 1D is

$$\tilde{C}^{-1} \sim \ln(d/R), \tag{A.103}$$

where the radius of the wire is denoted by R and the distance to a nearby metallic plate by d. With the help of the RHS of Eq. (A.102) we can calculate the (dimensionless) parameter K_0 as well as the screening length $L_s \equiv a\Lambda$. We find

$$K_0 \sim \sqrt{\frac{\tilde{C}}{r_s} N_{\mathrm{ch}}}\, \frac{l}{\xi}, \qquad\qquad L_s \sim \xi \sqrt{\frac{N_{\mathrm{ch}} r_s}{\tilde{C}}}. \tag{A.104}$$

The parameter $r_s \equiv e^2/v_{\mathrm{F}}$ is the ratio of the interparticle spacing to the Bohr radius, N_{ch} the number of channels, l the mean free path and ξ the coherence length of the superconductor in the dirty limit. The theory for the wire has continuous character but the bare coherence length ξ has the meaning of the ultraviolet (UV) cutoff. An effective dimensionless screening parameter Λ is given by the ratio of L_s and ξ:

$$\Lambda \sim \sqrt{\frac{N_{\mathrm{ch}} r_s}{\tilde{C}}}. \tag{A.105}$$

Depending on the number of channels, Λ can large or of the order of unity.

Random stray charges are not included in the theory of Ref. [67]. In order to find its strength an additional analysis is necessary. It is expected that the bare value of D_Q decreases with the number of channels. The value of the bare phase-slip fugacity was obtained in Ref. [67]. However, it analysis seems to require further work.

B Appendix B

Derivation of the effective theory for the antisymmetric mode

In this part of the appendix, we present the details of the derivation of the low-energy field theory for the antisymmetric mode of the two-chain device depicted in Fig. 4.1. We start from the lattice model given by Eq. (4.16). The charging energies related to the capacitances C_g, C_0, and C_1 are denoted by E_g, E_0, and E_1, respectively. We choose the convention $E_i = (2e)^2/C_i$.

The main idea behind the derivation is that in the limit of a small capacitance C_g, the large charging energy E_g leads to the suppression of the fluctuations of the symmetric mode, at least at large scales. As a result, we are left with a dynamical theory for the antisymmetric mode only. This type of reasoning was previously exploited in the literature to derive the an effective theory of the antisymmetric mode, see Refs. [168, 169]. We generalize the results of Refs. [168, 169] to the case of long-range Coulomb interaction, $C_1 \gg C_0$, and include stray-charge disorder. It is shown that the low-energy theory for the antisymmetric mode is of the form of the sine-Gordon model, Eqs. (4.1), (4.2) and (4.7), with the additional nonlinearity (4.14).

We use in the following two different approaches to derive the effective theory. In Sec. B.1, we outline a semi-quantitative approach starting from the field-theory description of the symmetric and antisymmetric modes. We present a more microscopic derivation at the level of the initial lattice model in Secs. B.2 and B.3 for the cases of short-range ($C_1 = 0$) and long-range ($C_1 \gg C_0$) Coulomb interaction, respectively. Both approaches lead to the same results.

B.1 Heuristic derivation from the continuum field theory

In this section, we outline the main steps of the derivation of the effective theory for the antisymmetric mode on the basis of the field theory corresponding to the lattice Hamiltonian (4.16). It is obtained in the same way as in the case of a single JJ chain. The fields $\phi_\uparrow$ and $\phi_\downarrow$ which are related to the charge density in the two chains are defined by $\partial_x \phi_\sigma = -\pi \mathcal{N}_\sigma$. We also introduce their symmetric and antisymmetric combinations,

$$\begin{pmatrix} \phi_s \\ \phi_a \end{pmatrix} = \frac{1}{2} \begin{pmatrix} 1 & 1 \\ 1 & -1 \end{pmatrix} \begin{pmatrix} \phi_\uparrow \\ \phi_\downarrow \end{pmatrix}. \tag{B.1}$$

Using these fields, the Gaussian part of the action is of the form

$$S_0 = \frac{1}{\pi^2}\int \frac{\mathrm{d}q}{2\pi}\frac{\mathrm{d}\omega}{2\pi}\left\{\left[\frac{(2e)^2q^2}{C_g+C_1q^2}+\frac{\omega^2}{E_\mathrm{J}}\right]|\phi_s(\mathbf{q})|^2+\left[\frac{(2e)^2q^2}{2C_0+C_g+C_1q^2}+\frac{\omega^2}{E_\mathrm{J}}\right]|\phi_a(\mathbf{q})|^2\right\}. \tag{B.2}$$

We can take into account the QPS by adding the term

$$S_\mathrm{ps} = yu_0\int \mathrm{d}x\mathrm{d}\tau\left\{\cos\left[2\phi_\uparrow+\mathcal{Q}_\uparrow(x)\right]+\cos\left[2\phi_\downarrow+\mathcal{Q}_\downarrow(x)\right]\right\}, \tag{B.3}$$

where

$$\mathcal{Q}_\sigma(x) = 2\pi\int_{-\infty}^{x}\mathrm{d}x' Q_\sigma(x'), \tag{B.4}$$

and $Q_{\uparrow(\downarrow)}(x)$ denotes the random stray charge in the two chains. We consider here QPS as independent processes in the two chains. This assumption is justified if $E_1 \ll E_g, E_0$. The phase-slip amplitude y is exponentially small in the parameter $\sqrt{E_\mathrm{J}/E_1}$ in this regime.

In the limit of low momenta, $q \ll \sqrt{C_g/C_1} \ll \sqrt{C_0/C_1}$, the Gaussian part of the action, Eq. (B.2), is of the form of a Luttinger liquid,

$$S_0 = \sum_{\rho=s,a}\frac{1}{2\pi^2 u_{0,\rho}K_{0,\rho}}\int \mathrm{d}x\mathrm{d}\tau[u_{0,\rho}^2(\partial_x\phi_\rho)^2+(\partial_\tau\phi_\rho)^2], \tag{B.5}$$

with

$$\begin{aligned} u_{0,s} &= \sqrt{E_\mathrm{J}E_g}, \quad & u_{0,a} &= \sqrt{E_\mathrm{J}E_0/2}, \\ K_{0,s} &= \frac{1}{2}\sqrt{\frac{E_\mathrm{J}}{E_g}}, \quad & K_{0,a} &= \sqrt{\frac{E_\mathrm{J}}{2E_0}}. \end{aligned} \tag{B.6}$$

We analyze in the following the perturbative expansion of the partition function Z in the small parameter y. The lowest order correction to the partition function is of second order in y,

$$\begin{aligned} \delta Z = \frac{y^2u_0^2}{4}\int \mathrm{d}^2r_1\mathrm{d}^2r_2 &\frac{1}{|\mathbf{r}_1-\mathbf{r}_2|^{2\pi K_{0,s}}} \\ \times \Big\langle &\cos[2(\phi_a(\mathbf{r}_1)-\phi_a(\mathbf{r}_2))+\mathcal{Q}_\uparrow(x_1)-\mathcal{Q}_\uparrow(x_2)]+\cos[2(\phi_a(\mathbf{r}_1)+\phi_a(\mathbf{r}_2))+\mathcal{Q}_\uparrow(x_1)-\mathcal{Q}_\downarrow(x_2)] \\ &+\cos[2(\phi_a(\mathbf{r}_1)+\phi_a(\mathbf{r}_2))-\mathcal{Q}_\downarrow(x_1)+\mathcal{Q}_\uparrow(x_2)]+\cos[2(\phi_a(\mathbf{r}_1)-\phi_a(\mathbf{r}_2))-\mathcal{Q}_\downarrow(x_1)+\mathcal{Q}_\downarrow(x_2)]\Big\rangle_{0,a}, \end{aligned} \tag{B.7}$$

where we introduced the short-hand notation $\mathbf{r} = (x, u_{0,a}\tau)$. Here, the average over the symmetric mode is performed explicitly; the average over the antisymmetric modes is kept unevaluated. After introducing symmetric and antisymmetric combinations of the random charges,

$$\mathcal{Q}_s(x) = \mathcal{Q}_\uparrow(x)+\mathcal{Q}_\downarrow(x), \qquad \mathcal{Q}_a(x) = \mathcal{Q}_\uparrow(x)-\mathcal{Q}_\downarrow(x), \tag{B.8}$$

we arrive at

$$\delta Z = y^2u_0^2\int \mathrm{d}^2r_1\mathrm{d}^2r_2\frac{\cos[\mathcal{Q}_s(x_1)-\mathcal{Q}_s(x_2)]}{|\mathbf{r}_1-\mathbf{r}_2|^{2\pi K_{0,s}}}\left\langle\cos[2\phi_a(\mathbf{r}_1)+\mathcal{Q}_a(x_1)]\cos[2\phi_a(\mathbf{r}_2)+\mathcal{Q}_a(x_2)]\right\rangle_{0,a}. \tag{B.9}$$

Under the assumption, $K_{0,s} \ll 1$, it is possible to approximate $|\mathbf{r}_1 - \mathbf{r}_2|^{2\pi K_{0,s}}$ by one. Provided that the charge disorder is weak, it is justified to approximate $\cos[\mathcal{Q}_s(x_1) - \mathcal{Q}_s(x_2)]$ by unity. In this limit, the integrations over $\mathbf{r}_1$ and $\mathbf{r}_2$ are decoupled. Moreover, we note that the correction (B.9) can be understood as originating from the effective action

$$S^{\text{eff}} = S_0^{\text{eff}} + S_{\text{ps}}^{\text{eff}}, \tag{B.10}$$

$$S_0^{\text{eff}} = \frac{1}{\pi^2} \int \frac{\mathrm{d}q}{2\pi} \frac{\mathrm{d}\omega}{2\pi} \left[\frac{(2e)^2 q^2}{2C_0 + C_1 q^2} + \frac{\omega^2}{E_{\text{J}}} \right] |\phi_a(\mathbf{q})|^2, \tag{B.11}$$

$$S_{\text{ps}}^{\text{eff}} = \sqrt{2} y u_0 \int \mathrm{d}^2 r \cos[2\phi_a(\mathbf{r}) + \mathcal{Q}_a(x)], \tag{B.12}$$

which (up to a rescaling of the amplitude y by an unimportant numerical factor) is equivalent to Eqs. (4.1), (4.2) and (4.7) stated in the main text with $\alpha = 2$. Here we took into account the assumption $C_g \ll C_0$ [see also Eq. (B.2)].

In the case of strong charge disorder, the cosine in Eq. (B.9) can be rewritten in the form

$$\cos[\mathcal{Q}_s(x_1) - \mathcal{Q}_s(x_2)] = \cos[\mathcal{Q}_s(x_1)] \cos[\mathcal{Q}_s(x_2)] + \sin[\mathcal{Q}_s(x_1)] \sin[\mathcal{Q}_s(x_2)]. \tag{B.13}$$

If the disorder is strong, both terms in Eq. (B.13) yield equivalent contributions in the partition function (B.9). For weak disorder (small $\mathcal{Q}_s$), the second term is less important than the first one. Accordingly, we obtain a result that is correct up to a numerical factor of order unity if we keep only the first term. Hence, we again obtain an effective action for QPS which is of first order in the amplitude y [see also the analysis of the weakly disordered situation above],

$$S_{\text{ps}}^{\text{eff}} = \sqrt{2} y u_0 \int \mathrm{d}^2 r \cos[\mathcal{Q}_s(x)] \cos[2\phi_a(\mathbf{r}) + \mathcal{Q}_a(x)]. \tag{B.14}$$

As a result, we obtain in the case of strong charge disorder, apart from the random phase, also a random amplitude in the phase-slip action. As demonstrated in Chap. 3, in the course of the RG, the QPS action without a random amplitude, Eq. (4.7), generates a phase-slip term with a random amplitude provided that the charge disorder is strong. Hence, the QPS action (4.7) adequately captures the effects of QPS on the antisymmetric mode in the disordered double chain.

We now turn to the discussion of the gradient anharmonicity emerging in the effective theory for the antisymmetric mode. Based on the gradient nonlinearities originating from the quartic expansion of the Josephson potential in each of the two chains, we obtain

$$S_{\text{nl}} = \frac{-1}{12\pi^4 E_{\text{J}}^3} \int \mathrm{d}x \left[(\partial_\tau \phi_a)^4 + (\partial_\tau \phi_s)^4 + 6(\partial_\tau \phi_s)^2 (\partial_\tau \phi_a)^2 \right]. \tag{B.15}$$

Averaging (B.15) over ϕ_s leads to a trivial constant as a result of the first term in Eq. (B.15) and a renormalization of E_{J} in Eq. (B.11) due to the last term. We omit both of these effects and obtain

$$S_{\text{nl}}^{\text{eff}} = -\frac{1}{12\pi^4 E_{\text{J}}^3} \int \mathrm{d}x \mathrm{d}\tau \, (\partial_\tau \phi_a)^4. \tag{B.16}$$

As a result, we find the same form as in Eq. (4.14) with $\alpha = 2$.

B.2 Elimination of the symmetric mode at the level of the lattice model: the case of local Coulomb interaction

After the elimination of the symmetric mode on the level of the field theory in the previous section, we integrate out the symmetric mode here directly in the lattice model (4.16). Our derivation closely follows the one for the effective action of a single chain presented in App. A.1. Within this section, we assume local Coulomb interaction ($C_1 = 0$). In Sec. B.3, we generalize this derivation to the long-range case, $C_1 \gg C_0$.

We begin with the derivation of the path-integral formulation of the partition function of the double-chain device. For this purpose, the imaginary time $\tau \in [0, \beta)$ is discretized into N_τ steps with spacing $\Delta\tau$ (its precise value is discussed below). Along the space direction we assume periodic boundary conditions with N_x grains in each of the chains. We denote by n and i the indices of the lattice in τ and x direction, respectively. The index $\sigma =\uparrow, \downarrow$ refers to the two chains. We introduce a resolution of unity of the form

$$\mathbb{1} = \sum_{\mathcal{N}_\uparrow, \mathcal{N}_\downarrow} \int_0^{2\pi} \frac{\mathrm{d}\theta_\uparrow}{2\pi} \int_0^{2\pi} \frac{\mathrm{d}\theta_\downarrow}{2\pi} \left|\mathcal{N}_\uparrow, \mathcal{N}_\downarrow\right\rangle \left\langle \theta_\uparrow, \theta_\downarrow\right| \mathrm{e}^{-i\theta_\uparrow \mathcal{N}_\uparrow} \mathrm{e}^{-i\theta_\downarrow \mathcal{N}_\downarrow} \tag{B.17}$$

at each point in the space-time lattice (n, i, σ). This leads to the action

$$\begin{aligned} S = -i \sum_{n,i,\sigma} \mathcal{N}^n_{i,\sigma} (\partial_\tau \theta)^n_{i,\sigma} + E_\mathrm{J} \Delta\tau \sum_{n,i,\sigma} (1 - \cos[(\partial_x \theta)^n_{i,\sigma}]) \\ + \frac{(2e)^2 \Delta\tau}{2} \sum_{n,i,\sigma,\sigma'} (C^{-1})_{\sigma,\sigma'} \left(\mathcal{N}^n_{i,\sigma} - Q_{i,\sigma}\right) \left(\mathcal{N}^n_{i,\sigma'} - Q_{i,\sigma'}\right), \end{aligned} \tag{B.18}$$

where the lattice derivatives

$$(\partial_x \theta)^n_{i,\sigma} = \theta^n_{i+1,\sigma} - \theta^n_{i,\sigma} \text{ and } (\partial_\tau \theta)^n_{i,\sigma} = \theta^{n+1}_{i,\sigma} - \theta^n_{i,\sigma} \tag{B.19}$$

are introduced. We denote by $Q_{i,\sigma}$ the stray charges and the inverse capacitance matrix in the case local Coulomb interaction ($C_1 = 0$) is of the form

$$C^{-1} = \frac{1}{C_g (C_g + 2C_0)} \begin{pmatrix} C_g + C_0 & C_0 \\ C_0 & C_g + C_0 \end{pmatrix}. \tag{B.20}$$

In order to evaluate the summation over the charges $\mathcal{N}^n_{i,\sigma}$, it is beneficial to define symmetric and antisymmetric combinations of charges and phases

$$\mathcal{N}^n_{i,s} = \frac{\mathcal{N}^n_{i,\uparrow} + \mathcal{N}^n_{i,\downarrow}}{2}, \qquad \mathcal{N}^n_{i,a} = \frac{\mathcal{N}^n_{i,\uparrow} - \mathcal{N}^n_{i,\downarrow}}{2}, \tag{B.21}$$

$$Q_{i,s} = \frac{Q_{i,\uparrow} + Q_{i,\downarrow}}{2}, \qquad Q_{i,a} = \frac{Q_{i,\uparrow} - Q_{i,\downarrow}}{2}, \tag{B.22}$$

$$\theta^n_{i,s} = \frac{\theta^n_{i,\uparrow} + \theta^n_{i,\downarrow}}{2}, \qquad \theta^n_{i,a} = \theta^n_{i,\uparrow} - \theta^n_{i,\downarrow}. \tag{B.23}$$

It is important to stress that the charge variables $\mathcal{N}^n_{i,s}$ and $\mathcal{N}^n_{i,a}$ are either both integer or both half-integer. In terms of the new variables, the partition function assumes the form

$$Z = \sum_{\{\mathcal{N}^n_{i,s}, \mathcal{N}^n_{i,a}\}} \int_0^{2\pi} \mathcal{D}\theta_\uparrow \mathcal{D}\theta_\downarrow \mathrm{e}^{-\sum_{i,n} S^n_i}, \tag{B.24}$$

with

$$S_i^n = -2i\mathcal{N}_{i,s}^n(\partial_\tau\theta)_{i,s}^n - i\mathcal{N}_{i,a}^n(\partial_\tau\theta)_{i,a}^n + (2e)^2\Delta\tau\left[\frac{(\mathcal{N}_{i,s}^n - Q_{i,s})^2}{C_g} + \frac{(\mathcal{N}_{i,a}^n - Q_{i,a})^2}{2C_0 + C_g}\right] + E_\mathrm{J}\Delta\tau\sum_\sigma(1-\cos[(\partial_x\theta)_{i,\sigma}^n]). \tag{B.25}$$

It can now be easily seen that in the limit of a small ground capacitance, $(2e)^2/C_g \gg E_\mathrm{J}, E_0$, the charges $\mathcal{N}_{i,s}$ are frozen. They are essentially pinned to the background charges $Q_{i,s}$ [1]

$$\mathcal{N}_{i,s}^n = \frac{1}{2}\lfloor 2Q_{i,s}\rfloor, \tag{B.26}$$

where $\lfloor\cdot\rfloor$ denotes the integer part. We can drop the first term in Eq. (B.25) since it has the form of a total derivative and the boundary conditions are periodic in imaginary time. Furthermore, we observe that a proper redefinition of the random charges $Q_{i,a}$ allows the summation over $\mathcal{N}_{i,a}^n$ to run over all integers independent of the (integer or half-integer) value of $\mathcal{N}_{i,s}$. Accordingly, if the dynamics of the charges $\mathcal{N}_{i,s}$ is frozen, the systems is described by the action

$$S = \sum_{n,i}\left\{-i\mathcal{N}_{i,a}^n(\partial_\tau\theta)_{i,a}^n + (2e)^2\Delta\tau\frac{(\mathcal{N}_{i,a}^n - Q_{i,a})^2}{C_g+2C_0} + 2E_\mathrm{J}\Delta\tau\left(1-\cos[(\partial_x\theta)_{i,s}^n]\cos[(\partial_x\theta)_{i,a}^n/2]\right)\right\}. \tag{B.27}$$

In order to derive the effective action for the antisymmetric mode, we still need to integrate over the phases $\theta_{i,s}^n$. Assuming open boundary conditions in the space direction (we are ultimately interested in the thermodynamic limit where the precise form of the boundary conditions should not matter), and introducing the new integration variables

$$\tilde{\theta_i^n} = \theta_{i,s}^n - \theta_{i-1,s}^n, \qquad i \geq 2, \tag{B.28}$$

allows us to decouple the integrations. The factor in the partition function which is relevant for the integration reads

$$\prod_{i=1}^{N_x-1}\prod_{n=1}^{N_\tau}\left(\int_0^{2\pi}\mathrm{d}\tilde{\theta}_{i+1,s}^n\,\exp\left\{-2E_\mathrm{J}\Delta\tau(1-\cos[(\partial_x\theta)_{i,a}^n/2]\cos[\tilde{\theta}_{i+1,s}^n])\right\}\right) \propto \exp\left\{-\Delta\tau\sum_{i=1}^{N_x-1}\sum_{n=1}^{N_\tau}g\left[(\partial_x\theta)_{i,a}^n\right]\right\}. \tag{B.29}$$

We omit here an unimportant normalization factor. The function $g(\gamma)$ is given by

$$g(\gamma) = -\frac{1}{\Delta\tau}\ln \mathrm{I}_0\left(2E_\mathrm{J}\Delta\tau\cos\frac{\gamma}{2}\right), \tag{B.30}$$

where I_0 is a modified Bessel function of the first kind. We note that the function $g(\gamma)$ is 2π periodic. Hence, we can view the effective action

$$S = \sum_{n,i}\left\{-i\mathcal{N}_{i,a}^n(\partial_\tau\theta)_{i,a}^n + (2e)^2\Delta\tau\frac{(\mathcal{N}_{i,a}^n - Q_{i,a})^2}{C_g+2C_0} + \Delta\tau\, g[(\partial_x\theta)_{i,a}^n]\right\} \tag{B.31}$$

[1] If the stray charge disorder is strong, we neglect here the rare sites where $2Q_{i,s}$ is half-integer.

of the antisymmetric mode as an action for a single chain of JJs with the effective Josephson potential given by $g(\partial_x\theta)$. From this stage, we can follow the steps outlined in App. A.1 for the derivation of the low-energy theory of a single chain. Our theory is developed from the superconducting side. As we show below, this means that we are in the parameter regime $E_\mathrm{J}\Delta\tau \gg 1$. In this regime, the main contribution originates from the close vicinity of $\partial_x\theta_a = 0 \pmod{2\pi}$. Hence, we can make use of the Villain approximation which is given by

$$\exp\left[-\Delta\tau\, g(\partial_x\theta_a)\right] \propto \sum_h \mathrm{e}^{-\frac{E_\mathrm{J}\Delta\tau}{4}(\partial_x\theta_a - 2\pi h)^2}. \tag{B.32}$$

We fix the time step $\Delta\tau$ to

$$\Delta\tau = \sqrt{\frac{2}{E_\mathrm{J}E_0}} = \sqrt{\frac{2C_0}{(2e)^2 E_\mathrm{J}}}, \tag{B.33}$$

which is the characteristic time scale of the local dynamics, and the numerical factor is chosen such that the model is isotropic in space-time. Proceeding along the lines of the derivation presented in App. A.1, we obtain (omitting the index "a")

$$S = \frac{1}{2\pi^2 K_0}\int \mathrm{d}x\mathrm{d}\tau[u_0^2(\partial_x\phi)^2 + (\partial_\tau\phi)^2] + yu_0\int \mathrm{d}x\mathrm{d}\tau\cos[2\phi(x,\tau) + \mathcal{Q}_a], \tag{B.34}$$

where

$$K_0 = \sqrt{\frac{E_\mathrm{J}}{2E_0}}, \qquad u_0 = \sqrt{E_\mathrm{J}E_0/2}. \tag{B.35}$$

We observe that Eq. (B.34) is equivalent to Eqs. (4.1), (4.2) and (4.7) if we consider the limit $\Lambda \to \infty$ (local Coulomb interaction). In order to extract the gradient anharmonicity, we expand the effective Josephson coupling (B.30) to the quartic order. We find

$$\mathcal{H}_\mathrm{nl} = -\frac{E_\mathrm{J}}{192}\int \mathrm{d}x\left(\partial_x\theta_a\right)^4. \tag{B.36}$$

This contribution to the effective Hamiltonian is identical to the nonlinear term (4.13) with $\alpha = 2$.

B.3 Elimination of the symmetric mode at the level of the lattice model: the case of long-range Coulomb interaction

We turn now to the analysis of the effective theory in the regime of long-range Coulomb interaction, $C_0 \ll C_1$. In this section, we set $C_g = 0$.

It is suitable to rewrite the partition function in terms of a path integral over the phases $\theta_{i,\sigma}(\tau)$

$$Z = \int \prod_{i,\sigma} \mathcal{D}\theta_{i,\sigma}(\tau) e^{-S} \tag{B.37}$$

with

$$S = \int \mathrm{d}\tau \left\{ \sum_{i,\sigma}\left[\frac{\left[(\partial_x\dot{\theta})_{i,\sigma}\right]^2}{2E_1} - E_\mathrm{J}\cos\left[(\partial_x\theta)_{i,\sigma}\right] + i\dot{\theta}_{i,\sigma}Q_{i,\sigma}\right] + \sum_i \frac{\left(\dot{\theta}_{i,\uparrow} - \dot{\theta}_{i,\downarrow}\right)^2}{2E_0}\right\}. \tag{B.38}$$

The action (B.38) corresponds to the Hamiltonian (4.16) with $C_g = 0$. The third term in Eq. (B.38) takes into account the effect of charge disorder. We impose the boundary condition

$$\theta_{i,\sigma}(\beta) = \theta_{i,\sigma}(0) + 2\pi n_{i,\sigma} \tag{B.39}$$

along the imaginary time, where β is the inverse temperature and $n_{i,\sigma}$ are integers. This condition is a consequence of the quantization of the grain charges $\mathcal{N}_{i,\sigma}$.

As a result of the considered limit $C_g = 0$, the action depends on the symmetric combination of the phases $\theta_{i,s} \equiv (\theta_{i,\uparrow} + \theta_{i,\downarrow})/2$ via its spatial derivative only. It is thus convenient to introduce

$$\Theta_{i,s} = \frac{(\partial_x\theta)_{i,\uparrow} + \partial_x(\theta)_{i,\downarrow}}{2}, \qquad \theta_{i,a} = \theta_{i,\uparrow} - \theta_{i,\downarrow} \tag{B.40}$$

as new integration variables and find

$$S = \int \mathrm{d}\tau \sum_i \left\{ \frac{\dot\Theta_{is}^2}{E_1} + \frac{\left[(\partial_x\dot\theta)_{i,a}\right]^2}{4E_1} + 2i\dot\Theta_{i,s}\mathcal{Q}_{i,s} + i\dot\theta_{i,a}Q_{i,a} - 2E_\mathrm{J}\cos\left[\Theta_{i,s}\right]\cos\left[\frac{(\partial_x\theta)_{i,a}}{2}\right] + \frac{\dot\theta_{i,a}^2}{2E_0}\right\}. \tag{B.41}$$

We introduced here

$$\mathcal{Q}_{i,s} = \sum_{j<i} Q_{j,s}, \tag{B.42}$$

where the symmetric and antisymmetric combinations of the random charges, $Q_{i,s}$ and $Q_{i,a}$, are defined in Eq. (B.22). We impose the boundary conditions in the imaginary time direction

$$\theta_{i,a}(\beta) = \theta_{i,a}(0) + 2\pi n_{i,a}\ , \tag{B.43}$$

$$\Theta_{i,s}(\beta) = \Theta_{i,s}(0) + 2\pi n_{i,s} + \pi\delta_i\ , \tag{B.44}$$

where $n_{i,s(a)}$ are integers and $\delta_i = (n_{i+1,a} - n_{i,a}) \mod 2$.

Now we are in a position to perform the functional integration over the symmetric mode by exploiting the fact that the integrations at different points in space are decoupled. The result of the integration over $\Theta_{i,s}(\tau)$ can be written in the form

$$\int \mathcal{D}\Theta_{i,s}(\tau)\exp\left\{-\int \mathrm{d}\tau\left[\frac{\dot\Theta_{is}^2}{E_1} + 2i\dot\Theta_{i,s}\mathcal{Q}_{i,s} - 2E_\mathrm{J}\cos\left[\Theta_{i,s}\right]\cos\left[\frac{(\partial_x\theta)_{i,a}}{2}\right]\right]\right\} = \mathrm{Tr}\,U(\beta) \equiv e^{-\delta S[\partial_x\theta_{i,a}(\tau)]}. \tag{B.45}$$

Here, $U(\tau)$ is the evolution operator in imaginary time determined by

$$\frac{\mathrm{d}U}{\mathrm{d}\tau} = -\mathcal{H}[\theta_{i,a}(\tau) - \theta_{i+1,a}(\tau)]U(\tau), \tag{B.46}$$

and the time dependent Hamiltonian

$$\mathcal{H} = E_1\left(\mathcal{N} - 2\mathcal{Q}_{i,s} - \frac{\delta_i}{2}\right)^2 - 2E_\mathrm{J}\cos\left(\Theta + \pi\delta_i\frac{\tau}{\beta}\right)\cos\frac{\theta_{i+1,a}(\tau) - \theta_{i,a}(\tau)}{2}, \tag{B.47}$$

where $\mathcal{N}$ is the (integer-valued) momentum canonically conjugate to the coordinate Θ.

In general, the contribution $\delta S[\partial_x \theta_{i,a}(\tau)]$ to the effective action of the antisymmetric mode given by Eqs. (B.45), (B.46) and (B.47) is a complicated functional of the phase difference $\partial_x \theta_{i,a}(\tau)$. However, since we are primarily interested in the low-energy modes of the field $\theta_{i,a}$ (energies much lower than the plasma frequency $\sqrt{E_1 E_\mathrm{J}}$), we can make use of the adiabatic approximation for the calculation of the time evolution operator. Furthermore, at low temperatures and in the limit $E_1 \ll E_\mathrm{J}$, we can infer the dynamics of Θ by minimizing the potential energy in the Hamiltonian (B.47). Following this route, we find

$$\delta S = -2E_\mathrm{J} \int \mathrm{d}\tau \left| \cos[(\partial_x \theta)_{i,a}/2] \right| . \tag{B.48}$$

Combining Eqs. (B.41) and (B.48) leads to the effective action

$$S = \int \mathrm{d}\tau \sum_i \left\{ \frac{\left[(\partial_x \dot{\theta})_{i,a} \right]^2}{4E_1} - 2E_\mathrm{J} \left| \cos\left[(\partial_x \theta)_{i,a}/2 \right] \right| + \dot{\theta}_{i,a} Q_{i,a} + \frac{\dot{\theta}_{i,a}^2}{2E_0} \right\} . \tag{B.49}$$

for the antisymmetric mode. The remaining steps in the derivation of the effective theory in terms of a sine-Gordon theory are completely analogous to the steps outlined in App. A.1. We finally obtain Eqs. (4.1), (4.2) and (4.7) with $\alpha = 2$. The gradient anharmonicity (4.13) is obtained by expanding the effective Josephson potential, Eq. (B.48), to the fourth order.

We make a final remark concerning the relation of this derivation to the heuristic derivation outlined in App. B.1. In both derivations we obtain the effective low-energy theory for the antisymmetric mode in terms of a sine-Gordon theory. We obtained in App. B.1 a spatially fluctuating QPS amplitude as a consequence of the random stray charges, cf. Eq. (B.14). This type of fluctuations is not explicitly seen in Eq. (B.49). It is expected that a more accurate analysis of QPS on the basis of Eqs. (B.46) and (B.47) will lead to a QPS amplitude which depends explicitly on the stray-charge configuration $Q_{i,s}$. Moreover, as we demonstrated in Chap. 3, the randomness in the phase-slip amplitude is automatically generated in the course of the RG. Accordingly, both derivations are equivalent.

Appendix C

C Relaxation of fermions

In this part of the appendix, we present some details of the derivation of the relaxation rate in fermionic systems discussed in Chap. 5. We start in Sec. C.1 with the analysis of isotropic higher-dimensional systems ($D \geq 2$). In the subsequent section, Sec. C.2, we discuss the relaxation in quasi-1D wires. Finally, Sec. C.3 is devoted to the analysis of the strictly 1D case at low energies.

C.1 Relaxation at ultra high energies: isotropic case

Here, we outline some details of the derivation of the relaxation rate of a high-energy particle in an isotropic Fermi sea in $D \geq 2$ dimensions. We derive Eqs. (5.4), (5.8), and (5.10) of Sec. 5.1 of the main text.

Starting from the expression (5.1) for the relaxation rate and exploiting the rotational symmetry, we recast the golden-rule expression (5.1) in the form

$$\frac{1}{\tau_k} = \frac{1}{mk^{D-2}S_{D-1}} \int \mathrm{d}\mathbf{p}_1 d\mathbf{p}_2 \mathrm{d}\mathbf{p}_1' \mathrm{d}\mathbf{p}_2' \, \delta\left(\frac{p_1^2}{2m} - \frac{k^2}{2m}\right) \delta\left(E_\mathrm{i} - E_\mathrm{f}\right) \delta\left(\mathbf{P}_\mathrm{i} - \mathbf{P}_\mathrm{f}\right) \times n_\mathrm{F}(\epsilon_2)[1 - n_\mathrm{F}(\epsilon_1')][1 - n_\mathrm{F}(\epsilon_2')] \left| M_{\mathbf{p}_1,\mathbf{p}_2}^{\mathbf{p}_1',\mathbf{p}_2'} \right|^2 . \tag{C.1}$$

It turns out to be useful to switch to the integrations variables to

$$\mathbf{P} = \mathbf{p}_1 + \mathbf{p}_2 = \mathbf{p}_1' + \mathbf{p}_2' , \qquad \mathbf{q} = \frac{\mathbf{p}_1 - \mathbf{p}_2}{2} , \qquad \mathbf{q}' = \frac{\mathbf{p}_1' - \mathbf{p}_2'}{2}, \tag{C.2}$$

which have the meaning of the center-of-mass momentum ($\mathbf{P}$) and the relative momenta before and after the collision ($\mathbf{q}$ and $\mathbf{q}'$, respectively). This leads to the expression

$$\frac{1}{\tau_k} = \frac{1}{2k^{D-2}S_{D-1}} \int \frac{\mathrm{d}\mathbf{P}\mathrm{d}\mathbf{q}\mathrm{d}\mathbf{q}'}{q} \, \delta\left(\epsilon_1 - \frac{k^2}{2m}\right) \delta\left(q - q'\right) n_\mathrm{F}(\epsilon_2)[1 - n_\mathrm{F}(\epsilon_1')][1 - n_\mathrm{F}(\epsilon_2')] \left| M_{\mathbf{p}_1,\mathbf{p}_2}^{\mathbf{p}_1',\mathbf{p}_2'} \right|^2 \tag{C.3}$$

for the relaxation rate. Here, the momenta $\mathbf{p}_i$ and $\mathbf{p}_i'$ are functions of the integration variables $\mathbf{P}$, $\mathbf{q}$ and $\mathbf{q}'$ [see Eq. (C.2)]. For example, for spinless particles, we have

$$\left| M_{\mathbf{p}_1,\mathbf{p}_2}^{\mathbf{p}_1',\mathbf{p}_2'} \right|^2 = \Big[V(|\mathbf{q} - \mathbf{q}'|) - V(|\mathbf{q} + \mathbf{q}'|) \Big]^2 . \tag{C.4}$$

The rotational invariance allows to fix the direction of $\mathbf{P}$ parallel to the x-axis. The integration over the direction of $\mathbf{P}$ yields only the factor S_{D-1}. We now parametrize the relative momenta $\mathbf{q}$ and $\mathbf{q}'$ according to

$$\mathbf{q} = q\left(\cos\varphi, \mathbf{n}\sin\varphi\right), \qquad \mathbf{q}' = q\left(\cos\varphi', \mathbf{n}'\sin\varphi'\right), \tag{C.5}$$

where $\mathbf{n}$ and $\mathbf{n}'$ are $(D-1)$-dimensional unit vectors (perpendicular to $\mathbf{P}$). The expression for the relaxation rate reads now

$$\begin{aligned}\frac{1}{\tau_k} = \frac{1}{2k^{D-2}}\int_0^\infty \mathrm{d}P\mathrm{d}q\; P^{D-1}q^{2D-3}\int_0^\pi \mathrm{d}\varphi\mathrm{d}\varphi'\left(\sin\varphi\sin\varphi'\right)^{D-2}\delta\left(\epsilon_1 - \frac{k^2}{2m}\right)\\ \times n_{\mathrm{F}}(\epsilon_2)[1-n_{\mathrm{F}}(\epsilon_1')][1-n_{\mathrm{F}}(\epsilon_2')]\int \mathrm{d}\mathbf{n}\mathrm{d}\mathbf{n}'\left|M^{\mathbf{p}_1',\mathbf{p}_2'}_{\mathbf{p}_1,\mathbf{p}_2}\right|^2,\end{aligned} \tag{C.6}$$

where

$$\int \mathrm{d}\mathbf{n}\mathrm{d}\mathbf{n}'\left|M^{\mathbf{p}_1',\mathbf{p}_2'}_{\mathbf{p}_1,\mathbf{p}_2}\right|^2 = \int \mathrm{d}\mathbf{n}\mathrm{d}\mathbf{n}'\left(V_+ - V_-\right)^2 \tag{C.7}$$

with

$$V_\pm = V\left(q\sqrt{2(1\pm\cos\varphi\cos\varphi'\pm\mathbf{n}\cdot\mathbf{n}'\sin\varphi\sin\varphi')}\right). \tag{C.8}$$

We observe now that the Eqs. (C.6), (C.7) and (C.8) are equivalent to the Eqs. (5.4), (5.8), and (5.10) stated in the main text.

C.2 Relaxation rate in quasi-1D wires

In this part of the appendix, we outline the details of the calculation of the decay rate in multi-channel quantum wires with one (App. C.2.1) and two lateral dimensions (App. C.2.2), which are analyzed in Sec. 5.2.

C.2.1 Quasi-1D: one lateral dimension

We begin with the discussion of the of the quasi-1D case with one lateral dimension. The details of the calculation leading to the results in Eq. (5.34) in Sec. 5.2.2 are presented here. Let us first look at the contribution of a specific process (fixed band indices n_i) to the decay rate given by Eq. (5.32). Figure C.1 shows an example of a particular process.

Since we assume a large number of available bands between the Fermi energy and the energy of the injected particle, the sum in Eq. (5.28) is dominated by the terms where the final particles $1'$ and $2'$ reside in otherwise empty bands. Accordingly, we need to consider only one Fermi function restricting (at $T=0$) the initial cold particle 2 to be within the Fermi sea. Hence, the range of the integration over the momentum transfer q is restricted by the inequality

$$\frac{1}{2m}\left(p_1 - q + \frac{m\Delta_{\mathrm{eff}}}{q}\right)^2 + \Delta_0 n_2^2 < \epsilon_{\mathrm{F}}, \tag{C.9}$$

where Δ_{eff} is defined in Eq. (5.33). It should be emphasized here that Eq. (C.9) limiting the possible values of q at the same time restricts the "transverse energy transfer" Δ_{eff} by $|\Delta_{\mathrm{eff}}| \lesssim (p_1^2 - p_{\mathrm{F}}^2)/2m$.

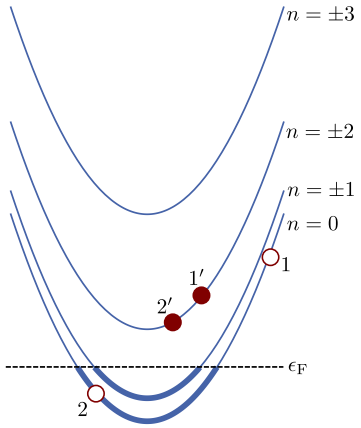

[Reprinted figure with permission from M. Bard, I. V. Protopopov, and A. D. Mirlin, Phys. Rev. B **97**, 195147 (2018), DOI: 10.1103/PhysRevB.97.195147, cf. Ref. [153]. Copyright 2018 by the American Physical Society.]

Figure C.1: A particular example of a process $12 \to 1'2'$ in a multi-channel wire contributing to the relaxation of electron 1.

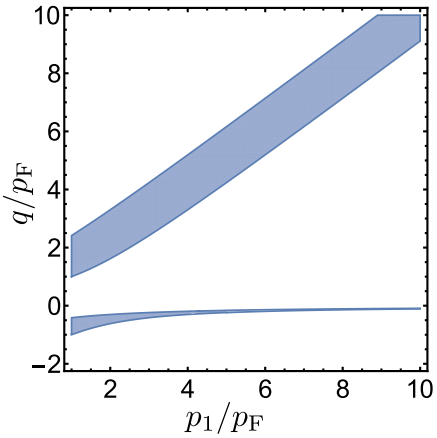

[Reprinted figure with permission from M. Bard, I. V. Protopopov, and A. D. Mirlin, Phys. Rev. B **97**, 195147 (2018), DOI: 10.1103/PhysRevB.97.195147, cf. Ref. [153]. Copyright 2018 by the American Physical Society.]

Figure C.2: Kinematic constraint (in the plane spanned by the initial longitudinal momentum p_1 and the longitudinal momentum transfer $q = p_1 - p_1'$) for the decay of a hot electron in a quasi-1D setup. In this process, a hole is created in the lowest band of transverse quantization ($n_2 = 0$), and the "transverse energy transfer" $\Delta_{\text{eff}} = 2\epsilon_F$ is considered. At large $p_1 \gg p_F$, two distinct regions contribute: (i) $q \simeq p_1$, Eq. (C.10), and (ii) small negative q, Eq.(C.11).

Due to the anisotropy in our model, it is not immediately obvious whether the relaxation rate of a hot electron with energy $\epsilon \gg \epsilon_\mathrm{F}$ depends on the direction of the momentum or only on its energy. In order to investigate this issue, we study two different limiting cases. The first one assumes the injected particle 1 to be in one of the lowest subbands, meaning that its energy is dominated by the longitudinal motions. Thus, the longitudinal momentum satisfies the condition $p_1 \gg |n_1|/d$, which means $p_1 \gg p_\mathrm{F}$ as well. In the opposite case, the particle resides in a highly excited band of transverse quantization with $p_1 \ll |n_1|/d$. Below we demonstrate that the dependence of the relaxation rate of an ultra-hot fermion is almost identical in both cases. Only at very high energies the discreteness of the energy spectrum becomes important for electrons moving in the transverse direction leading to deviations between both cases.

We start with case where the injected particle resides in one of the lowest bands and the longitudinal momentum is large, $p_1 \gg p_\mathrm{F}$. In this situation, momentum transfers close to zero and close to p_1 contribute to the relaxation rate, cf. Fig. C.2. More precisely, the possible momentum transfer is limited to the regions

$$p_1 - \tilde{p}_\mathrm{F}(n_2) < q < p_1 + \tilde{p}_\mathrm{F}(n_2) \tag{C.10}$$

and

$$-\frac{m\Delta_\mathrm{eff}}{p_1}\left(1+\frac{\mathrm{sign}(\Delta_\mathrm{eff})}{p_1}\tilde{p}_\mathrm{F}(n_2)\right) < q < -\frac{m\Delta_\mathrm{eff}}{p_1}\left(1-\frac{\mathrm{sign}(\Delta_\mathrm{eff})}{p_1}\tilde{p}_\mathrm{F}(n_2)\right), \tag{C.11}$$

where

$$\tilde{p}_\mathrm{F}(n_2) = \sqrt{p_\mathrm{F}^2 - 2m\Delta_0 n_2^2} \tag{C.12}$$

is the (positive) momentum at which the Fermi energy intersects the band n_2. We begin with case where the characteristic momentum scale of the interaction is the largest momentum scale, $p_1 \ll q_0$. For spinful fermions, we can set the matrix element constant. Both regions ($q \simeq -m\Delta_\mathrm{eff}/p_1$ and $q \simeq p_1$) lead to the same scaling

$$\frac{1}{\tau_{\{n_i\}}} \sim m|M|^2 \frac{\sqrt{p_\mathrm{F}^2 - 2m\Delta_0 n_2^2}}{p_1}, \qquad p_\mathrm{F} \ll p_1 \ll q_0. \tag{C.13}$$

This result yields the contribution from one particular process (with given band indices). The total relaxation rate is given by the sum over all possible processes,

$$\frac{1}{\tau} = \sum_{n_2,n_{1'},n_{2'}} \frac{1}{\tau_{\{n_i\}}} \delta_{n_1+n_2,n_{1'}+n_{2'}}. \tag{C.14}$$

Here, we sum n_2 over all occupied bands, $|n_2| < \sqrt{\epsilon_\mathrm{F}/\Delta_0} = p_\mathrm{F} d/2\pi$. Estimating this sum yields

$$\sum_{n_2=0}^{p_\mathrm{F} d/2\pi} \sqrt{p_\mathrm{F}^2 - \frac{4\pi^2}{d^2} n_2^2} \simeq \frac{p_\mathrm{F}^2 d}{8} \tag{C.15}$$

for $p_\mathrm{F} d \gg 1$. The summation over n_2' can be evaluated exploiting the conservation of the transverse momentum. Moreover, the maximum value of the remaining band index n_1' is obtained from energy considerations: $n_{1'}^\mathrm{max} \simeq n_1/2 + \sqrt{n_1^2/4 + p_1^2/4m\Delta_0}$. Since we assume here that the longitudinal momentum dominates over the transverse one, $p_1 \gg \sqrt{2m\Delta_0} n_1 = 2\pi n_1/d$, we find

$$\frac{1}{\tau} \sim m p_\mathrm{F}^2 d^2 |M|^2 \sim m V_0^2 p_\mathrm{F}^2, \qquad p_\mathrm{F} \ll p_1 \ll q_0 \tag{C.16}$$

for the relaxation rate. As can be seen, the decay rate does not depend on the momentum p_1 of the injected hot electron, and it coincides with the result (5.15) (with $D = 2$) found in the same regime of p_1 for an isotropic 2D system.

For spin-polarized fermions, the specific form of the interaction, Eq. (5.27), needs to be analyzed due to the Hartree-Fock cancellation. The momentum transfers read

$$q_{\rm dir}^2 = q^2 + \frac{4\pi^2}{d^2}(n_1 - n_{1'})^2, \tag{C.17}$$

$$q_{\rm ex}^2 = \frac{16\pi^4}{q^2 d^4}[(n_1 - n_{1'})(n_{1'} - n_2)]^2 + \frac{4\pi^2}{d^2}(n_{1'} - n_2)^2, \tag{C.18}$$

for the direct and exchange terms, respectively. We need to integrate the momentum q over the two regions given by Eqs. (C.10) and (C.11). The summation over $n_{1'}$ is cut at the upper limit by $n_{1'}^{\rm max} \approx p_1 d/2\sqrt{2}\pi$. For the majority of processes, we have $n_{1'} \gg n_{2'}$. Performing the summation over all processes, we obtain the scaling

$$\frac{1}{\tau_\epsilon} \sim m V_0^2 p_{\rm F}^2 \frac{p_1^4}{q_0^4} \sim m^3 V_0^2 \frac{p_{\rm F}^2}{q_0^4}\epsilon^2, \qquad p_{\rm F} \ll p_1 \ll q_0, \tag{C.19}$$

which is again identical to the scaling (5.16) for an isotropic system in two dimensions. Here the energy ϵ is introduced which facilitates the comparison of the cases in which the incident momentum of particle 1 is in the transverse and longitudinal direction, respectively. The two regions defined in Eqs. (C.10) and (C.11) in the integration over q contribute the same amount of the order of Eq. (C.19) to the relaxation rate. Let us briefly explain the origin of each of the factors using the example of the region given by Eq. (C.10). The integral in Eq. (5.32) can be estimated by setting $q = p_1$ and multiplying by the factor $\tilde{p}_{\rm F}(n_2)$ corresponding to the width of the integration domain. The n_2 dependence of the matrix element can be neglected for the majority of processes. The summation over n_2 brings a factor of $p_{\rm F}^2 d$, see Eq. (C.15). The final summation over $n_{1'}$ of the squared matrix element yields the factor $(V_0^2/q_0^4 d^2) \cdot p_1^5 d$. The combination of all those factors leads to the scaling (C.19).

In the case of the longitudinal momentum exceeding the momentum scale of the interaction, $p_1 \gg q_0 \gtrsim p_{\rm F}$, the square bracket in Eq.(5.30) is dominated by one of the terms. Accordingly, the Hartree-Fock cancellation does not occur leading to essentially identical results for spinful and spinless fermions. Moreover, only band indices $n_{1'}$ smaller than $n_{1'}^{\rm max} \approx q_0 d/2\pi$ contribute. Higher bands would involve a transverse momentum transfer that is larger than q_0. Hence, the contribution from those bands is small. As a consequence, we obtain the scaling

$$\frac{1}{\tau_\epsilon} \sim m V_0^2 p_{\rm F}^2 \frac{q_0}{p_1} \sim \sqrt{m} V_0^2 p_{\rm F}^2 \frac{q_0}{\sqrt{\epsilon}}, \qquad p_{\rm F} \lesssim q_0 \ll p_1, \tag{C.20}$$

for the relaxation rate in this case. It coincides with the behavior for an isotropic 2D system in the corresponding regime, Eq. (5.17). We get the result (C.20) from (C.13) and (C.14). A factor $p_{\rm F}^2 d$ is obtained from the summation over n_2, and the summation of the squared matrix element over $n_{1'}$ contributes the factor $(V_0^2/d^2) \cdot q_0 d$.

Let us now discuss the case when the transverse momentum of the injected particle is much larger than its longitudinal momentum. Such a case is realized when the hot electron occupies the close vicinity of the bottom of a high band, $p_1 \simeq 0$, $\Delta_0 n_1^2 \gg \epsilon_{\rm F}$. We analyze this case with the help of the general result Eq. (5.32) for $p_1 = 0$. As has been mentioned above, the most important contribution is related to processes in which the final particles $1'$ and $2'$ occupy otherwise empty bands, $n_1', n_2' > n_2^{\rm max}$.

Hence, we need to take into account only one Fermi function which restricts the initial cold particle to occupy the Fermi sea. At zero temperature, the integration over q is thus restricted to the two regions

$$\begin{aligned} -\frac{\tilde{p}_\mathrm{F}}{2} - \sqrt{\frac{\tilde{p}_\mathrm{F}^2}{4} + m\Delta_\mathrm{eff}} < q < \frac{\tilde{p}_\mathrm{F}}{2} - \sqrt{\frac{\tilde{p}_\mathrm{F}^2}{4} + m\Delta_\mathrm{eff}}, \\ -\frac{\tilde{p}_\mathrm{F}}{2} + \sqrt{\frac{\tilde{p}_\mathrm{F}^2}{4} + m\Delta_\mathrm{eff}} < q < \frac{\tilde{p}_\mathrm{F}}{2} + \sqrt{\frac{\tilde{p}_\mathrm{F}^2}{4} + m\Delta_\mathrm{eff}}, \end{aligned} \tag{C.21}$$

where $\tilde{p}_\mathrm{F}$ depends on n_2, cf. Eq. (C.12). It holds that $m\Delta_\mathrm{eff} \gtrsim \tilde{p}_\mathrm{F}^2$ for the dominant processes leading to the relaxation of a hot particle. Therefore, we can approximate the two integration regions (C.21) by

$$-\sqrt{m\Delta_\mathrm{eff}} - \tilde{p}_\mathrm{F}(n_2)/2 < q < -\sqrt{m\Delta_\mathrm{eff}} + \tilde{p}_\mathrm{F}(n_2)/2$$

and

$$\sqrt{m\Delta_\mathrm{eff}} - \tilde{p}_\mathrm{F}(n_2)/2 < q < \sqrt{m\Delta_\mathrm{eff}} + \tilde{p}_\mathrm{F}(n_2)/2.$$

Again, we begin with the case when the momentum q_0 is the largest scale, $p_\mathrm{F} \ll 2\pi n_1/d \ll q_0$. For spinful fermions, the matrix element can be replaced by a constant. The contribution from a particular process with given band indices reads then

$$\frac{1}{\tau_{\{n_i\}}} \simeq |M|^2 \tilde{p}_\mathrm{F} \sqrt{\frac{m}{\Delta_\mathrm{eff}}} = |M|^2 \tilde{p}_\mathrm{F} \sqrt{\frac{m}{2\Delta_0(n_1 - n_{1'})(n_{1'} - n_2)}}. \tag{C.22}$$

We can omit the n_2 dependence of Δ_eff because for the dominant processes $n_1, n_1' \gg n_2$. According to Eq. (C.15), the summation over n_2 yields the factor $p_\mathrm{F}^2 d$. The summation over $n_{1'}$ can be performed with the help of the Euler-Maclaurin formula:

$$\begin{aligned} \frac{1}{\tau} &= p_\mathrm{F}^2 d |M|^2 \sqrt{\frac{m}{2\Delta_0}} \sum_{n_{1'}=1}^{n_1-1} \frac{1}{\sqrt{n_{1'}(n_1 - n_{1'})}} \\ &\simeq p_\mathrm{F}^2 d |M|^2 \sqrt{\frac{m}{2\Delta_0}} \int_1^{n_1-1} \frac{\mathrm{d}x}{\sqrt{x(n_1 - x)}} + \mathcal{O}(n_1^{-1/2}) \\ &\sim m p_\mathrm{F}^2 d^2 |M|^2 \sim m V_0^2 p_\mathrm{F}^2, \qquad p_\mathrm{F} \ll \frac{2\pi n_1}{d} \ll q_0. \end{aligned} \tag{C.23}$$

This result coincides with the relaxation rate (C.16) for the corresponding regime in the case where the momentum of the hot particle points in the longitudinal direction. Hence, we observe that the relaxation rate essentially does not depend on the direction of the momentum of the injected hot particle. We show below that this is valid also in the other regimes.

For spinless particles, the above mentioned contribution (where the matrix element is replaced by a constant) vanishes as a consequence of the Hatree-Fock cancellation. Hence, we take into account the behavior of the matrix element as function of the relevant momentum transfers which are given by (C.17) and (C.18). Since we consider the limit where the initial momentum is smaller than q_0, the momentum transfer is always smaller than q_0. This means that the interaction potential does lead to further constraints on the relevant phase space. The total relaxation rate assumes thus the form

$$\frac{1}{\tau} \sim m p_\mathrm{F}^2 d \frac{V_0^2}{q_0^4 d^5} n_1^2 \sum_{n_{1'}=1}^{n_1-1} \frac{(n_1 - 2n_{1'})^2}{\sqrt{n_{1'}(n_1 - n_{1'})}}. \tag{C.24}$$

The remaining sum can be estimated, which yields the scaling

$$\frac{1}{\tau_\epsilon} \sim m V_0^2 \frac{p_\mathrm{F}^2}{q_0^4} \left(\frac{2\pi n_1}{d}\right)^4 \sim m^3 V_0^2 \frac{p_\mathrm{F}^2}{q_0^4} \cdot \epsilon^2, \qquad p_\mathrm{F} \ll \frac{2\pi n_1}{d} \ll q_0. \tag{C.25}$$

This result is identical to the rate for the case when the momentum $\mathbf{p}_1$ is along the longitudinal direction, Eq. (C.19).

If the transverse momentum is larger than the momentum scale of the interaction, $2\pi n_1/d \gg q_0 \gtrsim p_\mathrm{F}$, some processes are suppressed by the matrix element. The direct term yields a contribution if $n_{1'} > n_1 - q_0^2 d^2/4\pi^2 n_1$, whereas the exchange term contributes if $n_{1'} < q_0^2 d^2/4\pi^2 n_1$. Hence, the Hartree-Fock cancellation is not effective in the spin-polarized case, which means that we get the same scaling behavior as in the spinful situation. Since again for the majority of processes $n_{1'} \gg n_2$, the n_2 dependence can be neglected. We need to impose the constraint $q_0^2 d^2/4\pi^2 n_1 > 1$ for the summation over $n_{1'}$ to be finite. This condition can be recast in the form $p_{1\perp} < q_0^2 d/2\pi$ with the definition of the transverse momentum $p_{1\perp} = 2\pi n_1/d$. This constraint guarantees that the typical transverse momentum transfer $q_0^2/p_{1\perp}$ (see the discussion in the end of Sec. 5.1) is larger than the quantization step $2\pi/d$. If this condition is not satisfied, the decay rate is strongly suppressed because only the large-momentum behavior of the interaction potential $V(q)$ contributes. Accordingly, in the regime $p_{1\perp} > q_0^2 d$, the discreteness of the energy spectrum becomes important giving rise to an additional suppression for a quasi-1D setup compared to the an isotropic 2D system. The actual form of the decay is non-universal, and we do not further analyze it here.

Under the assumption that the condition $p_{1\perp} < q_0^2 d$ is satisfied, the decay rate is estimated in the following. According to Eq. (C.15), the summation over n_2 leads to a factor $\sim p_\mathrm{F}^2 d$. Since the direct and exchange contribute the same amount, it is sufficient to estimate the contribution from the exchange term. It is of the form

$$\frac{1}{\tau} \sim m p_\mathrm{F}^2 d \frac{V_0^2}{d^2} \sum_{n_{1'}=1}^{\frac{q_0^2 d}{2\pi p_{1\perp}}} \frac{d}{\sqrt{n_{1'}(n_1 - n_{1'})}}. \tag{C.26}$$

After replacing the sum by an integral, we obtain

$$\frac{1}{\tau_\epsilon} \sim m V_0^2 p_\mathrm{F}^2 \frac{q_0}{p_{1\perp}} \sim \sqrt{m} V_0^2 p_\mathrm{F}^2 \frac{q_0}{\sqrt{\epsilon}}, \qquad p_\mathrm{F} \lesssim q_0 \ll p_{1\perp} \ll q_0^2 d, \tag{C.27}$$

which coincides with the scaling of the relaxation rate for electrons moving in the longitudinal direction, Eq. (C.20).

As discussed above, when the momentum of the injected hot fermion is parallel to the transverse direction, the decay rate is additionally suppressed at $p_{1\perp} \gg q_0^2 d$ because of the discreteness of the spectrum. However, if the momentum points in the longitudinal direction, the only necessary condition to recover the isotropic 2D result at high momenta p_1 is $q_0 d > 1$. To study the crossover between both limits, we analyze the minimal momentum transfer in the case when the initial hot particle is in a high band, $n_1 \gg p_\mathrm{F}^2 d^2$, but has also a finite longitudinal momentum component p_1. We can estimate the longitudinal momentum transfer $q = p_1 - p_1'$ in this regime from the equation

$$-p_1 q + q^2 = \frac{n_{1'}(n_1 - n_{1'})}{d^2}. \tag{C.28}$$

If $p_1 = 0$, we find for the minimal longitudinal momentum transfer $q_\mathrm{min} = \sqrt{n_1}/d = \sqrt{p_{1\perp}/d}$. As a consequence, the condition for the universal regime of the scattering rate (decay as $1/p_{1\perp}^{-1}$) reads

$q_{\min} < q_0$. This yields the last condition in the last line of Eq. (C.27) limiting $p_{1\perp}$ from above. However, increasing the momentum component in the longitudinal direction p_1 above q_0 changes the behavior. Now, the condition for this regime is governed by the first term on the LHS of Eq. (C.28). Hence, we obtain the condition $p_1/p_{1\perp} > 1/q_0 d$ for the universal regime. Consequently, we obtain a non-universal regime, where the relaxation rate vanishes faster than $1/\sqrt{\epsilon}$ if the longitudinal (p_1) and transverse ($p_{1\perp}$) momentum components of the injected particle 1 fulfill the conditions

$$p_{1\perp} > q_0^2 d \quad \text{and} \quad \frac{p_1}{p_{1\perp}} < \frac{1}{q_0 d}. \tag{C.29}$$

We summarize all results for multi-channel wires with one lateral dimension in Eq. (5.34).

C.2.2 Quasi-1D: two lateral dimensions

In this section, we outline the steps leading to the scalings summarized in Eq. (5.36) in Sec. 5.2.3. The derivation is very similar to the one for one lateral dimension discussed in App. C.2.1 above.

We start from Eq. (5.32) and analyze at first the case where the longitudinal momentum dominates over the transverse one, $p_1 \gg 2\pi|\mathbf{n}_1|/d$. We begin with the case when the characteristic momentum of the interaction is the largest scale, $p_1 < q_0$. For spinful fermions, the contribution from a specific process can be obtained from Eq. (C.13) with the replacement $n_2 \to \mathbf{n}_2$. Here, the summation over of $\mathbf{n}_2$ over the occupied bands gives rise to the factor $\sim p_{\mathrm{F}}(p_{\mathrm{F}}d)^2$, and the summation over $\mathbf{n}_{1'}$ is cut off at the upper limit by $|\mathbf{n}_{1'}| < p_1 d/2\sqrt{2}\pi$ due to the energy conservation. Hence, we obtain the factor $\sim (p_1 d)^2$ from the summation over $\mathbf{n}_{1'}$. In total, we obtain for spinful fermions the scaling

$$\frac{1}{\tau_\epsilon} \sim m V_0^2 p_{\mathrm{F}}^3 p_1 \sim m^{3/2} V_0^2 p_{\mathrm{F}}^3 \sqrt{\epsilon}, \qquad p_{\mathrm{F}} \ll p_1 \ll q_0 \tag{C.30}$$

of the relaxation rate. Thus, we obtain full agreement with the behavior of the decay rate in the corresponding regime of an isotropic 3D system, Eq. (5.15).

For spin-polarized particles and for large q_0, the precise behavior of the interaction, Eq. (5.27), at the relevant momentum transfers is important (Hartree-Fock cancellation). The corresponding momentum transfers of the direct and exchange term are obtained from Eqs. (C.17) and (C.18) by replacing $n_i \to \mathbf{n}_i$. The dependencies on $\mathbf{n}_1$ and $\mathbf{n}_2$ can be neglected for the dominant processes. The integration over q over the regions (C.10) and (C.11) leads to a factor $\sim m/p_1 \cdot \sqrt{p_{\mathrm{F}}^2 - 2m\Delta_0 \mathbf{n}_2^2}$. Evaluating the summation of the squared matrix element over $\mathbf{n}_{1'}$ results in a factor $\sim V_0^2/(q_0^4 d^4) \cdot p_1^6 d^2$. We finally obtain

$$\frac{1}{\tau_\epsilon} \sim m V_0^2 p_{\mathrm{F}}^3 \frac{p_1^5}{q_0^4} \sim m^{7/2} V_0^2 \frac{p_{\mathrm{F}}^3}{q_0^4} \epsilon^{5/2}, \qquad p_{\mathrm{F}} \ll p_1 \ll q_0 \tag{C.31}$$

for the relaxation rate, which coincides with the bulk 3D result, Eq. (5.16).

In the regime $p_1 \gg q_0 \gtrsim p_{\mathrm{F}}$, the summation over $\mathbf{n}_{1'}$ is restricted to the unit disk with radius $q_0 d/2\pi$ due to the matrix element (interaction potential). We obtain for spinless and spinful fermions the same scaling,

$$\frac{1}{\tau_\epsilon} \sim m V_0^2 p_{\mathrm{F}}^3 \frac{q_0^2}{p_1} \sim \sqrt{m} V_0^2 p_{\mathrm{F}}^3 \frac{q_0^2}{\sqrt{\epsilon}}, \qquad p_{\mathrm{F}} \lesssim q_0 \ll p_1. \tag{C.32}$$

The integration over q and the summation over $\mathbf{n}_2$ yields the factor $m/p_1 \cdot p_{\mathrm{F}}(p_{\mathrm{F}}d)^2$. Performing the summation of the squared matrix element over $\mathbf{n}_{1'}$ gives rise to the factor $V_0^2/d^4 \cdot (q_0 d)^2$. The scaling (C.32) fully agrees with the corresponding behavior in the 3D case, Eq. (5.17).

We turn now to the discussion of the case when the momentum of the injected hot electron is parallel to the transverse direction. In other words, it occupies the bottom of a high band, $\Delta_0 \mathbf{n}_1^2 \gg \epsilon_\mathrm{F}$. We begin with case of spinless fermions. Under the assumption that the transverse momentum is in the regime $p_\mathrm{F} \ll 2\pi|\mathbf{n}_1|/d \ll q_0$, we make use of Eq. (C.22) with the replacement $n_i \to \mathbf{n}_i$, which yields the contribution from a particular process. Analogous to the previous cases, the dominant contribution is given by processes with $\Delta_\mathrm{eff} > 0$.

It is important to note a subtlety that emerges in quasi-1D wires with two lateral dimensions and was absent for only one lateral dimension. Here, Δ_eff has the trivial zeros $\mathbf{n}_{1'} = \mathbf{n}_1$ and $\mathbf{n}_{1'} = \mathbf{n}_2$ and additionally zeros which occur if the vector $\mathbf{n}_1 - \mathbf{n}_{1'}$ is orthogonal to $\mathbf{n}_{1'} - \mathbf{n}_2$. These zeros give rise to logarithmic singularities [cf. Eq. (5.32)]. A proper treatment regularizes these singularities. It turns out that these terms are of minor importance for our analysis. For a more detailed discussion of this issue, see Sec. 5.2.3. We thus omit these processes below.

The summation over $\mathbf{n}_2$ over the occupied bands gives again rise to the factor $\sim p_\mathrm{F}(p_\mathrm{F}d)^2$. In the summation over $\mathbf{n}_{1'}$, the $\mathbf{n}_2$ dependence can be omitted since for the majority of processes it holds $|\mathbf{n}_{1'}| \gg |\mathbf{n}_2|$. The summation over $\mathbf{n}_{1'}$ is restricted by $|\mathbf{n}_1|$ which follows from energy considerations. Instead of the summation over $\mathbf{n}_{1'}$, we can go over to an integration. Moreover, we parametrize the denominator in Eq. (C.22) as

$$\frac{1}{\sqrt{(\mathbf{n}_1 - \mathbf{n}_{1'})\mathbf{n}_{1'}}} = \frac{1}{\sqrt{|\mathbf{n}_1||\mathbf{n}_{1'}|\cos\varphi - |\mathbf{n}_{1'}|^2}}, \tag{C.33}$$

where $\cos\varphi > |\mathbf{n}_{1'}|/|\mathbf{n}_1|$ which ensures the condition $\Delta_\mathrm{eff} > 0$. Performing the integral over $|\mathbf{n}_{1'}|$ and the angle φ yields the factor $\mathbf{n}_1$. In total, we arrive at

$$\frac{1}{\tau_\epsilon} \sim m V_0^2 p_\mathrm{F}^3 \frac{2\pi|\mathbf{n}_1|}{d} \sim m^{3/2} V_0^2 p_\mathrm{F}^3 \sqrt{\epsilon}\,, \qquad p_\mathrm{F} \ll \frac{2\pi|\mathbf{n}_1|}{d} \ll q_0. \tag{C.34}$$

This result for the relaxation rate, which corresponds to the case where the momentum $\mathbf{p}_1$ points in the transverse direction, coincides with the behavior when the momentum is parallel to the wire axis, Eq. (C.30).

In the same regime of the momentum scales but for spin-polarized fermions, the form of the interaction is import due to the Hartree-Fock cancellation. The expressions for the momentum transfers of the direct and exchange term for a particular process are given by Eqs. (C.17) and (C.18) and the replacement $n_i \to \mathbf{n}_i$. The integration over q runs over the two regions specified in Eq. (C.21). Again, we can omit the dependence on $\mathbf{n}_2$ everywhere except for the width of the integration over q. In this way, we get the factor $\sim p_\mathrm{F}(p_\mathrm{F}d)^2$ from the evaluation of the sum over $\mathbf{n}_2$.

All momentum transfers allowed by the conservation laws are smaller than q_0 in the considered regime, $2\pi|\mathbf{n}_1|/d < q_0$. There is the constraint $|\mathbf{n}_{1'}| < |\mathbf{n}_1|$ on the sum over $\mathbf{n}_1$ which follows from energetic considerations. Moreover, the condition $\mathbf{n}_{1'}(\mathbf{n}_1 - \mathbf{n}_{1'}) > 0$ ensures $\Delta_\mathrm{eff} > 0$, which selects the most important processes. The sum over $\mathbf{n}_{1'}$ scales as $|\mathbf{n}_1|^5$. In total we obtain

$$\frac{1}{\tau_\epsilon} \sim m V_0^2 \frac{p_\mathrm{F}^3}{q_0^4} \left(\frac{2\pi|\mathbf{n}_1|}{d}\right)^5 \sim m^{7/2} V_0^2 \frac{p_\mathrm{F}^3}{q_0^4} \epsilon^{5/2}, \qquad p_\mathrm{F} \ll \frac{2\pi|\mathbf{n}_1|}{d} \ll q_0 \tag{C.35}$$

for the relaxation rate. This result coincides with rate obtained for the situation in which the momentum of the hot particle points along the axis of the wire, Eq. (C.31).

We now turn to the case when the transverse momentum of the hot electron is the largest scale, $2\pi|\mathbf{n}_1|/d \gg q_0 \gtrsim p_\mathrm{F}$. Here, the direct term yields a contribution if $(2\pi/d)^2(\mathbf{n}_1^2 - \mathbf{n}_1\mathbf{n}_{1'}) < q_0^2$, while the

exchange term contributes if $(2\pi/d)^2\mathbf{n}_1\mathbf{n}_{1'} < q_0^2$. Both regions restricting the summation over the $\mathbf{n}_{1'}$ do not overlap in this regime. Accordingly, we obtain the same scaling for the decay rate in the cases of spinful and spin-polarized fermions. The additional condition $\mathbf{n}_{1'}(\mathbf{n}_1 - \mathbf{n}_{1'}) > 0$ ensures $\Delta_{\text{eff}} > 0$ valid for the dominant processes. After replacing the sum by an integral, we arrive at

$$\frac{1}{\tau_\epsilon} \sim m V_0^2 p_{\text{F}}^3 q_0^2 \left(\frac{2\pi|\mathbf{n}_1|}{d}\right)^{-1} \sim \sqrt{m} V_0^2 p_{\text{F}}^3 \frac{q_0}{\sqrt{\epsilon}}, \qquad p_{\text{F}} \lesssim q_0 \ll \frac{2\pi|\mathbf{n}_1|}{d} \ll q_0^2 d \tag{C.36}$$

in accordance with the situation when the momentum of the injected hot electron is parallel to the wire axis, Eq. (C.32). Completely analogous to the case with only one lateral dimension, the result for an isotropic 3D system is recovered if the condition $q_0^2 d^2/|\mathbf{n}_1| > 1$ is satisfied. If this condition is not valid, the relaxation rate is characterized by an even stronger decay because only the tail of the interaction potential at large momenta contributes. As in the case of only one lateral dimension (cf. discussion in the end of App. C.2.1), this non-universal regime is given by the conditions

$$\frac{|\mathbf{n}_1|}{d} > q_0^2 d \quad \text{and} \quad \frac{p_1}{|\mathbf{n}_1|/d} < \frac{1}{q_0 d}, \tag{C.37}$$

where p_1 denotes the longitudinal component of the momentum of the injected particle.

A summary of all results for a multi-channel wire with two lateral dimensions is presented in Eq. (5.36).

C.3 Low-energy regime in 1D

In this part of the appendix we outline the derivation of the relaxation rate of fermions interacting via a short-range interaction potential in one dimension in the low energy limit, $p_1 - p_{\text{F}} \ll p_{\text{F}}$. The main steps leading to Eqs. (5.53) and (5.58) are presented here. We start with the expression for the decay rate given by Eq. (5.41). The Fermi functions $n_{\text{F}}(\epsilon_2)$ and $n_{\text{F}}(\epsilon_3)$ associated with the initial states restrict the area of integration in the q-P plane, see Fig. C.3.

In contrast to the case of high energies, $p_1 \gg p_{\text{F}}$, where the outgoing particles ($1'$, $2'$, and $3'$) are typically scattered into states well above the Fermi sea, in the low-energy limit, the Fermi functions related to these particles further restrict the integration region in the q-P plane. Due to the symmetry $\varphi' \to \varphi' + 2\pi/3$ (interchange of particles), it is sufficient to consider the interval $0 < \varphi' < 2\pi/3$. At low energies, $\delta = (p_1 - p_{\text{F}})/p_{\text{F}} \ll 1$, only the narrow region

$$\frac{\pi}{3} - \frac{\sqrt{3}}{4}\delta < \varphi' < \frac{\pi}{3} + \frac{\sqrt{3}}{4}\delta \tag{C.38}$$

contributes. Moreover, the integration region in the q-P plane is drastically reduced. Figure C.4 shows the integration domain taking into account all kinematic constraints. We observe that only the vicinity of the point $(q = 4p_{\text{F}}/3, P = p_1 \sim p_{\text{F}})$ yields a contribution. The area of the contributing region is proportional to $(p_1 - p_{\text{F}})^3/p_{\text{F}}$. According to Eq. 5.42, the angle φ is fixed to $\varphi_0 = \pm\pi/3 + \mathcal{O}(\delta)$. All involved particles occupy states close to the Fermi points; one of them is a left mover while the other two are right movers. Apart from these phase-space considerations, we need to take into account the behavior of the squared matrix element. We assume again the characteristic momentum scale of the

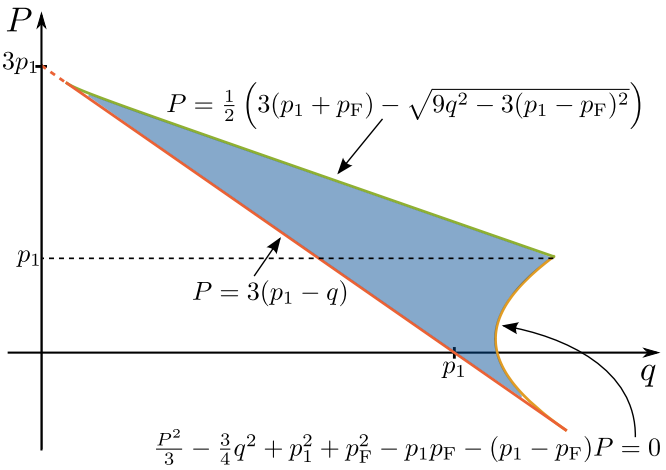

[Reprinted figure with permission from M. Bard, I. V. Protopopov, and A. D. Mirlin, Phys. Rev. B **97**, 195147 (2018), DOI: 10.1103/PhysRevB.97.195147, cf. Ref. [153]. Copyright 2018 by the American Physical Society.]

Figure C.3: Integration region in the q-P-plane for three-particle collisions at low energies in 1D, which is restricted by the Fermi functions related to the initial states. The additional constraints from the outgoing particles are illustrated in Fig. C.4.

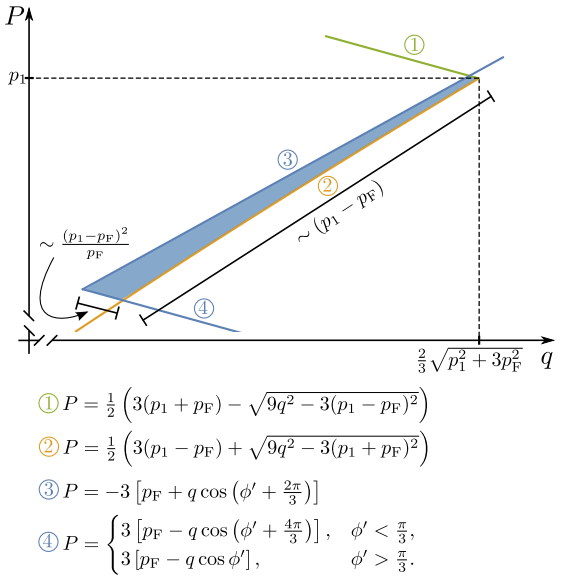

[Reprinted figure with permission from M. Bard, I. V. Protopopov, and A. D. Mirlin, Phys. Rev. B **97**, 195147 (2018), DOI: 10.1103/PhysRevB.97.195147, cf. Ref. [153]. Copyright 2018 by the American Physical Society.]

Figure C.4: Kinematic constraints for three-particle collisions in 1D in the low-energy regime. Due to the restrictions originating from the Fermi functions of the outgoing particles, only the vicinity of the upper right corner in the region in Fig. C.3 contributes.

interaction potential to be larger than the Fermi momentum, $q_0 \gg p_\mathrm{F}$. In the case of spin-polarized particles, Eq. (5.51) can be used leading to the behavior

$$\frac{1}{\tau_{p_1}} \sim \frac{m^3 p_\mathrm{F}^6 V_0^4}{q_0^{16}} (p_1 - p_\mathrm{F})^8, \quad p_1 - p_\mathrm{F} \ll p_\mathrm{F} \ll q_0 \quad \text{(spinless)} \tag{C.39}$$

for the relaxation rate, which is identical to Eq. (5.53) of the main text.

For spinful fermions, the squared matrix element scales as

$$w_q(\varphi, \varphi') \sim \frac{m^2 V_0^4}{q_0^4 \delta^2} \sim \frac{m^2 V_0^4 p_\mathrm{F}^2}{q_0^4 (p_1 - p_\mathrm{F})^2} \tag{C.40}$$

for $\varphi \approx \pi/3$ and $\varphi' \approx \pi/3$, with a typical distance between φ and φ' that is of the order of $\delta = (p_1 - p_\mathrm{F})/p_\mathrm{F}$. Due to the energy denominators and the absence of the Hartree-Fock cancellation, the matrix element is drastically enhanced in the low-energy limit. In total, we arrive at the relaxation rate

$$\frac{1}{\tau_{p_1}} \sim \frac{m^3 V_0^4}{q_0^4} (p_1 - p_\mathrm{F})^2, \quad p_1 - p_\mathrm{F} \ll p_\mathrm{F} \ll q_0 \quad \text{(spinful)}, \tag{C.41}$$

for fermions with spin in a 1D system at low energies. This result is identical to Eq. (5.58) in the main text.

Acknowledgments

First of all I want to thank my supervisor Prof. Dr. Alexander Mirlin for giving me the opportunity to work as a PhD student in his group. I am very grateful for his guidance, support and patience during many discussions. I am also much obliged to Prof. Dr. Alexander Shnirman for agreeing to be the second reviewer of this thesis, and in particular for the many fruitful discussions on Josephson junction chains.

I am deeply grateful to Ivan Protopopov for his guidance, support and patience during the time of my Master's thesis and PhD. I learned a lot during our numerous discussions and his advice motivated me a lot to proceed. I really enjoyed working with him. I also want to thank Igor Gornyi for many helpful discussions.

Moreover, I am thankful to Stefan Backens, Elmer Doggen, Egor Kiselev, Janina Klier, Tim Ludwig, and Stefan Rex for proofreading parts of this manuscript, and thereby helping me to improve the quality of the thesis.

I also want to thank all members of the TKM for the great atmosphere, interesting discussions, and our joint activities such as the outings, the evinings with cake, the barbecues, and the swimming sessions. Special thanks go to my roommates at TKM and INT: Ulf Briskot, Pia Gagel, Mareike Hoyer, Nikolaos Kainaris, Egor Kiselev, Janina Klier, Mathias Scheurer, and Davide Valentinis. It was nice sharing an office with them. I thank Andreas Poenicke for excellent IT support. Many thanks also to Christine Fischer, Patricia Jäger as well as Fabienne Flatter and Sonja König for managing all the bureaucratic stuff.

Finally, I want to thank my family and friends for their support and the pleasant time we spent together. In particular, I am very grateful to my parents for their unconditional support during my whole life and especially during the time of my PhD.